Pacific Northwest
NATIONAL LABORATORY

Proudly Operated by **Battelle** *Since 1965*

Radionuclide Migration through Sediment and Concrete: 16 Years of Investigations

November 2014

EC Golovich   LJ Powers
SV Mattigod   GA Whyatt
MMV Snyder   DM Wellman

Radionuclide Migration through Sediment and Concrete: 16 Years of Investigations

EC Golovich
SV Mattigod
MMV Snyder
LJ Powers
GA Whyatt
DM Wellman

November 2014

Pacific Northwest National Laboratory
Richland, Washington 99352

Executive Summary

The Waste Management Project provides safe, compliant, and cost-effective waste management services for the Hanford Site and the U.S. Department of Energy (DOE) complex. Part of these services includes safe disposal of low-level waste and mixed low-level waste at the Hanford Low-Level Waste Burial Grounds in accordance with the requirements of DOE Order 435.1, *Radioactive Waste Management.* To partially satisfy these requirements, performance assessment analyses were completed and approved. DOE Order 435.1 also requires continuing data collection to increase confidence in the critical assumptions used in these analyses to characterize the operational features of the disposal facility that are relied on to satisfy the performance objectives identified in the order.

Cement-based solidification and stabilization is considered for hazardous waste disposal because it is easily done and cost-efficient. One critical assumption is that concrete will be used as a waste form or container material at the Hanford Site to control and minimize the release of radionuclide constituents in waste into the surrounding environment. Concrete encasement would contain and isolate the waste packages from the hydrologic environment and act as an intrusion barrier. Any failure of concrete encasement may result in water intrusion and consequent mobilization of radionuclides from the waste packages. The radionuclides iodine-129, selenium-75, technetium-99, and uranium-238 have been identified as long-term dose contributors (Mann et al. 2001; Wood et al. 1995). Because of their anionic nature in aqueous solutions, these constituents of potential concern may be released from the encased concrete by mass flow and/or diffusion and migrate into the surrounding subsurface environment (Serne et al. 1989; 1992; 1993a, b; 1995). Therefore, it is necessary to assess the performance of the concrete encasement structure and the ability of the surrounding soil to retard radionuclide migration.

This report summarizes data collected over 16 years of testing (1998 – 2010). Results from this work have been previously published in PNNL reports, book chapters, and peer-reviewed technical publications. Each of the test methods performed throughout the lifetime of the project has focused on different aspects of the concrete waste form weathering process. The concrete composition specified in *Specification for Concrete Encasement for Contact-Handled Category 3 Waste* (HNF-198) was used as the basis to prepare concrete for these experiments. Diffusion of different radionuclides [technetium-99 (Tc-99), iodine-125 (I-125), and uranium (U)] and surrogates [stable iodine (I) and rhenium (Re)] has been quantified from experiments under both saturated and unsaturated conditions. The water-saturated conditions provide a conservative estimate of the concrete's performance in situ, and the unsaturated conditions provide a more accurate estimate of the diffusion of contaminants from the concrete.

Dynamic and static leach tests have been conducted to determine the effect of iron particle incorporation on the leaching of contaminants in concrete specimens. Iron sources contained within the concrete specimens for the two sets of experiments included steel fibers, metallic iron (-40 to +60 mesh), or reactive nanoscale zero valent iron particles (RNIP). Tests showed that I-125 in the concrete formulations used in these studies was about two orders of magnitude less leachable than Tc-99. Inclusion of RNIP relative to metallic iron particles significantly increases the leachability of Re and I from waste form specimens. The leaching indices indicate that in the presence of 4% and 8% RNIP, Tc-99 had higher leachability than Re. Given these test results, Re is not a suitable surrogate for Tc-99.

A series of half-cell diffusion experiments with unsaturated Hanford sediment were completed to investigate the effects of test duration, sediment moisture content, concrete carbonation, concrete

fractures, and concrete iron content on diffusivity of I and Tc-99 from sediment and from concrete. Results showed that diffusion coefficients varied over a range of 3 orders of magnitude with Tc-99 being slightly more retarded than I. Within the range of measurements, increasing moisture content of the sediment routinely increased diffusion rates. The addition of iron resulted in a decrease in diffusivity in comparison to half-cells that did not contain iron, though increasing the amount of iron added did not consistently enhance the reduction of diffusivity values.

Carbonation of concrete using supercritical CO_2 increased the rate of the natural carbonation process and, in turn, resulted in increased diffusivity of I and Tc-99 in the half-cell experiments. Using a super-saturated carbonate solution for concrete carbonation resulted in a decrease in diffusivity coefficients; however resolving the mechanism for the reduction requires further investigation.

Depth of carbonation was more significant (up to 8 mm depth) in samples carbonated by supercritical CO_2 treatment. Carbonation under simulated vadose zone conditions is a much slower process than the supercritical CO_2 carbonation process, resulting in only surface carbonation (2 mm depth) of the samples encased in Hanford sediment for up to 2 years. Depth of carbonation increases over time, as observed in the concrete cores obtained from the Hanford Site with carbonation rates ranging from 0.3 to 0.9 mm per year. Additional investigation is necessary to resolve how carbonation depth will affect contaminant diffusion.

Unlike the diffusion trends observed for I and Tc-99, U exhibited no measurable rate of diffusion in the leach tests or half-cell diffusion experiments. As such, additional investigations were conducted to understand the potential mechanisms resulting in the observed difference. Under both undersaturated and oversaturated conditions with respect to U solid phases, U solid phases were prevalent throughout concrete waste forms after 2 weeks. The significance of the U paragenetic sequence was clearly demonstrated during the subsequent 2-month time frame. Uranyl-oxyhydroxide phases were followed by the formation of mixed uranyl-oxyhydroxide/silicates, leading to the formation of uranyl-silicates, then mixed uranyl-silicate/phosphate and uranyl-phosphate phases.

As demonstrated through the saturated leaching tests and comparing these results to those measured from the unsaturated diffusion tests, concrete encasement of waste disposed at Hanford under planned unsaturated and atmospheric (carbonated) conditions will provide a significant delay in radionuclide release into the subsurface. These results are waste form specific; therefore similar testing programs are needed to determine diffusion coefficients for current and future compositions considered for waste encasement.

Acknowledgments

Acronyms and Abbreviations

ANSI	American National Standards Institute
ASTM	American Society for Testing and Materials
BSE	backscattered electron mode
CFD	computational fluid dynamics
COPC	constituents of potential concern
C-S-H	calcium-silicate-hydrate
DDI	distilled deionized
DOE	U.S. Department of Energy
EDS	energy dispersive X-ray spectroscopy
EPA	U.S. Environmental Protection Agency
EXAFS	extended X-ray absorption fine structure
FY	fiscal year
HFS	Hanford fine sands
ICP-MS	inductively coupled plasma-mass spectrometry
ICP-OES	inductively coupled plasma-optical emission spectrometry
ITZ	interfacial transition zone
LLBG	Hanford Low-Level Waste Burial Grounds
LSC	liquid scintillation counting
PVC	polyvinylchloride
RH	relative humidity
RNIP	reactive nanoscale zero valent iron particles
SEM	scanning electron microscopy
SSRL	Stanford Synchrotron Radiation Laboratory
SU	standard units
TCLP	Toxicity Characterization Leaching Protocol
TOC	total organic carbon
XANES	X-ray absorption near edge structure
XRD	X-ray diffraction
ZVI	zero valent iron

Contents

Figures

xiv

xviii

Tables

1.0   Introduction

The Waste Management Project provides safe, compliant, and cost-effective waste management services for the Hanford Site and the U.S. Department of Energy (DOE) complex. Part of these services includes safe disposal of low-level waste and mixed low-level waste at the Hanford Low-Level Waste Burial Grounds (LLBG) in accordance with the requirements of DOE Order 435.1, *Radioactive Waste Management.* To partially satisfy these requirements, performance assessment analyses were completed and approved. DOE Order 435.1 also requires continuing data collection to increase confidence in the critical assumptions used in these analyses to characterize the operational features of the disposal facility that are relied on to satisfy the performance objectives identified in the order.

Cement-based solidification and stabilization is considered for hazardous waste disposal because it is easily done and cost-efficient. One critical assumption is that concrete will be used as a waste form or container material at the Hanford Site to control and minimize the release of radionuclide constituents in waste into the surrounding environment. Concrete encasement would contain and isolate the waste packages from the hydrologic environment and act as an intrusion barrier. Any failure of concrete encasement may result in water intrusion and consequent mobilization of radionuclides from the waste packages. The radionuclides iodine-129 (I-129), selenium-75 (Se-75), technetium-99 (Tc-99), and uranium-238 (U-238) have been identified as long-term dose contributors (Mann et al. 2001; Wood et al. 1995). Because of their anionic nature in aqueous solutions, these constituents of potential concern (COPCs) may be released from the encased concrete by mass flow and/or diffusion and migrate into the surrounding subsurface environment (Serne et al. 1989; 1992; 1993a, b; 1995). Therefore, it is necessary to assess the performance of the concrete encasement structure and the ability of the surrounding soil to retard radionuclide migration. A critical component of this is to provide (1) quantitative estimates of radionuclide retention within concrete waste form materials (source term) similar to those used to encapsulate waste in the LLBG, and (2) measures of the effect of concrete waste form properties on radionuclide release and migration within the near-field environment.

Waste forms are considered for radioactive disposal, including encapsulating the waste, serving as a container for the waste, grouting space, and for a repository. For waste form technology to be considered, information is required from laboratory testing to evaluate factors that affect contaminant release (van der Sloot et al. 2007; Kosson et al. 2002). Factors include information pertaining to the monolith's durability, effects of carbonation, and mechanisms that control release (including diffusion). Leaching tests are frequently used to estimate the release of COPC from the waste form. Leach tests that are commonly used to provide release of radionuclides and other constituents from waste forms include the Toxicity Characterization Leaching Protocol (TCLP), U.S. Environmental Protection Agency (EPA) Method 1315 (*Mass Transfer Rates of Constituents in Monolithic or Compacted Granular Materials Using a Semi-Dynamic Tank Leaching Procedure*), American National Standards Institute/American Nuclear Society (ANSI/ANS)-16.1 (*Measurement of the Leachability of Solidified Low-Level Radioactive Wastes by a Short-Term Test Procedure*), and American Society for Testing and Materials (ASTM) C 1308 (*Standard Test Method for Accelerated Leach Test for Diffusive Releases from Solidified Waste and a Computer Program to Model Diffusive, Fractional Leaching from Cylindrical Waste Forms*). The TCLP, however, has been criticized because (1) it is has a high solution-to-solid ratio; (2) it does not represent the arid, water unsaturated conditions found at waste sites; and (3) the test is performed on size-reduced material, which does not evaluate the monolithic waste forms.

1.1 Saturated Leach Tests

Saturated leach tests provide information on the release of COPCs from waste forms and the mechanisms controlling release, including diffusion, solubility limitations, and kinetics. McGlinn et al. (2008) evaluated a waste form under a saturated condition leach test over a period of 92 months. Release rates for aluminum (Al), calcium (Ca), strontium (Sr), potassium (K), sodium (Na), and sulfur (S) were shown to peak after 3 months of leach time, and the release of Al, Ca, Sr, and S leach rates decreased between 3 and 6 months of leaching. This rate decrease suggests that after 3 months precipitation or sorption occurs that incorporates the Al, Ca, Sr, and S and removes them from solution. Additional energy dispersive X-ray spectroscopy (EDS) analysis on the waste form showed that the Na and K were higher in concentrations at locations closer to the monolith's surface after 92 months of leaching, suggesting that diffusion is a transport mechanism for these two elements. X-ray diffraction (XRD) conducted on both the unleached and leached waste forms confirmed that as leach time increased (up to 92 months), the crystallinity of the calcium silicate hydrate phase in the waste form also increased.

In another saturated leach test, Bhunia et al. (2007) evaluated the leaching of arsenic (As) (III and V) from pulverized CalSiCo (patented trade name) sludge waste form. The leachability of the As(III) and As(V) were evaluated under varying pH conditions using distilled water, tap water, and rainwater for leachates. The leachability of As(III) was higher than the leachability of As(V), regardless of variables. Leaching of As from the waste form was higher when the leachate pH was less than 3 or greater than 11, and in the presence of chloride ions.

Bobirica et al. (2010) conducted dynamic leach tests on monolith waste forms containing chromium with distilled water and varying solution-to-cement ratios. The diffusivity slowly decreased as the solution-to-cement ratio increased. The observed diffusivity determined for each leaching interval was 15.87 mg/m^2 for the 0.4 solution-to-cement ratio, 16.11 mg/m^2 for the 0.7 solution-to-cement ratio, and 16.38 mg/m^2 for the 1 solution-to-cement ratio. Based on previous work by Bobirica et al. (2010), the chromium immobilization may be due to adsorption of the chromate onto the calcium-silicate-hydrate (C-S-H) in the cement. As the solution-to-cement ratio increases, the hydration rate of the cement also increases and thus the C-S-H is more available, also supporting the hypothesis that the C-S-H is immobilizing the chromium.

In addition to saturated leach tests evaluating the release of heavy metals, saturated leach tests to evaluate release of radionuclides in waste forms is also evaluated. In a diffusion experiment on different waste form materials including bentonite, granite, and concrete, several radionuclides were measured in diffusion cells saturated with groundwater (Szanto et al. 2002). Specifically, Tc-99 was evaluated in concrete. However, Tc-99 could not be measured during the short time frame of the experiments (3 months) because at a pH of 12 under reducing conditions, Tc-99 would be tetravalent (as TcO$_2$ or Tc(OH)$_4$), which strongly sorbs to the solid material.

The leachability of Tc-99 from Portland, aluminous, and blast furnace cements was evaluated for the potential for storage in a salt mine repository in Germany (Brodda 1988). The different cement samples were immersed in a brine solution and sampled up through 500 days. Blast furnace cement performance exceeded that of the Portland and aluminous cements by a factor of 10 to 100 and immobilized the Tc-99 with only 0.1% of the Tc-99 released during the leach tests. It was postulated that Tc-99 was immobilized by the formation of new mineral phases, but no evidence was presented to confirm this.

Batch experiments conducted by Atkinson and Nickerson (1988), where granulated solids were contacted with water containing the isotope of interest, determined that there were different sorption results for Sr, cesium (Cs), and iodine (I). Cs and Sr both displayed linear isotherms and the sorption was reversible. Cs was shown to be influenced by the liquid-to-solid ratio, where Cs had negligible sorption at the lowest ratio. Iodine was also reversible, but not linear, and at low concentrations I sorbed more strongly than the Cs.

A long-term study carried out by Kienzler et al. (2000) compared different techniques for mixing intermediate-level waste in cement waste forms as well as varying water-to-cement ratios and radioactive spikes. The cement waste forms were submerged in brine solutions for periods of up to 14 years. Cesium was released from the waste form after 4527 days at 28.2% and 38%. After 4034 days, Cs released was as high as 58%. In waste forms with lower solid-to-cement ratios, only 10% of Cs was released after 3600 days, and remained constant for up to 6441 days. Visual inspection verified the formation of surface cracks on the samples with the highest release rates. Uranium (U) release rates were more unpredictable. After 2700 days, concentrations of U in the brine differed by greater than a factor of 400 between samples made in 1984 and those made in 1989. The cause for this could not be determined. However, U was found to be stable in solution in the U(VI) oxidation state and U in solution was controlled by the formation of U solids.

Uranium solubility has been studied due to its abundance in cement-stabilized radioactive waste and significant effect on the overall radiological contribution of waste forms. Uranium aqueous chemistry can be complicated due to the multiple valence states that it can exist under depending on chemical conditions including pH and Eh (Brownsword et al. 1990). In oxidizing environments, U exists in the (VI) valence state (Harfouche et al. 2006) and tends to react with silica to form calcium uranium silicate (Glasser 1997). Over years, the solubility of U(VI) decreases as the silica phases are forming. After 2 years, measured U(VI) solubilities in the presence of calcium-silica-hydrogel are 10^{-9} M (Glasser 1997).

Moroni and Glasser (1995) studied the reactions between 46 different compositions with calcium and silica oxide, which are primary constituents in cement. The phases studied incorporated U as schoepite. Increasing the temperature conditions to 85°C causes the C-S-H gel crystallize after heating for 4 months, which forms different minerals depending on the ratio of Ca and Si. Low Ca/Si ratios formed tobermorite (1.0) where higher ratios (1.5) formed afwillite and jennite. However, when U was present it prevented the crystallization of the C-S-H gel throughout the experiment. Although U was evenly distributed through the cement, as it crystallizes it forms uranium-rich phases. As with previous studies, Moroni and Glasser confirmed that in the presence of abundant silica, formation of a calcium-uranium-silicate phase decreases the availability and solubility of U. Additionally, it was determined that the boundaries where silica activity increases showed an increase in the formation of precipitates.

Uranium added to cementitious waste forms as an aqueous uranyl ion (UO_2^{2+}) was confirmed by X-ray absorption near edge structure (XANES) spectra to remain in the UO_2^{2+} form after 5 to 6 months of reaction time (Sylwester et al. 1999). Samples subjected to 8 months of heating at 200°C also confirmed U in the form of the uranyl ion. One difference between the heated and unheated cement was the indication of surface precipitation, which was only observed in the heat-treated cement (Sylwester et al. 1999).

Brownsword et al. (1990) studied the sorption and solubility of U in the form of uranyl salt added to three different backfill concrete waste forms subjected to hydrothermal treatment and leaching conditions.

They concluded that at pH greater than 7 the solubility of sodium and calcium uranate was not affected by the pH. At pH less than 7, the solubility values increased as the pH decreased. Brownsword et al. also concluded that the distribution ratio of U(VI) increased by a factor of two for the hydrothermally treated cement.

Saturated leach tests are also used to evaluate the effect of binders (such as fly ash) on COPCs and radionuclides and to provide a fundamental understanding of the release mechanisms involved. For example, one experiment used EPA Method 1315 to evaluate the release of COPCs using varying percentages of fly ash (0%, 20%, and 45%) from three different sources to replace the Portland cement in the waste form recipe (Garrabrants et al. 2014). Incorporating fly ash into the concrete has been shown to improve the strength and durability of the concrete. Eleven COPCs were evaluated for this study, but only release rates for barium, boron, chromium, and vanadium were determined because the other elements were not detectable in the eluate. The different fly ash sources and percentages had the most effect on the barium release results. This can be attributed to the changes in the leachable barium, which is determined under relevant field conditions, such as pH.

Garrabrants et al. (2014) determined that varying percentages of fly ash had little to no effect on the release rates of COPCs and the microconcretes (i.e., concrete material without the coarse aggregate) showed comparable results to the Portland cement (Kosson et al. 2014). Giergiczny and Krol (2008) evaluated the release of heavy metals (including lead, zinc, copper, chromium, manganese, and cadmium) when added to binders including fly ash, blast furnace slag, and Portland cement. Water extractions were performed on reduced grain size fractions of each material. All metals excluding Cr were immobilized in the hydrated binder (>99%). Chromium was immobilized from 85% to 93%. Immobilization was affected by the composition of the binder as well as the time the binder was allowed to cure prior to the sorption tests, with 180 days of cure time showing the highest immobilization of the metals. These results suggest that the addition of a binder can help stabilize some heavy metals (Giergiczny and Krol 2008).

Additives may be added to the cements and waste forms used for radioactive waste repositories to modify their properties (i.e., improve strength). Greenfield et al. (1998) evaluated the solubility of Tc-99, U, Plutonium (Pu), and Americium (Am) in Portland cement with two Japanese cement additives. Plutonium, Am, and U exhibited similar results, with solubility one to two orders of magnitude higher in concrete containing the additives. Technetium, however, only showed an increase in solubility with one of the additives, and much less of an increase with the other.

As discussed above, the release of COPCs from cement waste forms is typically evaluated under continuously saturated conditions. However, estimates of COPC release from waste forms based solely on continuously saturated leach conditions can result in overestimations of constituent release.

1.2 Unsaturated Leach Tests

While conservative estimates provide an understanding of in situ performance, additional investigations of unsaturated conditions are also important to provide more accurate measures of diffusion or leachability of contaminants from the waste forms. Additionally, field conditions at waste sites frequently present varied environmental conditions including wet and dry cycles and changes in carbonation. These changes in environmental conditions result in conditions under which advection may not be the predominant means for COPC release from the waste form, but rather diffusion under water

unsaturated conditions can be the governing means for release. Moreover, the natural variation in environmental conditions can lead to physical and chemical changes to the waste form, due to weathering processes, which may further affect the retention/release of COPCs from the waste form. For example, carbonation, microcracking, and the formation of secondary phases can all result from changes in the environment. The release of constituents is affected by factors including carbonation, pH, precipitation of new species, and relative humidity (RH). Understanding the diffusion of COPCs from concrete waste forms under relevant environmental conditions is necessary to quantify more representative release rates under arid and semi-arid conditions.

Previous investigations that evaluated the effect of intermittent wetting interspersed with storage indicated both chemical and physical changes in the matrix of the cement, including a significant change in the carbonation during dry cycles (Garrabrants et al. 2002; Gervais et al. 2004; Sanchez et al. 2003, 2002). Carbonation of samples was found to decrease the alkalinity and pH of the solution in contact with a carbonated wasteform (Garrabrants et al. 2002; 2004; Sanchez et al. 2002; Gervais et al. 2004). This has significant implications on the retention of heavy metals, including arsenic, cadmium, and lead, because the solubility of such contaminants is dependent on the pH of the aqueous phase.

In both saturated and unsaturated experiments, carbonation resulted in a decrease in the release of cationic constituents due to the formation of calcium carbonate precipitates (Garrabrants et al. 2002, 2004; Gervais et al. 2004; Sanchez et al. 2002; Venhuis and Reardon 2001). Similarly, carbonation resulted in a decrease in the release of most metals, including lead, mercury, and copper because they are absorbed or used to form new precipitates, and an increase in the release of arsenic and cadmium (Garrabrants et al. 2002, 2004; Gervais et al. 2004; Sanchez et al. 2002; Bertos et al. 2004; Chen et al. 2009; Lange et al. 1996a, b). Unlike cations, anionic constituents display either no effect or an increase in their release rate or diffusion due to carbonation (Garrabrants et al. 2002, 2004; Gervais et al. 2004; Sanchez et al. 2002; Bertos et al. 2004; Venhuis and Reardon 2001). Physical changes resulting from carbonation include an increase in the compressive strength due to a reduction in the porosity of the cement as well as a reduction in permeability (Chen et al. 2009; Hartmann et al. 1999; Lange et al. 1996a, b; Venhuis and Reardon 2001; Dewaele et al. 1991; Malviya and Chaudhary 2006). These physical changes, including porosity and permeability, are parameters that affect the performance of the waste forms. Other constituents of concrete or cement waste forms that have been studied to test whether they affect the release of COPCs include the effect of fly ash and the addition of minerals and heavy metals (Garrabrants, et al. 2014; Giergiczny and Krol 2008; Kosson et al. 2002; Malviya and Chaudhary 2006).

Calcium and hydroxide ions are part of the structure of cement-based waste forms because calcium hydroxide makes up to 25% by weight of Portland cement-based waste forms. The release of calcium hydroxide from cement affects the chemical components and the durability of the waste form. Additionally, the release of hydroxide from the cement affects the pH of the porewater. Studies from Garrabrants et al. (2002) and Sanchez et al. (2002, 2003) indicated that intermittent wetting, under varying RH, resulted in a higher pH during the first interval of the leaching cycles. This suggests pH gradient relaxation, which results in an increase in hydroxide being released and consequently an increase in the leachate pH. Studies by Gervais et al. (2004) suggest there was a decrease in the leachate pH when the experiment conditions were in 100% carbonate atmosphere, with the most significant decrease occurring at low RH conditions. The release of hydroxide in a carbonated atmosphere resulted in a decrease of release rates because the hydroxide ions were consumed in a carbonate reaction (consumption of hydroxide ions to form a carbonate species) (Gervais et al. 2004). Similar to the pH, the calcium release rate from the concrete waste form in the 100% carbonate atmosphere was significantly less and

released <32,000 mg of calcium/m^2 when compared to the noncarbonated concrete waste form, which released >60,000 mg of calcium/m^2 after 47 days of leaching (Gervais et al. 2004). Among the carbonated samples, calcium release from the concrete waste forms increased with an increase in the carbonate atmosphere due to formation of calcium carbonate precipitates that formed during dry cycles and then were later released during leaching (or "wet" cycles) (Garrabrants et al. 2002; Gervais et al. 2004).

Release rates for some COPCs, including heavy metals, are dependent on the changes in pH. For example, the release of arsenic, cadmium, and lead is affected by intermittent wetting conditions and the release of all three metals was lowest under higher RH (Garrabrants et al. 2002; Sanchez et al. 2002, 2003). Carbonation affected the behavior of As, Cd, and Pb (Sanchez et al. 2002, 2003). Arsenic and lead release rates increased in a carbonated atmosphere as a result of re-speciation from the carbonation. Within the carbonated leach tests, arsenic release decreased as a result of a decrease in pH, and in noncarbonated leach conditions, arsenic and cadmium release increased with a decrease in pH of the leachate (Sanchez et al. 2003, 2002). Lead release decreased as a result of decreasing pH for both leach tests with and without carbonation.

Unlike heavy metals, some soluble cement-based species, including Na, K, and chloride (Cl), are typically not influenced by the pH changes in the porewater. However, Garrabrants et al. (2002) and Gervais et al. (2004) found that release rates for chloride and to a lesser degree potassium were influenced by the creation of precipitates that formed during the drying phase of the intermittent wetting cycles. Sodium release rates increased under intermittent wetting conditions when compared to saturated conditions (Garrabrants et al. 2002; Gervais et al. 2004). Carbonation, conversely, resulted in a decrease in the release of sodium (Gervais et al. 2004; Sanchez et al. 2002). This may be due to the formation of a carbonate front, which acts as a barrier for the diffusion.

1.3   Carbonation

Carbonation can affect the structure of cement-based waste forms as well as the release rates of heavy metals. Therefore, it is important to understand the effect of carbonation on potential waste forms. As previously stated, carbonation decreases the alkalinity. Reducing the alkalinity also reduces the buffering capacity of the waste form so it may be more vulnerable to effects from an acid environment, which would also effect the release of COPCs in the long term (Bertos et al. 2004). Further exploring the effect of carbonation on concrete mixes, Al Khayat et al. (2002) tested different concrete mixes in hot, arid weather in Kuwait. Parameters studied included water-to-cement ratios, cement content, type of cement, admixtures (water reducing, water-retarding, and plasticizing admixtures), water-curing period, coatings on the concrete, and the addition of silica fume and pulverized fuel ash and their effects on carbonation. Curing compounds and coatings were varied and applied to the concrete to determine if they would reduce the amount of CO_2 diffusion into the concrete. The different concrete mixes were cured in air and/or water for varying periods. After curing, the depth of carbonation was measured by slicing the concrete to a minimum thickness of 20 mm and applying a phenolphthalein indicator solution all over the concrete surface. Al Khayat et al. (2002) found that the depth of carbonation was most affected by the water-to-cement ratio of the concrete. The water-to-cement ratios were varied between 0.45 to 0.80 and the cement content between 456 and 256 kg/m^3. As the water-to-cement ratio increased, the depth of carbonation also increased nearly three-fold, with a maximum carbonation depth of 24 mm. Haque and Al-Khaiat (1997) evaluated concrete that was used in buildings exposed to hot, dry, salty environments to

evaluate the density, compressive strength, and depth of carbonation of the concrete. They determined that the depth of carbonation is not directly attributed to the water-to-cement ratio, but rather to the more open pore structure found in cement with higher water-to-cement ratios, which subsequently lowers the compressive strength. The depth of carbonation is dependent on the quality of the concrete (specifically the compressive strength) and the exposure conditions (higher carbonate penetration in dry situations and lower in wet conditions) (Haque and Al-Khaiat 1997).

The physical reaction that occurs when the concrete waste form is carbonated is diffusion-controlled. The CO_2 gas diffuses into the solid waste form, which forms a carbonated material that grows around a zone that contains the non-carbonated material (Bertos et al. 2004). Similarly, Chang and Chen (2006) tested the depth of carbonation on Portland cement waste forms subjected to carbon dioxide (CO_2) for 8 and 16 weeks. They found that the degree of carbonation was dependent on the depth from the concrete surface, where the waste form was exposed to CO_2. The outermost part of the waste form resulted in full carbonation, followed by partly carbonated and noncarbonated zones moving in from the surface of the waste form. The degree of carbonation correlated to the pH of the pore solution. Fully carbonated zones (>50%) corresponded to pH less than 9, partly carbonated zones to pH between 9 and 11.5 (where calcium hydroxide and calcium carbonate were observed), and the noncarbonated zone had pH greater than 11.5 with no signs of carbonation (no calcium hydroxide or carbonate observed) (Chang and Chen 2006). A schematic depicting this reaction that is from Bertos is displayed in Figure 1.1.

After the CO_2 has diffused into the waste form, the hydration of CO_2 converts to carbonic acid (H_2CO_3), which is then ionized to H^+, HCO_3^-, and CO_3^{2-}. This causes the pH to decrease, which results in the dissolution of major calcium silicate phases that are found in cement waste forms. Initially, the calcium silicate grains are covered by a gel, but the gel quickly dissolves and Ca^{2+} and SiO_4^{4-} are released into solution, which eventually leads to re-precipitation of the calcium ions as calcium carbonate ($CaCO_3$) (Bertos et al. 2004).
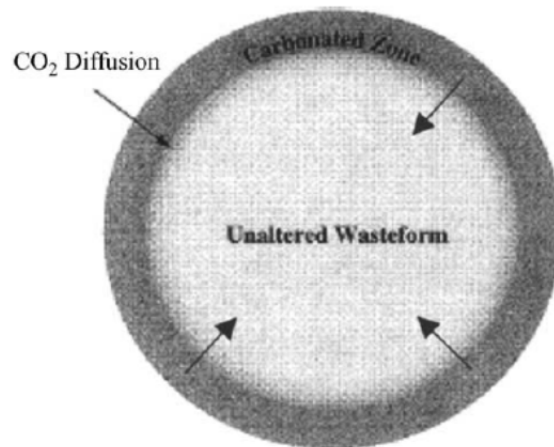
Figure 1.1. Schematic depicting the reaction that occurs with carbonation of the waste form (from Bertos et al. 2004)

Bertos et al. (2004) summarized how the reactivity and diffusion of the CO_2 affects the waste forms. Reactivity and diffusion of carbonate in waste forms is dependent on certain conditions, including the type of cement used, the water-to-cement ratio, the degree of hydration, compaction pressure, the

concentration of the CO_2, and the RH (Sims 1994). More specifically, the reactivity is dependent on the solid composition and the water content. The type of cement and the addition of binders such as blast furnace slag and fly ash, for example, can influence the carbonate reaction in waste forms. Lange et al. (1996b) found Portland cement displayed the most reactivity when exposed to CO_2 and the addition of blast furnace slag resulted in the highest carbonate uptake for several different waste forms tested. This may be because the blast-furnace slag contains less calcium hydroxide and the reaction with CO_2 may be more pronounced. Similarly, Macias et al. (1997) found chromium uptake to be the highest in Portland cement containing the additive blast furnace slag. Carbonation of the cement resulted in the development of separate Cr-rich and Cr-poor zones, with less Cr in the near-surface layers of the carbonated samples (Macias et al. 1997).

Carbonation occurs in waste forms that contain Ca. Higher concentrations of Ca result in more carbonation reactions. Similarly, the higher the ratio of Ca to Si, the higher the degree of carbonation reactions. The presence of Ca Al oxide phases that are typically found in the composition of the cement is important to the formation of the secondary precipitate ettringite. Ettringite is a secondary reaction product that forms as a result of hydration of Portland cement. In the presence of CO_2, ettringite $(Ca_6Al_2(SO_4)_3(OH)_{12} \cdot 26H_2O)$ decomposes to other minerals including gypsum, calcium carbonate, and an alumina gel. Other alteration phases that result from cement (including non-carbonated) include the minerals alite (Ca_3SiO_5), belite (Ca_2SiO_4), aluminate $(Ca_3Al_2O_6)$, and ferrite $(Ca_2(Al,Fe)_2O_5)$ (Malviya and Chaudhary 2006). The rate of carbonation is also influenced by the solid content of some metals including lead, cadmium, and nickel, which can increase the permeability, resulting in a decrease of the alkaline buffering capacity, which eventually leads to an acceleration of hydration.

Studies have shown that carbonated waste forms that contain metals can be as much as 40% higher in calcium carbonate deposited compared with waste forms that do not contain metals. The formation of calcite can affect the leachability of metals. Lange et al. (1996a) found that the release of metals such as lead, zinc, and nickel were lowest in carbonated samples with high calcite contents, suggesting the metals precipitated as carbonates and silicates. Similarly, Chen et al. (2009) conducted saturated leach tests on Portland cement waste forms made with varying ratios of sediment samples that were collected from a landfill leachate treatment lagoon over a range of solid-to-water ratios. Using an X-ray diffractometer, Chen et al. confirmed the presence of secondary minerals including portlandite, ettringite, and calcite. Compressive strength was measured in the samples and was found to increase as solid-to-water ratios decreased, and was higher in carbonated cement samples than it was in non-carbonated cement samples. As expected, the higher solid-to-water ratios resulted in a decrease in the release of mercury as a result of the reduction of mercury mobility due to carbonation. Additional studies by Hills et al. (1999) solidified synthetic heavy metal waste in Portland cement and subjected the cement to carbonated and non-carbonated conditions. The carbonated samples resulted in approximately 26% lower pore volume than the non-carbonated samples and indicated approximately a 15% decrease of the calcium in the carbonated cement.

Conversely, Bertos et al. (2004) summarized that organics and anions can decrease the amount of carbonation that occurs in the waste forms. Water must be present in the waste form to promote the reaction with CO_2, but having too much water can block pore spaces in the waste form and inhibit reactions. Studies using X-ray methods show that for water-to-cement ratios between 2 and 4, the acidity of the solution is very much affected and increases after CO_2 is added to the system, showing that there is effective penetration of the CO_2. However, these conditions do not result in strong waste forms. At water-to-cement ratios between 0.06 and 0.2, there is penetration and diffusion of the CO_2 into the waste

form without compromising strength. The strength of a carbonated waste form can be as much as 45% higher than waste forms cured in a nitrogen atmosphere.

The diffusivity of CO_2 into the waste form is dependent on physical properties of the waste form (Bertos et al. 2004). The compaction pressure of the granular material before it is subjected to carbonation influences the CO_2 diffusivity. The porosity and permeability are decreased when the compaction pressure increases, which results in a stronger waste form. Conversely, the lower porosity does not allow as much diffusion of CO_2 into the waste form, which decreases the formation of $CaCO_3$, resulting in lower strength. Several studies have been conducted that confirm the increase of strength in the waste form after being subjected to carbonation, and some established a rate for the depth of carbonation over time (Khan and Lynsdale 2002; Chen et al. 2009; Chang and Chen 2006; Lange et al. 1996c). Carbonation is found to affect the waste form the most at an RH of 50% to 70%, and decreases at RH outside of this range. The penetration of CO_2 increases as the temperature increases up to 60°C. At temperatures higher than 60°C, the solubility of CO_2 in water decreases, making it less available for carbonation. Lastly, a slight pressure when applying the CO_2 increases the rate of reaction. Supporting this information, Hartmann et al. (1999) found that the treatment of radioactive cement waste forms with supercritical CO_2 under low pressure conditions improved the leach resistance of radionuclides (specifically thorium-232 and europium-151 and 153).

Carbonation causes both physical and chemical changes in waste forms. As summarized in Bertos et al. (2004), these include changes in permeability, contaminant mobility, hydration, strength, porosity, and pore size distribution. As mentioned previously, calcium released from the waste form converts to a calcium carbonate when exposed to CO_2. The calcium carbonate forms in the pore structure of the waste form increasing the volume, resulting in a lower pore volume. Other precipitate products form as a result of reactions of the structure of the waste form with the leachate and carbonate, including calcite in the pores, a calcium silica gel, formation of ettringite, and subsequent formation of gypsum from decomposition of the ettringite. The formation of calcium carbonate in the pore spaces of the waste form results in approximately twice as much volume than in non-carbonated waste forms, which is attributed to the small pore spaces. The expansion on the volume also leads to the formation of microcracks where the carbonation reaction occurs. Microcracks have been shown to influence the fracture characteristics of concrete waste forms and result in greater-than-average depth of carbonation in the concrete along these microcracks (Campbell et al. 1991).

A common problem that affects the durability of the concrete is the corrosion of the steel used to reinforce the concrete (Papadakis et al. 1989). Corrosion of the reinforcing steel can cause the concrete to fracture parallel to the reinforcement bar. Typically, reinforced bars in concrete have a thin oxide layer that forms on the surface of the steel as a result of the highly alkaline environment (pH around 13) and serves as a protecting layer. Exposure of the concrete to CO_2 can reduce the pH to less than 9 and/or expose the bars to chloride ions that diffuse into the porewater due to a decrease in the pH. These processes cause the reinforcement bars to corrode. Microcracking of the concrete due to exposure to CO_2 can also affect the depth of the carbonation within the concrete, accelerating corrosion.

Castel et al. (1999) studied reinforced concrete beams stored for years (since 1984) exposed to atmospheric CO_2 and conditions representative of environmental conditions the concrete structures are found in. Microcracks were found primarily at the interfacial transition zone (ITZ). The ITZ is the region of the concrete around the aggregate particles that tends to have fewer cement particles and more water. Results showed that the microcracks played a significant role in the depth of carbonation. At locations of

microcracks, the carbonation penetration reached the middle of the concrete and displayed corrosion of the steel, whereas in locations where the tensile microcracks were not located, the steel reinforcements did not display any corrosion. Additionally, Castel et al. found that the microcracking was deeper laterally as opposed to measurements on the upper and bottom surface of the concrete beams.

In addition to affecting the depth of carbonation, fractures also influence the flow path and provide larger surface areas that can promote reactions. In a study conducted by Matzen et al. (2000), Portland cement used in the Yucca Mountain Project's Exploratory Studies Facility was fractured and solution containing iodide, neptunium (Np), and U was pumped through the cement at a constant flow rate. The breakthrough of iodide was conservative and was similar to previous experiments showing no measureable retardation. In contrast with batch sorption studies, the Np and U were not detected in the effluent from the fracture flow experiment. Gamma counting, alpha particle tracking, and secondary ion mass spectrometry revealed the highest concentrations to be on the inlet and on the face of the fracture, and 1 to 2 cm along the fracture, which suggested advective transport. The advective transport suggests the potential of a secondary fracture; however, this was not confirmed by additional two-dimensional maps adjacent to the fracture. Matzen et al. (2000) concluded that elution of U appeared to be solubility-limited while Np was likely controlled by sorption. Due to the large surface area and the reactivity of the minerals in the concrete, the reactions that occur in the fracture are rapid and produce alteration products that could make the fractures self-sealing and form particle filters.

The studies discussed represent the majority of experimental work performed on potential waste form candidates. Similar to the studies summarized, laboratory testing is required to understand and evaluate factors that affect COPC release. Characterization of the waste forms, including the monolith's durability, effects of carbonation and other environmental influences, and mechanisms that control release (including diffusion), must be well understood. For concrete to be considered as a waste form for disposal of hazardous waste at the Hanford Site, it is critical to understand diffusion of radionuclides from the waste form under conditions expected at the waste disposal site. Carbonation, changes in wet and dry cycles (affecting the moisture content present), and the presence or omission of iron under both saturated and unsaturated conditions will provide the information needed to evaluate the waste form's durability and performance. In summary:

- Release rates for some metals, including Cr, are shown to decrease over time due to adsorption onto C-S-H.

- Release rates of different elements are affected by chemical changes, such as pH. The release of lead, for example, has been shown to decrease as a result of decreasing pH.

- Intermittent wetting during storage of the waste form can cause both chemical and physical changes.

- Carbonation can affect the structure of waste forms and release rates of COPCs.

  - Carbonation can result in an increase in the compressive strength of the waste form due to a reduction in porosity.

  - Exposure to CO_2 decreases the pH of the solution in contact with the waste form, which results in dissolution of calcium silicate phases in the waste form.

  - Over time, carbonation encourages the formation of calcium carbonate precipitates, which decreases the release of cationic constituents.

- Uranium (U(VI)) reacts with silica to form calcium uranium silicates.

- The addition of binders, including fly ash and furnace slag, can help immobilize some COPCs.

- Fractures can influence the flow path, provide larger surface areas to promote reactions, and affect the depth of carbonation.

    – An increase in the depth of carbonation can lead to more rapid corrosion of iron in the concrete.

The purpose of this report is to summarize the data obtained from tests conducted over the past 16 years. Results from this work has been previously published in PNNL reports, book chapters, and peer-reviewed technical publications and include Mattigod et al. (1999, 2001, 2004); Wellman et al. (2006b; 2007b, c; 2008a, b), Mattigod et al. (2009; 2010; 2011; 2012a) Bovaird et al. (2011), Wellman et al. (2012), Mattigod et al. (2012b), and Snyder et al. (2013). Each of the test methods performed has focused on different aspects of the concrete waste form weathering process. Diffusion of different analytes has been quantified from experiments under both saturated and unsaturated conditions. The water-saturated conditions provide a conservative estimate of the concrete's performance in situ, and the unsaturated conditions provide a more accurate estimate of the diffusion of contaminants from the concrete. Variables evaluated to determine what, if any, affect they have on the leach of contaminants from the concrete include iron content and carbonation in the concrete, and moisture content of the sediment (for half-cell experiments).

2.0 Materials and Methods

2.1 Concrete Composition

The concrete composition for the burial encasement was specified in *Specification for Concrete Encasement for Contact-Handled Category 3 Waste* (HNF-1981). This specification was used as the basis to prepare a concrete for fabrication of test specimens. The composition includes sulfate-resistant Portland Type I or Type II cement, a pozzolanic material (Class F fly ash), fine and coarse aggregates, and steel fiber. Additional specifications include a water-to-cement ratio of 0.4 and an air content of 6.0 ± 1.5%. The nominal proportions and material specifications based on this initial design are listed in Table 2.1.

Table 2.1. Concrete material specifications and composition

Material	Specifications	Specified Field Mix	Normalized Specification Design
Cement	Portland Type I or Type I/II sulfate-resistant cement	381 kg/m^3	0.27
Fly Ash	Class F fly ash; nominal 15% of cement by volume	54 kg/m^3	0.04
Coarse Aggregate	No. 676 or equivalent (3/4 in. nominal size)	55% by volume	0.04
Fine Aggregate	Sand	45% by volume	0.51
Water	Nominal water-to-cement ratio: 0.4	399 kg/m^3	0.10
Steel Fiber	Deformed Type I, nominal length 2.5 to 3.8 cm (1 to1.5 in.)	59 kg/m^3	0.04
Air Content		6.0±1.5%	

2.2 Materials and Laboratory-Scale Mixture Design

The laboratory-scale concrete mixtures (Table 2.2) were prepared based on specifications shown in Table 2.1. Often when making concrete samples, because of the required small dimensions of the laboratory test specimens, the coarse aggregate was omitted and 40 to 60 mesh sized sand was used instead. Based on these modifications, a concrete mix was prepared that consisted of Portland cement (Type I/II sulfate resistant, ASTM C-150 compliant cement); Class F fly ash, sand, steel or an iron powder (when applicable); and a water-entraining agent (PolyHeed 997). A water-entraining agent was included in the mix to facilitate the workability of the concrete. The volumes of the PolyHeed 997 were not included in the normalization calculations because of their negligible contribution to the overall mix volume. The material specification and composition for the laboratory-scale concrete mixture is given in Table 2.2.

The contaminant of concern was either added to the water component used to prepare the concrete monoliths or to the sediment component used for the half-cell experiments. Contaminants that were used in experiments included stable I, rhenium (Re), and U, added as sodium iodide, sodium perrhenate, and uranyl nitrate, respectively. Radionuclides used included Tc-99 and I-125. I-125 was added as a commercially available stock solution. Technetium metal was dissolved in concentrated hydrochloric

acid and diluted with distilled deionized (DDI) water to create a stock solution that was used in these experiments.

Table 2.2. Laboratory-scale material specification and composition

Material	Material Specifications for Field Mix	Normalized Laboratory Design	Material Specifications Used in Revised Laboratory Mix Comparison
Cement	Portland Type I or Type I/II sulfate-resistant cement	0.27	Portland Type III
Fly Ash	Class F fly ash; nominal 15% of cement by volume	0.04	Class F fly ash; nominal 20% of cement by volume
Fine Aggregate	Sand	0.51	Industrial quartz Accusand 40 to 60 mesh (0.420 to 0.250 mm)
Water	Nominal water-to-cement ratio: 0.4	0.10	Water-to-cement ratio: 0.5
Steel Fiber	Deformed Type I, nominal length 2.5 to 3.8 cm (1 to 1.5 in.)	0.04	Deformed, nominal length 8 mm (0.32 in.) or iron powder 40 to 60 mesh (0.149 to 0.177 mm).
PolyHeed 997	--	0.00375	Water-entraining agent
Air Content	6.0 ± 1.5%	6.0 ± 1.5%	--

2.3   Concrete Mix and Specimen Preparation

Concrete monoliths were prepared by mixing the dry ingredients (steel or iron powder [if applicable], sand, fly ash, and cement), adding the PolyHeed 997 and water, and mixing. The concrete was mixed with a whisk in steel bowl for 3 to 5 minutes prior to pouring into molds. As required for testing, contaminant spikes were added as part of the water component prior to mixing.

The molds for casting concrete specimens were fabricated from a variety of materials (Fisher brand poly sample vials with a hinged cap, 7 mL flat bottom poly vials, small poly beakers, Fisher brand Polystyrene (pill bottles) containers, or Schedule 40 polyvinylchloride [PVC] piping material). Gaskets were glued to the bottom of the PVC molds and leak tested before use. The forms were pre-treated with form release, a liquid that allows the concrete specimen to release easily from the mold. The first treatment was applied 3 days prior, and the second treatment was applied a few hours before wet concrete was added to the molds.

The molds were filled in the vertical positions. After filling, the molds were lightly tapped on the laboratory bench or vibrated using a handheld vibrator until a significant decrease in the release of air bubbles was observed. The forms were stored in a plastic bag with damp paper towels (monoliths made 1998 to 2001) or a humidity chamber (monoliths made 2002 to 2013) for 28 days while the concrete set.

2.3.1   Variables in Sample Preparation

Key variables affecting the physical stability and possible chemical mechanisms of retention/release for the contaminant of concern from the concrete waste form were varied during the preparation of the concrete to assess the effect of these variables on the leaching of contaminants from the concrete.

Experimental components varied included carbonation, iron, moisture content, and fracturing of the monolith samples. Table 2.3 lists the variations in each of the experiments presented in this report.

2.3.1.1   Carbonation

Concrete specimens prepared prior to and including 2006 were carbonated using supercritical CO_2 treatments. Carbonation was achieved by putting the monolith concrete samples under vacuum at 35°C for one week. After 1 week, samples were injected with 2.2 mL of water containing CO_2, also at 35°C and 8.4 MPa. The samples were kept in the vacuum chamber for 24 hours to allow the water to convert to carbonic acid. The carbonic acid subsequently reacted with $Ca(OH)_2$ contained in the cement matrix.

Starting in 2007, carbonation of the concrete was achieved by soaking the monoliths in a saturated carbonate solution. Sodium-bicarbonate was added to water until a saturated solution was achieved. The monolith concrete samples were submerged in the saturated solution for 7 days. This modification in procedure was made to reduce the time needed for carbonation when the size and number of monoliths needed for testing increased.

2.3.1.2   Iron

Prior to 2002, Bekaert Dramix brand steel wire fibers cut to a nominal length of 8 mm (0.31 in.) were used as the iron source when preparing the concrete specimens. The deformed ends were used for the concrete mixture and the straight middle section was discarded (Figure 2.1).

The steel fibers were of varying length and there was a coating on the fibers that resulted in a shiny surface, which may have resulted in limited contact of the iron with the concrete materials. Beginning in 2002, an iron powder with particle diameters 40 to 60 mesh (0.231 to 0.389 mm) was used in the concrete mixture instead of the fibers.

Figure 2.1. Steel wire fiber

Table 2.3. Experimental variable test matrix

Test	Started Fiscal Year	Spike Concentration (mg/g)	Test Duration (days)	Moisture Content (wt%)	Iron Content (wt%)	Carbonation	Sediment
			Half-Cell Diffusion				
Sediment-Sediment	1999	I: 5.8×10^{-2} (4%) Tc: 6.38×10^{-4} (4%) U: 5.6×10^{-7} (4%) I: 6.5×10^{-2} (7%) Tc: 8.9×10^{-4} (7%) U: 5.7×10^{-7} (7%)	64, 170	4, 7	4	No	Trench 8
Sediment-Concrete	2006	I: 1.2×10^{1} (4%) Re: 1.5×10^{1} (4%) I: 1.2×10^{1} (7%) Re: 1.2×10^{1} (7%) I: 1.3×10^{1} (15%) Re: 1.3×10^{1} (15%)	348 (4%) 354 (7%) 355 (15%)	4, 7, 15	0, 4	Yes/No	HFS
	2008	I: 7.0×10^{0} Tc: 4.2×10^{-4}	351	4, 7, 15	0, 4, 8, 12	Yes/No	HFS
Concrete-Sediment	1999	I: 4.6×10^{-1} I-125: 2.1×10^{-8} Tc: 1.7×10^{-3} U: 1.0×10^{-2}	64, 170	4, 7	4	No	Trench 8
	2002 (7%) 2004 (4%)	I: 4.7×10^{-1} Re: 7.0×10^{-1}	357 (7%) 397 (4%)	4, 7	0, 4	Yes/No	HFS
	2007	Tc: 5.9×10^{-4}	698	4, 7, 15	0, 4	No	HFS
Fractured Concrete-Sediment	2008	I: 3.2×10^{1} Re: 3.2×10^{1}	385	4, 7, 15	0, 4, 8, 12	Yes/No	HFS
	2010	Tc: 5.9×10^{-4} I: 3.2×10^{1} (not analyzed)	182	4	0, 4, 8, 12	Yes/No	HFS
Sediment-Fractured Concrete	2006	I: 7.0×10^{0} Re: 7.0×10^{0}	467	4, 7, 15	0, 4	Yes/No	HFS
	2010	Tc: 3.2×10^{-4}	182	4	0, 4, 8, 12	Yes/No	HFS
			Leaching				
Dynamic & Static Leach	2000	I: 4.6×10^{-1} I-125: 2.06×10^{-8} Tc: 1.73×10^{-3} U: 1.03×10^{-2}	92	-	0, 4	No	-

Test	Started Fiscal Year	Spike Concentration (mg/g)	Test Duration (days)	Moisture Content (wt%)	Iron Content (wt%)	Carbonation	Sediment
Dynamic Leach	2006	I: 3.2×10^1 Re: 3.2×10^1 Tc: 5.9×10^{-4}	92	-	0, 4, 8, 12	No	-
Carbonation and Microcracking							
Carbonation Microcracking	2002	I: 4.74×10^{-1} Re: 7.0×10^{-1}	357 (7%) 397 (4%)	4, 7	0, 4	Yes/No	HFS
Carbonation Microcracking	2004	-	~182 ~730	4, 7, 15	0	No	HFS
HFS is Hanford fine sands							

2.3.1.3 Fractured Concrete

To assess the effect of fractures in the concrete on diffusion of the contaminants, the monoliths were wrapped in shrink-wrap to prevent the formation of rubble; the end of a flathead screwdriver was placed directly in the center of the core and struck once. Each fractured concrete monolith had a single midline fracture that penetrated the length of the core.

2.3.1.4 Moisture Content

The moisture content of the sediment used in the half-cell experiments was varied between 4%, 7%, and 15% by weight. These percentages are representative of the moisture content found on the Hanford Site (Serne et al. 1993a, b). Initial sediment moisture content was determined by weighing out a 3 to 4 g sample of the sediment and allowing it to dry in an oven at 105°C for a minimum of 24 hours, at which time another mass measurement would be obtained. Oven drying continued until a constant mass was observed and the amount of moisture required (by weight) to achieve the desired moisture content was calculated. To reduce moisture content, sediment was left at room temperature on the laboratory bench in an open pan until the necessary water evaporated from the sediment, as confirmed by moisture content measurements. To increase the moisture content, additional DDI water was added to the sediment, the sediment was well mixed. As required for testing, contaminant spikes were added as part of the DDI water addition to achieve the necessary moisture content.

Prior to 2008, sediment was placed in a pan, stirred with a spoon until the additional water was incorporated, and allowed to sit in a closed container on the laboratory bench overnight. Starting in 2008, sediment and additional DDI were placed in a 1-gallon, Teflon-coated paint can and placed on a rock tumbler device with rollers and allowed to tumble approximately 8 hours or overnight. Another sample of the sediment was taken and moisture content was calculated to determine the actual moisture content of the sediment.

Sediment used for the sediment-sediment and concrete-sediment half-cell experiments initiated in fiscal year (FY) 1999 used Trench 8 sediment, which is medium coarse sand that was obtained from the sidewall of W-5 burial ground located on the Hanford Site. The remaining experiments used Hanford fine sands (HFS) obtained from a sand lens located in the submarine pit in the 200 East Area of the Hanford Site. The mineralogical properties of these sediments have been characterized by Serne et al. (1993a, b).

2.4 Half-Cell Testing and Data Analysis

Diffusion tests were conducted to assess the effects of varying cement compositions on the rate of diffusion of radionuclides in unsaturated sediments. Experiments were conducted using cylindrical cells made of Schedule 40 PVC pipe. Caps were machined to fit into both ends of the PVC pipe and fitted with O-rings to minimize moisture loss during the test. Cells contained a contaminant-spiked material (sediment or concrete monolith) in contact with a non-spiked material (sediment or concrete monolith). Half-cells for the sediment-sediment experiments contained only sediment with one-half of the sediment spiked prior to cell preparation. Concrete-sediment half-cells contained one concrete monolith in contact with sediment. Type of sediment, contaminant spike, and direction of diffusion are listed in Table 2.3.

The diffusion tests were run horizontally and undisturbed for predetermined timeframes, with periodic rotation of the cell by 90 degrees. At the conclusion of the test period for the FY 1999 tests, sediment half-cells were frozen (dry ice or freezer) to aid in the extrusion and slicing of low moisture sediments. Sediment half-cells were extruded in intervals (~0.5 to 1 cm) along the length of the half-cell. The apparatus used at the end of the FY 1999 tests is shown in Figure 2.2. Starting with the FY 2002 tests, half-cells were not frozen prior to slicing and a modified caulking gun was used to extract samples.

Sediment samples were weighed and one-to-one water extracts (by mass) with DDI water were measured for the contaminant of concern. Nitric acid (0.1M) had been used for extractions of the FY 1999, 64-day sediment-sediment and concrete-sediment samples, resulting in loss of I. After that time, DDI water was used for all other extractions. Samples were mixed on a shaker table at 60 rpm for a minimum of 24 hours then filtered through a 0.45 μm syringe filter. The concentrations of the contaminants of concern were analyzed by inductively coupled plasma-optical emission spectrometry (ICP-OES) and inductively coupled plasma-mass spectrometry (ICP-MS).

Concrete half-cells were sectioned parallel to the concrete-sediment interface using a Buehler slow-speed saw fitted with a diamond blade. The concrete slices were then ground using an agate mortar and pestle. Two-to-one extracts by mass (due to small sample size) were performed on concrete fractions, Nitric acid (0.1M) had been used for extractions of the FY 1999, 64-day concrete-sediment samples, resulting in loss of I. After that time, DDI water was used for all extractions. Samples were mixed on a shaker table at 60 rpm for a minimum of 24 hours then filtered through a 0.45 μm syringe filter. Solutions were analyzed for the concentrations of contaminants by ICP-OES and ICP-MS.
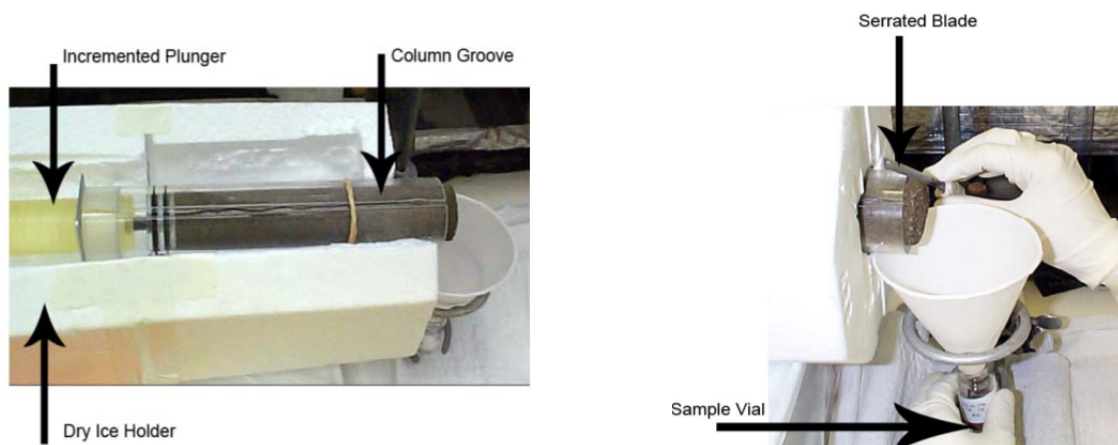
Figure 2.2. Mechanism for sediment sampling from a concrete-sediment diffusion half-cell (left) and sediment sampling from a diffusion half-cell (right)

2.4.1   Effective Diffusion Coefficient Calculations

Diffusivities were reduced using the probit analysis approach. Details of the probit analysis are provided in Finney's *Probit Analysis* (Finney 1971). This technique allows the transformation of a sigmoid curve of concentrations, normalized with respect to the initial concentration (C/C_0), as a function of diffusion distance produced in a half-cell diffusion experiment to a linear plot. The slope (b) of this plot is then used to calculate the diffusivity (D) as $D = 1/(2b^2 t)$, where t is the sampling time. This

approach has been used previously to determine diffusivity in half-cell diffusion experiments, such as those conducted by Brown et al. (1964) and Lamar (1989).

In a diffusion test where one boundary can be represented by a constant concentration, the concentration profile that develops is one-half of the normal sigmoid curve produced in the half-cell diffusion experiment. Thus, to apply the probit transformation, the concentrations are normalized by dividing by 2* C_i, where C_i is the concentration at the constant concentration interface. This approach has been used to model diffusion from a non-depleting reservoir into asphalt (Martin et al. 1994).

In the case of diffusion occurring between two dissimilar media, one of which is spiked and both of which are semi-infinite in dimension from the interface, the concentration at the interface will quickly reach and remain at a constant concentration as the diffusion proceeds. For an explanation of why this occurs, refer to Crank (1975). Because of this result, the mathematical description is the same as the case where a boundary is held at a constant concentration and the data can be normalized by dividing by 2*C_i, where C_i is the concentration at the interface. However, because the concentration C_i at the interface of the two dissimilar materials is not known, the concentration in the slice nearest the interface is used to approximate this value. This approximation introduces some bias in the calculated diffusivity because the concentration profile averaged over the first slice is systematically lower than the concentration at the interface. The extent of the error is estimated to be about 12% from one of the concentration profiles (Crane et al. 1992). It was assumed the relative errors for the other tests were similar. This magnitude of error is considered acceptable relative to the variance in the diffusivity values for all the tests.

For purposes of data reduction, the radionuclide diffusivity is defined by the equation:

$$J = - D_w \, dC_w/dx \qquad (2.1)$$

where
J = flux of radionuclide at a given point
D_w = the diffusivity of water-based radionuclide concentration
C_w = the radionuclide concentration in the porewater.

Using this definition, and acknowledging that in the case of a two-phase system (water and sediment) there will be insignificant amounts of radionuclides within the air phase of the unsaturated sediment, a mass balance can be performed over a small volume, leading to the equation:

$$dC_w/dt = D_w/\theta * (d^2C_w/dx^2) \qquad (2.2)$$

where
θ = the volume porewater per total pore volume.

However, the slope on the probit plot provides the diffusivity that solves the equation for diffusion in a homogeneous single-phase medium:

$$dC/dt = D * (d^2C/dx^2) \qquad (2.3)$$

The diffusion coefficient, D_w, was calculated from D obtained from the probit plot based on concentrations in the porewater that must then be multiplied by θ.

For the diffusion calculations presented in this report, the concentration from the first slice of the non-spiked half-cell was used as the initial concentration (C_0). Probit fits and diffusivity calculations are presented for probit fit slopes greater than 0.05. Diffusion coefficients presented were not corrected for θ, as not all tests included the water content measurement.

2.5 Leach Testing and Data Analysis

There are two types of leach tests (dynamic and static) available to assess the leachability of constituents of interest from the concrete specimens. The dynamic leach test is an ANSI-16.1 standard test designed to examine the leaching rate of contaminants in concrete and grout specimens to determine the cumulative fractions leached and effective diffusion coefficients. This dynamic test maintains an aggressive leaching regime in that a high chemical potential difference of a contaminant is created between a concrete specimen and the leach solution, by replacing all of the solution with fresh DDI water after a specified period. In comparison, the non-regulatory static test is much less aggressive in that only a small portion of the leaching solution is renewed periodically to monitor the radionuclide activities in solution. Therefore, in a static test the chemical potential difference of a contaminant will decrease as a function of time.

The procedure was modified slightly by using Hanford Site groundwater instead of DDI water. The ratio of leachant volume to the surface area of test specimens was held constant at ~10 cm (350 cm^3/35 cm^2). In leachates, the activities of I-125 and Tc-99 were measured with liquid scintillation counting (LSC). Additionally, the concentrations of Tc-99 and U in leachates of selected leach experiments were measured using ICP-MS. Table 2.3 lists the variables investigated for this set of tests.

2.5.1 Calculations for Leach Tests

Based on a number of leach studies, Serne et al. (1992; 1993a, b; 1995) concluded that leaching from a semi-infinite solid source would be the most appropriate model to describe the release of trace contaminants from grout and cement specimens. Seven critical assumptions in their model were:

- The concentration of leaching contaminant species at the surface of the specimen is always zero; i.e., the contaminant is instantaneously removed by the liquid as soon as the species diffusing from the solid reaches the solid-liquid interface.

- The composition of the liquid in contact with the solid being leached is constant. This implies that the leaching contaminant will not significantly change the liquid composition.

- The solid waste form does not alter physically or chemically during the leaching process. A critical part of this assumption is that the mass of constituents leached is insignificant when compared to the total mass of these constituents in the solid, thus fulfilling the semi-infinite solid requirement.

- The surface area of the solid is constant and does not change by armoring (i.e., formation of a protective layer during leaching).

- Any chemical reaction is rapid enough so that chemical equilibrium always exists between leaching species in the solid and the liquid.

- Each contaminant exists as a single chemical species such as all free, cationic, anionic, or neutral species, or in a complexed form (i.e., a single cationic, anionic, or neutral species).

- Bulk diffusion is the rate-limiting process for contaminant leaching.

Leaching of semi-infinite solids has been described mathematically using either incremental leach rates or cumulative leach rates (Serne et al. 1992; 1993a, b; 1995). Using incremental leach rates, the effective diffusion coefficient for each leach interval (D_{ei}) for a species of interest is expressed as:

$$D_{ei} = \pi \left[\left(\frac{a_n}{A_o} \right) / \Delta t_n \right]^2 \left[\frac{V}{S} \right]^2 [T]$$

(2.4)

Using cumulative leaching rates, the effective diffusion coefficient (D_{ec}) is expressed as:

$$D_{ec} = \pi / 4 \left[\left(\frac{\Sigma a_n}{A_o} \right) / \Delta t_n \right]^2 \left[\frac{V}{S} \right]^2 \left[\frac{1}{t} \right]$$

(2.5)

where
D_{ei} = effective diffusivity coefficient (cm^2/s) for the leaching interval, $t_n - t_{n-1}$
D_{ec} = effective diffusivity coefficient (cm^2/s) for the cumulative leach interval, $t_n - t_o$
a_n = activity of radionuclide leached during the leaching interval, $t_n - t_{n-1}$
Σa_n = total activity of radionuclide cumulatively leached during the interval, $t_n - t_o$
A_o = total initial activity of radionuclide in the specimen
a_n/A_o = fraction of radionuclide leached during interval, $t_n - t_{n-1}$

$\dfrac{\Sigma a_n}{A_o}$ = cumulative fraction of radionuclide leached during the interval $t_n - t_o$

Δt_n = duration of the nth leaching interval, $t_n - t_{n-1}$ in seconds
V = volume of the specimen, cm^3
S = geometric surface area of the specimen, cm^2
T = mean leaching time = $\left[\dfrac{1}{2} \left(\sqrt{t_n} + \sqrt{t_{n-1}} \right) \right]^2$
t = total elapsed time from leaching initiation in seconds.

According to Serne et al. (1992; 1993a, b; 1995), if the leach experiments satisfy all seven conditions listed above for semi-infinite solids, both Eqs. (2.1) and (2.2) would provide the same effective diffusion coefficient for all times. However, in actual leaching experiments, many of the conditions cannot be met; therefore, the calculated average D_{ei} and D_{ec} are different. For instance, Serne et al. (1992; 1993a, b; 1995) observed that armoring is a common phenomenon in leach studies of cement specimens, which would affect the leach rates depending on the rate of formation, thickness, and the chemical nature of surface armoring. Additionally, certain species may leach out in sufficient quantities, which would invalidate the third assumption of insignificant leach fraction. Also, chemical speciation studies have indicated that in cement specimens, each leaching species does not exist as a single chemical species. Therefore, the assumption of single diffusing chemical species may not be valid.

In leaching experiments where the leaching fraction of a species is significant (>20% the amount contained initially in a specimen), the ANSI protocol recommends a specimen shape-specific solution of

the mass transport equation. The effective diffusion coefficient in this case for a cylindrical specimen is calculated by using the equation:

$$D_{ec} = \frac{Gd^2}{t}$$

(2.6)

where G = a dimensionless time factor for the cylinder
        d = the diameter of the cylinder in cm
        t = total elapsed time from leaching initiation in seconds.

The average effective diffusion coefficients were calculated from the values determined for each leaching interval (D_{ei}) and each cumulative leach time (D_{ec}). The leachability index for each radionuclide was calculated from the average effective diffusion coefficient values as:

$$LI = log\ (\beta/D_e)$$

(2.7)

where LI = leachability index
        β = a constant = 1 cm^2/s
        D_e = average effective diffusion coefficient.

2.6 Petrographic Analyses: Carbonation and Microcracking

Petrographic studies were conducted in general accordance with the relevant portions of ASTM C 856, *Standard Practice for Petrographic Examination of Hardened Concrete*. Phenolphthalein was used as an indicator to establish the extent of carbonation within the concrete monolith. A 2% phenolphthalein: 98% ethyl alcohol solution was applied directly to a freshly broken, fractured surface and immediately examined via petrographic microscopy. The phenolphthalein indicator affords a maximum color, deep reddish-purple, at pH $\geq$ 9.8. Below pH = 9.8, the color may be varying shades of red and/or pink, and colorless at pH 8. The depth of carbonation was measured from the cast surface to where the indicator colored the monolith pink. In other words, the measured depth of carbonation corresponded to the location where the concrete remained colorless.

Scanning electron microscopy (SEM) studies were performed to identify microcracks with widths less than 2 to 3 micrometers. A small block measuring approximately 20 mm on each side was cut from central portion of each of the concrete samples. Each block was placed in a plastic cup and impregnated with low-viscosity epoxy resin. After the resin hardened, the embedded samples were polished using successively finer alumina grits down to a final stage of 0.05 micron. The polished surfaces were carbon coated and then examined in backscattered electron mode (BSE) using an ASPEX Personal scanning electron microscope. The relative extent of microcracking can be judged from a comparison of the images. However, it is necessary to note that microcracking can result from any, or a combination, of the preparation steps, which include drying in a low-temperature oven, carbon coating under a vacuum, and SEM studies conducted in a vacuum of about 6×10^{-6} Torr.

Concrete monoliths were prepared based on the composition outlined in Table 2.2 following the sample preparation described in section 2.3. Sample variables are listed in Table 2.3. Four concrete monoliths, spiked with I and Re, from the concrete-sediment half-cell experiments started in 2002, were

subjected to petrographic studies to evaluate the extent of carbonation and the degrees of microcracking induced by carbonation, and to discern correlations between the diffusion of I and Re from the monoliths.

Monoliths included in the set of tests started in 2004 were grouped into three groups of three and encased in HFS with moisture contents of 4%, 7%, and 15% by mass. The sediment-encased cement specimens were sealed in 1-gallon buckets to prevent moisture loss and were aged for various periods ranging from 6 months to 2 years. The encased samples were periodically vented to maintain the CO_2 content near ambient conditions. At the end of each set aging period, three monoliths, one representing each respective moisture content, were removed and subjected to petrographic analyses to determine the depth of carbonation under simulated vadose zone conditions.

3.0   Leaching Experiments

ANSI 16.1 is the standard method to measure the leachability of contaminants from solidified low-level radioactive waste. Leach tests have been conducted to determine the effect of iron particle incorporation on the leaching of contaminants in concrete specimens. Contaminants in these experiments include Tc-99, I-125, U, and Re. Iron sources contained within the concrete specimens for the two sets of experiments included steel fibers, metallic iron (-40 to +60 mesh), or reactive nanoscale zero valent iron particles (RNIP).

3.1   Leaching of Technetium-99 and Iodine-125 from Concrete Specimens

Dynamic leach tests were conducted according to protocol specified by ANSI 16.1 (1986). These leach tests were conducted on specimens of intact concrete cylinders of ~2 cm in diameter and 4 cm in length. The characteristics of the specimens used are listed in Table 3.1. The test protocol was slightly modified in that actual groundwater from the Hanford Site was used as the leachant instead of ANSI 16.1-specified demineralized water. In all tests, the ratio of leachant volume to the surface area of test specimens was held constant at ~10 cm ($350 cm^3/35 cm^2$). The composition of Hanford groundwater is listed in Table 3.2.

The static leach test was designed to determine the diffusion coefficient under conditions of decreasing chemical potential between solid and solution phases. As discussed previously, the static leach test differs from the dynamic leach test because the chemical potentials of leaching constituents between the solid and the solution phases in the static test are maintained at a near-constant level by periodically renewing the solution phase. The static leach tests were also conducted on specimens of intact concrete cylinders ~2 cm in diameter and ~4 cm in length and the leachant consisted of Hanford Site groundwater. At prescribed times, 50 ml of leachate was removed for analysis, and 50 ml of fresh groundwater was added to the containers to maintain the total volume of the leach solution at ~350 ml.

Table 3.1. Characteristics of cement specimens used in the dynamic and static leach tests

Specimen No.	Length (cm)	Diameter (cm)	Surface Area (cm^2)	Volume (cm^3)	Iron	Carbonation
1	4.20	2.10	34.64	14.55	No	No
2	4.10	2.10	33.98	14.20	No	No
3	4.10	2.10	33.98	14.20	No	No
5	4.30	2.10	35.30	14.89	No	No
6	4.50	2.10	36.62	15.59	Yes	No
7	4.20	2.10	34.64	14.55	Yes	No
8	4.30	2.10	35.30	14.89	Yes	No
9	4.20	2.10	34.64	14.55	Yes	No

Table 3.2. Composition of Hanford Site groundwater used in the leaching tests

Constituent	Concentration (mg/L)	Constituent	Concentration (mg/L)
Al	0.14	Si	16.2
B	0.05	Sr	0.28
Ba	0.069	U	0.0067
Ca	67.5	Cl	22.0
Fe	3.0	NO_3	1.7
K	3.0	SO_4	108.0
Mg	16.4	Tot Alk (as CO_3)	67.5
Mn	0.046	TOC	0.73
Na	27.6	pH	8.46 (SU)

TOC = total organic carbon
SU = standard units

For both leach tests, 50 ml aliquots were filtered through a 0.45 μm membrane and analyzed for activities of I-125 and Tc-99 using LSC. Additionally, the concentrations of Tc-99 and U in leachates of selected leach experiments were measured using ICP-MS. The cumulative leached fraction, the effective diffusion coefficient, and the leaching index for each contaminant were calculated from the data.

3.1.1 Results and Discussion

The leaching data from both dynamic and static tests are plotted as cumulative leach fractions as a function of leaching time (Figure 3.1 through Figure 3.4). The calculated effective diffusion coefficients are listed in Table 3.3. Dynamic test data are listed in tables in Appendix A.

3.1.1.1 Leaching Characteristics

The results showed that in the dynamic leach test, I-125 leaches rapidly during the first 5 days. Iodine continues to leach at an attenuated rate for the remainder of the experiment. All four specimens showed differing leaching rates. One explanation for these small differences in leaching may be due to the type of I redox species that exist in these specimens. For instance, the steel fibers in specimens 6 and 7 may reduce I species through oxidation, and this reduced species may have a lower rate of diffusion than the oxidized species. For example, if the original I spike was in the form of iodate ions (IO_3^-), the reduction of this species coupled by oxidation of metallic iron would result in the formation of iodide ions (I^-). This redox reaction may be represented by:

$$IO_3^- + 3Fe^0 + 3H_2O = I^- + 3Fe^{2+} + 6OH \tag{3.1}$$

Therefore, if the original spike is in the form of iodate, the differing diffusion behavior of iodate and iodide species may be reflected in the observed differences in the leach rates. However, there is no data at present to confirm either the initial redox state of the I spike or the chemical species of I in the leachate.

The results from the static leach test (Figure 3.2) indicated that, in general, the leaching tendency of I was similar to what was observed in dynamic leach tests except that the overall cumulative leach fractions were on average lower than that of dynamic leach tests. Also, one of the specimens (specimen 3) cumulatively leached about four times more I than the other three specimens. Because all the specimens

were prepared at the same time, the anomalous leaching of I from specimen 3 may be due to the more porous nature of this specimen. Additional characterization of this specimen was not completed to confirm this explanation. When compared to the results of the dynamic leach test, there was no difference in I leachability between specimens with and without steel fibers.

The cumulative leaching data for Tc-99 is included in Figure 3.3 and Figure 3.4. As a check, the leach fractions were calculated using both LSC activity data and the mass measured by using ICP-MS. The cumulative leach fractions calculated by both these methods agreed well in all cases except for specimen 1. For this specimen, the LSC data consistently indicated about 20% higher leaching than the data obtained from the ICP-MS measurements. The dynamic leach test indicated that Tc-99 in these specimens had a greater leaching tendency than I-125. In these tests, Tc-99 appeared to leach rapidly during the first 5 days and leached at a significantly reduced rate for the remaining period. The leaching behavior of Tc-99 is similar to the leaching pattern of I-125 observed from the same cement specimens. There were no significant differences in cumulative leach fractions of Tc-99 between specimens with or without the addition of steel fibers, indicating that steel fibers did not cause significant changes in the species of Tc-99 as indicated by the redox reaction:

$$2TcO_4^- + 3Fe^0 + 4H^+ = 3Fe^{2+} + 2TcO_2 + 4OH^- \qquad (3.2)$$
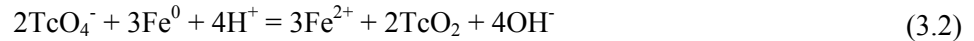
The leaching data from the static tests also indicated that Tc-99 leaches to a greater degree than I-125 from the same set of specimens. As compared to all other specimens, specimen 3, which leached anomalously high fractions of I-125, also leached significantly higher fractions (about 5 times) of Tc-99. Such leaching behavior suggested that specimen 3, due to some unknown reason, had distinctly different physical characteristics than other specimens, most likely microcracks that promoted a significantly higher rate of leaching for these two radionuclides.

ANSI Leach Test (I-125)
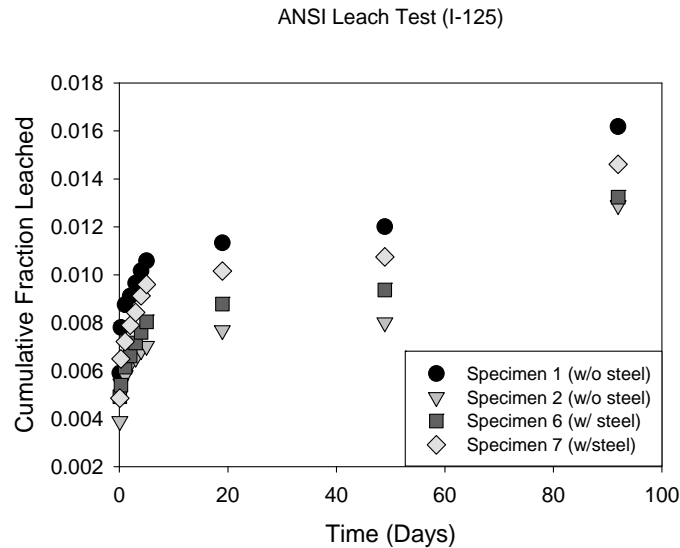
Figure 3.1. Dynamic leach test: cumulative leaching fraction as a function of time for I-125

ANSI Leach Test (I-125)
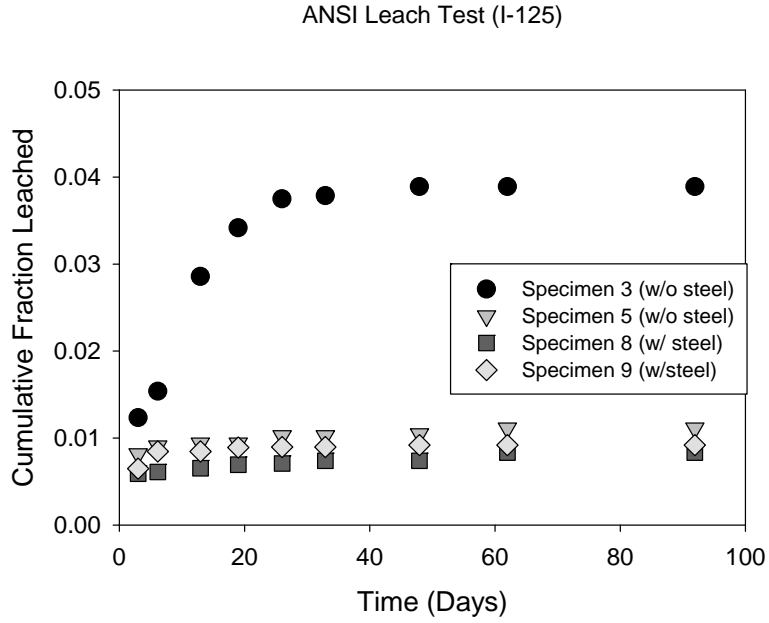
Figure 3.2. Static leach test: cumulative leaching fraction as a function of time for I-125

ANSI Leach Test (Tc-99)
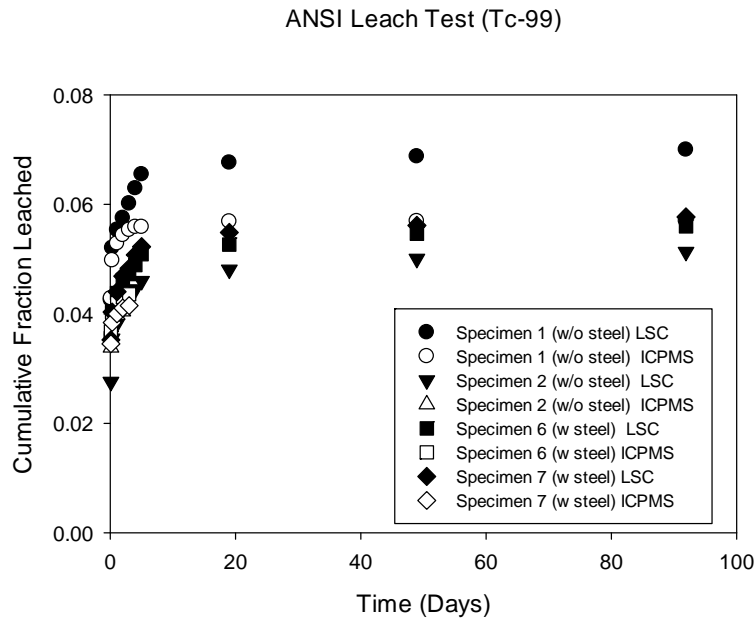
Figure 3.3. Dynamic leach test: cumulative leaching fraction as a function of time for Tc-99

ANSI Leach Test (Tc-99)
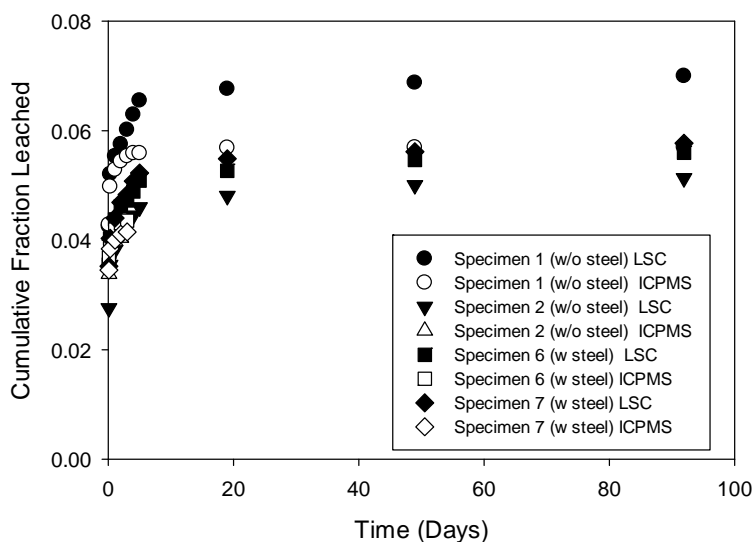
Figure 3.4. Static leach test: cumulative leaching fraction as a function of time for Tc-99

3.1.1.2   Effective Diffusion Coefficients

The calculated average effective diffusion coefficients and the corresponding leachability indices are listed in Table 3.3. The results of the dynamic leach test indicated that the average D_{ei} for I-125 ranged from 3.59×10^{-11} to 7.77×10^{-11} cm^2/s, and the average D_{ec} ranged from 7.36×10^{-11} to 1.32×10^{-10} cm^2/s. Although, the cumulative leach fractions from specimens with and without the steel fibers showed slight differences, there were no significant differences in the calculated average diffusion coefficients. In all cases, the calculated D_{ec} values were about twice as high the D_{ei} values. As discussed in section 2.5, these differences can be attributed to the lack of conformity with the conditions imposed by the semi-infinite solid leaching formulation.

The static leach test data yielded average D_{ei} values for I-125 that ranged from 3.06×10^{-12} to 6.4×10^{-11} cm^2/s, and average D_{ec} values that ranged from 5.42×10^{-12} to 6.79×10^{-11} cm^2/s. Excluding the data from specimen 3, (which exhibited anomalous leaching behavior), there were no significant differences in diffusion coefficient values calculated from leaching of specimens with or without steel fibers. The data from the static tests yielded D_{ec} values that were about 50% higher the average D_{ei} values.

The effective diffusion coefficients for I-125 derived from the dynamic leach tests are, on average, about an order of magnitude higher than the values calculated from the static leach tests. These differences can be attributed to the differences in the leaching regime between these tests. In dynamic leach tests, all contact solution is renewed at each sampling time, whereas in static tests only about 15% of the contact solution is replaced. The dynamic leach tests subject the specimens to more aggressive leaching conditions; therefore, these tests yield higher effective diffusion coefficients (and higher leachability indices) than the values generated under moderate leaching conditions encountered in the static tests.

The data from the dynamic leach tests on Tc-99 indicated that the average D_{ei} ranged from 1.61×10^{-9} to 3.69×10^{-9} cm^2/s, and the average D_{ec} ranged from 3.39×10^{-9} to 7.68×10^{-9} cm^2/s as measured by LSC. No significant differences were found in average diffusion coefficients between specimens with or without steel fibers, indicating that if a redox reaction occurred, it did not cause measurable leaching differences between the specimens. The D_{ec} values for Tc-99 were about twice as high as the D_{ei} values, indicating that leaching of concrete specimens in this test did not meet all the requirements inherent in the semi-infinite solid leaching model.

The static test data for Tc-99 measured by LSC resulted in average D_{ei} values that ranged from 2.21×10^{-10} to 5.81×10^{-9} cm^2/s, and average D_{ec} values that ranged from 4.30×10^{-10} to 4.25×10^{-9} cm^2/s. There were no significant differences between the diffusion coefficient values calculated from either the activity or mass measurements. Excluding the data from specimen 3, which exhibited anomalous leaching behavior, there were no significant differences in diffusion coefficient values calculated from leaching of specimens with or without steel fibers. As in the case of I-125, the data from the static tests (except for specimen 3) resulted in calculated D_{ec} values that were about 50% higher than the average D_{ei} values. Also, the more aggressive leaching regime used in the dynamic leach tests resulted in effective diffusion coefficients which were, on average, about an order of magnitude higher than the values calculated from the static leach tests.

Table 3.3. Calculated effective diffusion coefficients and leaching indices for I-125 and Tc-99 from dynamic and static leach tests

	I-125		Tc-99[a]		Tc-99[b]		I-125		Tc-99[a]		Tc-99[b]	
	Effective Diffusion Coefficient (cm^2/s)						Leachability Index					
Specimen #	D_{ei}	D_{ec}	D_{ei}	D_{ec}	D_{ei}	D_{ec}	L_i	L_c	L_i	L_c	L_i	L_c
Dynamic Leach Test												
1[c]	7.77×10^{-11}	1.32×10^{-10}	3.69×10^{-9}	7.68×10^{-9}	3.58×10^{-9}	7.36×10^{-9}	10.1	9.9	8.4	8.1	8.4	8.1
2[c]	3.59×10^{-11}	7.36×10^{-11}	1.61×10^{-9}	3.39×10^{-9}	(e)	(e)	10.4	10.1	8.8	8.5	(e)	(e)
6[d]	4.94×10^{-11}	1.00×10^{-10}	3.15×10^{-9}	5.18×10^{-9}	(e)	(e)	10.3	10.0	8.5	8.3	(e)	(e)
7[d]	5.44×10^{-11}	9.17×10^{-11}	2.42×10^{-9}	4.03×10^{-9}	(e)	(e)	10.3	10.0	8.6	8.4	(e)	(e)
Static Leach Test												
3[c]	6.40×10^{-11}	6.79×10^{-11}	5.81×10^{-9}	4.25×10^{-9}	5.81×10^{-9}	3.77×10^{-9}	10.2	10.2	8.2	8.4	8.2	8.4
5[c]	6.64×10^{-12}	1.08×10^{-11}	2.40×10^{-10}	5.36×10^{-10}	2.25×10^{-10}	5.02×10^{-10}	11.2	11.0	9.6	9.3	9.6	9.3
8[d]	3.06×10^{-12}	5.42×10^{-12}	3.20×10^{-10}	4.30×10^{-10}	2.21×10^{-10}	3.78×10^{-10}	11.5	11.3	9.5	9.4	9.7	9.4
9[d]	6.76×10^{-12}	8.02×10^{-12}	3.56×10^{-10}	5.85×10^{-10}	1.88×10^{-10}	2.07×10^{-10}	11.2	11.1	9.4	9.2	9.7	9.7

(a) Tc-99 activity measured by using LSC.
(b) Tc-99 concentration measured by using ICP-MS.
(c) Specimen without steel fibers.
(d) Specimen with steel fibers.
(e) Tc-99 concentration was below the instrument detection limit, so calculation was not performed.

These tests showed that I-125 in these concrete formulations was about two orders of magnitude less leachable than Tc-99. I-125 in these cement specimens also appears to be significantly less leachable (three to four orders of magnitude) than I in some of the Hanford Site grout formulations studied by Serne et al. (1993a, b; 1992). These differences in I leachability can be attributed to a different concrete formulation used in these studies as compared to Hanford Site grouts (which contained several waste types, higher waste loadings, and different grout formulations). Previous studies have shown that leaching of Tc-99 varies as a function of waste type, waste loading (mix ratio), grout fluid density, and amount of blast furnace slag in the blend (Serne et al. 1993a, b; 1992). These factors can cause Tc-99 leachability to range over four to five orders of magnitude (leachability index ranging from ~7 to 12). The leachability index for Tc-99 in this study ranged from about 8.1 to 9.6, which is within the range of 7 to 12 observed for various types of grouts.

3.2 Effect of Iron on the Release of Rhenium, Iodine, and Technetium from Concrete

Another set of dynamic leach tests was conducted to assess the effect of metallic iron particle incorporation on the leaching of contaminants in concrete specimens. Based on the laboratory concrete composition presented in section 2.0, a set of concrete monoliths spiked with (1) I and Re, or (2) I and Tc-99, was prepared with 4%, 8%, and 12% by mass, of metallic iron particles. Iron particles consisted of metallic iron (-40 to +60 mesh) and RNIP (Toda America, Inc., Schaumburg, IL). The characteristics of the specimens used are listed in Table 3.4.

Table 3.4. Characteristics of cement specimens used in dynamic leach tests

| Specimen No. | Length (cm) | Diameter (cm) | Surface Area (cm^2) | Volume (cm^3) | Iron | | | | | Contaminant | | | Carbonation |
					Metal	RNIP	4%	8%	12%	I	Re	Tc	
1	3.67	2.50	38.65	18.02	x		x			x	x		No
2	3.15	2.49	34.48	15.41	x			x		x	x		No
3	3.96	2.51	40.99	19.50	x				x	x	x		No
4	4.50	2.50	45.17	22.06		x	x			x	x		No
5	4.18	2.51	42.87	20.70		x		x		x	x		No
6	4.44	2.51	44.91	21.96		x			x	x	x		No
7	4.48	2.52	45.32	22.25		x	x			x		x	No
8	4.39	2.49	44.12	21.41		x		x		x		x	No
9	4.22	2.50	42.86	20.64		x			x	x		x	No

The concrete monoliths were subjected to dynamic leach tests to determine the rate of leaching of I, Re, and Tc-99 in concrete, based on the inclusion of Fe, and to determine the cumulative fraction leached and effective diffusion coefficient. The test protocol was slightly modified in that actual groundwater from the Hanford Site was used as the leachant instead of the demineralized water specified in ANSI-16.1. The composition of Hanford Site groundwater is listed in Table 3.5.

Table 3.5. Composition of Hanford Site groundwater used in dynamic leach tests

Constituent	Conc. (mg/L)	Constituent	Conc. (mg/L)
Ba	0.043	Mg	27.29
Ca	35.27	Na	73.71
Cl	12.24	P	<0.025
CO$_3$	191.59	Sr	0.14
K	15.19	Si	35.37
F	0.83	SO$_4$	167.28
Fe	0.14	pH	8.12 (SU)

3.2.1   Results and Discussion

Figure 3.5 presents the cumulative fraction of I, Re, and Tc-99, respectively, released as a function of time during dynamic leach testing. Similar to the previous tests, the results indicate that in the dynamic leach test all contaminants leach rapidly during the first 5 days. Subsequent release continued at an attenuated rate for the remainder of the test for all contaminants.
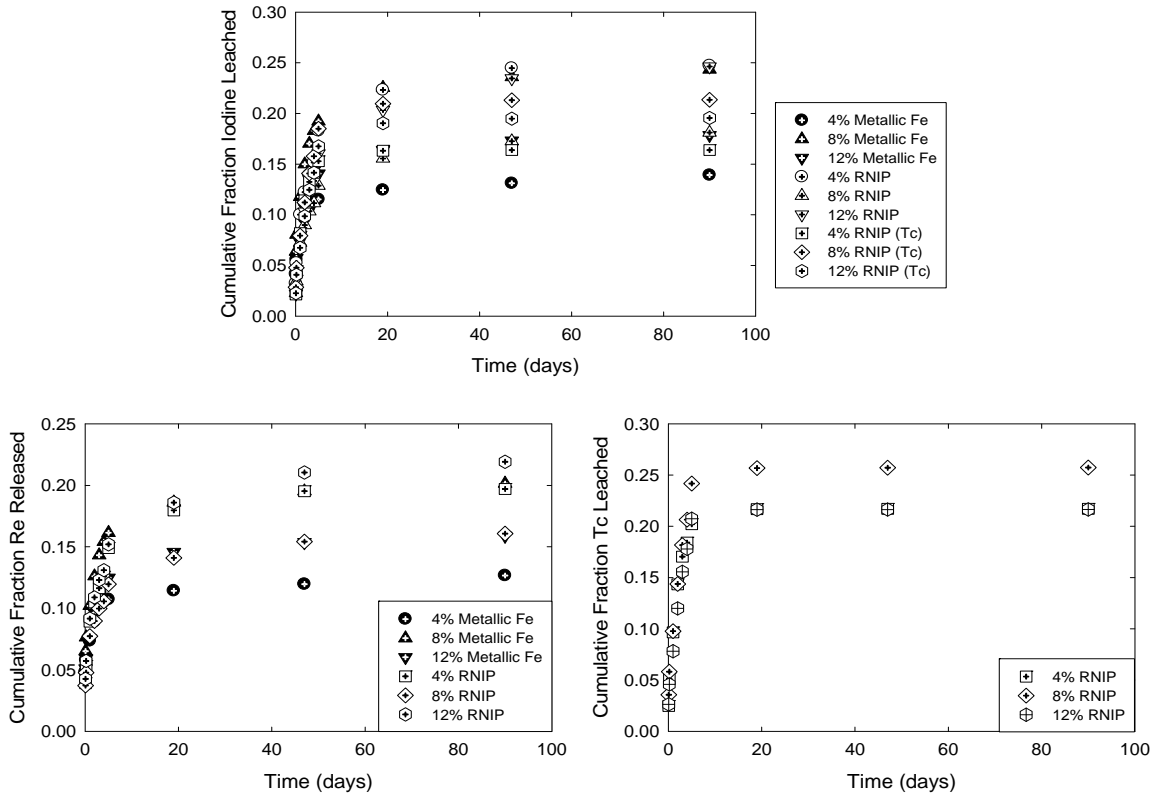
Figure 3.5. Dynamic leach test: cumulative leaching fraction as a function of time for I (top), Re (bottom left), and Tc-99 (bottom right)

Table 3.6 presents the effective diffusion coefficient for I and Re at 4%, 8%, and 12% iron as metallic iron (-40 to +60 mesh) and as RNIP. Inclusion of RNIP relative to metallic iron particles significantly increases the leachability of Re and I from waste form specimens. The leaching behavior of I and Re in the presence of RNIP was at a significantly increased rate throughout the test. The RNIP formulation

consists of elemental iron, magnetite, water, and a water-soluble polymer to maintain a stable iron slurry. It is hypothesized that the polymer may form a surface coating on the iron particles, which reduces their reactivity and may inhibit reaction with redox-sensitive contaminants within the concrete waste forms.

Table 3.7 presents the calculated effective diffusion coefficient for Tc-99 and I at 4%, 8%, and 12% iron as RNIP. The leaching indices for I were comparable to those previously quantified from waste forms containing 4%, 8%, and 12% iron, as metallic iron (-40 to +60 mesh) and RNIP (Table 3.6). The leaching indices indicate that in the presence of 4% and 8% RNIP, Tc-99 had higher leachability than Re. However, there was no difference in the leachability of Tc-99 and Re when the waste form contained 12% RNIP.

Deviations in the chemical reduction of pertechnetate and perrhenate in the presence of organic ligands have been recently noted (Maset et al. 2006). Our results indicated that the presence of organic ligands did not cause a measurable difference in the solubility of Tc-99. Moreover, Wellman et al. (2006b) noted a decrease in the diffusion of Tc-99 versus Re from concrete waste forms. Thus, although the pertechnetate and perrhenate anions are comparable surrogates based on size, Re does not function as an analogue for Tc-99 under redox conditions.

Table 3.6. Leach index data for Re and I as a function of metallic iron-particle concentration

	Re/I concrete column with 4% Metallic Fe				Re/I concrete column with 4% RNIP			
	Re	I	Re	I	Re	I	Re	I
Time (hr)	D eff cm^2/s	D eff cm^2/s	Leach index	Leach index	D eff cm^2/s	D eff cm^2/s	Leach index	Leach index
2	2.20×10^{-7}	1.64×10^{-7}	6.7	6.8	1.6×10^{-7}	1.1×10^{-7}	6.8	7.0
7	2.00×10^{-9}	4.31×10^{-9}	8.7	8.4	4.5×10^{-9}	9.3×10^{-9}	8.3	8.0
24	1.94×10^{-9}	3.55×10^{-9}	8.7	8.4	1.1×10^{-8}	2.0×10^{-8}	7.95	7.7
48	8.63×10^{-10}	1.35×10^{-9}	9.1	8.9	9.8×10^{-10}	2.0×10^{-9}	9.0	8.7
72	3.39×10^{-10}	2.77×10^{-10}	9.5	9.6	3.6×10^{-10}	7.7×10^{-10}	9.4	9.1
96	3.35×10^{-11}	5.54×10^{-11}	10.5	10.3	1.9×10^{-10}	3.4×10^{-10}	9.7	9.5
120	8.88×10^{-12}	1.29×10^{-11}	11.1	10.9	9.2×10^{-10}	1.7×10^{-9}	9.0	8.8
456	2.38×10^{-11}	4.19×10^{-11}	10.6	10.4	5.1×10^{-10}	8.8×10^{-10}	9.3	9.1
1200	4.70×10^{-12}	7.16×10^{-12}	11.3	11.1	4.0×10^{-11}	7.7×10^{-11}	10.4	10.1
2208	4.12×10^{-12}	5.44×10^{-12}	11.4	11.3	2.9×10^{-13}	5.7×10^{-13}	12.5	12.3
		[a]L bar =	9.7	9.6		[a]L bar =	9.3	9.0

	Re/I concrete column with 8% Metallic Fe				Re/I concrete column with 8% RNIP			
	Re	I	Re	I	Re	I	Re	I
Time (hr)	D eff cm^2/s	D eff cm^2/s	Leach index	Leach index	D eff cm^2/s	D eff cm^2/s	Leach index	Leach index
2	3.70×10^{-7}	3.53×10^{-7}	6.4	6.5	1.4×10^{-7}	5.3×10^{-8}	6.9	7.3
7	2.69×10^{-9}	5.85×10^{-9}	8.6	8.2	2.8×10^{-8}	1.5×10^{-8}	7.6	7.8
24	5.14×10^{-9}	1.10×10^{-8}	8.3	8.0	2.1×10^{-8}	1.9×10^{-8}	7.7	7.7
48	2.11×10^{-9}	3.76×10^{-9}	8.7	8.4	1.2×10^{-8}	1.2×10^{-8}	7.9	7.9
72	7.23×10^{-10}	1.04×10^{-9}	9.1	9.0	8.5×10^{-9}	9.2×10^{-9}	8.1	8.0
96	2.30×10^{-10}	3.07×10^{-10}	9.6	9.5	6.8×10^{-9}	7.6×10^{-9}	8.2	8.1
120	8.47×10^{-11}	1.32×10^{-10}	10.1	9.9	6.7×10^{-9}	7.8×10^{-9}	8.2	8.1
456	2.98×10^{-10}	5.40×10^{-10}	9.5	9.3	3.9×10^{-9}	4.7×10^{-9}	8.4	8.3
1200	1.30×10^{-11}	1.79×10^{-11}	10.9	10.7	1.5×10^{-9}	1.9×10^{-9}	8.8	8.7
2208	3.32×10^{-12}	4.69×10^{-12}	11.5	11.3	7.9×10^{-10}	1.0×10^{-9}	9.1	9.0
		[a]L bar=	9.3	9.1		[a]L bar =	8.1	8.1

	Re/I concrete column with 12% Metallic Fe				Re/I concrete column with 12% RNIP			
	Re	I	Re	I	Re	I	Re	I
Time (hr)	D eff cm^2/s	D eff cm^2/s	Leach index	Leach index	D eff cm^2/s	D eff cm^2/s	Leach index	Leach index
2	2.57×10^{-7}	2.00×10^{-7}	6.6	6.7	1.9×10^{-7}	5.1×10^{-8}	6.7	7.3
7	1.44×10^{-9}	3.28×10^{-9}	8.8	8.5	4.2×10^{-8}	1.7×10^{-8}	7.4	7.8
24	2.18×10^{-9}	4.28×10^{-9}	8.7	8.4	3.1×10^{-8}	2.3×10^{-8}	7.5	7.6
48	1.67×10^{-9}	2.80×10^{-9}	8.8	8.6	1.8×10^{-8}	1.6×10^{-8}	7.8	7.8
72	5.17×10^{-10}	7.10×10^{-10}	9.3	9.1	1.3×10^{-8}	1.3×10^{-8}	7.9	7.9
96	1.40×10^{-10}	2.07×10^{-10}	9.9	9.7	1.1×10^{-8}	1.1×10^{-8}	8.0	8.0
120	5.72×10^{-11}	7.04×10^{-11}	10.2	10.2	1.1×10^{-8}	1.2×10^{-8}	8.0	7.9
456	2.24×10^{-10}	2.73×10^{-10}	9.7	9.6	6.9×10^{-9}	8.3×10^{-9}	8.2	8.1
1200	1.05×10^{-11}	1.46×10^{-11}	11.0	10.8	3.0×10^{-9}	3.7×10^{-9}	8.5	8.4
2208	2.29×10^{-12}	2.57×10^{-12}	11.6	11.6	1.5×10^{-9}	1.9×10^{-9}	8.8	8.7
		[a]L bar=	9.5	9.3		[a]L bar =	7.9	7.9

(a) Average leach index.

Table 3.7. Leach index data for Tc-99 and I as a functions of RNIP particle concentration

Time (hr)	Tc-99 D eff cm²/s	I D eff cm²/s	Tc-99 Leach index	I Leach index
		Tc/I concrete column with 4% RNIP		
2	6.5×10^{-8}	4.8×10^{-8}	7.2	7.3
7	3.4×10^{-8}	2.5×10^{-8}	7.5	7.6
24	3.4×10^{-8}	2.5×10^{-8}	7.5	7.6
48	3.1×10^{-8}	2.0×10^{-8}	7.5	7.7
72	2.6×10^{-8}	1.6×10^{-8}	7.6	7.8
96	2.1×10^{-8}	1.3×10^{-8}	7.7	7.9
120	2.0×10^{-8}	1.1×10^{-8}	7.7	7.9
456	9.5×10^{-9}	5.4×10^{-9}	8.0	8.3
1200	3.2×10^{-9}	1.8×10^{-9}	8.5	8.7
2208	1.5×10^{-9}	8.5×10^{-10}	8.8	9.1
		L bar =	7.8	8.0
		Tc/I concrete column with 8% RNIP		
2	1.3×10^{-7}	8.4×10^{-8}	6.9	7.1
7	4.2×10^{-8}	2.9×10^{-8}	7.4	7.5
24	3.5×10^{-8}	2.3×10^{-8}	7.5	7.6
48	3.0×10^{-8}	1.8×10^{-8}	7.5	7.7
72	2.9×10^{-8}	1.7×10^{-8}	7.5	7.8
96	2.6×10^{-8}	1.5×10^{-8}	7.6	7.8
120	2.8×10^{-8}	1.6×10^{-8}	7.6	7.8
456	1.3×10^{-8}	8.7×10^{-9}	7.9	8.1
1200	4.3×10^{-9}	3.0×10^{-9}	8.4	8.5
2208	2.0×10^{-9}	1.4×10^{-9}	8.7	8.9
		L bar =	7.7	7.9
		Tc/I concrete column with 12% RNIP		
2	7.0×10^{-8}	5.2×10^{-8}	7.2	7.3
7	2.6×10^{-8}	2.1×10^{-8}	7.6	7.7
24	2.2×10^{-8}	1.6×10^{-8}	7.7	7.8
48	2.1×10^{-8}	1.4×10^{-8}	7.7	7.9
72	2.1×10^{-8}	1.3×10^{-8}	7.7	7.9
96	1.9×10^{-8}	1.2×10^{-8}	7.7	7.9
120	2.0×10^{-8}	1.3×10^{-8}	7.7	7.8
456	9.1×10^{-9}	7.0×10^{-9}	8.0	8.2
1200	3.0×10^{-9}	2.4×10^{-9}	8.5	8.6
2208	1.4×10^{-9}	1.2×10^{-9}	8.9	8.9
		L bar =	7.9	8.0

4.0   Half-Cell Diffusion Results

This section compiles the results from half-cell diffusion experiments that have been completed over the lifetime of the project. Half-cell diffusion tests investigated the effect of test duration, sediment moisture content, carbonation of concrete, and iron content on the diffusion of contaminants. Description of the half-cell experiments is found in section 2.4. Table 2.3 summarizes the sets of diffusion tests completed.

Results presented in this section are separated by contaminant (I, Tc, and Re) and organized by type of diffusion experiment (sediment to sediment, sediment to concrete, concrete to sediment, fractured concrete to sediment, and sediment to fractured concrete). Tables accompanying the half-cell concentration profile plots are found in Appendix B. Iodine diffusion results are summarized and discussed in section 4.1.6. Technetium diffusion results are summarized and discussed in section 4.2.6. Rhenium is discussed in section 4.3. The half-cell diffusion results are discussed in section 4.4.

4.1   Iodine Diffusion

4.1.1   Sediment to Sediment

Sediment-sediment diffusion experiments were initiated to investigate the effect of sediment moisture content and test duration on diffusivity. These experiments consisted of half-cells (~4 cm diameter and ~39 cm long) filled with Trench 8 sediment. The general preparation of the half-cells is described in section 2.4. The characteristics of these half-cells, including the dimensions, bulk densities, and moisture contents, are listed in Table 4.1. The hot side sediment was spiked with I at levels of 0.0581 mg/g and 0.0655 mg/g in the 4% and 7% moisture content sediments. Half-cell sampling was conducted at 64 and 170 days.

Table 4.1. Characteristics of sediment-sediment half cells

Cell ID	Length of Hot Sediment (cm)	Length of Cold Sediment (cm)	Spiked Sediment Bulk Density (g/cm^3)	Non-Spiked Sediment Bulk Density (g/cm^3)	Moisture Content (%)	Test Duration (days)
SS-I-7%	18.2	19.7	1.41	1.53	7	64
SS-II-7%	17.5	20.5	1.45	1.62	7	170
SS-III-4%	21.1	22.0	1.32	1.40	4	64
SS-IV-4%	18.0	20.7	1.50	1.53	4	170

4.1.1.1   Concentration Profiles

The concentration profiles for I from the sediment-sediment 170-day half-cell diffusion experiments are shown in Figure 4.1 and listed in Table B.1. Concentration is shown as a function of position along the length of sediment for 4% (black circles) and 7% (white circles) sediment moisture content. Concentrations observed for the 4% moisture content sediment are higher than the 7% moisture content sediment through ~15 cm of the cell length, at which time the concentration curves are similar. Results

are not available for the 64-day testing because test samples were extracted with nitric acid and I was lost through volatilization in the process.
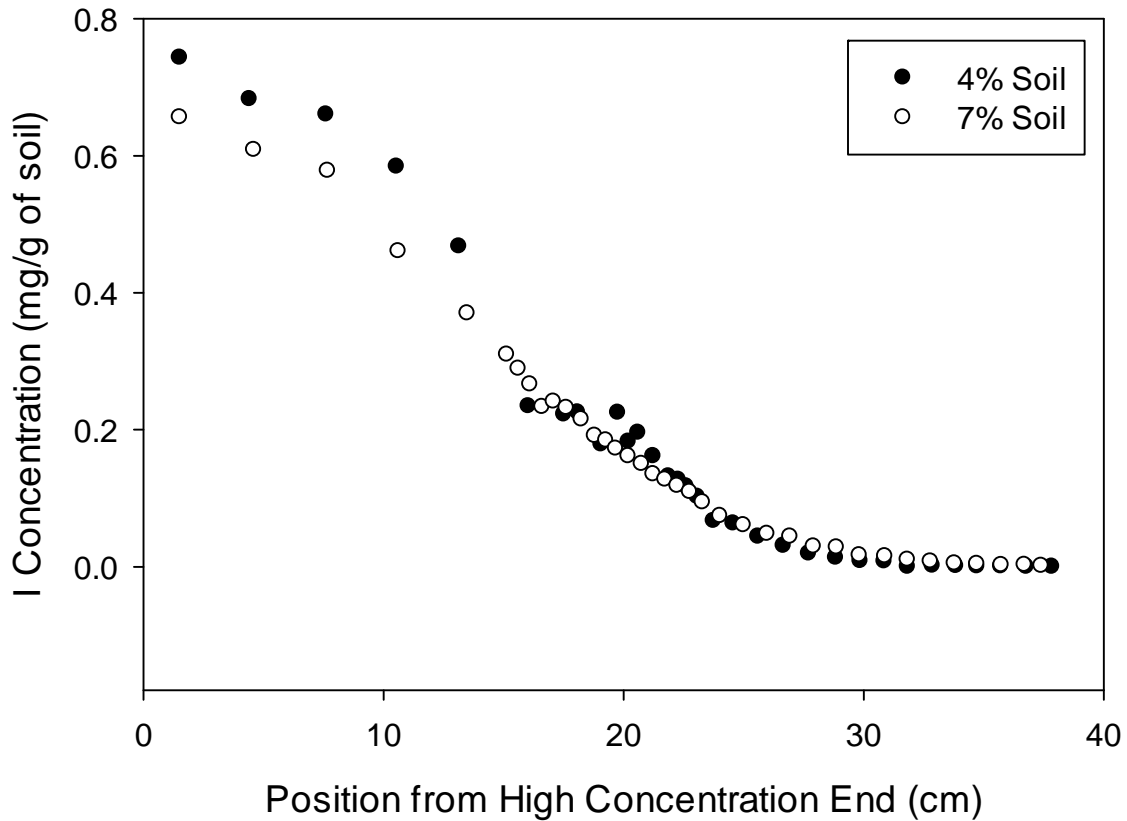
Figure 4.1. Sediment I concentration profiles from sediment-sediment 170-day half-cell experiments for 4% sediment moisture (black circles) and 7% sediment moisture (white circles)

4.1.1.2   Probit Analysis

Probit plots for I diffusion in the sediment-sediment experiments are shown in Figure 4.2. Calculated probit values are plotted as a function of position along the length of sediment for 4% (black circles) and 7% (white circles) sediment moisture content samples and fit by linear regression. Noticeably different slopes were observed for the spiked side (0 to 18 cm), so only data from the cold side (more closely spaced data points) was used for the probit analysis to calculate the diffusivity coefficients that are summarized in Table 4.2.

Calculated diffusivities for I were 2.89×10^{-6} cm^2/s for the 7% moisture content sediment and 1.42×10^{-6} cm^2/s for the 4% moisture content sediment. For this set of experiments, diffusivity increased by a factor of 2 as sediment moisture content increased from 4% to 7%.
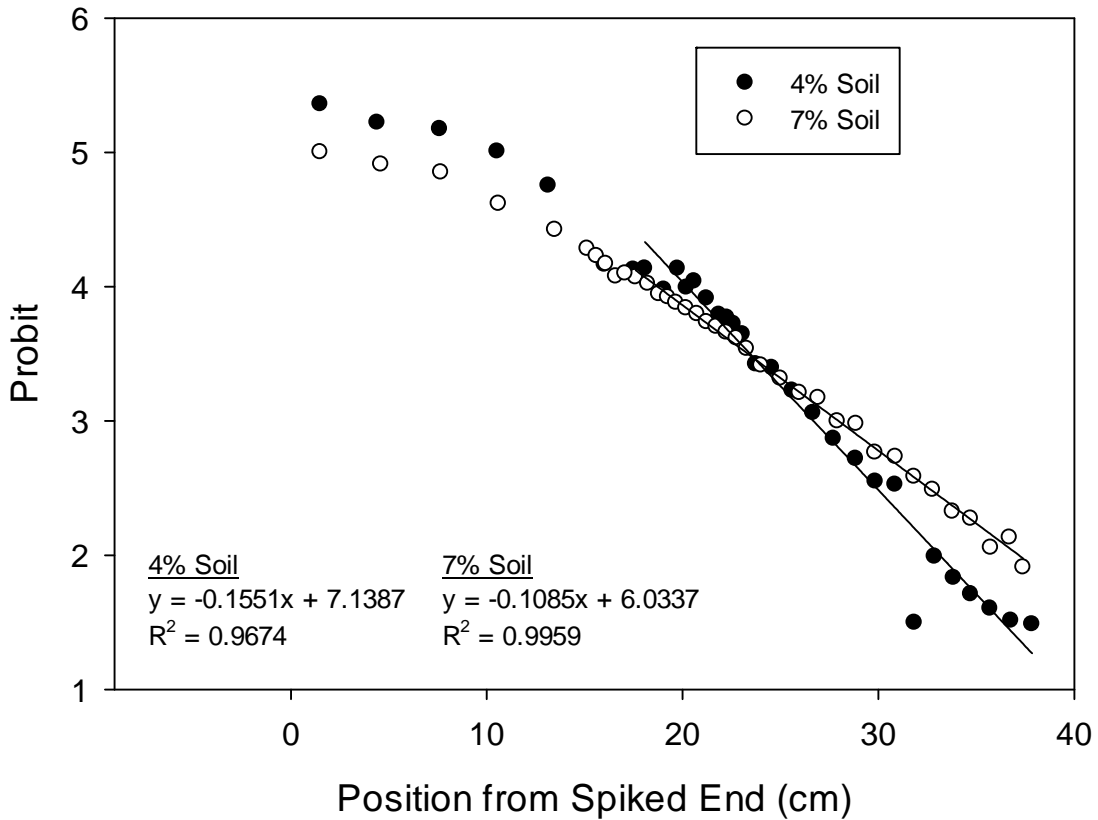
Figure 4.2. Probit analysis for I diffusion from sediment-sediment 170-day half-cell experiments for 4% sediment moisture (black circles) and 7% sediment moisture (white circles)

Table 4.2. Calculated I diffusion parameters from sediment-sediment half-cell experiments

Cell ID	Test Duration (days)	Moisture Content (%)	I Diffusivity (cm²/s)	Probit Slope
SS-II-7%	170	7	2.89×10^{-6}	0.1085
SS-IV-4%	170	4	1.42×10^{-6}	0.1551

4.1.2   Sediment to Concrete

A set of diffusion experiments was initiated during FY 2006 to investigate the effect of sediment moisture content, iron content in the concrete, and carbonation of the concrete on the diffusion of I from sediment into concrete monoliths. The general preparation of the half-cells is described in section 2.4. Sediment half-cell specimens were spiked with stable I at concentrations of ~12 mg I/g sediment. HFS was used for the sediment half-cell. In these experiments, iron content was varied in the concrete specimens at 0% or 4%, sediment moisture content was varied (4%, 7%, or 15%), and half of the concrete monoliths were carbonated prior to preparing the half-cells. The characteristics of the concrete half-cell specimen are listed in Table 4.3.

Table 4.3. Characteristics of concrete specimens used in FY 2006 sediment-concrete half-cell experiments

Cell ID	Length (cm)	Diameter (cm)	Surface Area (cm²)	Volume (cm³)	Weight (g)	Density (g/cm³)	Iron (wt%)	Carbonated	Moisture Content (wt%)	Test Duration (days)
CS-I-4%	4.21	4.32	86.26	61.50	135.92	2.21	4	Y	4	348
CS-II-4%	4.33	4.32	87.99	63.37	138.15	2.18	4	N	4	348
CS-III-4%	4.26	4.32	87.23	62.55	130.10	2.08	0	Y	4	348
CS-IV-4%	4.39	4.33	89.09	64.55	131.68	2.04	0	N	4	348
CS-I-7%	4.34	4.32	88.16	63.55	141.72	2.23	4	Y	7	354
CS-II-7%	4.26	4.33	87.22	62.54	138.21	2.21	4	N	7	354
CS-III-7%	4.15	4.32	85.69	60.89	127.87	2.10	0	Y	7	354
CS-IV-7%	4.38	4.32	88.72	64.16	132.17	2.06	0	N	7	354
CS-I-15%	4.27	4.32	87.15	62.46	139.29	2.23	4	Y	15	355
CS-II-15%	4.27	4.32	87.39	62.73	137.38	2.19	4	N	15	355
CS-III-15%	4.15	4.33	85.76	60.95	126.78	2.08	0	Y	15	355
CS-IV-15%	4.43	4.32	89.58	65.09	134.09	2.06	0	N	15	355

In FY 2008, another set of sediment-concrete diffusion experiments was initiated, expanding the test matrix to include additional percentages of iron in the concrete specimens. The general preparation of the half-cells is described in section 2.4. Sediment half-cell specimens were spiked with stable I at concentrations of ~7 mg I/g sediment. Hanford fine was used for the sediment half-cell. In these experiments, iron content was varied in the concrete specimens from 0% to 12%, sediment moisture content was varied (4%, 7%, or 15%), and half of the concrete monoliths were carbonated prior to preparing the half-cells. The characteristics of the concrete half-cell specimen are listed in Table 4.4. The test duration was 351 days.

Table 4.4. Characteristics of concrete specimens used in FY 2008 sediment-concrete half-cell experiments

Core ID	Length (cm)	Diameter (cm)	Surface Area (cm^2)	Volume (cm^3)	Weight (g)	Density (g/cm^3)	Iron (wt%)	Carbonated	Moisture Content (wt%)
C-08-3-0-325	4.09	4.33	84.97	60.10	131.44	2.19	0	N	4
C-08-3-0-329	4.32	4.33	88.13	63.53	139.50	2.20	0	N	7
C-08-3-0-330	3.85	4.33	81.77	56.65	123.50	2.18	0	N	15
C-08-3-0-332	4.33	4.32	88.09	63.48	139.65	2.20	0	Y	4
C-08-3-0-333	4.35	4.33	88.57	64.00	140.79	2.20	0	Y	7
C-08-3-0-334	4.07	4.32	84.56	59.67	130.55	2.19	0	Y	15
C-08-3-4-350	3.84	4.32	81.43	56.28	127.25	2.26	4	N	4
C-08-3-4-351	4.00	4.33	83.92	58.96	132.78	2.25	4	N	7
C-08-3-4-353	4.01	4.33	83.99	59.04	133.38	2.26	4	N	15
C-08-3-4-357	3.90	4.32	82.19	57.11	128.77	2.25	4	Y	4
C-08-3-4-359	3.83	4.32	81.25	56.09	126.50	2.26	4	Y	7
C-08-3-4-360	4.11	4.33	85.47	60.64	136.11	2.24	4	Y	15
C-08-3-8-401	4.07	4.32	84.40	59.50	135.91	2.28	8	N	4
C-08-3-8-402	3.81	4.32	81.02	55.84	127.31	2.28	8	N	7
C-08-3-8-403	4.00	4.33	83.87	58.91	133.35	2.26	8	N	15
C-08-3-8-404	4.05	4.33	84.61	59.71	133.69	2.24	8	Y	4
C-08-3-8-405	3.86	4.33	81.77	56.65	126.96	2.24	8	Y	7
C-08-3-8-406	3.94	4.33	83.08	58.05	130.61	2.25	8	Y	15
C-08-3-12-425	4.33	4.27	87.54	62.88	143.44	2.28	12	N	4
C-08-3-12-426	4.33	4.33	88.35	63.76	145.77	2.29	12	N	7
C-08-3-12-427	4.33	4.22	86.94	62.23	141.71	2.28	12	N	15
C-08-3-12-432	4.02	4.32	83.83	58.88	134.09	2.28	12	Y	4
C-08-3-12-433	4.15	4.33	85.81	61.01	139.80	2.29	12	Y	7
C-08-3-12-435	3.88	4.33	82.22	57.12	130.04	2.28	12	Y	15

4.1.2.1   Concentration Profiles

Concentration profiles of the sediment portion of the FY 2006 half-cells spiked with stable I are shown in Figure 4.3 and listed in Table B.2. Profiles for half-cells containing 4% sediment moisture content are shown at the top of Figure 4.3; 7% sediment moisture content is shown in the middle and 15% sediment moisture content is shown at the bottom. Concentration profiles are shown for sediment adjacent to monoliths with 0% iron content (black circles) and 4% iron content (white circles) that had been carbonated (left graphs) or left un-carbonated (right graphs). Except very near the interfaces, concentration gradients were not observed in any of the sediment half-cells. A fairly uniform distribution of I is observed through the length of the sediment half-cells.

Concentration profiles of the concrete portion of the FY 2006 half-cells are shown in Figure 4.4 and listed in Table B.3. Profiles for half-cells containing 4% sediment moisture content are shown at the top, 7% sediment moisture content in the middle and 15% sediment moisture content at the bottom. Concentration profiles are shown for monoliths with 0% iron content (black circles) and 4% iron content (white circles) that had been carbonated (left graphs) or left un-carbonated (right graphs). Concentrations of I at the interface were the greatest for 4% moisture content, followed by 7% moisture content and 15% moisture content, respectively. Depth of diffusion was greatest at the higher moisture content (7% and

15%). Carbonated samples (Figure 4.4A, C, and E) exhibited larger depth of diffusion in comparison to the non-carbonated samples. Concentration gradients were linearized by probit analyses to calculate diffusion coefficients.

The concentration profiles of the sediment portion of the FY 2008 half-cells spiked with stable I are shown in Figure 4.5 and listed in Table B.4. Profiles for half-cells containing 4% sediment moisture content are shown at the top, 7% sediment moisture content is shown in the middle and 15% sediment moisture content is shown at the bottom. Concentration profiles are shown for sediment adjacent to monoliths with 0% iron (black circles), 4% iron (white circles), 8% iron (black triangles), and 12% iron (white triangles) content that have been carbonated (left graphs) or left un-carbonated (right graphs). Except very near the interfaces, concentration gradients were not observed in any of the sediment half-cells.

Concentration profiles of the concrete portion of the FY 2008 half-cells are shown in Figure 4.6 and listed in Table B.5. Profiles for half-cells containing 4% sediment moisture content are shown at the top, 7% sediment moisture content is shown in the middle, and 15% sediment moisture content is shown at the bottom. Concentration profiles are shown for monoliths with 0% iron (black circles), 4% iron (white circles), 8% iron (black triangles), and 12% iron (white triangles) content that have been carbonated (left graphs) or left un-carbonated (right graphs). Well-developed concentration gradients were observed for all samples. The non-carbonated samples (Figure 4.6B, D, and F) exhibit a larger depth of diffusion than the carbonated samples. These concentration gradients were linearized by probit analyses to calculate diffusion coefficients.
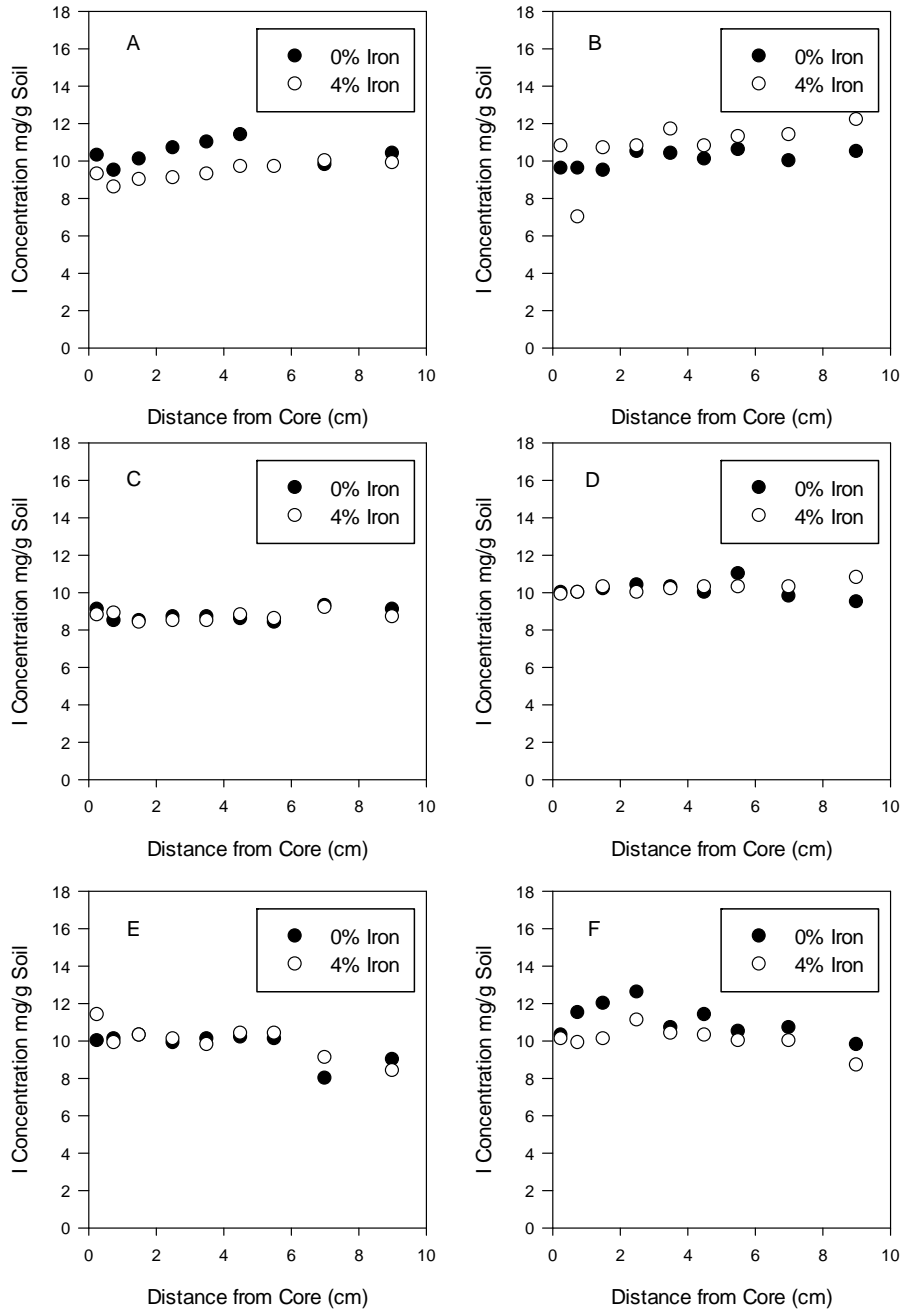
Figure 4.3. Sediment I concentration profiles from FY 2006 sediment-concrete half-cell experiments for concrete monoliths with 0% iron content (black circles) and 4% iron content (white circles) with (A) 4% sediment moisture content, carbonated monoliths, (B) 4% sediment moisture content, non-carbonated monoliths, (C) 7% sediment moisture content, carbonated monoliths, (D) 7% sediment moisture content, non-carbonated monoliths, (E) 15% sediment moisture content, carbonated monoliths, and (F) 15% sediment moisture content, non-carbonated monoliths
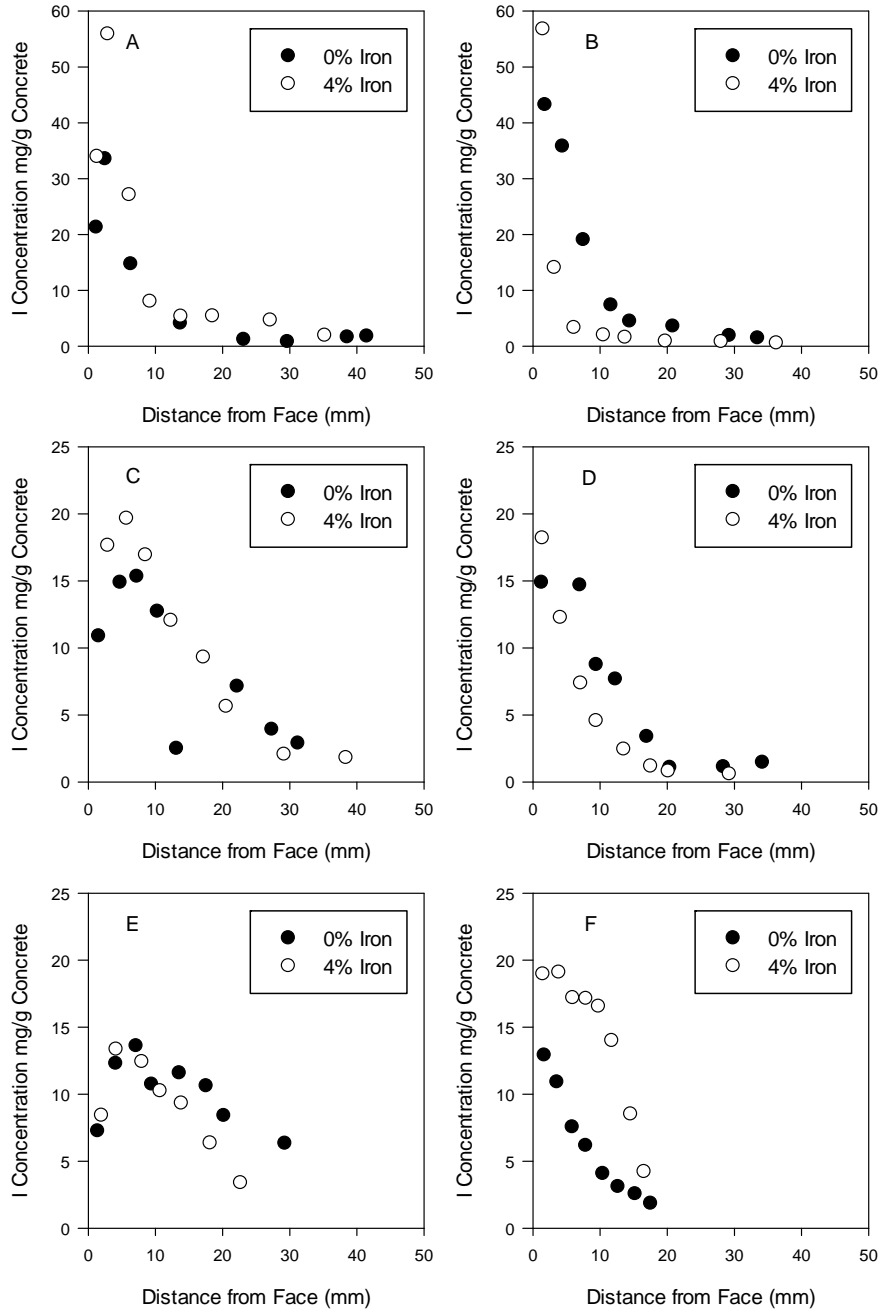
Figure 4.4. Concrete I concentration profiles from FY 2006 sediment-concrete half-cell experiments for concrete monoliths with 0% iron content (black circles) and 4% iron content (white circles) with (A) 4% sediment moisture content, carbonated monoliths, (B) 4% sediment moisture content, non-carbonated monoliths, (C) 7% sediment moisture content, carbonated monoliths, (D) 7% sediment moisture content, non-carbonated monoliths, (E) 15% sediment moisture content, carbonated monoliths, and (F) 15% sediment moisture content, non-carbonated monoliths
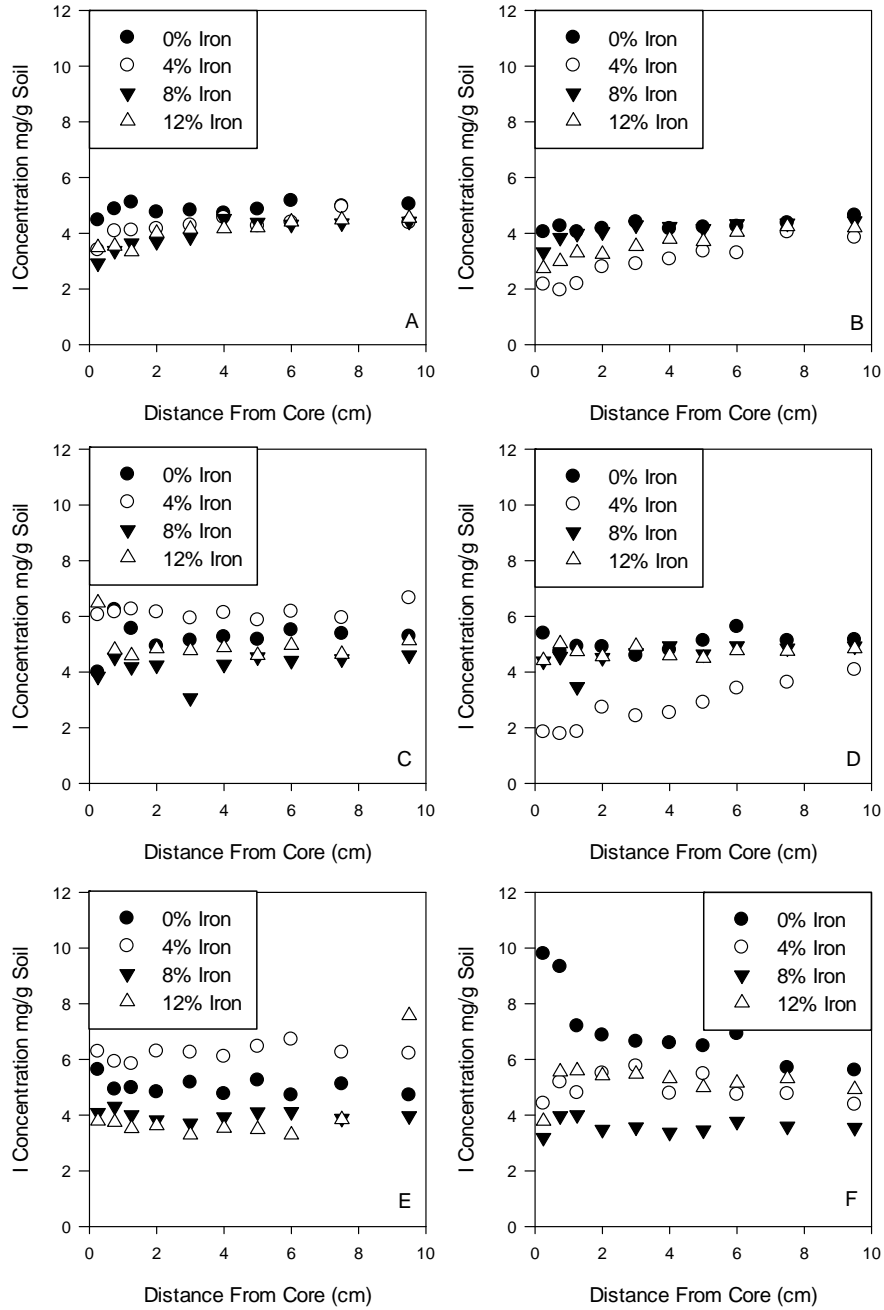
Figure 4.5. Sediment I concentration profiles from FY 2008 sediment-concrete half-cell experiments for concrete monoliths with 0% iron content (black circles), 4% iron content (white circles), 8% iron content (black triangles), and 12% iron content (white triangles) with (A) 4% sediment moisture content, carbonated monoliths, (B) 4% sediment moisture content, non-carbonated monoliths, (C) 7% sediment moisture content, carbonated monoliths, (D) 7% sediment moisture content, non-carbonated monoliths, (E) 15% sediment moisture content, carbonated monoliths, and (F) 15% sediment moisture content, non-carbonated monoliths

4.9
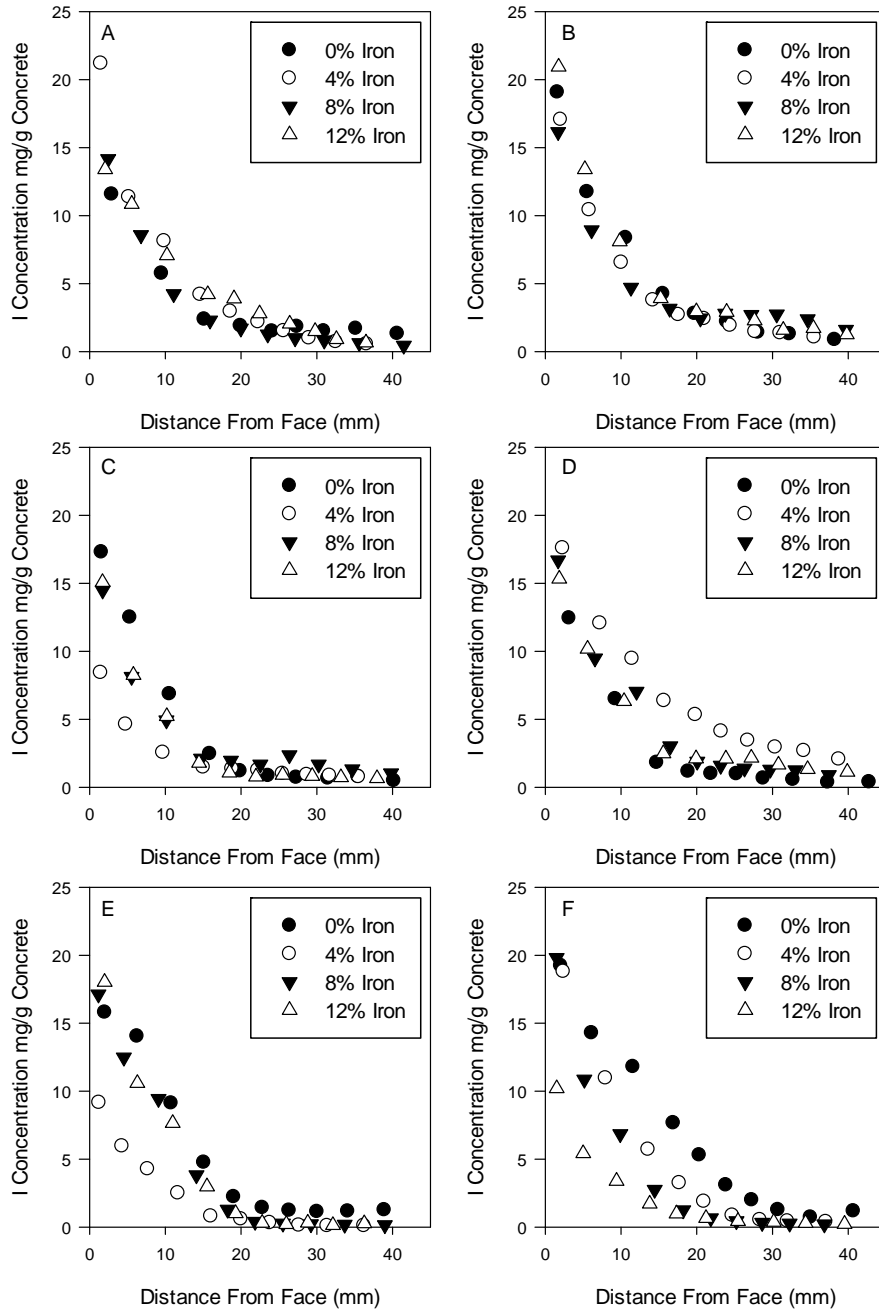
Figure 4.6. Concrete I concentration profiles from FY 2008 sediment-concrete half-cell experiments for concrete monoliths with 0% iron content (black circles), 4% iron content (white circles), 8% iron content (black triangles), and 12% iron content (white triangles) with (A) 4% sediment moisture content, carbonated monoliths, (B) 4% sediment moisture content, non-carbonated monoliths, (C) 7% sediment moisture content, carbonated monoliths, (D) 7% sediment moisture content, non-carbonated monoliths, (E) 15% sediment moisture content, carbonated monoliths, and (F) 15% sediment moisture content, non-carbonated monoliths

4.10

4.1.2.2   Probit Analysis

Probit analysis of the concentration gradients from the FY 2006 sediment-concrete diffusion experiments are shown in Figure 4.7 through Figure 4.9 as a function of distance from the interface. Figure 4.7 shows the results for 4% moisture content sediment adjacent to monoliths that were carbonated (black circles) and non-carbonated (white circles) with iron content of 0% (left) and 4% (right). Probit analysis for the 7% and 15% moisture content sediments are shown in Figure 4.8 and Figure 4.9, respectively. Diffusivities were tabulated from the slope of the linear fits and are listed in Table 4.5. Overall diffusivities ranged from 3.63×10^{-9} cm^2/s to 6.23×10^{-8} cm^2/s. Diffusivities for 7% and 15% moisture content were larger than those for 4% moisture content by a factor of ~2 to 3 for the non-carbonated specimens, up to a factor ~4 to 8 for the carbonated specimens.

Carbonation of the concrete resulted in increased diffusivities for all the samples. The increase in diffusivity was more pronounced as moisture content was increased. A 2x increase was observed for 4% moisture content, a 3x increase for 7% moisture content, and a 4x increase for the 15% moisture content.

The addition of iron to the concrete resulted in an overall decrease in I diffusivity values with a reduction by 8% to 60%. The smallest change was observed in the 15% moisture content, carbonated samples and the largest change observed in the 4% moisture content, non-carbonated samples.
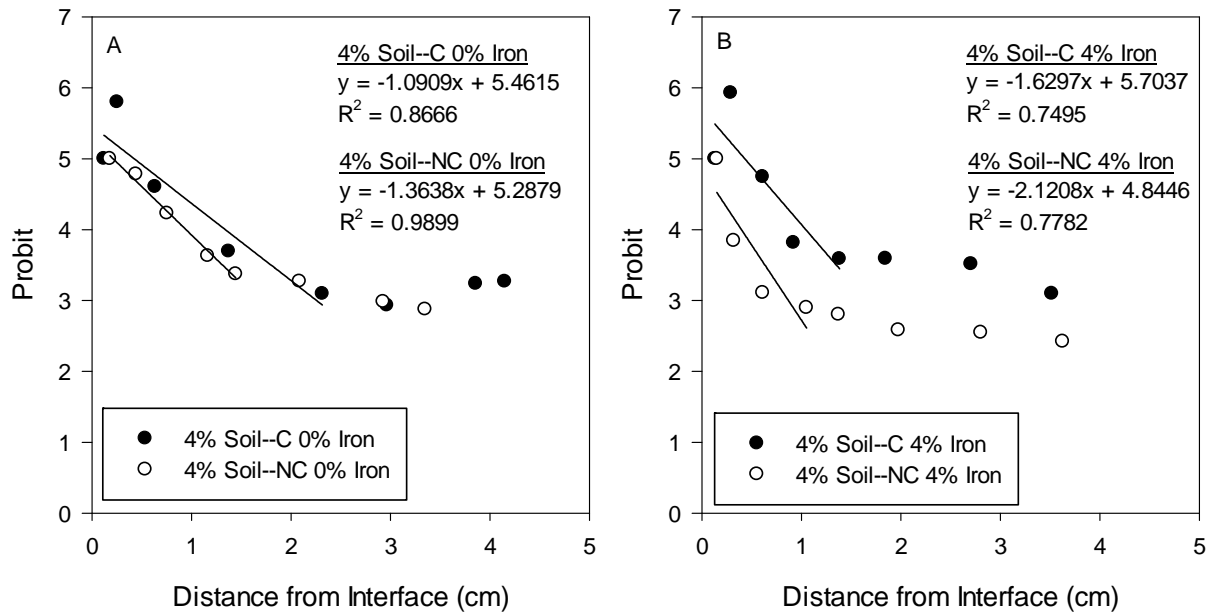
Figure 4.7. Probit plots for I diffusion from FY 2006 sediment-concrete half-cell experiments in 4% moisture content sediment for carbonated (black circles) and non-carbonated (white circles) concrete monoliths with (A) 0% iron and (B) 4% iron

4.11
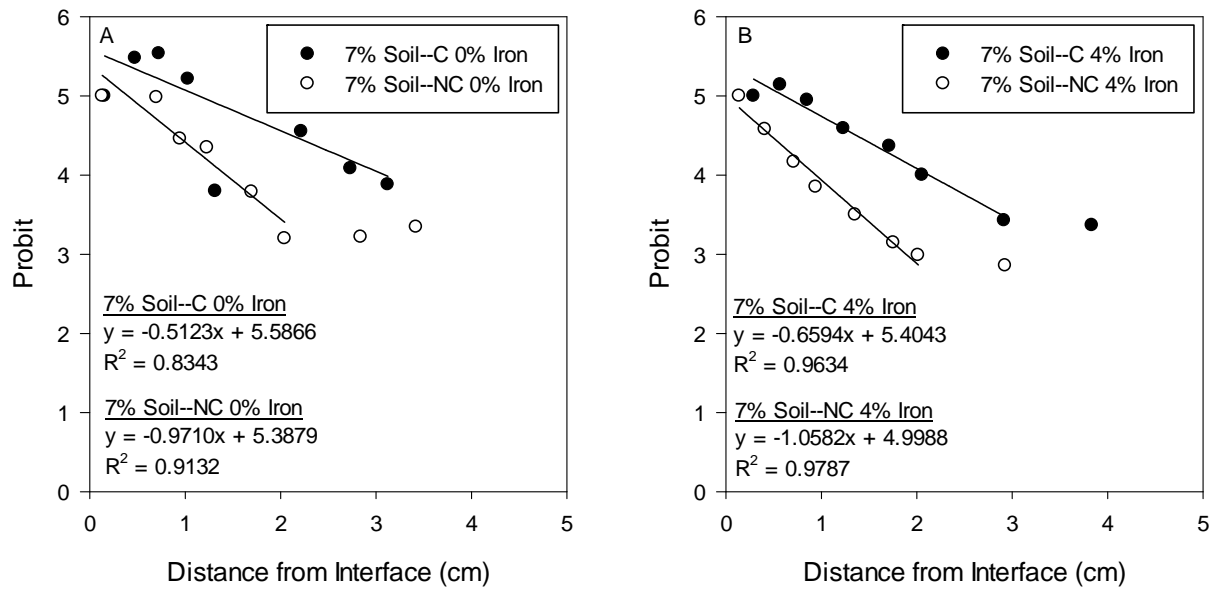
Figure 4.8. Probit plots for I diffusion from FY 2006 sediment-concrete half-cell experiments in 7% moisture content sediment for carbonated (black circles) and non-carbonated (white circles) concrete monoliths with A) 0% iron and B) 4% iron
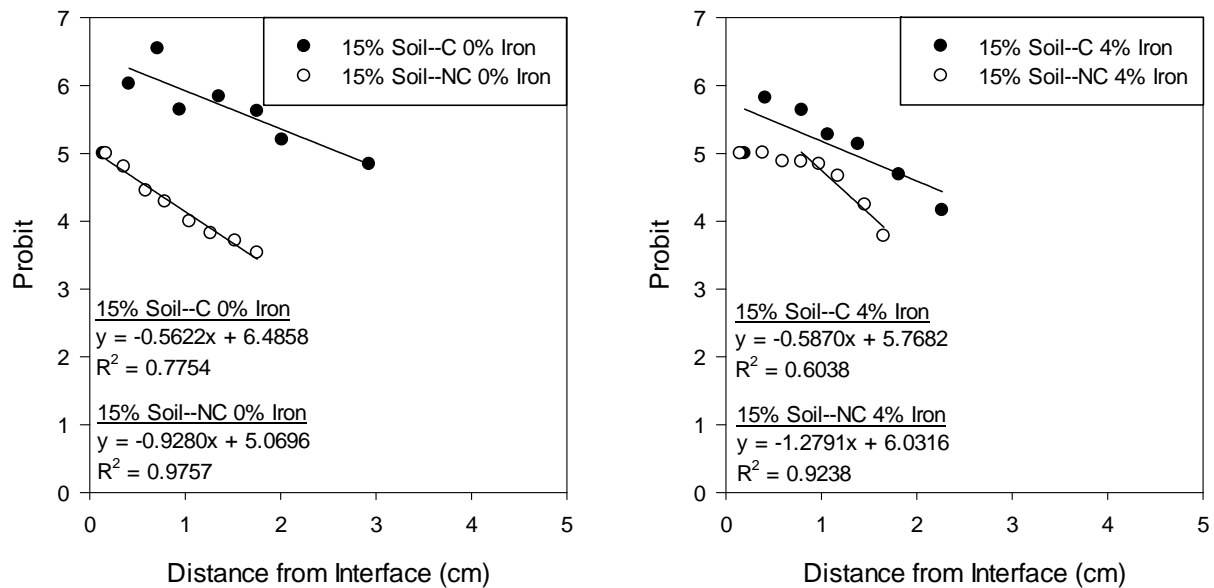
Figure 4.9. Probit plots for I diffusion from FY 2006 sediment-concrete half-cell experiments in 15% moisture content sediment for carbonated (black circles) and non-carbonated (white circles) concrete monoliths with (A) 0% iron and (B) 4% iron

Table 4.5. Calculated I diffusion parameters from FY 2006 sediment-concrete half-cell experiments

Core ID	Moisture (wt%)	Carbonated	Fe (wt %)	I Diffusivity (cm^2/s)	Probit Slope
CS-I-4%	4	Y	4	6.16×10^{-9}	1.6297
CS-II-4%	4	N	4	3.63×10^{-9}	2.1208
CS-III-4%	4	Y	0	1.37×10^{-8}	1.0909
CS-IV-4%	4	N	0	8.79×10^{-9}	1.3638
CS-I-7%	7	Y	4	3.76×10^{-8}	0.6594
CS-II-7%	7	N	4	1.46×10^{-8}	1.0582
CS-III-7%	7	Y	0	6.23×10^{-8}	0.5123
CS-IV-7%	7	N	0	1.73×10^{-8}	0.9710
CS-I-15%	15	Y	4	4.74×10^{-8}	0.5870
CS-II-15%	15	N	4	9.99×10^{-9}	1.2791
CS-III-15%	15	Y	0	5.17×10^{-8}	0.5622
CS-IV-15%	15	N	0	1.90×10^{-8}	0.9280

Probit analysis results of the FY 2008 sediment-concrete diffusion experiments are shown in Figure 4.10 through Figure 4.12 as a function of distance from the interface. Figure 4.10 shows the results for 4% moisture content sediment adjacent to monoliths that were carbonated (black circles) and non-carbonated (white circles) with 0% iron (A), 4% iron (B), 8% iron (C), and 12% iron (D). Probit analysis for the 7% and 15% moisture content sediments are shown in Figure 4.11 and Figure 4.12, respectively. Diffusivities were tabulated from the slope of the linear fits and are listed in Table 4.6. Diffusivities ranged from 1.38×10^{-8} to 9.47×10^{-8} cm^2/s. As sediment moisture content was increased from 4% to 7% or 15%, a decrease in the diffusivity value was observed ranging from a 10% to 80% reduction. Two exceptions to this trend were for the non-carbonated, 4% iron samples with a sediment moisture content increase from 4% to 7% and the carbonated, 0% iron samples with a sediment moisture content increase from 4% to 15%.

Generally, carbonation of the concrete resulted in a decrease in diffusivity coefficients. Diffusivity values were reduced by as little as 13% for 4% iron, 15% moisture content samples to as much as 82% for 4% iron, 7% moisture content samples. The only increase in diffusivity was observed for 8% iron, 4% moisture content. There were no clear trends observed with the addition of iron to the concrete.
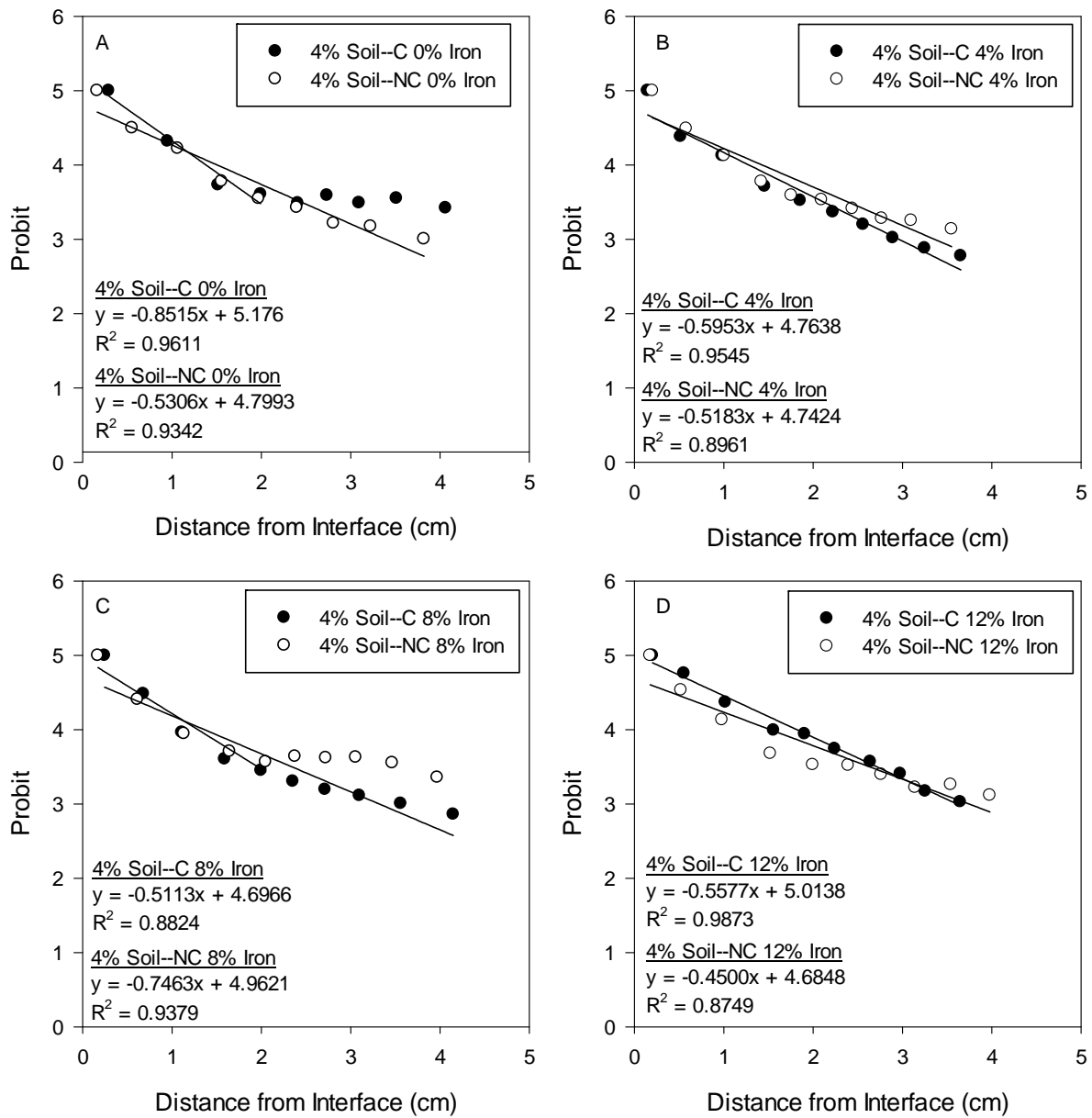
Figure 4.10. Probit plots for I diffusion from FY 2008 sediment-concrete half-cell experiments in 4% moisture content sediment for carbonated (black circles) and non-carbonated (white circles) concrete monoliths with (A) 0% iron, (B) 4% iron, (C) 8% iron, and (D) 12% iron
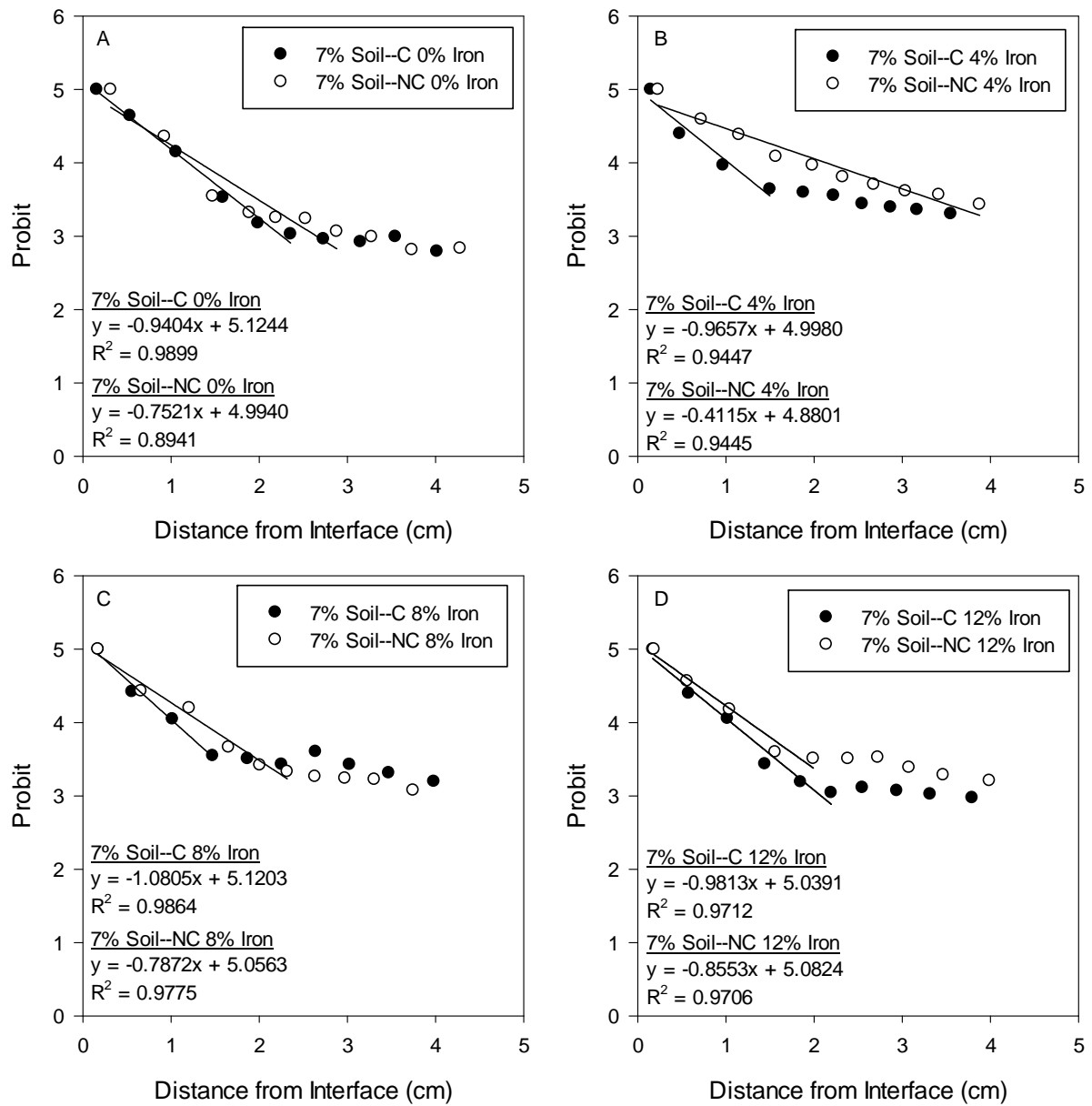
Figure 4.11. Probit plots for I diffusion from FY 2008 sediment-concrete half-cell experiments in 7% moisture content sediment for carbonated (black circles) and non-carbonated (white circles) concrete monoliths with (A) 0% iron, (B) 4% iron, (C) 8% iron, and (D) 12% iron
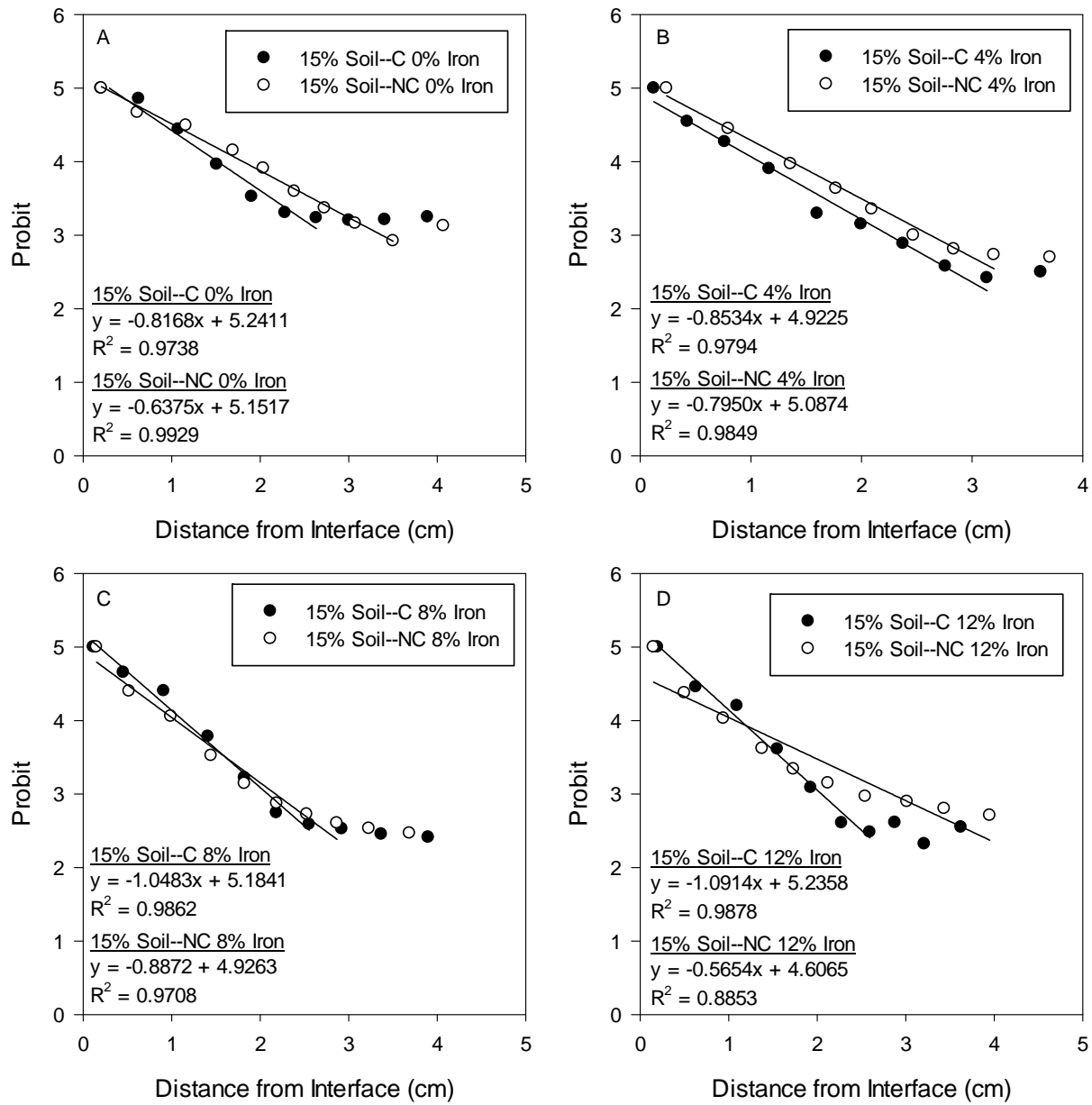
Figure 4.12. Probit plots for I diffusion from FY 2008 sediment-concrete half-cell experiments in 15% moisture content sediment for carbonated (black circles) and non-carbonated (white circles) concrete monoliths with (A) 0% iron, (B) 4% iron, (C) 8% iron, and (D) 12% iron

Table 4.6. Calculated I diffusion parameters from FY 2008 sediment-concrete half-cell experiments

Core ID	Moisture (wt%)	Carbonated	Fe (wt%)	I Diffusivity (cm^2/s)	Probit Slope
C-08-3-0-325	4	N	0	5.86×10^{-8}	0.5306
C-08-3-0-329	7	N	0	2.91×10^{-8}	0.7521
C-08-3-0-330	15	N	0	4.06×10^{-8}	0.6375
C-08-3-0-332	4	Y	0	2.27×10^{-8}	0.8515
C-08-3-0-333	7	Y	0	1.86×10^{-8}	0.9404
C-08-3-0-334	15	Y	0	2.47×10^{-8}	0.8168
C-08-3-4-350	4	N	4	6.14×10^{-8}	0.5183
C-08-3-4-351	7	N	4	9.74×10^{-8}	0.4115
C-08-3-4-353	15	N	4	2.61×10^{-8}	0.7950
C-08-3-4-357	4	Y	4	4.65×10^{-8}	0.5953
C-08-3-4-359	7	Y	4	1.77×10^{-8}	0.9657
C-08-3-4-360	15	Y	4	2.26×10^{-8}	0.8534
C-08-3-8-401	4	N	8	2.96×10^{-8}	0.7463
C-08-3-8-402	7	N	8	2.66×10^{-8}	0.7872
C-08-3-8-403	15	N	8	2.09×10^{-8}	0.8872
C-08-3-8-407	4	Y	8	6.31×10^{-8}	0.5113
C-08-3-8-409	7	Y	8	1.41×10^{-8}	1.0805
C-08-3-8-410	15	Y	8	1.50×10^{-8}	1.0483
C-08-3-12-425	4	N	12	8.14×10^{-8}	0.4500
C-08-3-12-426	7	N	12	2.25×10^{-8}	0.8553
C-08-3-12-427	15	N	12	5.16×10^{-8}	0.5654
C-08-3-12-432	4	Y	12	5.30×10^{-8}	0.5577
C-08-3-12-433	7	Y	12	1.71×10^{-8}	0.9813
C-08-3-12-435	15	Y	12	1.38×10^{-8}	1.0914

4.1.3   Concrete to Sediment

A set of concrete-sediment diffusion experiments was initiated during FY 1999 to investigate the effect of moisture content and test duration on the diffusion of I from concrete to sediment. Concrete half-cell specimens were spiked with stable I (0.46 mg I/g concrete) and I-125 (2.06×10^{-8} mg I-125/g concrete) to achieve a measurable diffusion profile in the sediment part of the half-cell. The general preparation of the half-cells is described in section 2.4. The characteristics of the concrete half-cells are listed in Table 4.7. Trench 8 sediment was used for the sediment half-cell. Tests were run for 64 and 169 days.

Table 4.7. Characteristics of concrete specimens used in FY 1999 concrete-sediment half-cell experiments

Core ID	Length (cm)	Diameter (cm)	Surface Area (cm²)	Volume (cm³)	Weight (g)	Density (g/cm³)	Iron (wt%)	Carbonated	Moisture Content (wt%)	Duration (days)
CS-I-4%	4.3	8.255	218.56	230.14	513.21	2.23	4	N	4	64
CS-II-4%	4.2	8.255	215.96	224.79	496.78	2.21	4	N	4	169
CS-III-7%	4.2	8.255	215.96	224.79	505.77	2.25	4	N	7	64
CS-IV-7%	4.2	8.255	215.96	224.79	496.78	2.21	4	N	7	169

Another set of concrete-sediment diffusion experiments was initiated during FY 2002 (7% moisture content half-cells) and FY 2004 (4% moisture content half-cells) to investigate the effect of sediment moisture content, concrete iron content, and carbonation of concrete on the diffusion of I from concrete to sediment. Concrete half-cell specimens were spiked with stable I (0.47 mg I/g concrete) to achieve a measurable diffusion profile in the sediment part of the half-cell. The general preparation of the half-cells is described in section 2.4. HFS was used for the sediment half-cell. In these experiments, iron content was varied in the concrete specimens at 0% and 4%, sediment moisture content was varied (4% or 7%), and half of the concrete monoliths were carbonated prior to preparing the half-cells. The characteristics of the concrete half-cells are listed in Table 4.8. Tests were run for 357 days for the 4% moisture content tests and 397 days for the 7% moisture content tests.

Table 4.8. Characteristics of concrete specimens used in FY 2002 and FY 2004 concrete-sediment half-cell experiments

Core ID	Length (cm)	Diameter (cm)	Surface Area (cm²)	Volume (cm³)	Weight (g)	Density (g/cm³)	Iron (wt%)	Carbonated	Moisture Content (wt%)	Duration (days)
CS-I-4%	4.20	5.75	128.02	109.08	203.98	1.87	0	Y	4	357
CS-II-4%	4.35	5.67	127.75	109.66	199.58	1.82	0	N	4	357
CS-III-4%	4.20	5.99	135.58	118.19	239.93	2.03	4	Y	4	357
CS-IV-4%	4.25	6.01	136.79	120.76	247.56	2.05	4	N	4	357
CS-I-7%	4.00	5.68	122.27	101.53	185.80	1.83	0	Y	7	397
CS-II-7%	4.30	5.69	127.76	109.29	200.00	1.83	0	N	7	397
CS-III-7%	4.20	6.05	137.00	120.72	249.89	2.07	4	Y	7	397
CS-IV-7%	4.30	6.02	137.87	122.24	250.59	2.05	4	N	7	397

4.1.3.1   Concentration Profiles

The concentration profiles of the 4% (black circles) and 7% (white circles) moisture content sediment half-cells for the FY 1999 concrete-sediment experiments are shown as a function of distance from the concrete monolith in Figure 4.13 and listed in Table B.6. Concentration gradients for I were observed from the interface in the sediment half-cells with higher concentrations and greater diffusion depth observed in the half-cells with the 7% moisture content sediment. These concentration gradients were linearized by probit analyses to calculate diffusion coefficients. Results are not available for the 64-day testing because as test samples were extracted with nitric acid, iodide was oxidized to I and lost through volatilization. Concentration profiles of the concrete portion of the half-cells were not measured.
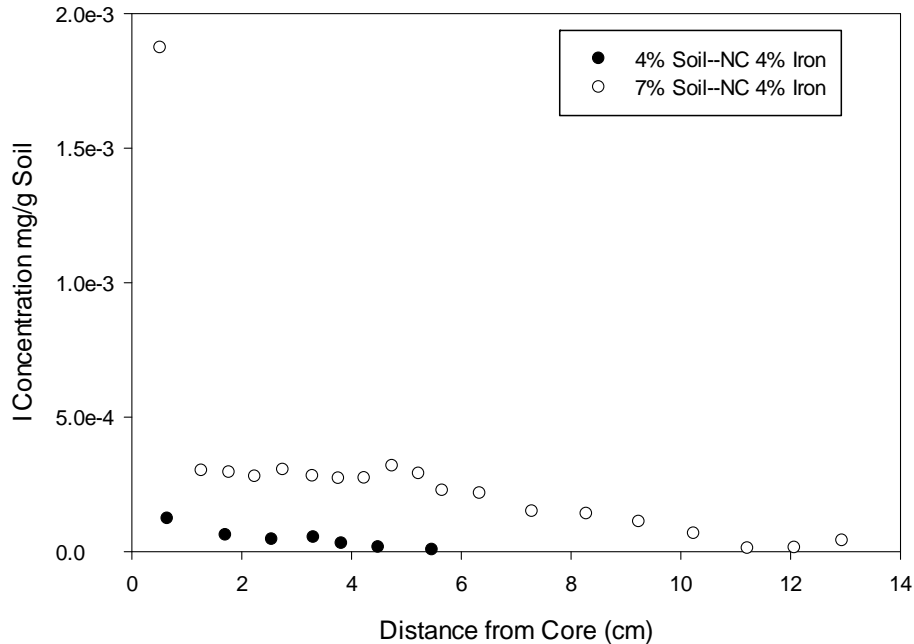
Figure 4.13. Sediment I concentration profiles from FY 1999 concrete-sediment 170-day half-cell experiments for 4% sediment moisture, non-carbonated concrete with 4% iron (black circles) and 7% sediment moisture, non-carbonated concrete with 4% iron (white circles)

The concentration profiles of the sediment half-cells for the FY 2002 and FY 2004 concrete-sediment experiments are shown in Figure 4.14 and listed Table B.7. Profiles for half-cells containing 4% sediment moisture content are shown at the top and 7% sediment moisture content are at the bottom. Concentration profiles are shown for sediment adjacent to monoliths with 0% iron content (black circles) and 4% iron content (white circles) that had been carbonated (left graphs) or left un-carbonated (right graphs). Concentration gradients were observed from the interface in all of the sediment half-cells. A larger diffusion depth was observed for the half-cells with 7% moisture content sediment (Figure 4.14C and D). Concentration profiles were greater for the 0% iron, non-carbonated tests (Figure 4.14B and D) when compared to the iron containing counterparts. These concentration gradients were linearized by probit analyses to allow calculation of diffusion coefficients. Concentration profiles of the concrete portion of the half-cells were not measured.
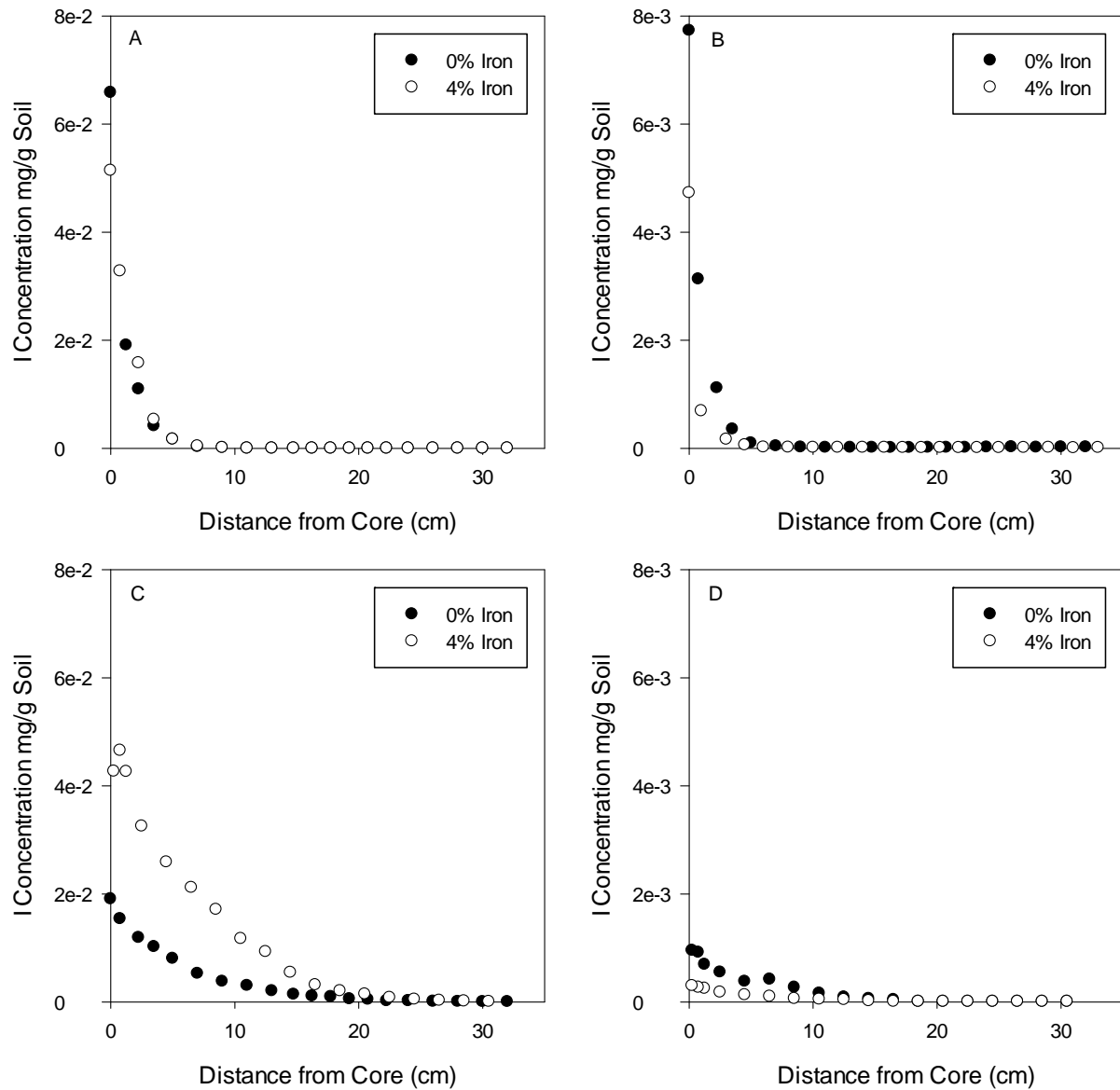
Figure 4.14. Sediment I concentration profiles from FY 2002 and FY 2004 concrete-sediment half-cell experiments for (A) 4% sediment moisture, carbonated monolith, (B) 4% sediment moisture, non-carbonated monolith, (C) 7% sediment moisture, carbonated monolith, (D) 7% sediment moisture, non-carbonated monolith

4.1.3.2   Probit Analysis

Probit analysis of the FY 1999 concrete-sediment diffusion experiments is shown in Figure 4.15. Calculated probit values are plotted as a function of distance from the interface for 4% (black circles) and 7% (white circles) sediment moisture content. The slope from the linear fits was used to calculate the diffusivities listed in Table 4.9. The calculated diffusivities for I were 2.63×10^{-7} cm^2/s for 4% moisture content and 2.01×10^{-6} cm^2/s for 7% moisture content. Diffusivity increased by nearly an order of magnitude with the increase in moisture content. Due to the volatilization of I during the extraction process for the 64-day tests, the effect of test duration on I diffusivity could not be determined with this set of tests.

4.20
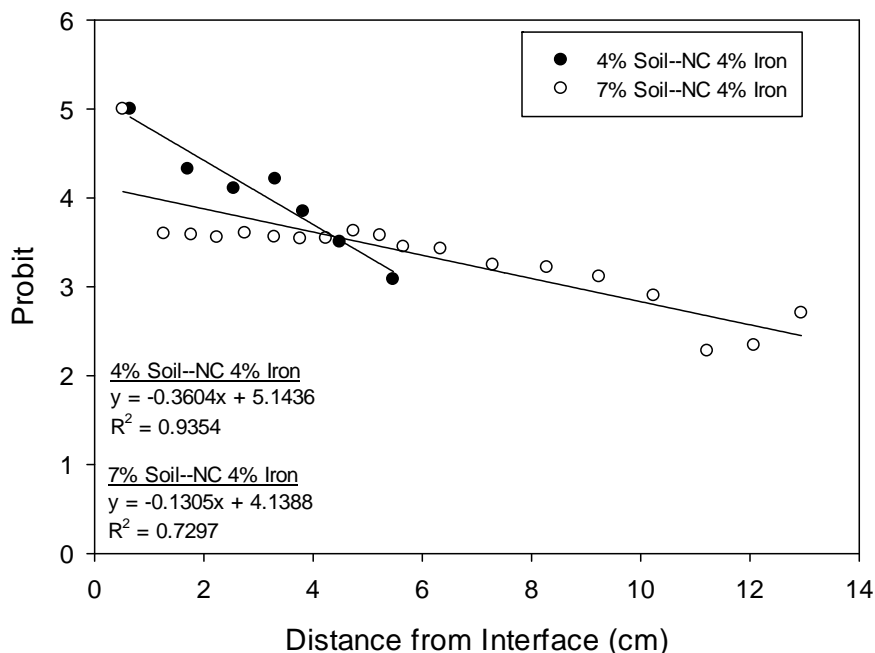
Figure 4.15. Probit plot for I diffusion from FY 1999 concrete-sediment 170-day half-cell experiments for 4% sediment moisture, non-carbonated monolith with 4% iron (black circles) and 7% sediment moisture, non-carbonated monolith with 4% iron (white circles)

Table 4.9. Calculated I diffusion parameters from FY 1999 concrete to sediment half-cell experiments

Core ID	Moisture (wt%)	Carbonated	Fe (wt %)	I Diffusivity (cm^2/s)	Probit Slope
CS-II-4%	4	N	4	2.63×10^{-7}	0.3605
CS-IV-7%	7	N	4	2.01×10^{-6}	0.1305

Probit analysis of the FY 2002 and FY 2004 concrete-sediment diffusion experiments is shown in Figure 4.16. The results for the 4% (top) and 7% (bottom) moisture content sediments adjacent to monoliths that were carbonated (black circles) and non-carbonated (white circles) with iron content of 0% (left) and 4% (right) as a function of distance from the interface. Slopes from the linear fits were used to calculate the diffusivities listed in Table 4.10. Diffusivity values range over an order of magnitude from 9.17×10^{-8} to 1.59×10^{-6} cm^2/s. Similar to the previous set of results, nearly an order of magnitude increase in diffusivity values was observed with the increase in sediment moisture content. The addition of iron resulted in a reduction in diffusivity values (~10% to 20%) in all samples, except the non-carbonated, 7% moisture content samples, where a 16% increase in diffusivity was observed. Carbonation of the concrete specimens resulted in approximately a factor of 2 increase in diffusivity values.
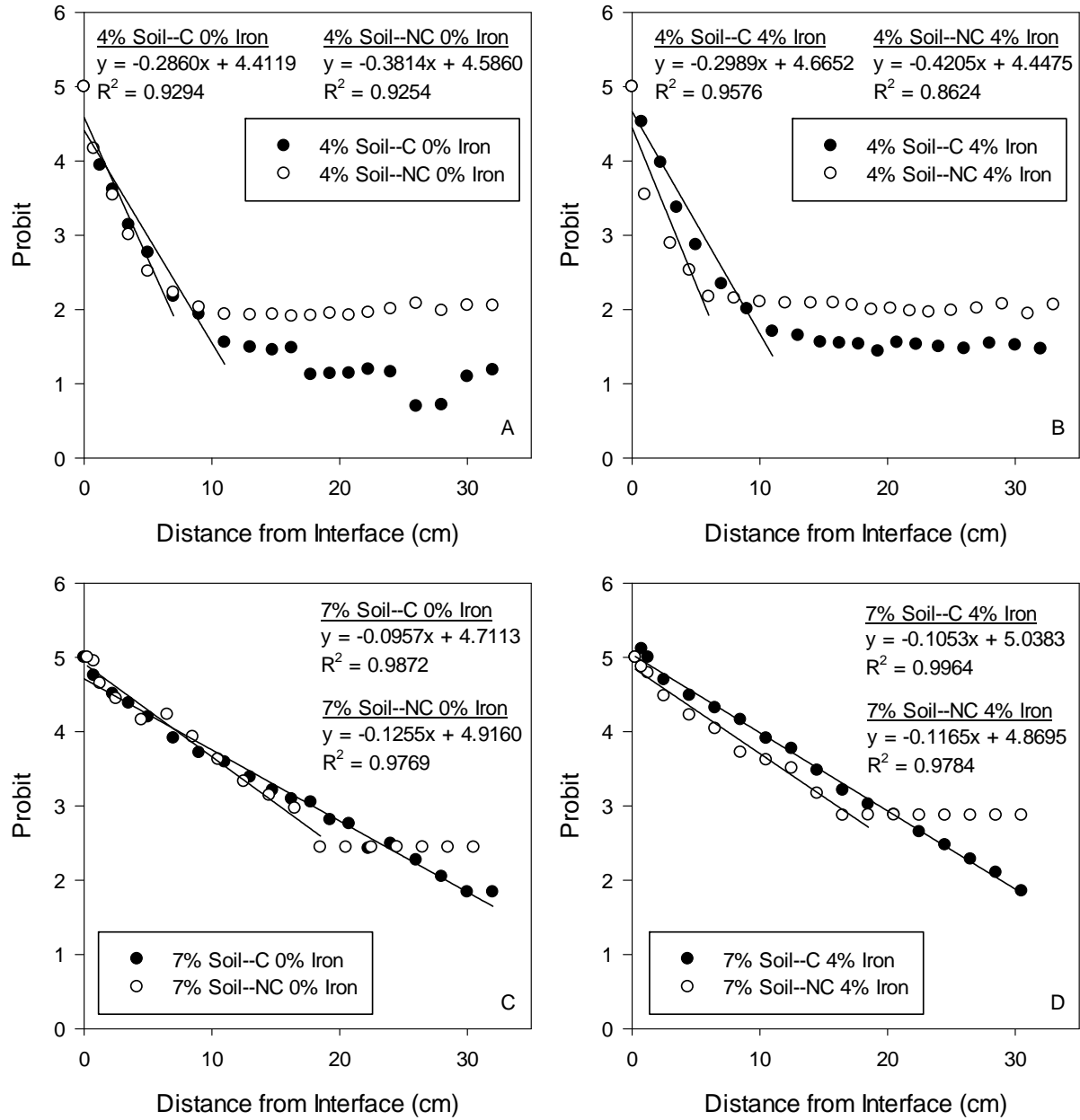
Figure 4.16. Probit plots for I diffusion from FY 2002 and FY 2004 concrete-sediment half-cell experiments for carbonated (black circles) and non-carbonated (white circles) concrete monoliths in 4% moisture content sediment with (A) 0% iron, (B) 4% iron, and in 7% moisture content sediment with (C) 0% iron, and (D) 4% iron

Table 4.10. Calculated diffusion parameters for I from FY 2002 and FY 2004 concrete-sediment half-cell experiments

Core ID	Moisture Content (wt%)	Carbonated	Iron (wt%)	I Diffusivity (cm^2/s)	Probit Slope
CS-I-4%	4	Y	0	1.98×10^{-7}	0.2860
CS-II-4%	4	N	0	1.11×10^{-7}	0.3814
CS-III-4%	4	Y	4	1.81×10^{-7}	0.2989
CS-IV-4%	4	N	4	9.17×10^{-8}	0.4205
CS-I-7%	7	Y	0	1.59×10^{-6}	0.0957
CS-II-7%	7	N	0	9.26×10^{-7}	0.1255
CS-III-7%	7	Y	4	1.31×10^{-6}	0.1053
CS-IV-7%	7	N	4	1.07×10^{-6}	0.1165

4.1.4   Fractured Concrete to Sediment

A set of diffusion experiments was initiated to assess the effect of fractures within the concrete monolith on the diffusion of Tc-99 into the sediment. Fractures within concrete may create preferential pathways for diffusion of contaminants. The test matrix included varied sediment moisture content, concrete iron content, and carbonation of the concrete monoliths. Concrete half-cell specimens were spiked with stable I (32 mg I/g concrete) to achieve a measurable diffusion profile in the sediment part of the half-cell. The characteristics of the concrete half-cells are listed in Table 4.11. HFS was used for the sediment half-cell. The general preparation of the half-cells is described in section 2.4. Test duration was 385 days.

Table 4.11. Characteristics of concrete specimens used in fractured concrete-sediment half-cell experiments

Core ID	Length (cm)	Diameter (cm)	Surface Area (cm^2)	Volume (cm^3)	Weight (g)	Density (g/cm^3)	Iron (wt%)	Carbonated	Moisture Content (wt%)
C-08-5-0-504	4.00	4.32	83.43	58.45	141.89	2.43	0	Y	4
C-08-5-4-530	3.96	4.33	83.27	58.26	139.27	2.39	4	Y	4
C-08-5-8-555	3.95	4.30	82.40	57.36	140.05	2.44	8	Y	4
C-08-5-12-580	4.06	4.31	84.27	59.36	144.46	2.43	12	Y	4
C-08-5-0-501	3.92	4.32	82.37	57.31	137.08	2.39	0	N	4
C-08-5-4-526	3.86	4.32	81.77	56.65	136.50	2.41	4	N	4
C-08-5-8-552	4.12	4.31	84.94	60.08	146.32	2.44	8	N	4
C-08-5-12-576	4.05	4.31	84.03	59.10	144.99	2.45	12	N	4
C-08-5-0-505	3.86	4.32	81.68	56.55	138.20	2.44	0	Y	7
C-08-5-4-531	4.11	4.32	85.16	60.31	145.56	2.41	4	Y	7
C-08-5-8-556	3.92	4.30	82.12	57.05	140.48	2.46	8	Y	7
C-08-5-12-581	4.29	4.31	87.17	62.49	153.33	2.45	12	Y	7
C-08-5-0-502	3.94	4.31	82.48	57.43	137.23	2.39	0	N	7
C-08-5-4-527	4.14	4.32	85.43	60.61	145.87	2.41	4	N	7
C-08-5-8-553	4.04	4.32	84.28	59.36	145.89	2.46	8	N	7
C-08-5-12-577	4.08	4.31	84.36	59.46	144.82	2.44	12	N	7
C-08-5-0-507	3.99	4.31	83.28	58.29	141.02	2.42	0	Y	15
C-08-5-4-532	3.85	4.32	81.45	56.31	134.81	2.39	4	Y	15

Core ID	Length (cm)	Diameter (cm)	Surface Area (cm^2)	Volume (cm^3)	Weight (g)	Density (g/cm^3)	Iron (wt%)	Carbonated	Moisture Content (wt%)
C-08-5-8-557	4.07	4.30	84.05	59.13	145.19	2.46	8	Y	15
C-08-5-12-552	3.92	4.31	82.11	57.04	141.77	2.49	12	Y	15
C-08-5-0-503	4.13	4.32	85.35	60.52	145.80	2.41	0	N	15
C-08-5-4-528	3.80	4.32	81.02	55.83	134.05	2.40	4	N	15
C-08-5-8-554	3.89	4.30	81.63	56.53	138.57	2.45	8	N	15
C-08-5-12-578	3.84	4.31	81.11	55.96	137.24	2.45	12	N	15

4.1.4.1 Concentration Profiles

Concentration profiles of the concrete half-cells spiked with stable I are shown as a function of distance from the sediment interface in Figure 4.17 and listed Table B.8. Profiles for half-cells containing 4% sediment moisture content are shown at the top, 7% sediment moisture content in the middle, and 15% sediment moisture content at the bottom. Concentration profiles are shown for monoliths with 0% iron (black circles), 4% iron (white circles), 8% iron (black triangles), and 12% iron (white triangles) content that had been carbonated (left graphs) or left un-carbonated (right graphs). One feature of these profiles is the bidirectional diffusion in the concrete cores. During storage of these half-cells, some of the sediment had worked into the gap between the concrete half-cells and the surrounding plastic tube. Sediment contacting both ends of the concrete half-cells seemed to have caused the bidirectional diffusion.

Concentration profiles of the sediment half-cells as a function of distance from the concrete monolith are shown in Figure 4.18 and listed in Table B.9. Profiles for half-cells containing 4% sediment moisture content are shown at the top, 7% sediment moisture content in the middle, and 15% sediment moisture content at the bottom. Concentration profiles are shown for sediment adjacent to monoliths with 0% iron (black circles), 4% iron (white circles), 8% iron (black triangles), and 12% iron (white triangles) that had been carbonated (left graphs) or left un-carbonated (right graphs). The 4% moisture content half-cells exhibited well-developed concentration gradients (Figure 4.18A and B). The 4% moisture content sediment in contact with the non-carbonated concrete exhibited increased diffusivity compared to sediment in contact with carbonated concrete. These concentration gradients were linearized by probit analyses to calculate diffusion coefficients.

Depth of diffusion was increased in both 7% and 15% moisture content sediment and the majority of the half-cells exhibited relatively constant concentrations throughout the sediment (Figure 4.18C, D, E, and F). Reduced concentrations are observed in sediment in contact with carbonated concrete (Figure 4.18C and E).
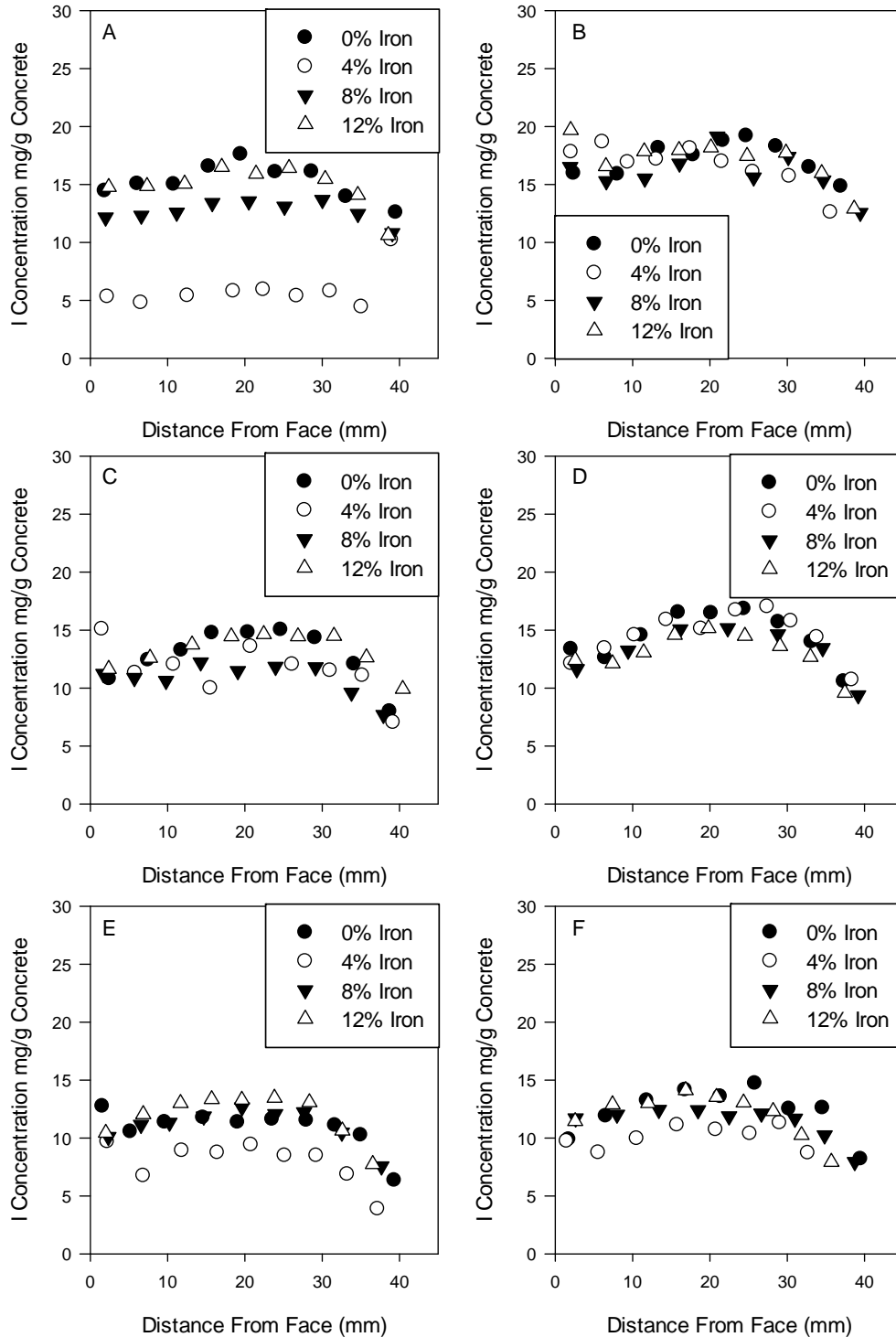
Figure 4.17. Concrete I concentration profiles from fractured concrete-sediment half-cell experiments for monoliths with 0% iron (black circles), 4% iron (white circles), 8% iron (black triangles), and 12% iron (white triangles) for (A) 4% sediment moisture, carbonated monoliths, (B) 4% sediment moisture, non-carbonated monoliths, (C) 7% sediment moisture, carbonated monolith, (D) 7% sediment moisture, non-carbonated monoliths, (E) 15% sediment moisture, carbonated monoliths, and (F) 15% sediment moisture, non-carbonated monoliths

4.25
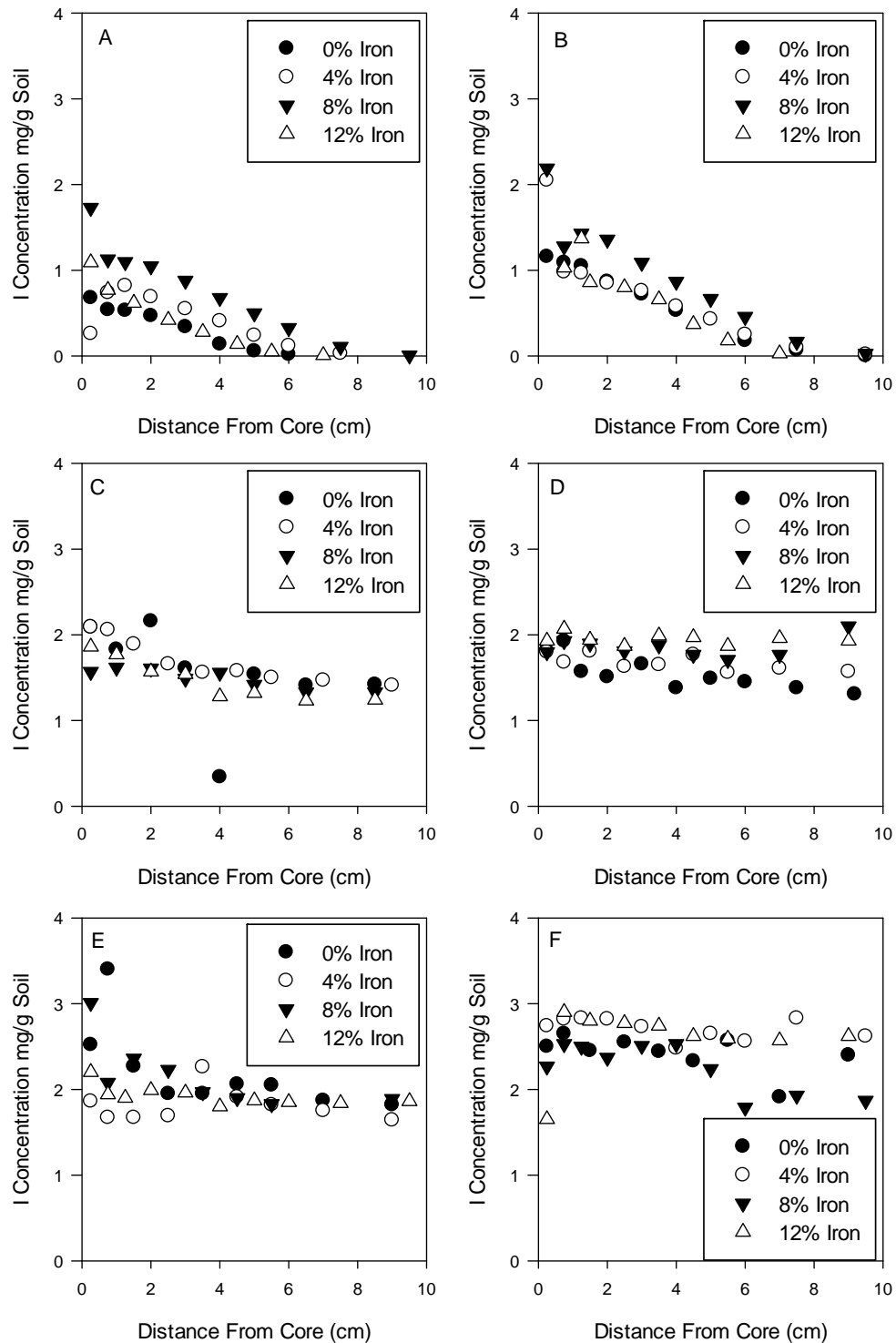
Figure 4.18. Sediment I concentration profiles from fractured concrete-sediment half-cell experiments with 0% iron monoliths (black circles), 4% iron monoliths (white circles), 8% iron (black triangles), and 12% iron (white triangles) for (A) 4% sediment moisture, carbonated monoliths, (B) 4% sediment moisture, non-carbonated monoliths, (C) 7% sediment moisture, carbonated monolith, (D) 7% sediment moisture, non-carbonated monoliths, (E) 15% sediment moisture, carbonated monoliths, and (F) 15% sediment moisture, non-carbonated monoliths

4.26

4.1.4.2 Probit Analysis

Probit analysis of the fractured concrete-sediment diffusion experiments is shown in Figure 4.19 (4% moisture content) and Figure 4.20 (7% moisture content) as a function of distance from the interface. Figure 4.19 shows the results for 4% moisture content sediment adjacent to monoliths that were carbonated (black circles) and non-carbonated (white circles) with 0% iron (A), 4% iron (B), 8% iron (C), and 12% iron (D). Probit analysis for the 7% moisture content sediment adjacent to carbonated concrete monoliths with 0% iron (black circles), 4% iron (white circles), and 12% iron (white triangles) is shown in Figure 4.20. Diffusivities were tabulated from the slope of the linear fits and are listed in Table 4.12. Overall, diffusivities range over an order of magnitude from 1.06×10^{-7} cm^2/s to 5.99×10^{-6} cm^2/s. Due to a lack of concentration gradients, diffusion coefficients were not calculated for any of the 15% moisture content sediment half-cells or the 7% moisture content sediment half-cells in contact with non-carbonated concrete.

As sediment moisture content increased from 4% to 7%, diffusivity values increased 35 times, 40 times, and 8 times for sediment adjacent to carbonated concrete with iron content of 0%, 4%, and 12%, respectively. The probit analysis for the 7% moisture content sediment is not available for the non-carbonated samples, so a similar comparison cannot be made.

Carbonation of concrete reduced diffusion values in sediment by up to 50% for the 4% moisture content sediment half-cells, with larger effects observed for the 0% and 4% iron content samples. The probit analysis for the 7% moisture content sediment is not available for the non-carbonated samples, so a similar comparison cannot be made.

Adding 4% iron to the concrete resulted in an increase in diffusivity values relative to concrete with no iron, increases ranging from 40% to 60%. The largest effect observed was for the 7% moisture content carbonated samples. The addition of 8% iron again showed an increase in diffusivity values relative to the concrete without iron, but exhibited mixed results when compared to the 4% iron content samples. Increasing the iron content from 8% to 12% caused a decrease in diffusivity for the 4% moisture content samples. Comparing the 0% iron diffusivity values with the 12% iron values gave mixed results, as two sets of diffusivity values decreased and one (4% moisture content, carbonated) increased.
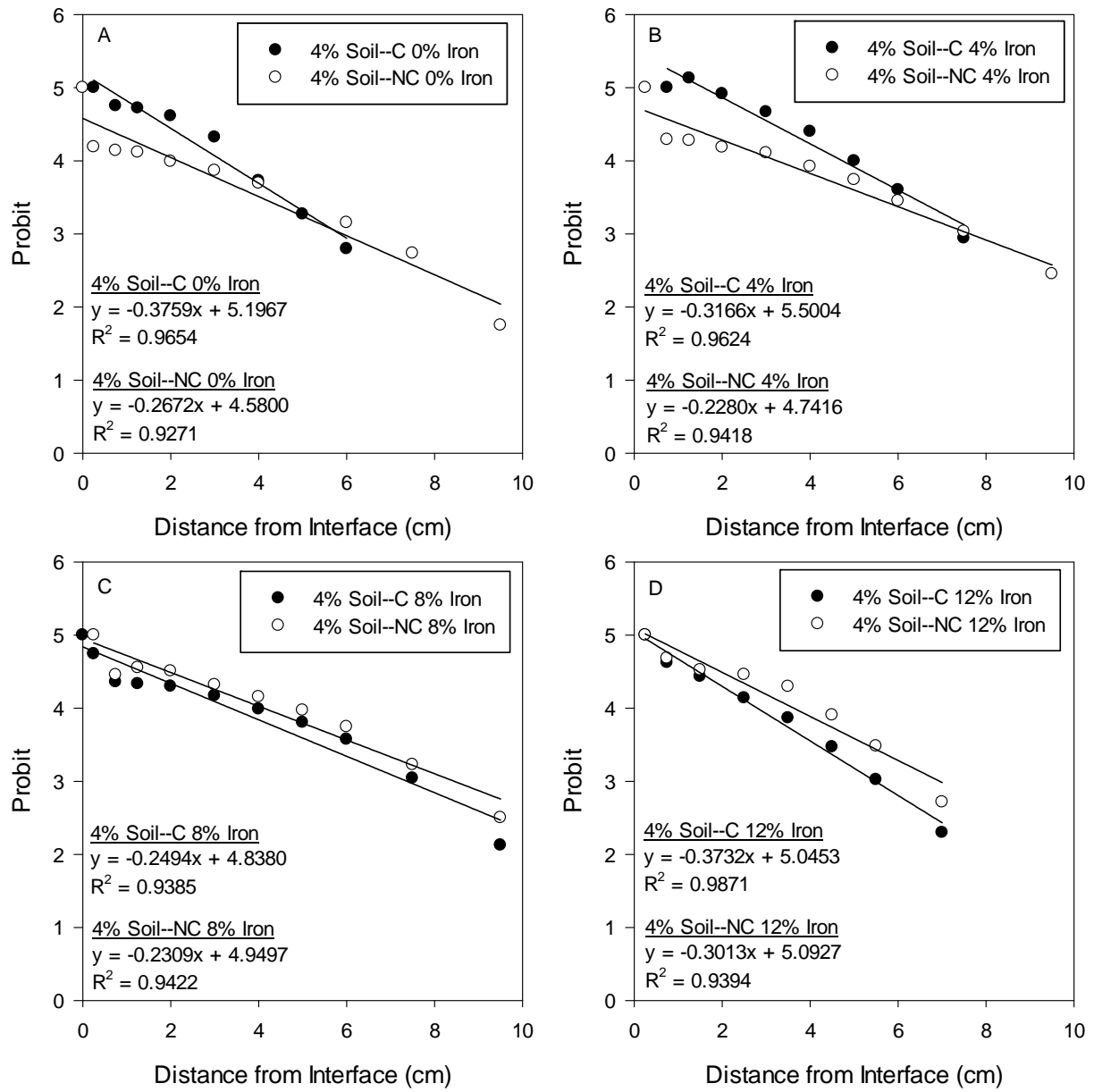
Figure 4.19. Probit plots for I diffusion from fractured concrete-sediment half-cell experiments in 4% moisture content sediment for carbonated (black circles) and non-carbonated (white circles) concrete monoliths with (A) 0% iron, (B) 4% iron, (C) 8% iron, and (D) 12% iron
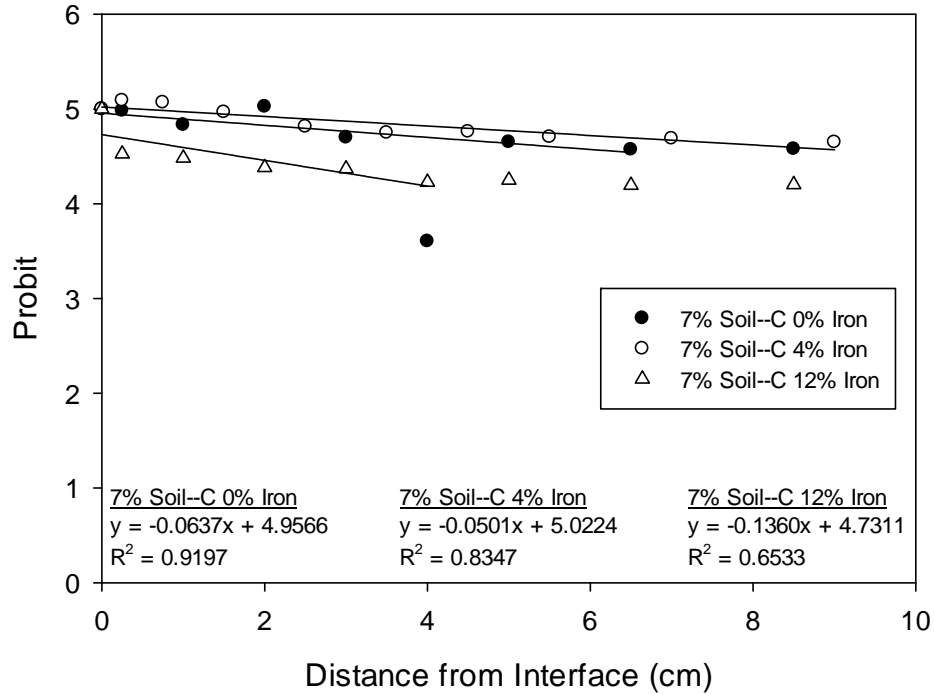
Figure 4.20. Probit plot for I diffusion from fractured concrete-sediment half-cell experiments in 7% moisture content sediment for carbonated concrete monoliths with 0% iron (black circles), 4% iron (white triangles), and 12% iron (black squares)

Table 4.12. Calculated I diffusion parameters from fractured concrete-sediment half-cell experiments

Core ID	Moisture (wt%)	Carbonated	Iron (wt %)	I Diffusivity (cm^2/s)	Probit Slope
C-08-5-0-504	4	Y	0	1.06×10^{-7}	0.3759
C-08-5-4-530	4	Y	4	1.50×10^{-7}	0.3166
C-08-5-8-555	4	Y	8	2.42×10^{-7}	0.2494
C-08-5-12-580	4	Y	12	1.08×10^{-7}	0.3732
C-08-5-0-501	4	N	0	2.11×10^{-7}	0.2672
C-08-5-4-526	4	N	4	2.89×10^{-7}	0.2280
C-08-5-8-552	4	N	8	2.82×10^{-7}	0.2309
C-08-5-12-576	4	N	12	1.66×10^{-7}	0.3013
C-08-5-0-505	7	Y	0	3.70×10^{-6}	0.0637
C-08-5-4-531	7	Y	4	5.99×10^{-6}	0.0501
C-08-5-12-581	7	Y	12	8.13×10^{-7}	0.1360

4.1.5   Sediment to Fractured Concrete

Half-cell experiments were initiated to investigate the effect of sediment moisture content, concrete carbonation, and concrete iron content on the diffusion from sediment into fractured concrete. Sediment half-cell specimens were spiked with stable I (7 mg/g sediment) to achieve a measureable diffusion in the fractured concrete part of the half-cell. The characteristics of the half-cells are listed in Table 4.13. HFS was used for the sediment half-cell. The general preparation of the half-cells is described in section 2.4. Test duration was 467 days.

Table 4.13. Characteristics of concrete specimens used in sediment-fractured concrete half-cell experiments

Core ID	Length (cm)	Diameter (cm)	Surface Area (cm^2)	Volume (cm^3)	Weight (g)	Density (g/cm^3)	Moisture (wt %)	Carbonated	Fe (wt%)
C-5-0-1	4.15	4.33	86.04	61.25	130.11	2.12	4	Yes	0
C-5-4-21	4.02	4.33	84.04	59.10	132.46	2.24	4	Yes	4
C-5-0-2	4.15	4.33	85.89	61.10	127.99	2.09	4	No	0
C-5-4-26	3.89	4.34	82.44	57.35	125.77	2.19	4	No	4
C-5-0-5	4.18	4.34	86.63	61.89	132.10	2.13	7	Yes	0
C-5-4-23	4.12	4.34	85.68	60.87	135.82	2.23	7	Yes	4
C-5-0-7	4.24	4.33	87.02	62.32	130.55	2.09	7	No	0
C-5-4-27	3.98	4.34	83.75	58.77	126.81	2.16	7	No	4
C-5-0-6	4.76	4.34	94.54	70.48	149.70	2.12	15	Yes	0
C-5-4-24	4.52	4.34	91.26	66.91	149.12	2.23	15	Yes	4
C-5-0-10	4.37	4.34	89.05	64.51	135.19	2.10	15	No	0
C-5-4-30	3.95	4.34	83.31	58.29	126.14	2.16	15	No	4

4.1.5.1 Concentration Profiles

Concentration profiles of the sediment half-cells spiked with stable I are shown in Figure 4.21 and listed in Table B.10. Profiles for half-cells containing 4% sediment moisture content are shown at the top, 7% sediment moisture content in the middle, and 15% sediment moisture content at the bottom. Concentration profiles are shown for sediment adjacent to monoliths with 0% iron content (black circles) and 4% iron content (white circles) that had been carbonated (left graphs) or left un-carbonated (right graphs). A fairly uniform distribution of I is observed through the length of the sediment half-cells. The 15% moisture content sediment had an overall reduced concentration of I throughout the length of the sediment relative to the 4% and 7% moisture content sediment. Only the 15% moisture content sediment adjacent to carbonated concrete with 0% iron showed a significant concentration gradient near the interface.

Concentration profiles of the concrete half-cells spiked with stable I are shown in Figure 4.22 and listed in Table B.11. Profiles for half-cells containing 4% sediment moisture content are shown at the top, 7% sediment moisture content in the middle, and 15% sediment moisture content at the bottom. Concentration profiles are shown for monoliths with 0% iron content (black circles) and 4% iron content (white circles) that had been carbonated (left graphs) or left un-carbonated (right graphs). Distinct concentration gradients were observed for all concrete half-cells. The highest interface concentrations were observed for the 4% moisture content sediment adjacent to non-carbonated concrete. Depth of diffusion was greatest for concrete half-cells beside 15% moisture content sediment. These concentration gradients were linearized by probit analyses to calculate diffusion coefficients.
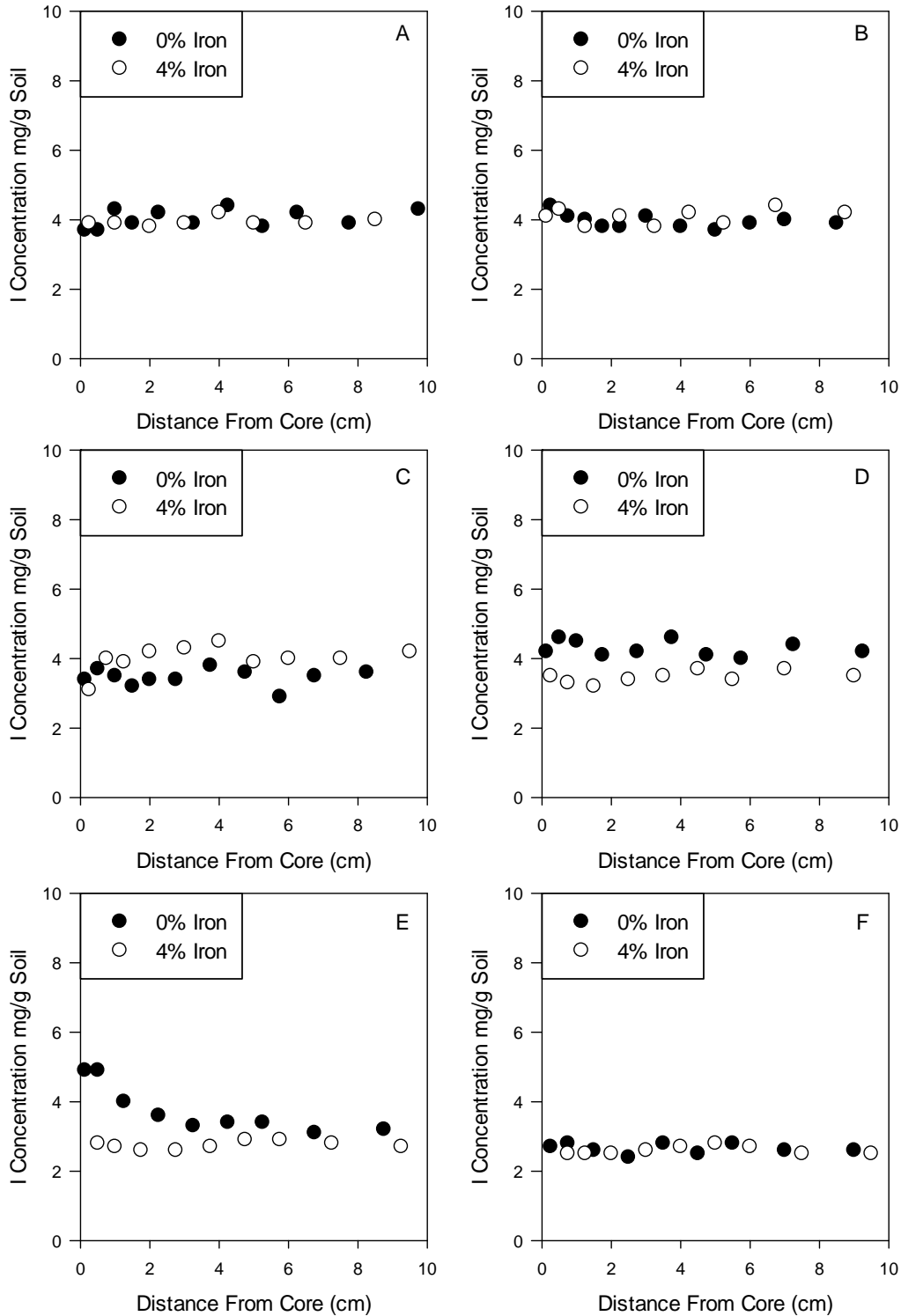
Figure 4.21. Sediment I concentration profiles from sediment-fractured concrete half-cell experiment with 0% iron monoliths (black circles), 4% iron monoliths (white circles) for (A) 4% sediment moisture, carbonated monoliths, (B) 4% sediment moisture, non-carbonated monoliths, (C) 7% sediment moisture, carbonated monoliths, (D) 7% sediment moisture non-carbonated monoliths, (E) 15% sediment moisture, carbonated monoliths, and (F) 15% sediment moisture, non-carbonated monoliths
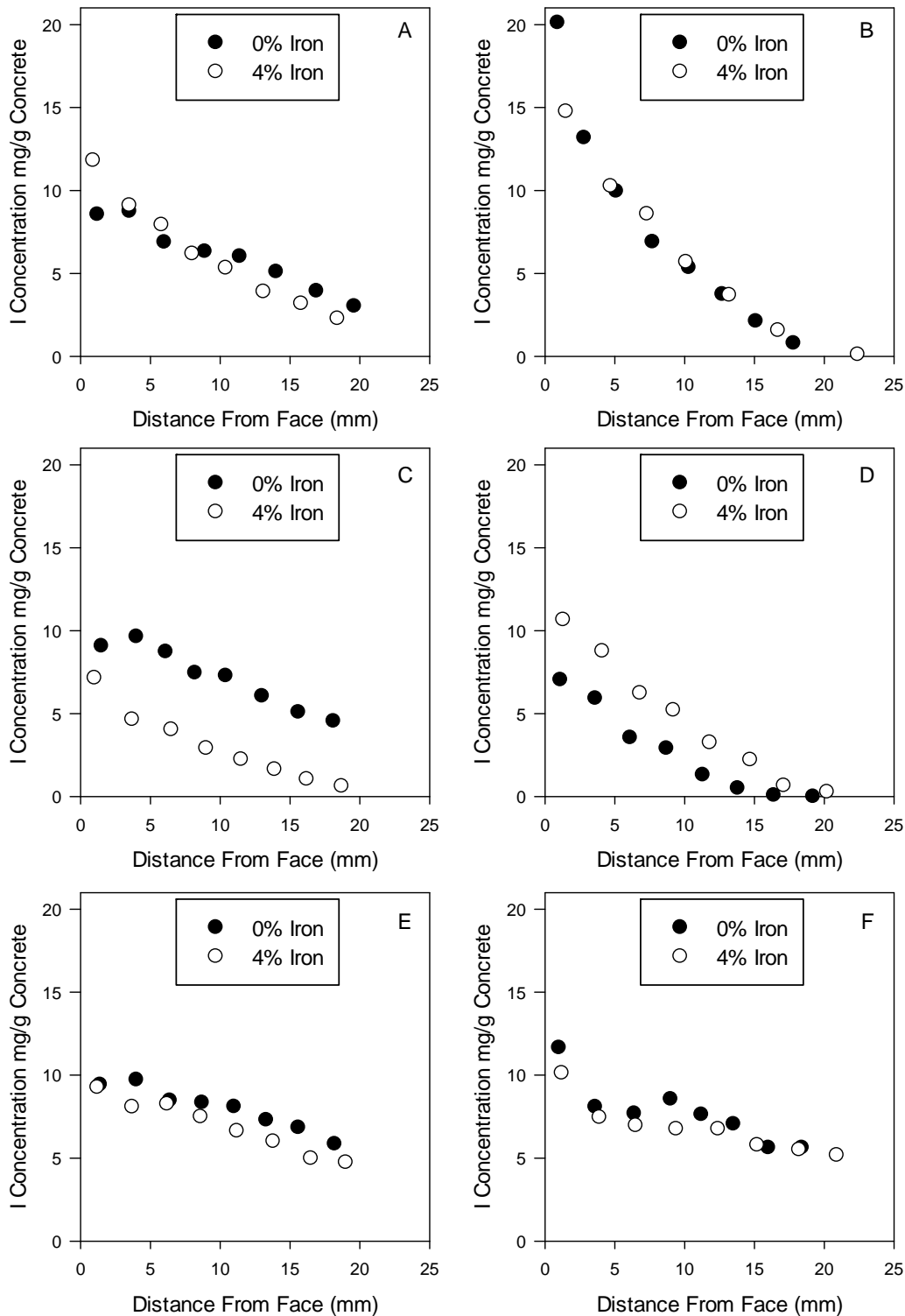
Figure 4.22. Concrete I concentration profiles from sediment-fractured concrete half-cell experiments with 0% iron monoliths (black circles), 4% iron monoliths (white circles) for (A) 4% sediment moisture, carbonated monoliths, (B) 4% sediment moisture, non-carbonated monoliths, (C) 7% sediment moisture, carbonated monoliths, (D) 7% sediment moisture non-carbonated monoliths, (E) 15% sediment moisture, carbonated monoliths, and (F) 15% sediment moisture, non-carbonated monoliths

Fractures within concrete half-cells introduce a possible preferential pathway for contaminant migration. One-half of each of the concrete monoliths was sectioned parallel to the fracture (perpendicular to the concrete-sediment interface). Figure 4.23 and Table B.12 present the concentration of I measured as a function of distance from the fracture face for 4% sediment (A), 7% sediment (B), and 15% sediment (C) moisture content. Only some of the 4% iron content monoliths with 4% sediment moisture content samples showed slight concentration gradients. The remaining monoliths had relatively uniform concentrations throughout the length measured.
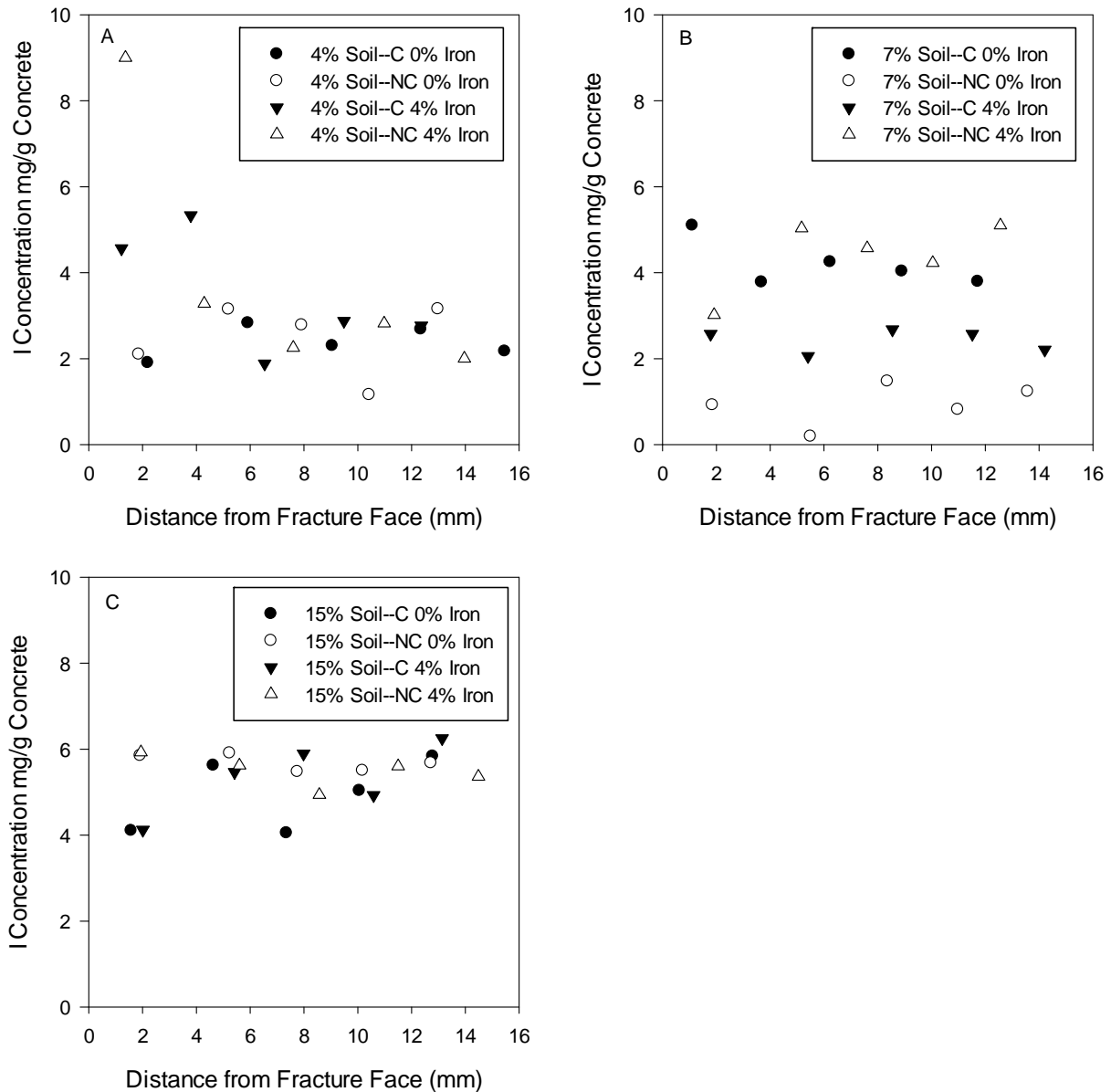
Figure 4.23. Fracture face concrete I concentration profiles from sediment-fractured concrete half-cell experiments for 0% iron, carbonated monoliths (black circles), 0% iron, non-carbonated monoliths (white circles), 4% iron, carbonated monoliths (black triangles), 4% iron, non-carbonated monoliths (white triangles) with (A) 4% sediment moisture, (B) 7% sediment moisture, and (C) 15% sediment moisture.

4.1.5.2   Probit Analysis

Probit analysis of the sediment-fractured concrete diffusion experiments is shown in Figure 4.24 through Figure 4.26 as a function of distance from the interface. Figure 4.24 shows the results for 4% moisture content sediment adjacent to monoliths that were carbonated (black circles) and non-carbonated (white circles) with iron content of 0% (left) and 4% (right). Probit analysis for the 7% and 15% moisture content sediment is shown in Figure 4.25 and Figure 4.26, respectively. Diffusivities were tabulated from the slope of the linear fits and are listed in Table 4.14. Overall, diffusivities range over an order of magnitude from 4.72×10^{-9} cm^2/s to 8.40×10^{-8} cm^2/s. The increase in sediment moisture content from 4% to 7% resulted in a decrease in diffusivity for all the samples ranging from a 7% to 60% reduction. The exception to this result was the non-carbonated, 4% iron content samples. When sediment moisture content was increased to 15%, diffusivity values increased when compared to both the 4% and 7% moisture content samples.

The effect of carbonation resulted in mixed results for this set of data. Carbonation of samples resulted in a factor of ~2 increase in diffusivity values for the 4% and 7% moisture content samples. Nearly a three times reduction in diffusivity values was observed for carbonated samples with 15% moisture content sediment.

The addition of iron to concrete specimens also resulted in mixed results. A reduction in diffusivity values (20% to 50%) was observed for samples with 4% and 15% moisture content sediment, with the largest effect exhibited by the non-carbonated, 4% moisture content samples. Diffusivity values for the 7% moisture content samples increased with the addition of iron by 60% for the non-carbonated samples and 20% for the carbonated samples.
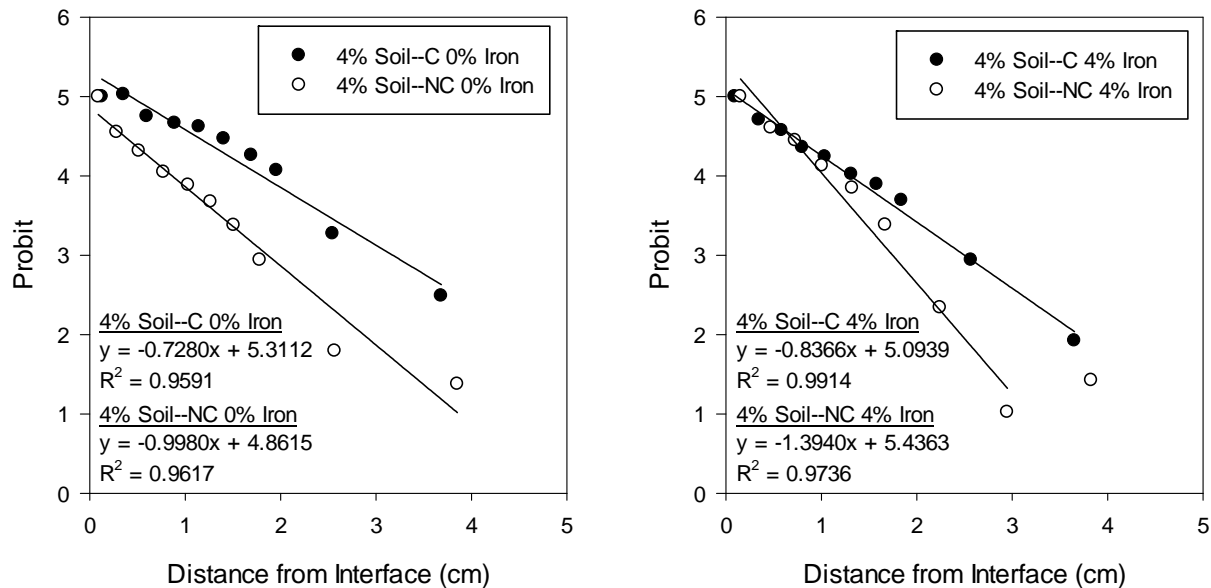
Figure 4.24. Probit plots for I diffusion from sediment-fractured concrete half-cell experiments in 4% moisture content sediment for carbonated (black circles) and non-carbonated (white circles) concrete monoliths with (A) 0% iron and (B) 4% iron
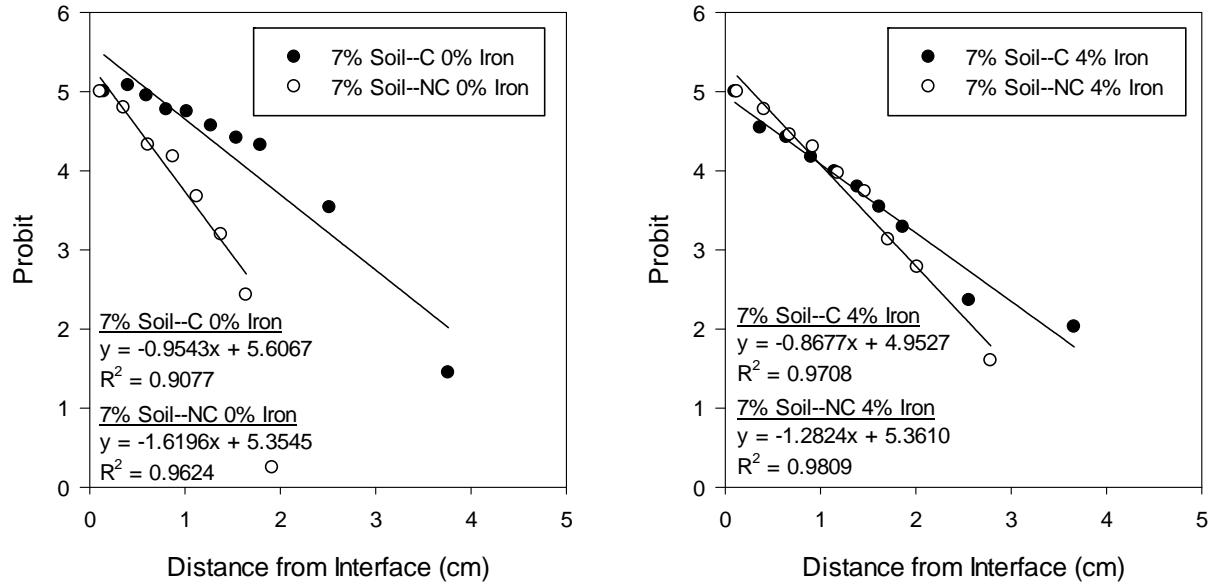
Figure 4.25. Probit plots for I diffusion from sediment-fractured concrete half-cell experiments in 7% moisture content sediment for carbonated (black circles) and non-carbonated (white circles) concrete monoliths with (A) 0% iron and (B) 4% iron
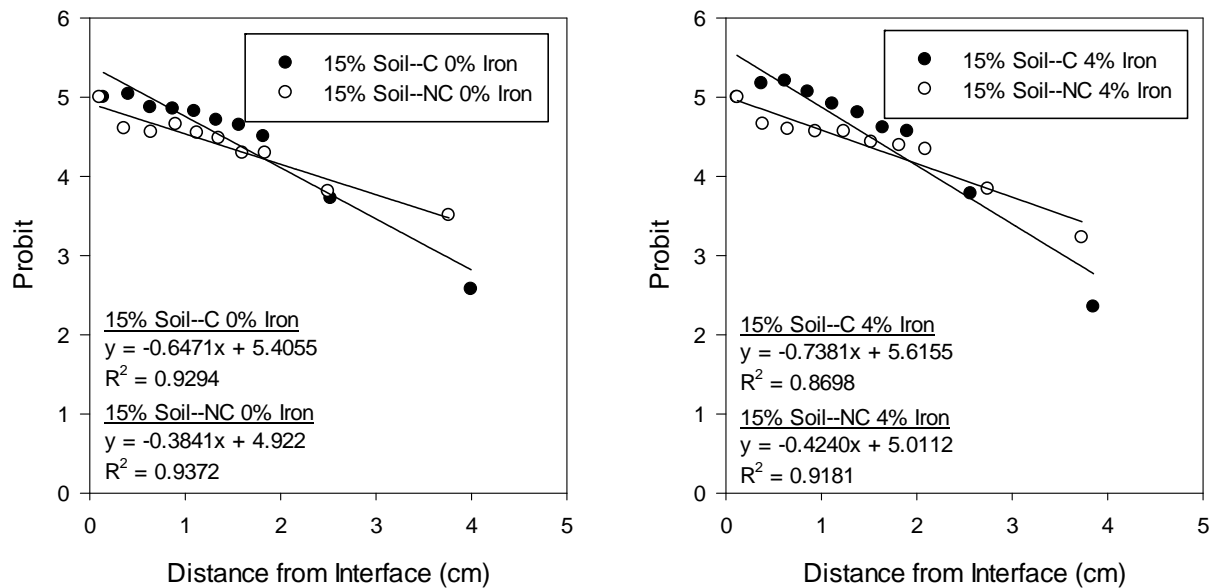
Figure 4.26. Probit plots for I diffusion from sediment-fractured concrete half-cell experiments in 15% moisture content sediment for carbonated (black circles) and non-carbonated (white circles) concrete monoliths with (A) 0% iron and (B) 4% iron

Table 4.14. Calculated I diffusion parameters from sediment-fractured concrete half-cell experiments

Core ID	Moisture (wt%)	Carbonated	Fe (wt%)	I Diffusivity (cm^2/s)	Probit Slope
C-5-0-1	4	Y	0	2.34×10^{-8}	0.7280
C-5-4-21	4	Y	4	1.77×10^{-8}	0.8366
C-5-0-2	4	N	0	1.24×10^{-8}	0.9980
C-5-4-26	4	N	4	6.38×10^{-9}	1.3940
C-5-0-5	7	Y	0	1.36×10^{-8}	0.9543
C-5-4-23	7	Y	4	1.65×10^{-8}	0.8677
C-5-0-7	7	N	0	4.72×10^{-9}	1.6196
C-5-4-27	7	N	4	7.54×10^{-9}	1.2824
C-5-0-6	15	Y	0	2.96×10^{-8}	0.6471
C-5-4-24	15	Y	4	2.27×10^{-8}	0.7381
C-5-0-10	15	N	0	8.40×10^{-8}	0.3841
C-5-4-30	15	N	4	6.89×10^{-8}	0.4240

4.1.6 Iodine Diffusion Summary

Over the suite of half-cell diffusion experiments, some general trends were observed. Increasing the sediment moisture content from 4% to 7% or 15% within the half-cell resulted in an increase in I diffusivity. The direction of diffusion affected the intensity of observed effect. Diffusivity coefficients increased by an order of magnitude in concrete-sediment experiments, but in the sediment-concrete tests the effect was less than an order of magnitude. Increasing sediment moisture content from 7% to 15% did not consistently result in further increases in I diffusion.

The method of carbonation used to prepare the concrete monoliths resulted in opposite effects on calculated diffusivity values, no matter the direction of diffusion. The supercritical CO_2 process used in the early years of the project is thought to have caused microcracks within the concrete, creating preferential diffusion pathways resulting in increased calculated diffusivities. A reduction in diffusivity values was observed when an alternative method of soaking concrete specimen in a super-saturated carbonate solution was used. One possibility is that the carbonate solution caused a chemical or physical change within the concrete surface that attenuated I diffusion. An alternative scenario, for the concrete to sediment diffusion experiments, is that I was leached from the concrete during the carbonation process, so there was less I available for diffusion. The carbonate solution was never tested for I concentrations, so this mechanism was not confirmed.

The effect of the addition of iron was mixed. The sediment-concrete and concrete-sediment experiments both showed a distinct decrease in diffusivity with the addition of 4% iron. An increase in diffusivity was observed with the addition of iron in the fractured concrete-sediment experiments. The remaining half-cell diffusion tests exhibited mixed results with no clear trends within the test results.

4.2 Technetium Diffusion

4.2.1   Sediment to Sediment

Sediment-sediment diffusion experiments were initiated to investigate the effect of sediment moisture content and test duration on Tc-99 diffusivity. These experiments consisted of half-cells (~4 cm diameter and ~39 cm long) filled with Trench 8 sediment. The characteristics of these half-cells, including the dimensions, bulk densities, and moisture contents, are listed in Table 4.15. The hot side sediment was spiked with Tc-99 at concentrations of 6.28×10^{-4} mg Tc-99/g sediment and 8.94×10^{-4} mg Tc-99/g sediment in the 4% and 7% moisture content sediments. Half-cell sampling was conducted at 64 and 170 days.

Table 4.15. Characteristics of sediment-sediment half-cells

Cell ID	Length of Hot Sediment (cm)	Length of Cold Sediment (cm)	Hot Sediment Bulk Density (g/cm^3)	Cold Sediment Bulk Density (g/cm^3)	Moisture Content (%)	Test Duration (days)
SS-I-7%	18.2	19.7	1.41	1.53	7	64
SS-II-7%	17.5	20.5	1.45	1.62	7	170
SS-III-4%	21.1	22.0	1.32	1.40	4	64
SS-IV-4%	18.0	20.7	1.50	1.53	4	170

4.2.1.1   Concentration Profiles

The concentration profiles for Tc-99 from the sediment-sediment diffusion experiments are shown for 4% sediment (black circles) and 7% sediment (white circles) moisture content as a function of half-cell length for the 64-day (left) and 170-day (right) test durations in Figure 4.27 and listed in Table B.13. Concentrations for the 7% moisture content sediment experiments were larger than those of the 4% moisture content sediment up to 20 cm from the spiked end of the sediment for the 64-day tests. At 20 cm, the 4% moisture content concentrations were higher than the 7% moisture content sediment. The Tc-99 concentrations in the 7% moisture content sediment experiments were larger than those of the 4% moisture content sediment throughout the half-cell for the 170-day tests.
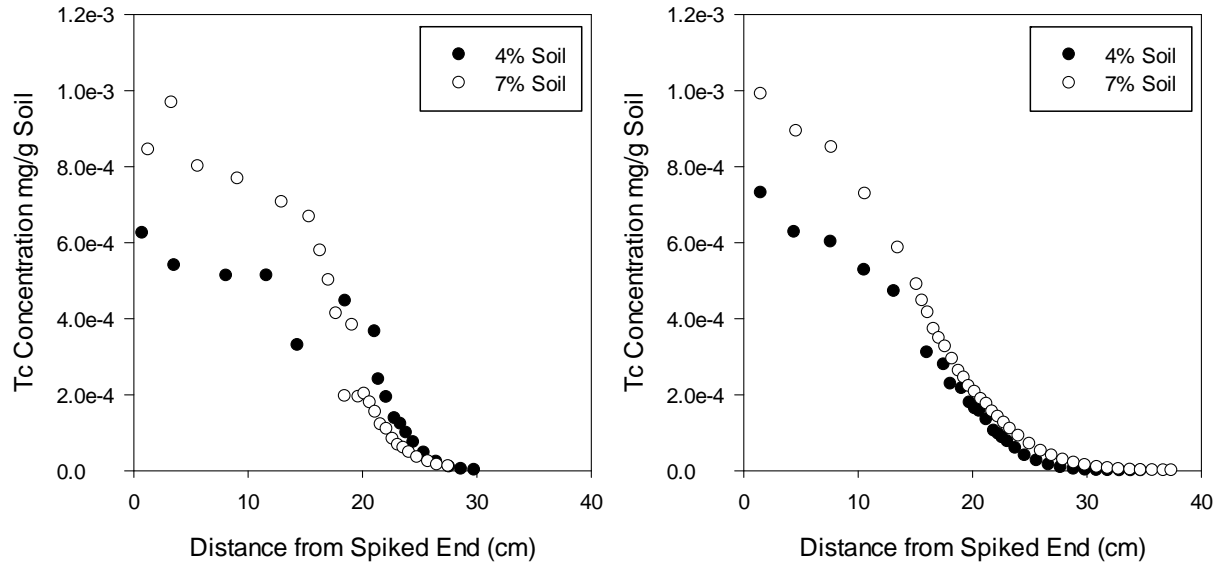
Figure 4.27. Sediment Tc-99 concentration profiles from sediment-sediment half-cell experiments at 64-day (left) and 170-day (right) test durations

4.2.1.2   Probit Analysis

Probit plots for Tc-99 diffusion in the sediment-sediment experiments are shown in Figure 4.28. Probit values were plotted as a function of distance from the spiked end of the half-cell for 4% sediment (black circles) and 7% sediment (white circles) moisture content half-cells at 64-day (left) and 170-day (right) test durations. Noticeably different slopes were observed for the spiked side, so only data from the cold side (more closely spaced data points) was used for the probit analysis to calculate the diffusivity coefficients that are summarized in Table 4.16.

Overall, the calculated diffusivities for Tc-99 ranged from 8.86×10^{-7} cm^2/s to 3.07×10^{-6} cm^2/s. Diffusivity coefficients for the 7% moisture content are two times larger than those of the 4% moisture content. Diffusivity slowed down over time, as indicated by the 35% reduction in diffusivity values for the 170-day experiments compared to the 64-day experiments.
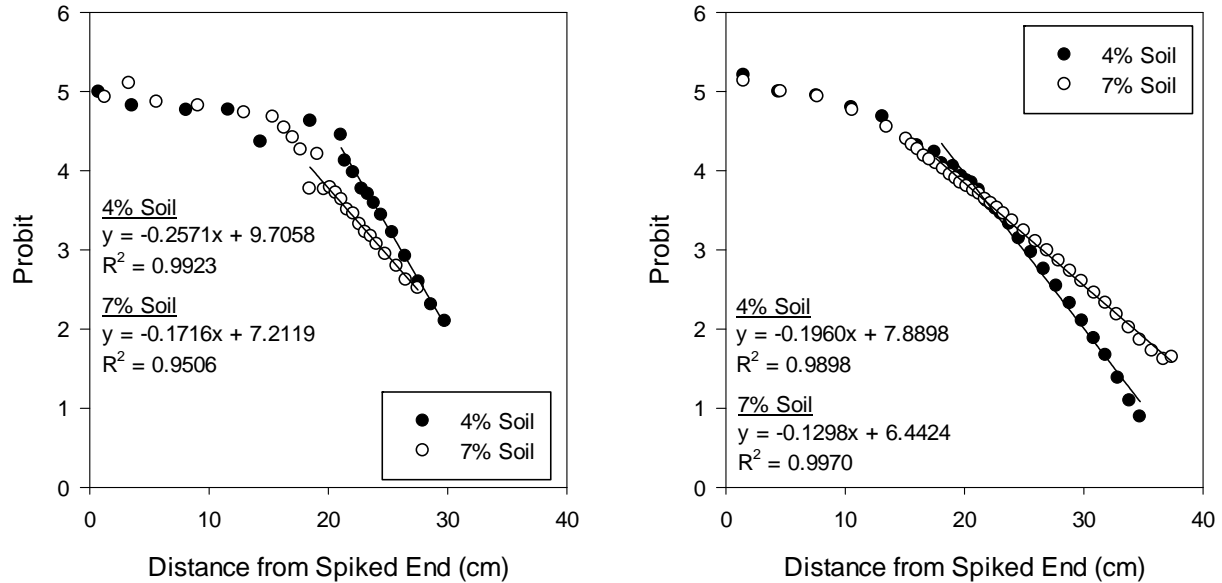
Figure 4.28. Probit plots for Tc-99 diffusion from sediment-sediment experiments at 64-day (left) and 170-day (right) test durations

Table 4.16. Calculated Tc-99 diffusion parameters from sediment-sediment half-cell experiments

Cell ID	Test Duration (days)	Moisture Content (wt%)	Tc-99 Diffusivity (cm^2/s)	Probit Slope
SS-I-7%	64	7	3.07×10^{-6}	0.1716
SS-II-7%	170	7	2.02×10^{-6}	0.1298
SS-III-4%	64	4	1.37×10^{-6}	0.2571
SS-IV-4%	170	4	8.86×10^{-7}	0.1960

4.2.2   Sediment to Concrete

Sediment-concrete diffusion experiments were initiated to investigate the effect of sediment moisture, concrete iron content, and concrete carbonation on the diffusivity of Tc-99 from sediment into concrete. Sediment half-cell specimens were spiked with Tc-99 (4.2×10^{-4} mg Tc-99/g sediment) to achieve a measurable diffusion profile in the concrete part of the half-cell. The general preparation of the half-cells is described in section 2.4. HFS was used for the sediment half-cell. In these experiments, iron content was varied in the concrete specimens from 0% to 12%, sediment moisture content was varied (4%, 7%, or 15%), and half of the concrete monoliths were carbonated prior to preparing the half-cells. The characteristics of the concrete half-cells are listed in Table 4.17. Half-cell sampling was conducted at 351 days.

Table 4.17. Characteristics of concrete specimens used in sediment-concrete half-cell experiments

Core ID	Length (cm)	Diameter (cm)	Surface Area (cm²)	Volume (cm³)	Weight (g)	Density (g/cm³)	Iron (wt%)	Carbonated	Moisture Content (wt%)
C-08-3-0-325	4.09	4.33	84.97	60.10	131.44	2.19	0	N	4
C-08-3-0-329	4.32	4.33	88.13	63.53	139.50	2.20	0	N	7
C-08-3-0-330	3.85	4.33	81.77	56.65	123.50	2.18	0	N	15
C-08-3-0-332	4.33	4.32	88.09	63.48	139.65	2.20	0	Y	4
C-08-3-0-333	4.35	4.33	88.57	64.00	140.79	2.20	0	Y	7
C-08-3-0-334	4.07	4.32	84.56	59.67	130.55	2.19	0	Y	15
C-08-3-4-350	3.84	4.32	81.43	56.28	127.25	2.26	4	N	4
C-08-3-4-351	4.00	4.33	83.92	58.96	132.78	2.25	4	N	7
C-08-3-4-353	4.01	4.33	83.99	59.04	133.38	2.26	4	N	15
C-08-3-4-357	3.90	4.32	82.19	57.11	128.77	2.25	4	Y	4
C-08-3-4-359	3.83	4.32	81.25	56.09	126.50	2.26	4	Y	7
C-08-3-4-360	4.11	4.33	85.47	60.64	136.11	2.24	4	Y	15
C-08-3-8-401	4.07	4.32	84.40	59.50	135.91	2.28	8	N	4
C-08-3-8-402	3.81	4.32	81.02	55.84	127.31	2.28	8	N	7
C-08-3-8-403	4.00	4.33	83.87	58.91	133.35	2.26	8	N	15
C-08-3-8-404	4.05	4.33	84.61	59.71	133.69	2.24	8	Y	4
C-08-3-8-405	3.86	4.33	81.77	56.65	126.96	2.24	8	Y	7
C-08-3-8-406	3.94	4.33	83.08	58.05	130.61	2.25	8	Y	15
C-08-3-12-425	4.33	4.27	87.54	62.88	143.44	2.28	12	N	4
C-08-3-12-426	4.33	4.33	88.35	63.76	145.77	2.29	12	N	7
C-08-3-12-427	4.33	4.22	86.94	62.23	141.71	2.28	12	N	15
C-08-3-12-432	4.02	4.32	83.83	58.88	134.09	2.28	12	Y	4
C-08-3-12-433	4.15	4.33	85.81	61.01	139.80	2.29	12	Y	7
C-08-3-12-435	3.88	4.33	82.22	57.12	130.04	2.28	12	Y	15

4.2.2.1　Concentration Profiles

The concentration profiles of sediment portions of the half-cells spiked with Tc-99 are shown in Figure 4.29 and listed in Table B.14. Profiles for half-cells containing 4% sediment moisture content are shown at the top, 7% sediment moisture content in the middle, and 15% sediment moisture content at the bottom. Concentration profiles are shown for sediment adjacent to monoliths with 0% iron (black circles), 4% iron (white circles), 8% iron (black triangles), and 12% iron (white triangles) content that had been carbonated (left graphs) or left un-carbonated (right graphs). Except very near the interfaces (<3 cm), concentration gradients were not observed in any of the sediment half-cells.

Tc-99 concentration profiles for the concrete half of the half-cells are shown in Figure 4.30 and listed in Table B.15. Profiles for half-cells containing 4% sediment moisture content are shown at the top, 7% sediment moisture content in the middle, and 15% sediment moisture content at the bottom. Concentration profiles are shown for monoliths with 0% iron (black circles), 4% iron (white circles), 8% iron (black triangles), and 12% iron (white triangles) content that had been carbonated (left graphs) or left un-carbonated (right graphs). Tc-99 concentration gradients from the interface were observed in the concrete half-cells. Carbonation of concrete treatment seemed to reduce the diffusivity of Tc-99 (Figure 4.30 left plots). Also, diffusivities seem to be attenuated by the presence of iron particles, more noticeably in the non-carbonated half-cells. The highest Tc-99 concentrations were observed at the interface of the 15% moisture content half-cells (Figure 4.30E and F). Concentration gradients were linearized by probit analyses to calculate of diffusion coefficients.
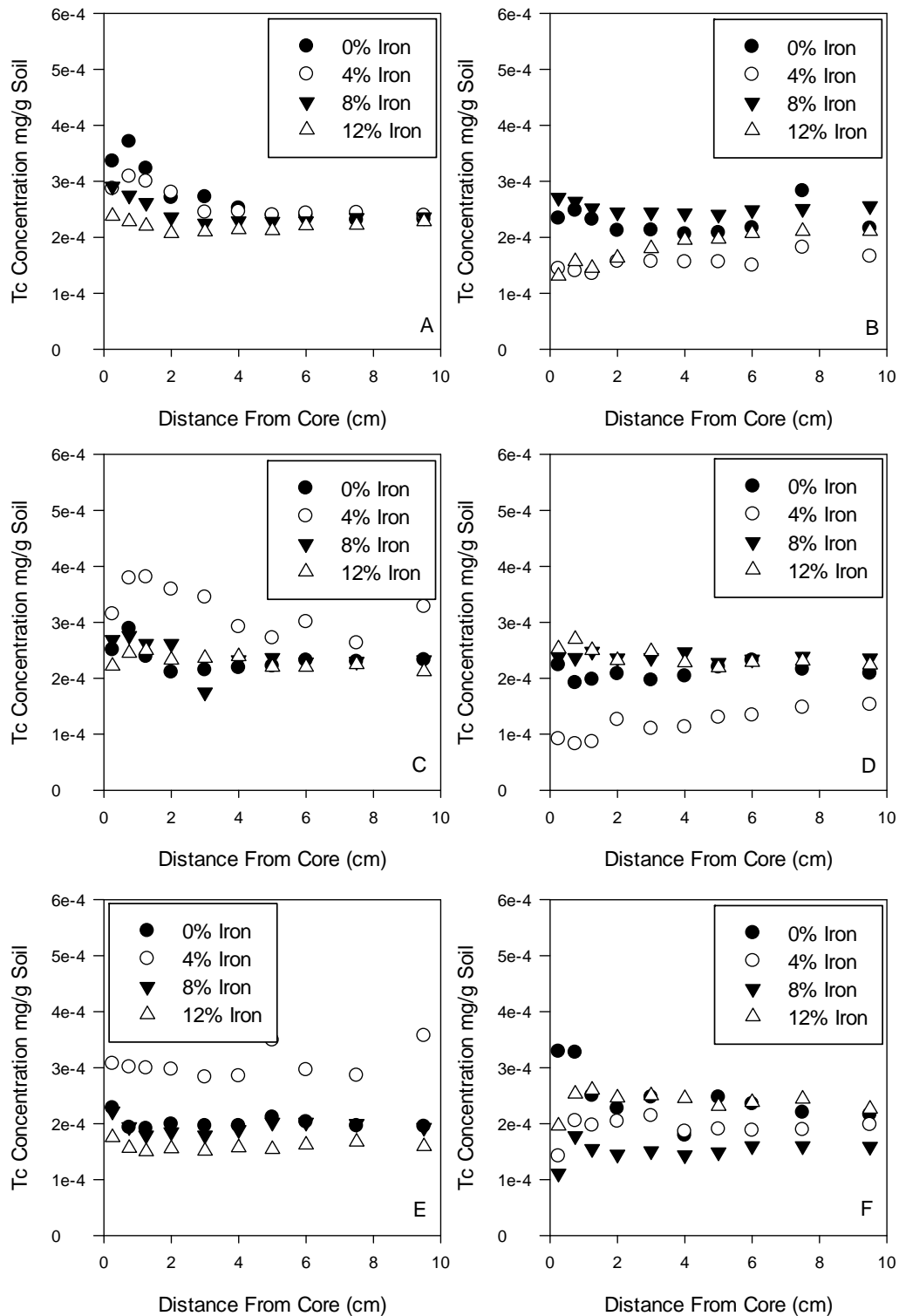
Figure 4.29. Sediment Tc-99 concentration profiles from sediment-concrete half-cell experiments for 0% iron (black circles), 4% iron (white circles), 8% iron (black triangles), and 12% iron (white triangles) with (A) 4% sediment moisture, carbonated monoliths, (B) 4% sediment moisture, non-carbonated monoliths, (C) 7% sediment moisture, carbonated monoliths, (D) 7% sediment moisture, non-carbonated monoliths, (E) 15% sediment moisture, carbonated monoliths, and (F) 15% sediment moisture, non-carbonated monoliths

4.41
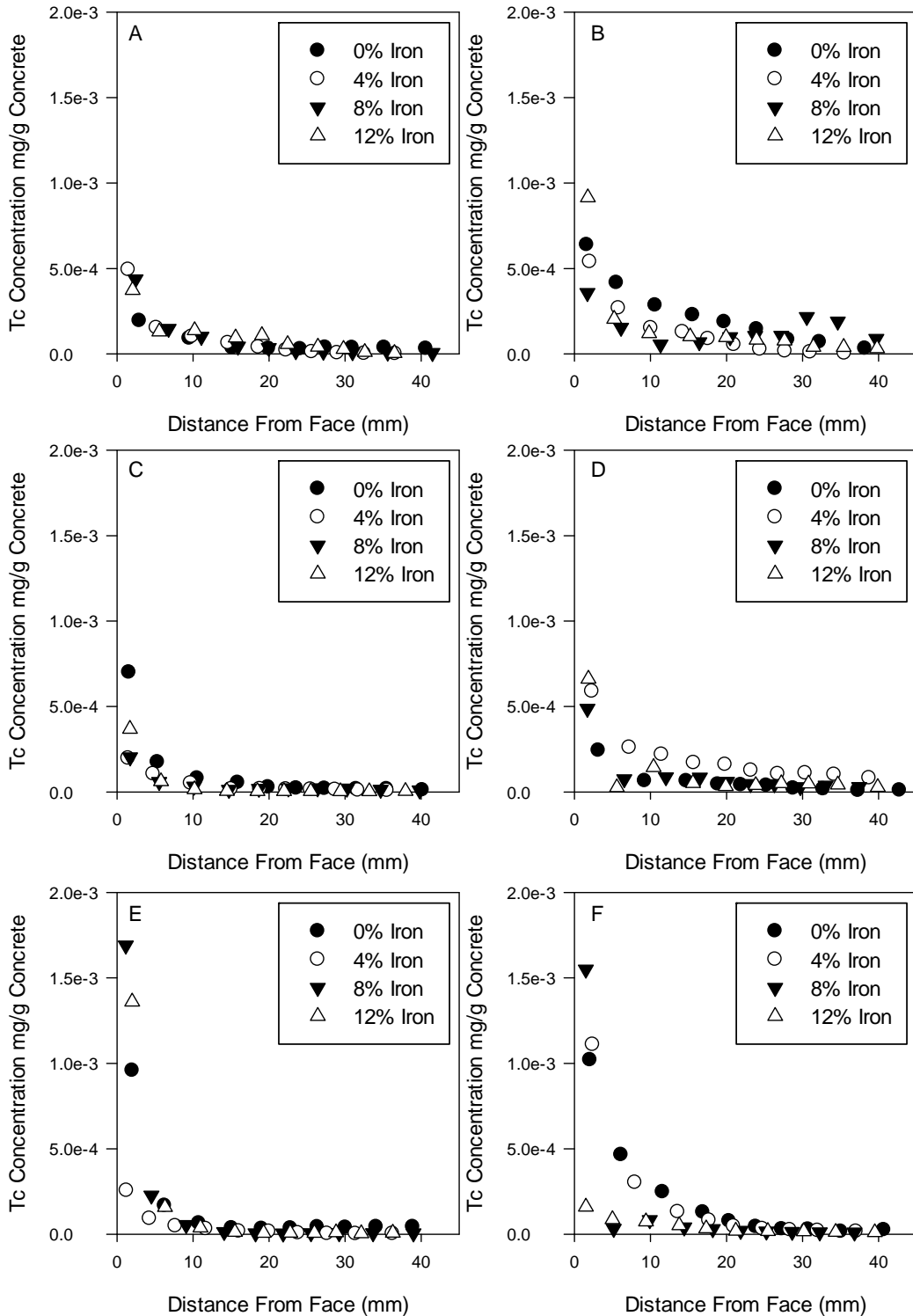
Figure 4.30. Concrete Tc-99 concentration profiles from sediment-concrete half-cell experiments for 0% iron (black circles), 4% iron (white circles), 8% iron (black triangles), and 12% iron (white triangles) with (A) 4% sediment moisture, carbonated monoliths, (B) 4% sediment moisture, non-carbonated monoliths, (C) 7% sediment moisture, carbonated monoliths, (D) 7% sediment moisture, non-carbonated monoliths, (E) 15% sediment moisture, carbonated monoliths, and (F) 15% sediment moisture, non-carbonated monoliths

4.42

4.2.2.2 Probit Analysis

Probit analysis results of the sediment-concrete diffusion experiments are shown in Figure 4.31 through Figure 4.33 as a function of distance from the interface. Figure 4.31 shows the results for 4% moisture content sediment adjacent to monoliths that were carbonated (black circles) and non-carbonated (white circles) with 0% iron (A), 4% iron (B), 8% iron (C), and 12% iron (D). Probit analysis for the 7% and 15% moisture content sediment half-cells are shown in Figure 4.32 and Figure 4.33, respectively. Diffusivities were tabulated from the slope of the linear fits and are listed in Table 4.18. Overall, the calculated diffusivities for Tc-99 ranged from 6.61×10^{-9} cm^2/s to 1.57×10^{-7} cm^2/s. For the majority of samples, an increase in sediment moisture content from 4% to either 7% or 15% resulted in a reduction in diffusivity values by as little as 4% to as much as almost 90% (8% and 12% iron-containing samples).

The highest Tc-99 diffusivities were predominantly observed in the non-carbonated concrete cores contacting spiked sediments. Carbonation reduced diffusivity coefficients by 2 to 14 times, except for two instances (4% moisture content with 8% iron and 15% moisture with 4% iron) where there was an increase in diffusivity.

A clear effect from the addition of iron was not observed, as diffusivities increased (7 samples) and decreased (11 samples) without a distinct connection to the other variables.
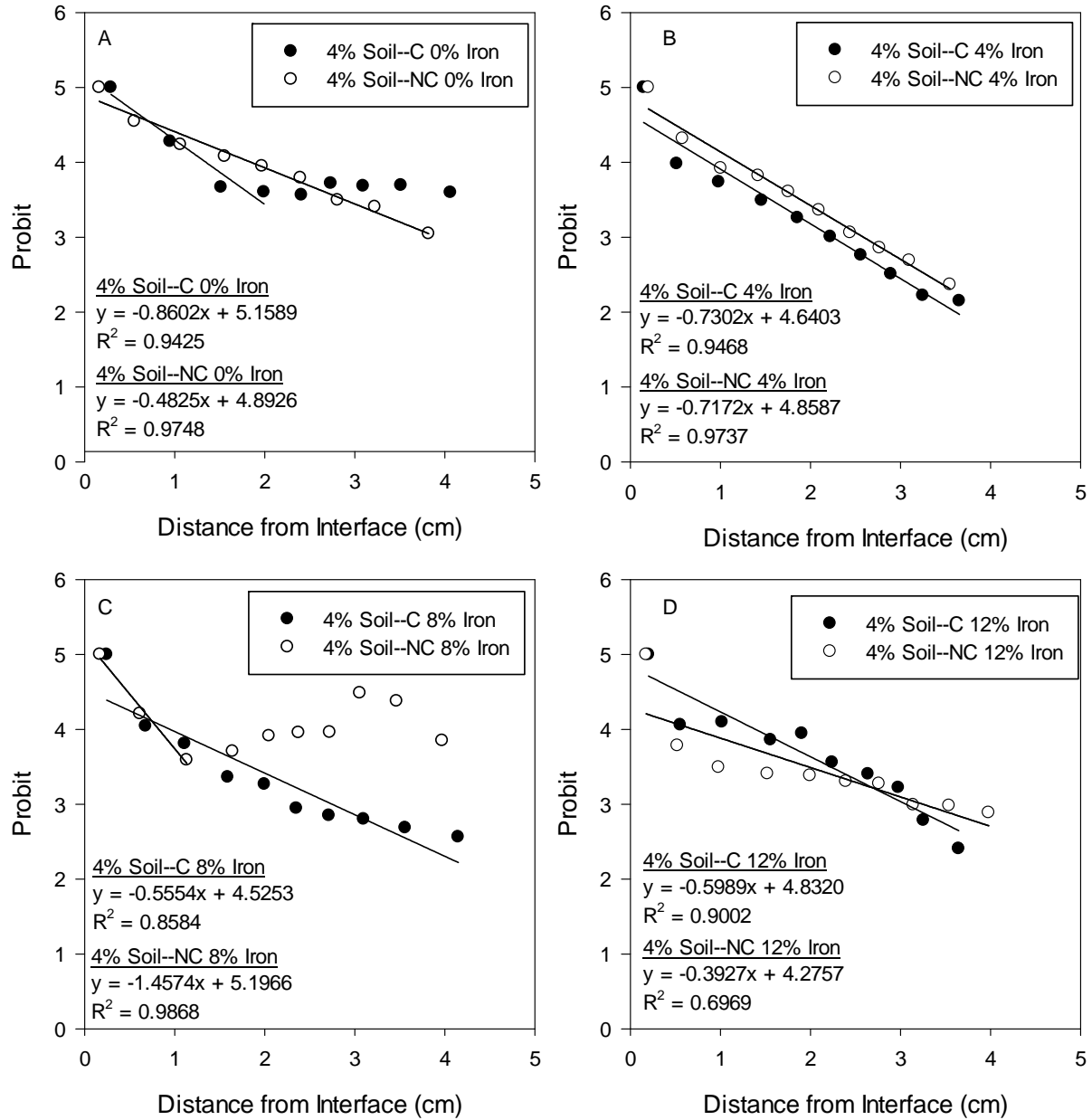
Figure 4.31. Probit plots for Tc-99 diffusion from sediment-concrete half-cell experiments in 4% moisture content sediment for carbonated (black circles) and non-carbonated (white circles) concrete monoliths with (A) 0% iron, (B) 4% iron, (C) 8% iron, and (D) 12% iron
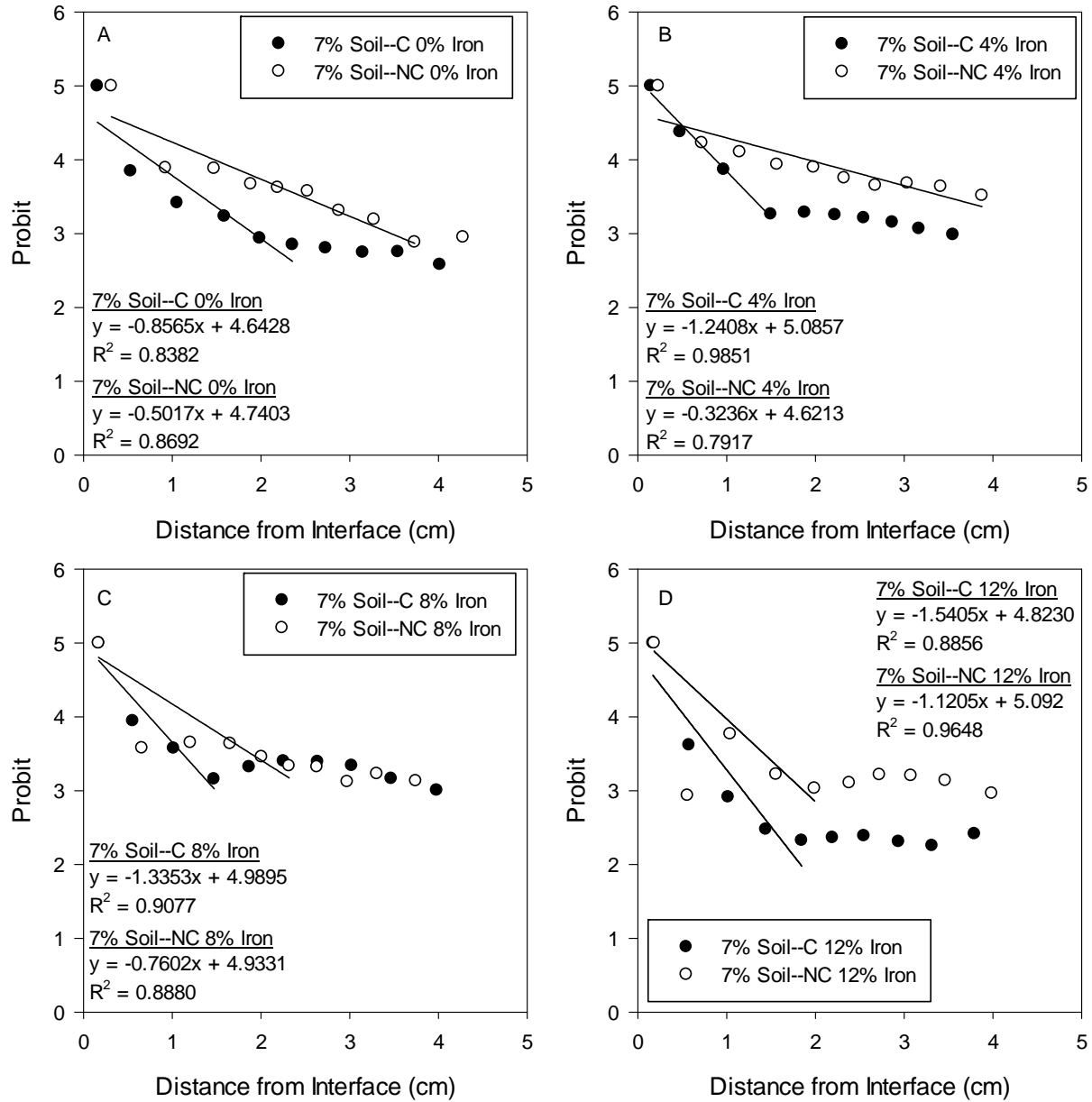
Figure 4.32. Probit plots for Tc-99 diffusion from sediment-concrete half-cell experiments in 7% moisture content sediment for carbonated (black circles) and non-carbonated (white circles) concrete monoliths with (A) 0% iron, (B) 4% iron, (C) 8% iron, and (D) 12% iron
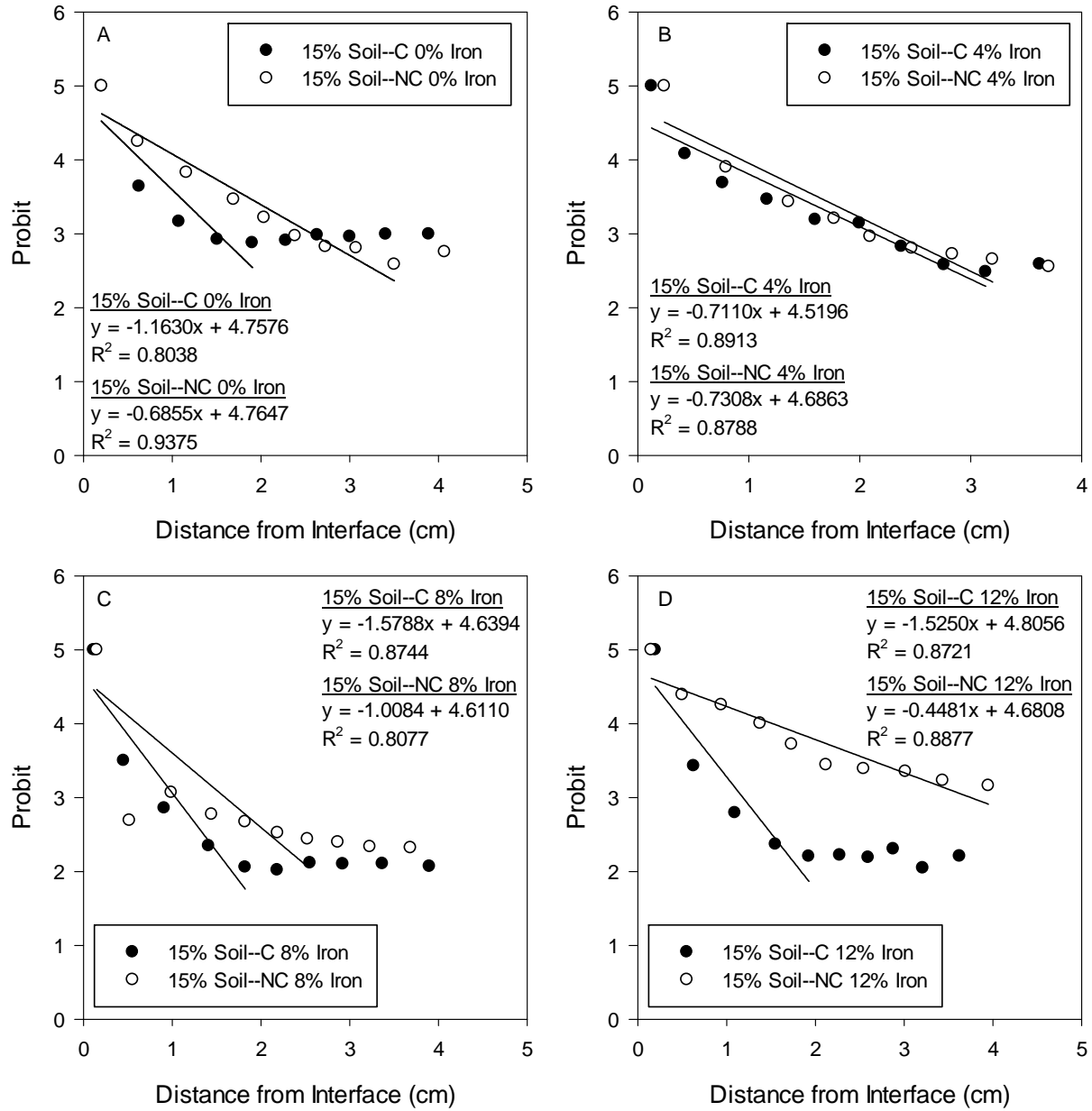
Figure 4.33. Probit plots for Tc-99 diffusion from sediment-concrete half-cell experiments in 15% moisture content sediment for carbonated (black circles) and non-carbonated (white circles) concrete monoliths with (A) 0% iron, (B) 4% iron, (C) 8% iron, and (D) 12% iron

Table 4.18. Calculated Tc-99 diffusion parameters from sediment-concrete half-cell experiments

Core ID	Moisture (wt%)	Carbonated	Iron (wt%)	Tc-99 Diffusivity (cm^2/s)	Probit Slope
C-08-3-0-325	4	N	0	7.08×10^{-8}	0.4825
C-08-3-0-329	7	N	0	6.55×10^{-8}	0.5017
C-08-3-0-330	15	N	0	3.51×10^{-8}	0.6855
C-08-3-0-332	4	Y	0	2.23×10^{-8}	0.8602
C-08-3-0-333	7	Y	0	2.25×10^{-8}	0.8565
C-08-3-0-334	15	Y	0	1.22×10^{-8}	1.163
C-08-3-4-350	4	N	4	3.21×10^{-8}	0.7172
C-08-3-4-351	7	N	4	1.57×10^{-7}	0.3236
C-08-3-4-353	15	N	4	3.09×10^{-8}	0.7308
C-08-3-4-357	4	Y	4	3.09×10^{-8}	0.7302
C-08-3-4-359	7	Y	4	1.07×10^{-8}	1.2408
C-08-3-4-360	15	Y	4	3.26×10^{-8}	0.711
C-08-3-8-401	4	N	8	7.76×10^{-9}	1.4574
C-08-3-8-402	7	N	8	2.85×10^{-8}	0.7602
C-08-3-8-403	15	N	8	1.62×10^{-8}	1.0084
C-08-3-8-407	4	Y	8	5.34×10^{-8}	0.5554
C-08-3-8-409	7	Y	8	9.25×10^{-9}	1.3353
C-08-3-8-410	15	Y	8	6.61×10^{-9}	1.5788
C-08-3-12-425	4	N	12	1.07×10^{-7}	0.3927
C-08-3-12-426	7	N	12	1.31×10^{-8}	1.1205
C-08-3-12-427	15	N	12	8.21×10^{-8}	0.4481
C-08-3-12-432	4	Y	12	4.60×10^{-8}	0.5989
C-08-3-12-433	7	Y	12	6.95×10^{-9}	1.5405
C-08-3-12-435	15	Y	12	7.09×10^{-9}	1.525

4.2.3   Concrete to Sediment

Concrete-sediment diffusion experiments were initiated in FY 1999 to investigate the effect of moisture content and test duration on the diffusion of Tc-99 from concrete to sediment. Concrete half-cell specimens were spiked with Tc-99 (1.73×10^{-3} mg Tc-99/g concrete) to achieve a measurable diffusion profile in the sediment part of the half-cell. The general preparation of the half-cells is described in section 2.4. The characteristics of the concrete half-cells are listed in Table 4.19. Trench 8 sediment was used for the sediment half-cell. Tests were run for 64 and 169 days.

Table 4.19. Characteristics of concrete specimens used in FY 1999 concrete-sediment half-cell experiments

Core ID	Length (cm)	Diameter (cm)	Surface Area (cm^2)	Volume (cm^3)	Weight (g)	Density (g/cm^3)	Iron (wt%)	Carbonated	Moisture Content (wt%)	Duration (days)
CS-I-4%	4.3	8.255	218.56	230.14	513.21	2.23	4	N	4	64
CS-II-4%	4.2	8.255	215.96	224.79	496.78	2.21	4	N	4	169
CS-III-7%	4.2	8.255	215.96	224.79	505.77	2.25	4	N	7	64
CS-IV-7%	4.2	8.255	215.96	224.79	496.78	2.21	4	N	7	169

Another set of diffusion experiments was initiated during FY 2007 to investigate the effect of iron within the concrete and sediment moisture content on the diffusion of Tc-99 from concrete into the

sediment. Concrete half-cell specimens were spiked with Tc-99 ($\sim 5.93 \times 10^{-4}$ mg/g concrete) to achieve a measurable diffusion profile in the sediment part of the half-cell. The characteristics of the concrete specimens used are listed in Table 4.20. HFS was used for the sediment half-cell. This set of tests was run for 698 days.

Table 4.20. Characteristics of concrete specimen used in FY 2007 concrete-sediment half-cell experiments

Core ID	Length (cm)	Diameter (cm)	Surface Area (cm^2)	Volume (cm^3)	Weight (g)	Density (g/cm^3)	Iron (%)	Carbonated	Moisture Content (%)
Tc-C-4-0-204	4.17	4.32	85.84	61.05	124.54	2.04	0	N	4
Tc-C-4-4-213	4.26	4.31	86.91	62.2	138.71	2.23	4	N	4
Tc-C-4-0-203	4.34	4.31	88.01	63.39	131.22	2.07	0	N	7
Tc-C-4-4-212	4.23	4.31	86.51	61.77	137.75	2.23	4	N	7
Tc-C-4-0-202	4.39	4.31	88.74	64.18	133.49	2.08	0	N	15
Tc-C-4-4-211	4.37	4.31	88.41	63.82	142.32	2.23	4	N	15

4.2.3.1 Concentration Profiles

Tc-99 concentration profiles of the sediment section of the half-cells of FY 1999 concrete-sediment half-cell experiments are shown in Figure 4.34 and listed in Table B.16. Concentrations from 4% sediment (black circles) and 7% sediment (white circles) are plotted as a function of distance from the concrete monolith for the 64-day (left) and 169-day (right) test durations. Tc-99 concentration gradients from the interface were observed in the sediment half-cells, with higher concentrations observed in the half-cells with the 7% moisture content sediment. These concentration gradients were linearized by probit analyses to allow calculation of diffusion coefficients. Concentration profiles of Tc-99 in the concrete portion of the half-cells were not measured.
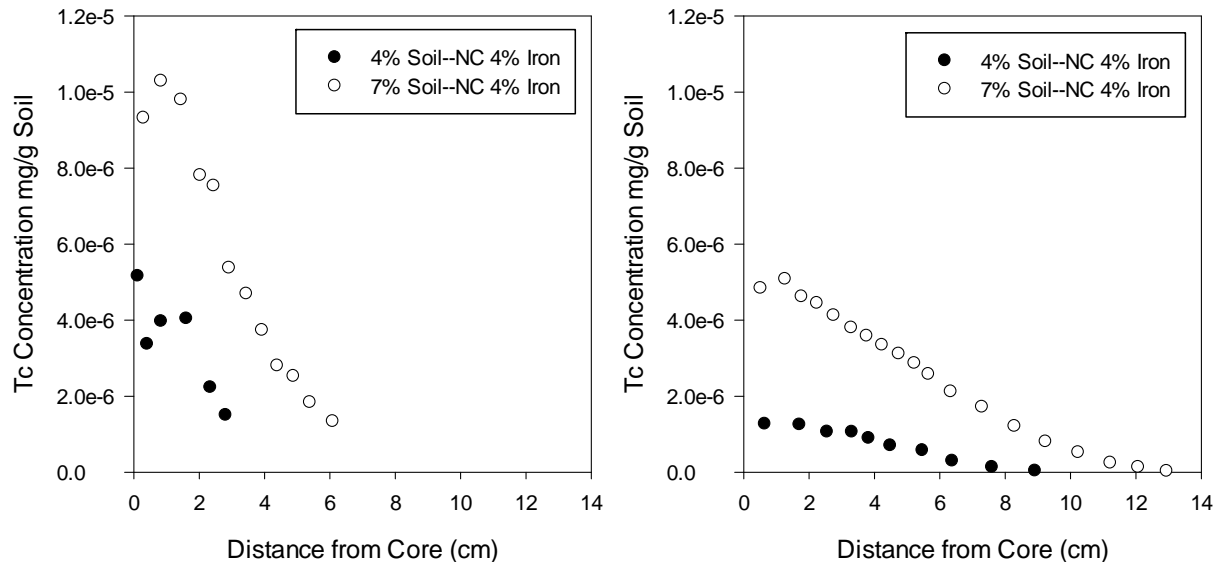
Figure 4.34. Sediment Tc-99 concentration profiles from FY 1999 concrete-sediment half-cell experiments for 4% sediment moisture (black circles) and 7% sediment moisture (white circles) at 64-day (left) and 169-day (right) test durations

The concentration profiles of sediment half-cells for the experiments started in FY 2007 are shown in Figure 4.35 and listed in Table B.17. Concentration profiles are shown for 4% moisture content (A), 7% moisture content (B), and 15% moisture content (C) sediment adjacent to monoliths with 0% iron content (black circles) and 4% iron content (white circles) that were not carbonated. Tc-99 concentration gradients from the interface were observed in the sediment half-cells containing 4% moisture content sediments. The iron-containing half-cell had lower concentrations of Tc-99 than the half-cell without iron. Tc-99 concentration profiles were greater for both the 4% and 7% moisture content sediments in contact with iron-containing monoliths. At 7% sediment moisture content, the concentration of Tc-99 in the sediment showed a slight increase as a function of increasing distance from the concrete-sediment interface. The concentration profiles for the 15% moisture content were nearly constant over the length of the core. Opposite from the 4% and 7% moisture content half-cells, the sediment in contact with the 0% iron content concrete had the higher concentration. Only the concentration gradients for the 4% moisture content sediments were linearized by probit analyses to allow calculation of diffusion coefficients. Concentration profiles of Tc-99 in the concrete half-cells were not measured.
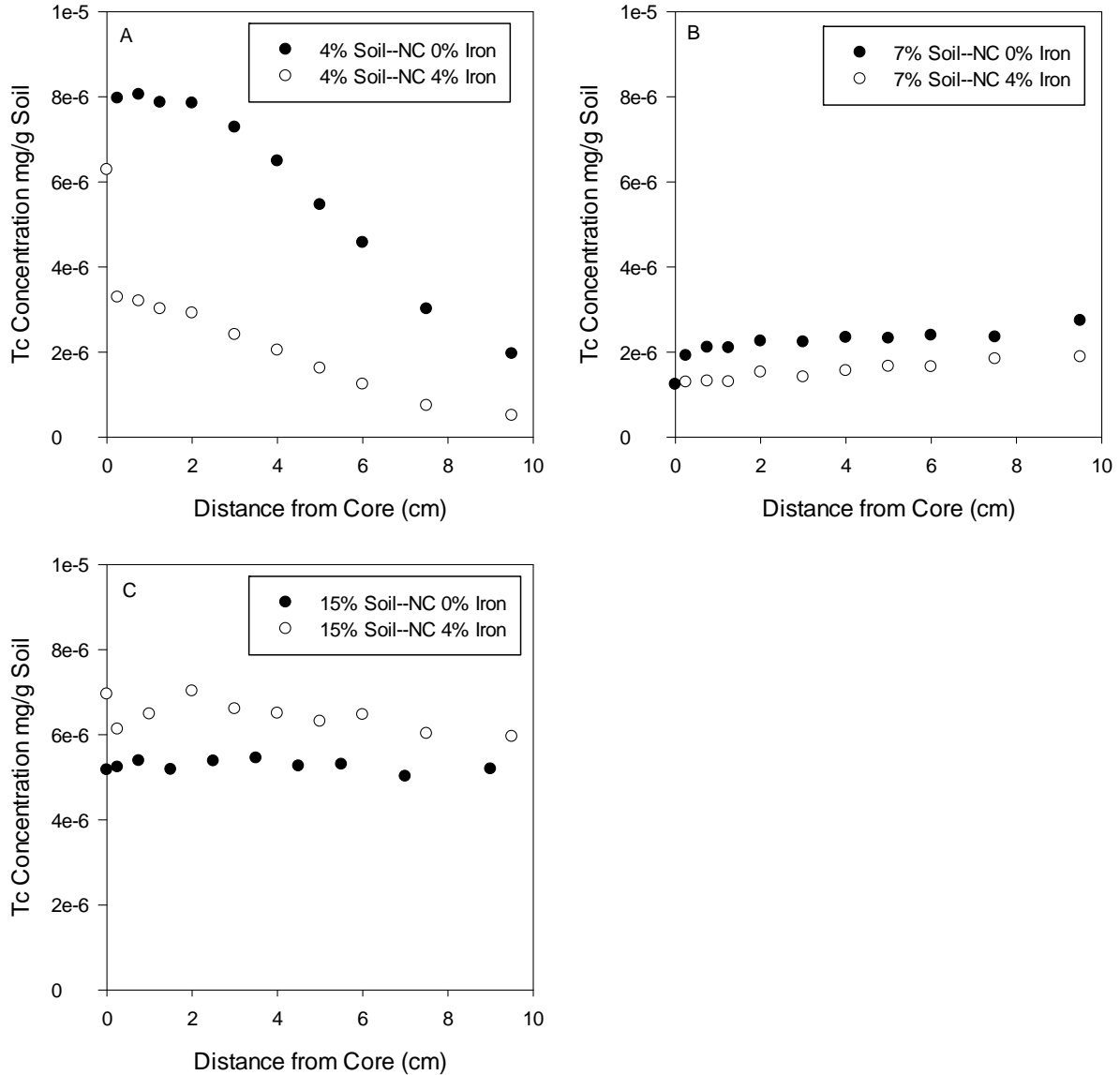
Figure 4.35. Sediment Tc-99 concentration profiles from FY 2007 concrete-sediment half-cell experiments for 0% iron (black circles) and 4% iron (white circles) with (A) 4% sediment moisture, (B) 7% sediment moisture, and (C) 15% sediment moisture

4.2.3.2   Probit Analysis

Probit analysis of the FY 1999 concrete-sediment diffusion experiments is shown in Figure 4.36 for 64-day (left) and 169-day (right) test durations. Calculated probit values are plotted as a function of distance from the interface for 4% (black circles) and 7% (white circles) moisture content sediment. The slopes from the linear fits were used to calculate the diffusivities listed in Table 4.21. Overall, the calculated diffusivities for Tc-99 ranged from 4.70×10^{-7} cm^2/s to 1.04×10^{-6} cm^2/s. An increase in sediment moisture content increased Tc-99 diffusivity by 10% for the 64-day test and almost 70% for the 169-day test. As observed in the sediment-sediment experiments, the longer test duration resulted in a reduction in the diffusivity values. The 4% moisture content sediment was reduced by 50% and the 7% moisture content had a 25% decrease.

4.50
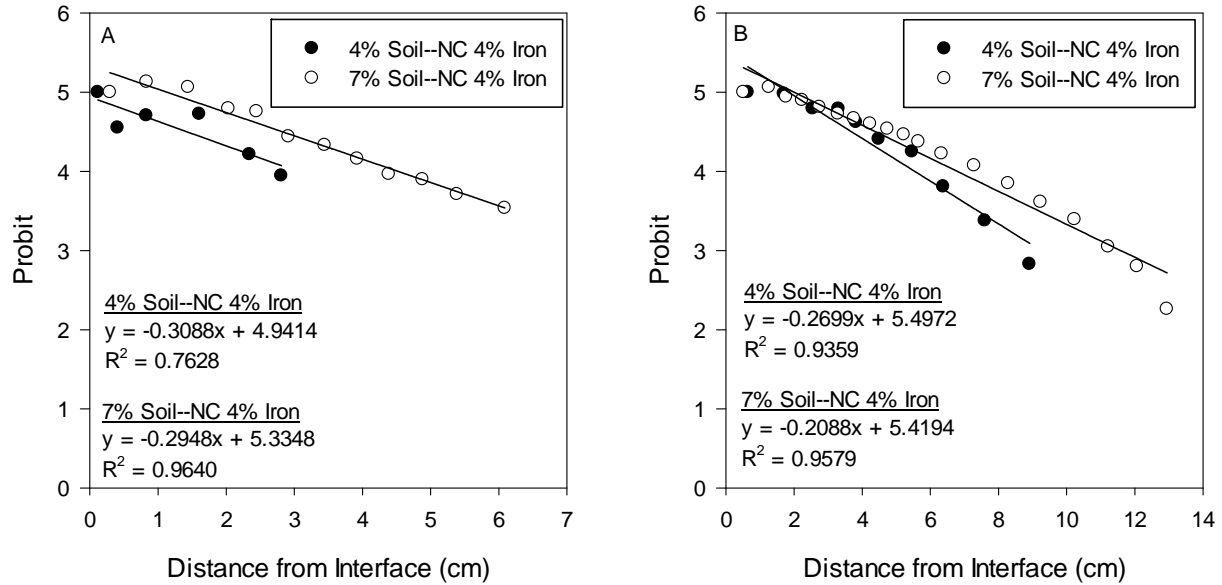
Figure 4.36. Probit plots for Tc-99 diffusion from FY 1999 concrete-sediment half-cell experiments with 4% sediment moisture (black circles) and 7% sediment moisture (white circles) at 64-day (left) and 169-day (right) test durations

Table 4.21. Calculated Tc-99 diffusion parameters from FY 1999 concrete-sediment half-cell experiments

	Core ID	Moisture Content (%)	Carbonated	Iron (%)	Tc-99 Diffusivity (cm^2/s)	Probit Slope
64 days	CS-1-4%	4	N	4	9.48×10^{-7}	0.3088
	CS-III-7%	7	N	4	1.04×10^{-6}	0.2948
169 days	CS-II-4%	4	N	4	4.70×10^{-7}	0.2699
	CS-IV-7%	7	N	4	7.85×10^{-7}	0.2088

Probit analysis of the FY 2007 concrete-sediment diffusion experiments for 4% moisture content sediment adjacent to non-carbonated concrete with 0% iron (black circles) and 4% iron (white circles) is shown as a function of distance from the interface in Figure 4.37. Slopes from the linear fits were used to calculate the diffusivities listed in Table 4.22. Diffusivity values were only calculated for the 4% moisture content experiments, as diffusion gradients were not observed for the 7% and 15% moisture content experiments. Calculated diffusivities were 4.82×10^{-7} cm^2/s for the half-cell with the 0% iron concrete monolith and 3.90×10^{-7} cm^2/s for the half-cell with the 5% iron concrete monolith. A 20% reduction in diffusivity as a result of the iron addition was observed.
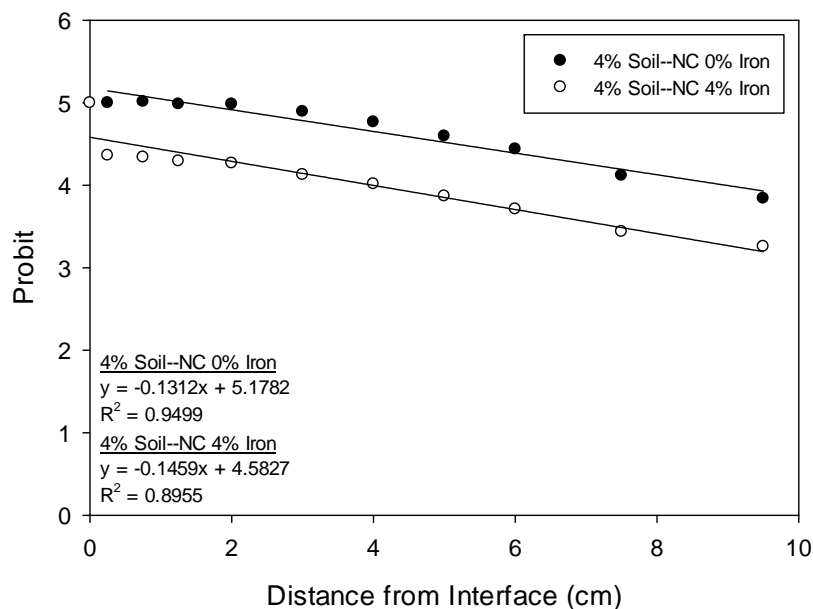
Figure 4.37. Probit plots for Tc-99 diffusion from FY 2007 concrete-sediment half-cell experiments for 0% iron (black circles) and 4% iron (white circles) with 4% sediment moisture content

Table 4.22. Calculated Tc-99 diffusion parameters from FY 2007 concrete-sediment half-cell experiments

Core ID	Moisture Content (wt%)	Carbonated	Iron (wt%)	Tc-99 Diffusivity (cm²/s)	Probit Slope
Tc-C-4-0-204	4	N	0	4.82×10^{-7}	0.1312
Tc-C-4-0-213	4	N	4	3.90×10^{-7}	0.1459

4.2.4   Fractured Concrete to Sediment

Fractured concrete to sediment diffusion experiments were initiated to assess the effect of fractures within the concrete monolith on the diffusion of Tc-99 into the sediment. Fractures within concrete may create preferential pathways for diffusion of contaminants. The test matrix included varied concrete iron content and carbonation of the concrete monoliths. Concrete half-cell specimens were spiked with Tc-99 (5.15×10^{-4} mg Tc/g concrete) to achieve a measurable diffusion profile in the sediment part of the half-cell. The general preparation of the half-cells is described in section 2.4. The characteristics of the concrete half-cells are listed in Table 4.23. HFS was used for the sediment half-cell. Test duration was 182 days.

Table 4.23. Characteristics of concrete specimens used in fractured concrete-sediment half-cell
experiments

Core ID	Length (cm)	Diameter (cm)	Surface Area (cm^2)	Volume (cm^3)	Weight (g)	Density (g/cm^3)	Iron (wt%)	Carbonated	Moisture Content (wt%)
Tc-C-10-5-0-202	4.29	4.32	57.52	62.87	140.34	2.23	0	N	4
Tc-C-10-5-0-203	4.51	4.34	91.09	66.73	149.74	2.24	0	Y	4
Tc-C-10-5-4-204	4.42	4.32	89.21	64.68	146.88	2.27	4	N	4
Tc-C-10-5-4-205	4.67	4.32	92.64	68.39	155.53	2.27	4	Y	4
Tc-C-10-5-8-207	4.56	4.32	91.19	66.82	153.63	2.30	8	N	4
Tc-C-10-5-8-208	4.53	4.32	90.85	66.46	152.56	2.30	8	Y	4
Tc-C-10-5-12-210	4.63	4.32	92.22	67.94	157.43	2.32	12	N	4
Tc-C-10-5-12-211	4.61	4.32	91.90	67.95	157.06	2.32	12	Y	4

4.2.4.1   Concentration Profiles

Concentration profiles of the concrete half-cells spiked with Tc-99 are shown in Figure 4.38 and listed in Table B.18. Concentration profiles are shown for monoliths with 0% iron (A), 4% iron (B), 8% iron (C), and 12% iron (C) that have been carbonated (black circles) or non-carbonated (white circles) adjacent to sediment with 4% moisture content. The concentration profiles exhibit bidirectional diffusion with a higher concentration towards the center and lower concentrations near the ends of the monoliths. At the end of the experiment, it was noted that some of the sediment had moved during the experiment and was contacting both ends of the concrete monolith, resulting in bidirectional diffusion.

The concentration profiles of the associated sediment half-cells are shown in Figure 4.39 and listed in Table B.19. Concentration profiles are shown for sediment adjacent to monoliths with 0% iron (A), 4% iron (B), 8% iron (C), and 12% iron (C) that had been carbonated (black circles) or left un-carbonated (white circles). Concentration gradients within the sediment were only observed very near the interfaces (<2.5 cm from the interface). Concentration profiles were similar for all the experiments. Concentration gradients were linearized by probit analyses to allow calculation of diffusion coefficients.
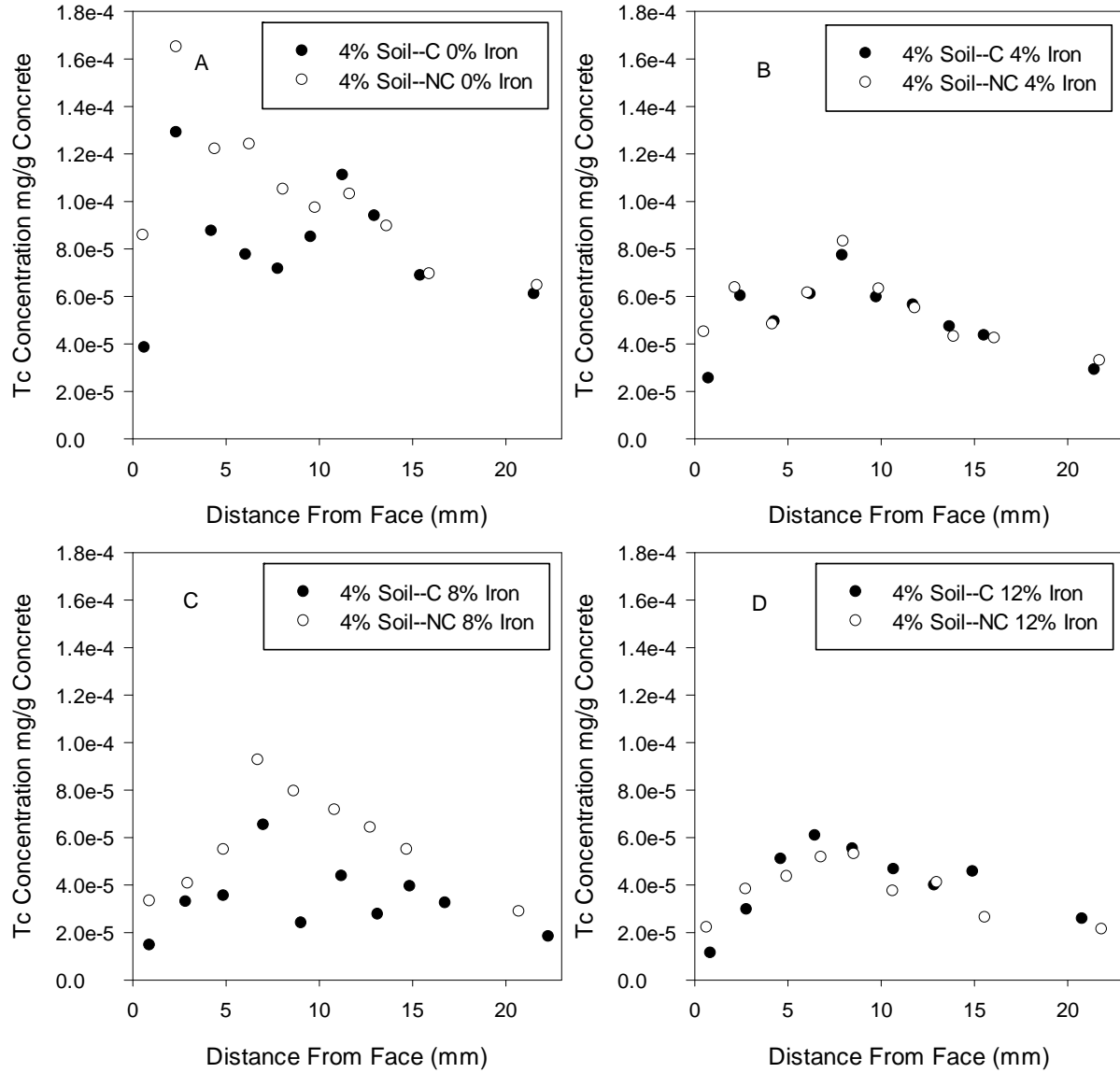
Figure 4.38. Concrete Tc-99 concentration profiles from fractured concrete-sediment half-cell
experiments with carbonated monoliths (black circles) and non-carbonated monoliths
(white circles) containing (A) 0% iron, (B) 4% iron, (C) 8% iron, and (D) 12% iron
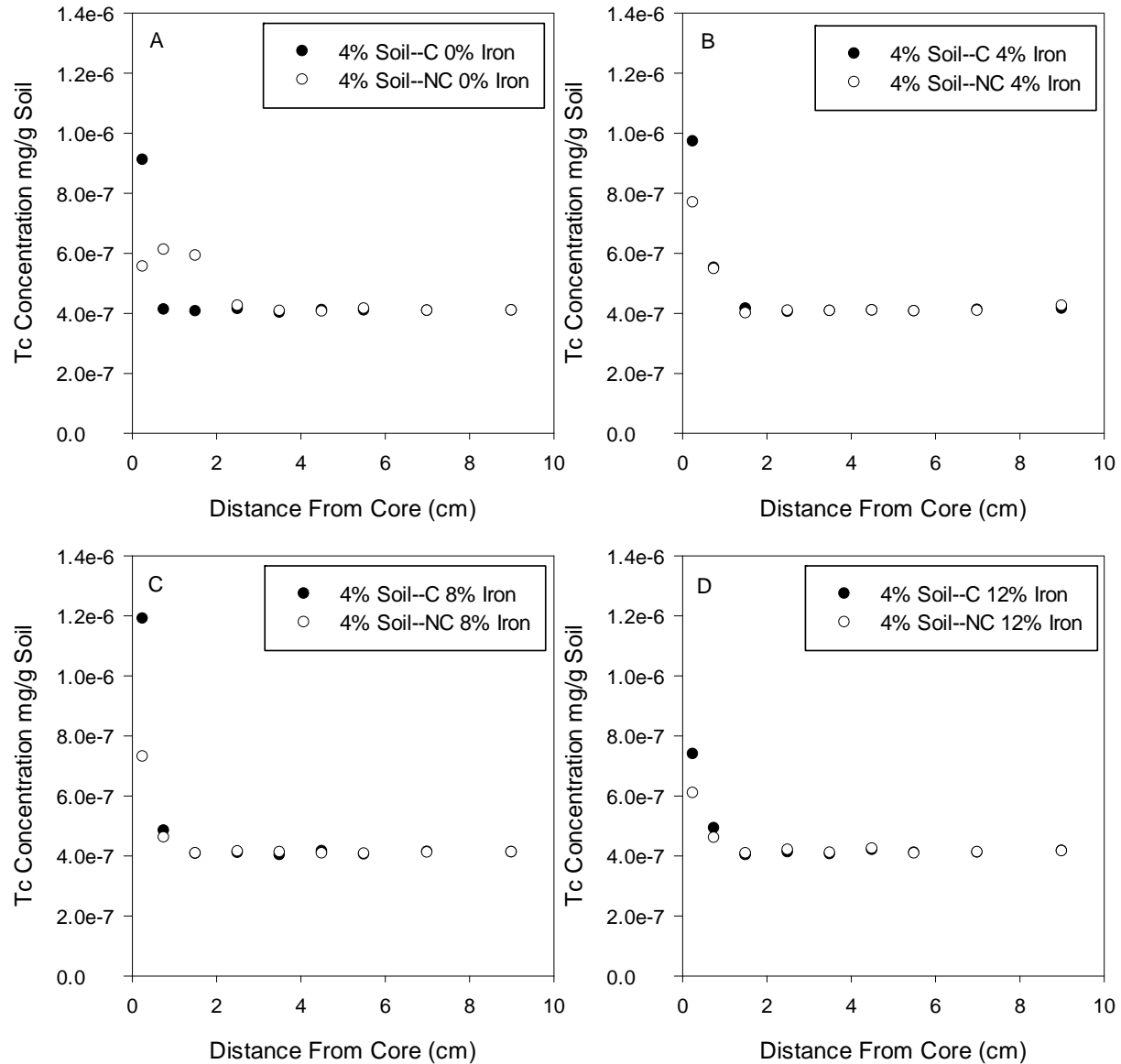
Figure 4.39. Sediment Tc-99 concentration profiles from fractured concrete-sediment half-cell experiments with carbonated monoliths (black circles) and non-carbonated monoliths (white circles) containing (A) 0% iron, (B) 4% iron, (C) 8% iron, and (D) 12% iron

4.2.4.2   Probit Analysis

Figure 4.40 shows the probit analysis from the fractured concrete-sediment diffusion experiment half-cells containing 4% moisture content sediment adjacent to monoliths that were carbonated (black circles) and non-carbonated (white circles) with 0% iron (A), 4% iron (B), 8% iron (C), and 12% iron (D). In most cases, only three data points were used in the linear fit to obtain the slope to calculate the diffusivities listed in Table 4.24. Diffusivity values ranged over an order of magnitude from 6.28×10^{-8} cm^2/s (4% moisture content sediment, carbonated with 8% iron) to 1.56×10^{-6} cm^2/s (4% moisture content sediment, non-carbonated with 0% iron).

As observed in the sediment to concrete tests, carbonation of the monolith resulted in smaller diffusivity values. Reductions ranged from 32% to 60% for the available data, with the smallest change observed in the 4% iron samples. The addition of iron reduces diffusivity in the non-carbonated monoliths when compared to the 0% iron sample. Reductions were most significant (12x) for the 4% addition of iron. The effect was not as pronounced as the iron additions increased with a 10x and 5x reduction in diffusivity observed for the 8% and 12% iron samples. The decrease in diffusion rates could be due to the reduction of Tc-99 from Tc(VII) to the insoluble Tc(IV) form. There was not sufficient data to calculate the diffusivity for the carbonated, 0% iron monolith half-cell, so a similar comparison cannot be made for the carbonated samples.
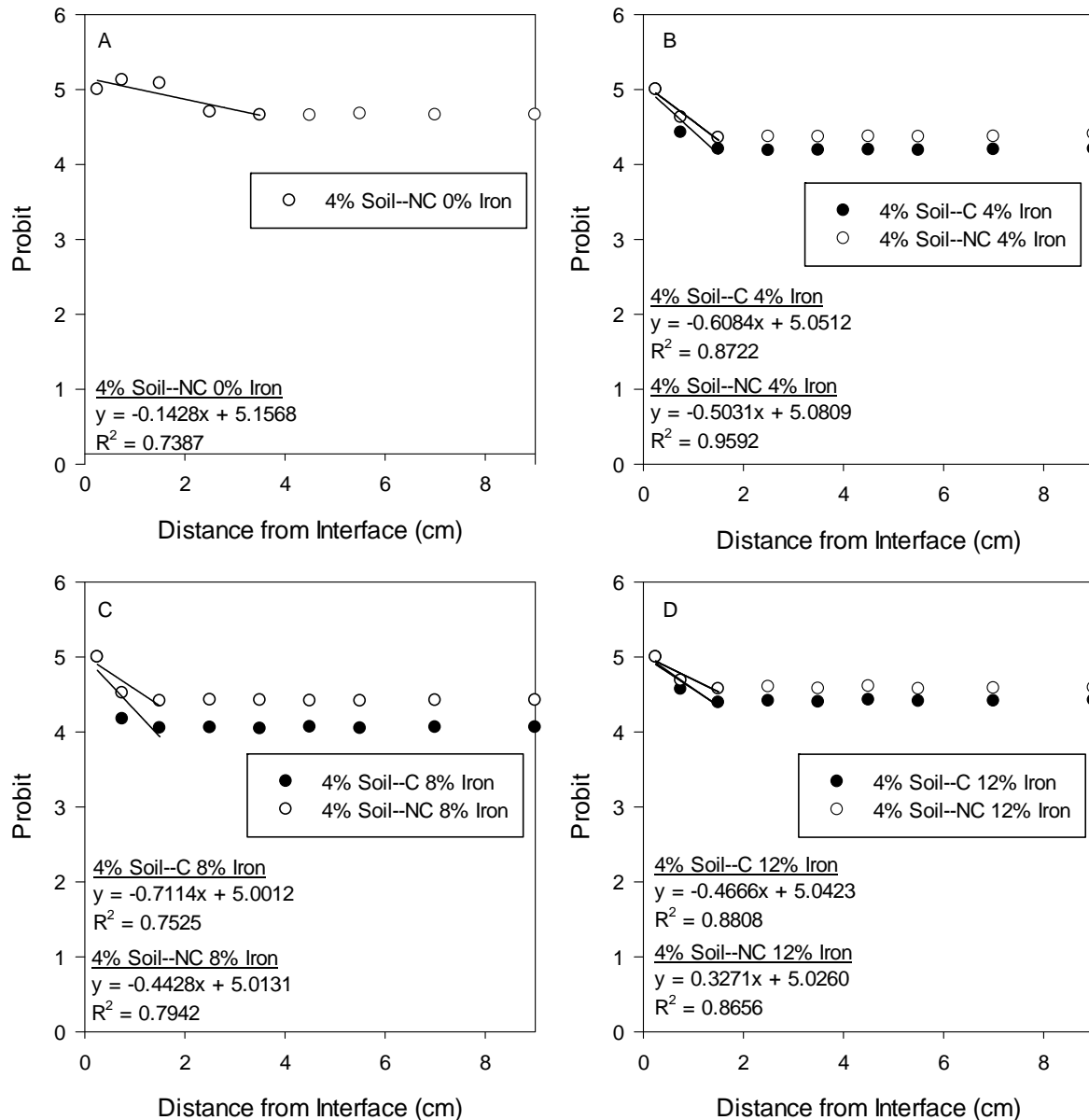
Figure 4.40. Probit plots for Tc-99 diffusion from fractured concrete-sediment half-cell experiments in 4% moisture content sediment with carbonated monoliths (black circles) and non-carbonated monoliths (white circles) containing (A) 0% iron, (B) 4% iron, (C) 8% iron, and (D) 12% iron

Table 4.24. Calculated Tc-99 diffusion parameters from fractured concrete-sediment half-cell experiments

Core ID	Moisture Content (wt%)	Carbonated	Iron (wt%)	Diffusivity (cm²/s)	Probit Slope
Tc-C-10-5-0-202	4	N	0	1.56×10^{-6}	0.1428
Tc-C-10-5-4-204	4	N	4	1.26×10^{-7}	0.5031
Tc-C-10-5-4-205	4	Y	4	8.59×10^{-8}	0.6084
Tc-C-10-5-8-207	4	N	8	1.62×10^{-7}	0.4428
Tc-C-10-5-8-208	4	Y	8	6.28×10^{-8}	0.7114
Tc-C-10-5-12-210	4	N	12	2.97×10^{-7}	0.3271
Tc-C-10-5-12-211	4	Y	12	1.46×10^{-7}	0.4666

4.2.5   Sediment to Fractured Concrete

A set of sediment to fractured concrete diffusion experiments was initiated to assess the effect of fractures within the concrete monolith on the diffusion of Tc-99 into the concrete. The test matrix included varied iron content and carbonation of the monoliths. For these tests, sediment half-cell specimens were spiked with Tc-99 (3.24×10^{-4} mg Tc-99/g sediment) to achieve a measurable diffusion profile in the concrete part of the half-cell. The characteristics of the concrete half-cells are listed in Table 4.25. HFS was used for the sediment half-cell. The general preparation of the half-cells is described in section 2.4. This set of tests ran for 182 days.

Table 4.25. Characteristics of concrete specimens used in sediment-fractured concrete half-cell experiments

Core ID	Length (cm)	Diameter (cm)	Surface Area (cm²)	Volume (cm³)	Weight (g)	Density (g/cm³)	Iron (wt%)	Carbonated	Moisture Content (wt%)
C-10-5-0-101	4.36	4.34	88.99	64.46	138.83	2.15	0	N	4
C-10-5-0-102	4.37	4.34	89.25	64.74	139.22	2.15	0	Y	4
C-10-5-4-105	4.28	4.34	88.00	63.37	137.39	2.17	4	N	4
C-10-5-4-106	4.25	4.34	87.52	62.86	135.92	2.16	4	Y	4
C-10-5-8-107	4.19	4.32	86.22	64.46	136.41	2.22	8	N	4
C-10-5-8-108	4.14	4.32	85.54	60.73	134.3	2.21	8	Y	4
C-10-5-12-110	4.23	4.32	86.79	62.07	138.96	2.24	12	N	4
C-10-5-12-111	4.38	4.34	89.33	64.83	145.49	2.24	12	Y	4

4.2.5.1   Concentration Profiles

The concentration profiles of sediment half-cells spiked with Tc-99 are shown in Figure 4.41 and listed in Table B.20. Concentration is plotted as a function of distance from the concrete monolith for sediment adjacent to monoliths with 0% iron (A), 4% iron (B), 8% iron (C) and 12% iron (D) content that had been carbonated (black circles) or left un-carbonated (white circles). No concentration gradients were observed in the sediment half-cells except near the interface (<2 cm).

The concentration profiles of the associated concrete half-cells are shown in Figure 4.42 and listed in Table B.21. Concentration is plotted as a function of distance from the concrete monolith for monoliths with 0% iron (A), 4% iron (B), 8% iron (C) and 12% iron (D) content that had been carbonated (black

circles) or left un-carbonated (white circles). Tc-99 concentration gradients were observed in concrete half-cells in the first 5 to 10 cm from the interface. These concentration gradients were linearized by probit analyses to calculate diffusion coefficients.
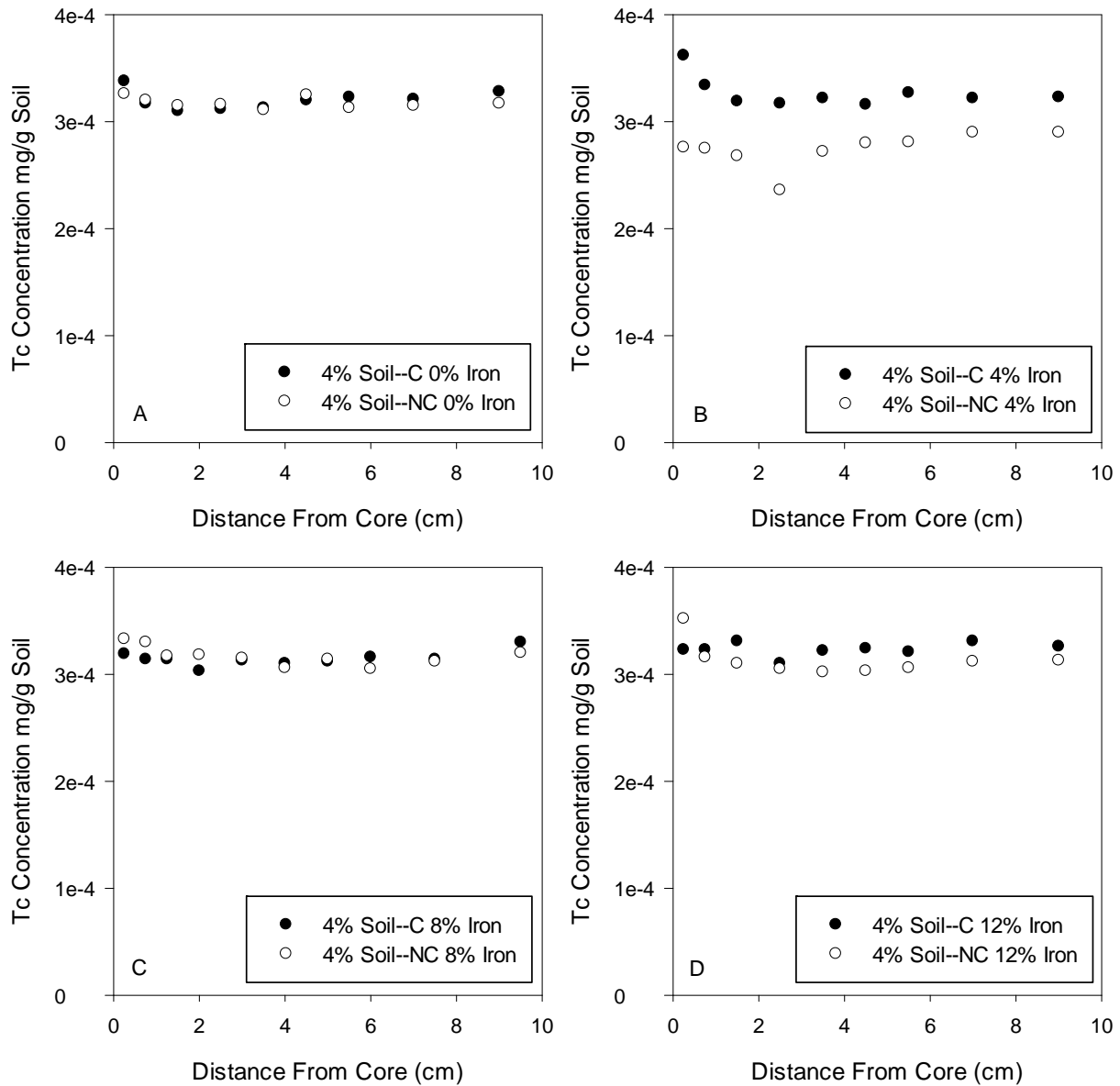
Figure 4.41. Sediment Tc-99 concentration profiles from sediment-fractured concrete half-cell experiments with carbonated monoliths (black circles) and non-carbonated monoliths (white circles) containing (A) 0% iron, (B) 4% iron, (C) 8% iron, and (D) 12% iron
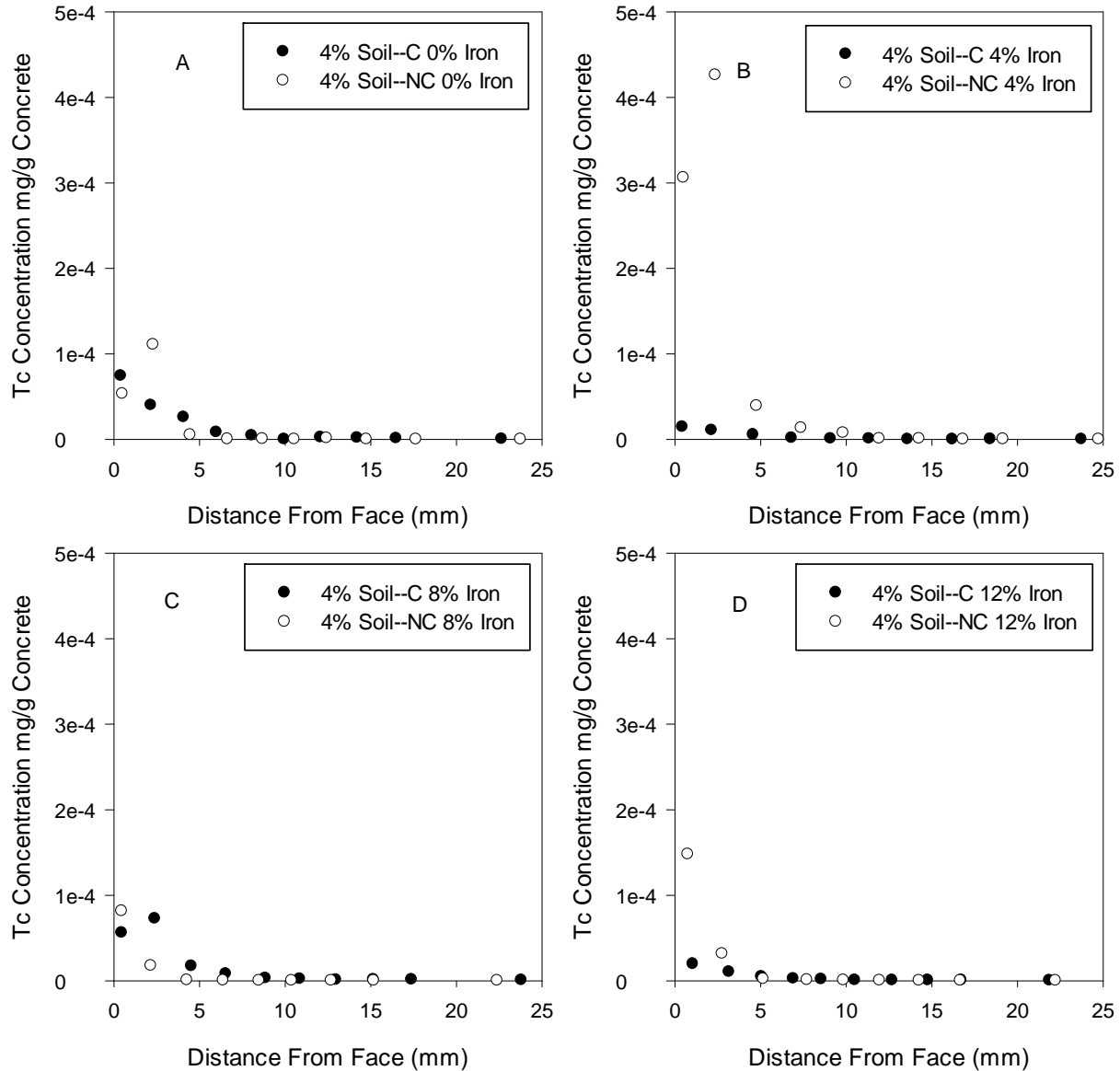
Figure 4.42. Concrete Tc-99 concentration profiles from sediment-fractured concrete half-cell experiments with carbonated monoliths (black circles) and non-carbonated monoliths (white circles) containing (A) 0% iron, (B) 4% iron, (C) 8% iron, and (D) 12% iron

4.2.5.2   Probit Analysis

Probit analysis of the sediment-fractured concrete diffusion experiments is shown in Figure 4.43 as a function of distance from the interface. Figure 4.43 shows the results for half-cells containing 4% moisture content sediment adjacent to monoliths that were carbonated (black circles) and non-carbonated (white circles) with iron content of 0% iron (A), 4% iron (B), 8% iron (C), and 12% iron (D). Diffusivities were tabulated from the slope of the linear fits and are listed in Table 4.26. Diffusivity values ranged from 1.96×10^{-9} cm^2/s to 2.51×10^{-8} cm^2/s.

Opposite of previous tests, carbonation of the monoliths resulted in higher diffusivity values. The concrete was carbonated via saturated solution, so increased diffusivity as a result of microcracks was not expected. The reason for the increased diffusivities is unclear.

The addition of iron reduced diffusivity values 2 to 7 times compared to the 0% iron samples. Increasing the iron addition did not consistently continue to reduce diffusivity values as 12% iron content cores exhibited larger diffusivity values than the 8% iron content cores. The decrease in diffusion rates could be due to the reduction of Tc-99 from Tc(VII) to the insoluble Tc(IV) form.
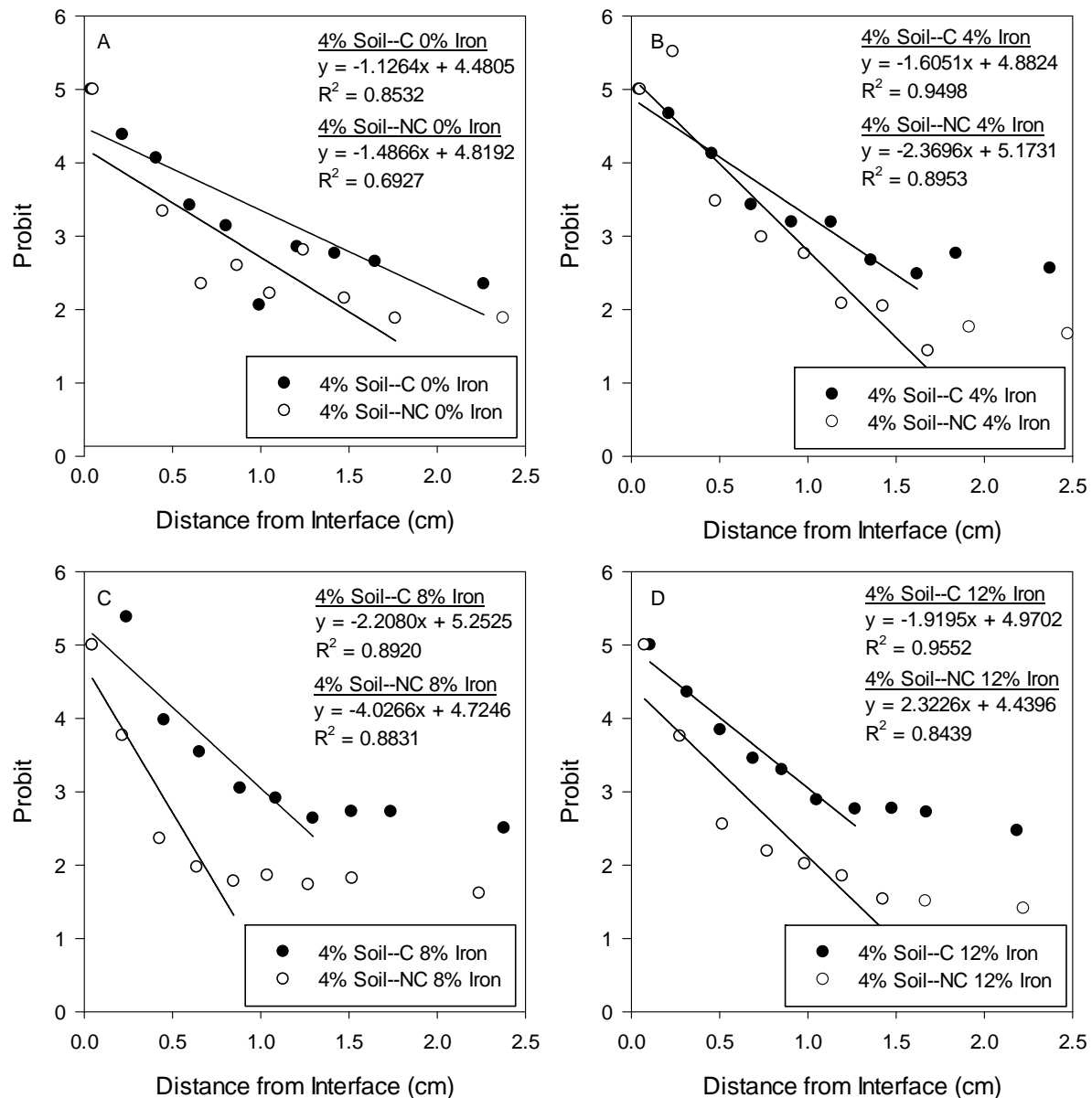
Figure 4.43. Probit plots for Tc-99 diffusion from sediment-fractured concrete half-cell experiments in 4% moisture sediment with carbonated monoliths (black circles) and non-carbonated monoliths (white circles) containing (A) 0% iron, (B) 4% iron, (C) 8% iron, and (D) 12% iron

4.60

Table 4.26. Calculated Tc-99 diffusion parameters from sediment-fractured concrete half-cell experiments

Core ID	Moisture Content (wt%)	Carbonated	Iron (wt%)	Diffusivity (cm^2/s)	Probit Slope
C-10-5-0-101	4	N	0	1.44×10^{-8}	1.4866
C-10-5-0-102	4	Y	0	2.51×10^{-8}	1.1264
C-10-5-4-105	4	N	4	5.66×10^{-9}	2.3696
C-10-5-4-106	4	Y	4	1.23×10^{-8}	1.6051
C-10-5-8-107	4	N	8	1.96×10^{-9}	4.0266
C-10-5-8-108	4	Y	8	6.52×10^{-9}	2.2080
C-10-5-12-110	4	N	12	5.89×10^{-9}	2.3226
C-10-5-12-111	4	Y	12	8.63×10^{-9}	1.9195

4.2.6 Technetium Diffusion Summary

Similar to the I diffusion results, general trends were observed when looking at all of the completed experiments. Lengthening the test duration resulted in a decrease in the Tc-99 diffusion coefficient. For the majority of the experiments, increasing the sediment moisture content within the half-cell resulted in an increase in Tc-99 diffusivity. The exception to this trend was the sediment-concrete test that had more mixed results, with 11 of the samples showing a decrease in diffusion and only 5 samples with increased diffusivity as a result of increased sediment moisture content.

The only method used to carbonate samples for the Tc-99 half-cell diffusion experiments was the supersaturated carbonate solution method. Two of the three experiments that investigated the effect of carbonation on diffusion had similar results to the I diffusion tests and exhibited a reduction in diffusivity with carbonation. The decrease in Tc-99 diffusivity could be the result of a chemical or physical change of the concrete due to carbonation or due to less Tc-99 being available as a result of leaching during the carbonation process. The carbonate solutions were not tested for Tc-99 concentrations, so the mechanism is unknown. The sediment-fractured concrete experiments showed an increase in diffusivity with carbonation. At this time, i the cause of this opposite response is unclear.

Overall, the addition of iron resulted in a decrease in diffusivity in comparison to the half-cells that did not contain iron. The sediment-concrete experiment had mixed results, in that 11 samples showed a decrease in Tc-99 diffusivity with the addition of iron and 7 samples exhibited an increase in diffusivity, but the general trend was observed for the majority of the samples. The decrease in diffusion rates could be due to the reduction of Tc-99 from Tc(VII) to the insoluble Tc(IV) form.

4.3 Rhenium Diffusion

Rhenium had been used as a substitute for Tc-99 in experiments over the course of this project due to its stable nature and size similar to Tc. Investigators in the United Kingdom have noted deviations in the chemical reduction of pertechnetate and perrhenate in the presence of organic ligands (Maset et al. 2006). Although perrhenate is a suitable surrogate based on size, it has been found that Re does not function as a comparable analogue for Tc-99 under redox conditions.

Additionally, the dynamic leach experiments (described in section 3.2) showed there was a difference in the leachability of Tc-99 and Re at the lower concentrations of iron added to the concrete (4% and 8% RNIP). Therefore, Re diffusion results from the half-cell experiments are not presented in this report.

4.4 Half-Cell Diffusion Summary

A series of half-cell diffusion experiments were completed to investigate the effects of test duration, sediment moisture content, concrete carbonation, concrete fractures, and concrete iron content on diffusivity of I and Tc-99 from sediment and from concrete. The conclusions from these tests are as follows:

- Diffusion coefficients for I ranged from 3.63×10^{-9} to 5.99×10^{-6} cm^2/s and Tc-99 diffusion coefficients ranged from 1.96×10^{-9} to 3.07×10^{-6} cm^2/s throughout all the half-cell diffusion experiments. The range of diffusion coefficients for Tc-99 was lower than that of I, but coefficients for both nuclides spanned over 3 orders of magnitude.

- Increasing the sediment moisture content from 4% to 7% or 15% within the half-cell leads to an increase in both I and Tc-99 diffusion rates.

- Lengthening the test duration results in a decrease in Tc-99 diffusion coefficients. Data is not available for I diffusion.

- Carbonation by supercritical CO_2 treatment increased diffusivity of I and Tc-99 through preferential pathways in the microcracks that were created. Additional discussion on carbonation is in the following section.

- Using a super-saturated carbonate solution to carbonate concrete resulted in a decrease in diffusivity coefficients through a chemical or physical change within the concrete or due to a reduction in available nuclide through leaching during the carbonation process. Further analysis is required to determine the mechanism for the observed reduction of diffusivity values.

- The addition of iron resulted in a decrease in diffusivity in comparison to the half-cells that did not contain iron. Increasing the iron addition did not consistently enhance the reduction of diffusivity values. The decrease in Tc-99 diffusion rates could be due to the reduction of Tc-99 from Tc(VII) to the insoluble Tc(IV) form, though the mechanism of diffusion attenuation of I still needs further investigation.

The radionuclide spikes were added to the half-cells as pertechnetate and iodide. The redox speciation of these elements in the concrete was not determined at the conclusion of any of the diffusion experiments. Based on Eh-pH stability of I species (Pourbaix 1966) and the highly alkaline conditions in the concrete matrix, the iodide may have oxidized into iodate so diffusivity values may pertain to iodate rather than iodide. Pertechnetate is stable under highly alkaline conditions as indicated by Eh-pH stability (Pourbaix 1966), so diffusivity values presented here may reflect the diffusion of that species.

5.0 Carbonation and Microcracking Studies

Carbonation can affect both the physical and chemical properties of concrete. Carbonation depth into the outer surface of concrete, induced microcracking, and the accumulation of secondary phases may influence the rate of contaminant release from concrete either positively or negatively.

5.1 Concrete Half-Cells

Four concrete monoliths spiked with I and Re, from concrete-sediment half-cell experiments (Table 2.3 and Table 4.8), were subjected to petrographic studies to evaluate the extent of carbonation and the degrees of microcracking induced by carbonation, and to discern correlations between the diffusion of I from the monoliths (Table 5.1).

Table 5.1. Concrete monoliths subject to carbonation/microcracking analysis

Monolith ID	Iron	CO_2	Moisture Content
CS-II-4%	No	No	4%
CS-IV-4%	Yes	No	4%
CS-I-7%	No	Yes	7%
CS-III-7%	Yes	Yes	7%

5.1.1 Petrographic Analyses

5.1.1.1 CS-II-4%

Images of the CS-II-4% sample are shown in Figure 5.1. The concrete monolith hydration characteristics are normal. Partly hydrated cement grains are coated with transparent, colorless hydration rims. Portlandite (calcium hydroxide) is relatively abundant. The crystals are small and uniformly distributed. The concrete is air entrained with an estimated 6% to 8% small, spherical air voids. Clustering of the voids is common. Small air voids in the outer 1 mm of the concrete are lined with ettringite crystals. Concrete volume is estimated at 30% to 35%, interpreted water-cementitious materials ratio is 0.53 to 0.58.

The surface of the concrete monolith in contact with the sediment half-cell is carbonated to a depth of 2 mm (right image of Figure 5.1). The concrete surfaces are carbonated to an average depth of 0.4 mm (right image of Figure 5.1). The carbonated concrete has a fine-grained texture and consists of impure calcium carbonate. No significant cracks or microcracks are observed.
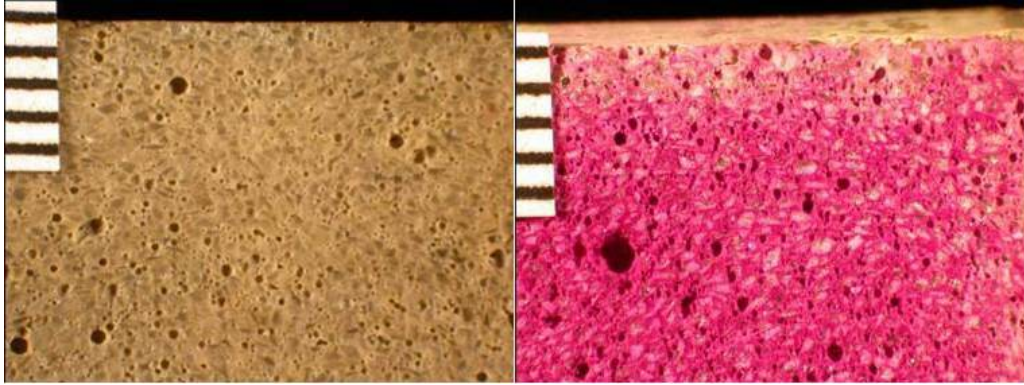
Figure 5.1. Left: Lapped surface of CS-II-4%. The top surface shown in the photo is a cast surface. Air voids are non-uniformly distributed. Right: Close view of a fracture surface treated with phenolphthalein pH indicator solution. Non-carbonated concrete is stained magenta. A cast surface is at the top of the photo. Scale is marked in millimeter increments.

A low magnification view in backscattered electron mode (BSE) is shown in the left image of Figure 5.2. Narrow microcracks passing between aggregate particles and between air voids are common. Microcracks in the concrete near the aggregate boundary and separation cracks at the aggregate interface are also fairly common. The higher magnification view shown in Figure 5.2 (right image) illustrates the width of the microcracks and the discontinuous nature of many of the microcracks. The width of the microcracks is generally 1 to 2 micrometers or less. No deposits are detected in the microcracks.
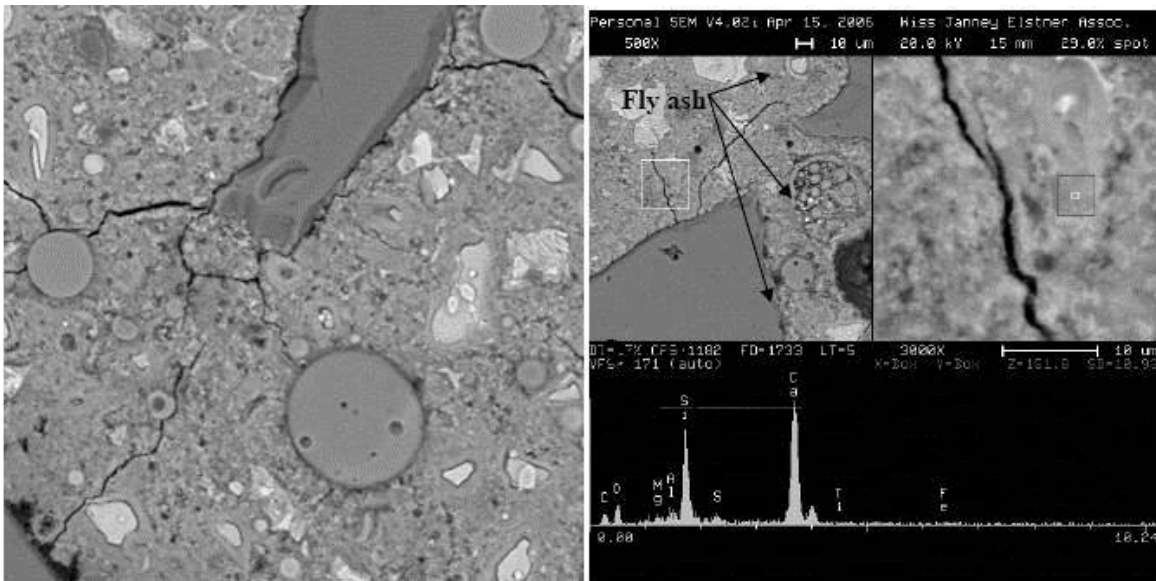
Figure 5.2. Left: BSE image showing microcracks and aggregate boundary microcracks and separation of the CS-II-4% sample. Spherical objects are fly ash particles (250x magnification). Right: BSE images at 500x and 3000x showing a typical microcrack. The area enclosed by the white box in the image on the left is enlarged in the image on the right. The scale bars are above and below the left and right images, respectively. The image on the right shows that the microcracks are substantially less than 10 micrometers wide. The X-ray analysis at the bottom is for a small region of concrete adjacent to the microcrack. The area of the analysis is indicated in the image on the right by the gray box containing the small white square.

5.1.1.2   CS-IV-4%

Images of the CS-IV-4% sample are shown in Figure 5.3. The concrete monolith hydration characteristics are normal. Partly hydrated cement grains are coated with transparent, colorless hydration rims. The level of fly ash replacement/substitution is moderate to high, based on the relative proportions of unhydrated and partly hydrated cement and residual fly ash. Portlandite (calcium hydroxide) is relatively abundant. The crystals are small and uniformly distributed. The concrete is air entrained with an estimated 5% to 7% small, spherical air voids; clustering of the voids is common. Concrete monolith volume is estimated at 30% to 35% and the interpreted water-cementitious materials ratio is 0.50 to 0.55. No secondary precipitates are observed.

The surface of the concrete monolith in contact with the sediment half-cell is carbonated to a depth of 1 to 2 mm (right image of Figure 5.3). The monolith surfaces are carbonated to an average depth of 0.4 mm (right image of Figure 5.3). The carbonated monolith has a fine-grained texture and consists of impure calcium carbonate. No significant cracks or microcracks are observed.
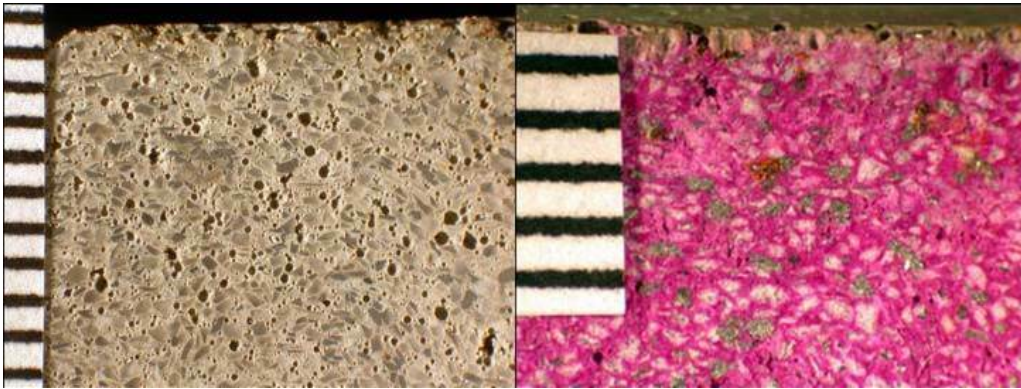
Figure 5.3. Left: Lapped surface of CS-IV-4%. The top surface shown in the photo is a cast surface. Clustering of the entrained air voids can be clearly seen. Right: Close view of a fracture surface treated with phenolphthalein pH indicator solution. Non-carbonated concrete is stained magenta. A cast surface is at the top of the photo. Scale is marked in millimeter increments.

A low magnification view in BSE mode is shown in the left image of Figure 5.4. Narrow microcracks passing between aggregate particles and between air voids are common. Separation cracks along the aggregate interface are frequent. The higher magnification views are shown in the right image of Figure 5.4. The width of the microcracks is generally 1 to 2 micrometers or less. No deposits are detected in the microcracks.
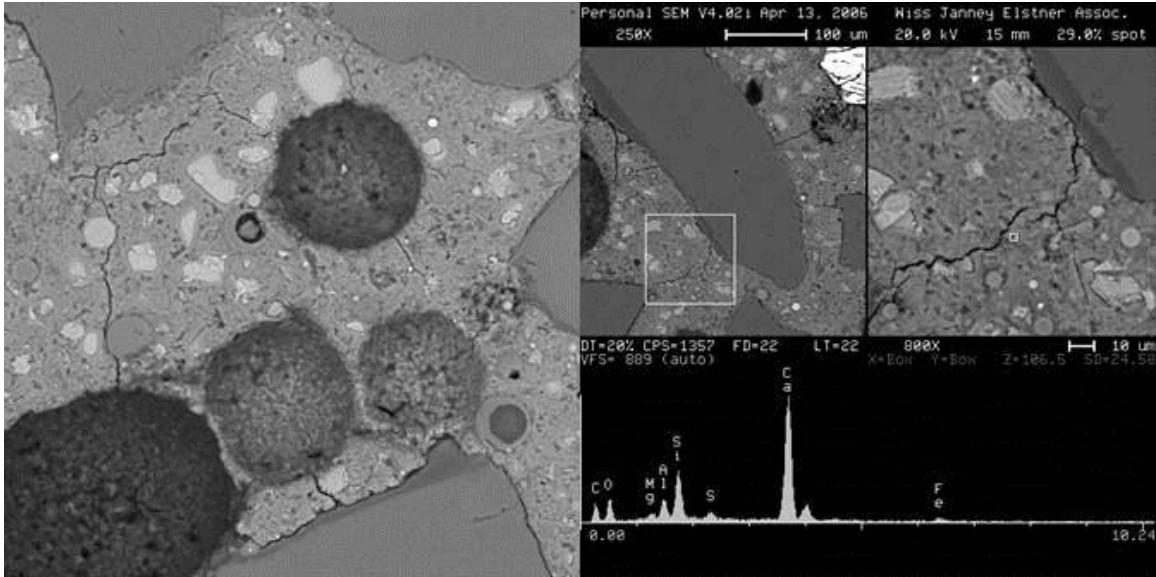
Figure 5.4. Left: BSE image showing typical concrete microcracks and aggregate boundary microcracks and separation of the CS-IV-4% sample (250x magnification). Right: BSE images of CS-IV-4% at 250x and 800x showing a typical discontinuous microcrack. The area enclosed by the white box on the left is enlarged in the image on the right. The scale bars are above and below the left and right images, respectively. The image on the right shows that the microcracks are substantially less than 10 micrometers wide. The X-ray analysis at the bottom is for a small region of concrete adjacent to the microcrack. The analysis spot is indicated by the small white square in the image on the right**.**

5.1.1.3   CS-I-7%

Images of the CS-I-7% sample are shown in Figure 5.5. The interior portion of the monolith is dark beige-gray and white (secondary deposits). The concrete in the outer portion of the monolith is medium beige-gray. The concrete contains scattered unhydrated Portland cement clinker particles, abundant partly hydrated Portland cement grains, and abundant residual fly ash particles. Cement hydration characteristics are normal. Partly hydrated cement grains are coated with transparent, colorless hydration rims. Portlandite (calcium hydroxide) is relatively abundant. The crystals are small and uniformly distributed. The concrete is air entrained with an estimated 7% to 9% small, spherical air voids. Air voids in the interior portion of the concrete are lined with ettringite deposits (bottom right image of Figure 5.5). Clustering and coalescence of the voids are common. The concrete volume is estimated at 30% to 35%, interpreted water-cementitious materials ratio is 0.53 to 0.58.

The concrete is carbonated to a depth of 5 to 8 mm from the outside surfaces (top and cast surfaces). The carbonated concrete has a fine-grained texture and consists of impure calcium carbonate. No significant cracks or microcracks are observed.
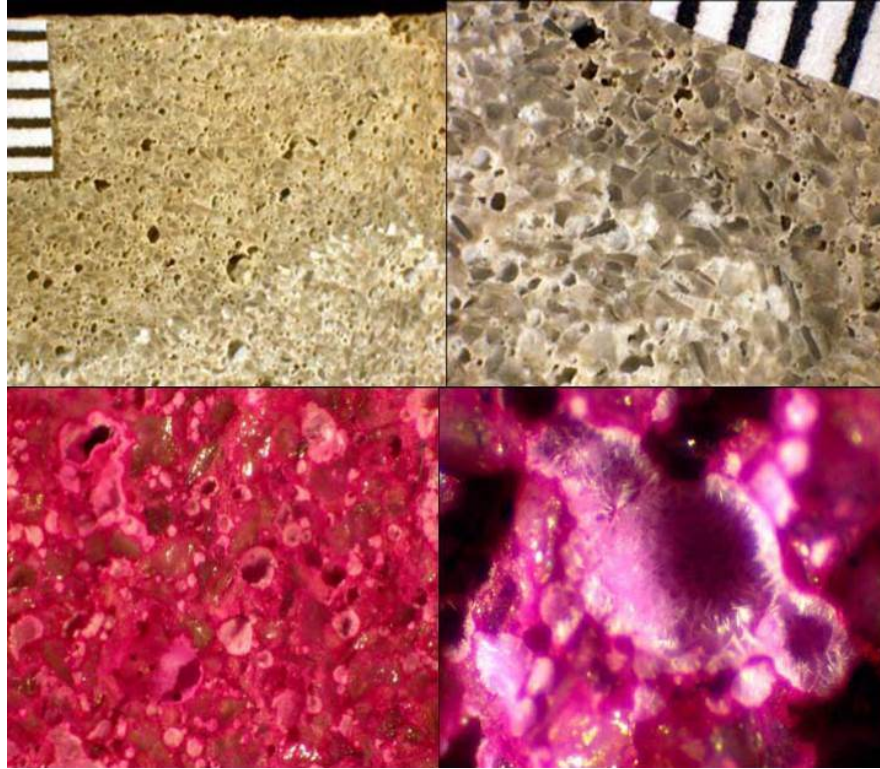
Figure 5.5. Top left: Lapped surface of CS-I-7%. The top surface of the cast specimen is at the top of the photo. Note concrete color change and abundance of white deposits in the bottom portion of the photo. Top right: Closer view of concrete and air voids lined with ettringite deposits. Bottom left: Fracture surface of the interior portion of CS-I-7% after treatment with phenolphthalein pH indicator solution. No concrete carbonation is observed. Bottom right: Closer view of ettringite needles lining air voids in the interior of the monolith. Scale is marked in millimeter increments.

A low magnification view in BSE mode is shown in the left image of Figure 5.6. Narrow microcracks passing between aggregate particles and fly ash particles are common. Separation microcracks along the interface between aggregates and paste and also around the larger fly ash particles are abundant. Higher magnification views illustrating the microcracks are shown in the right image of Figure 5.6. The width of the widest microcracks is generally ~1 micrometer. Short, narrow microcracks branching from the wider, longer microcracks are a common feature of this sample. No deposits are detected in the microcracks.
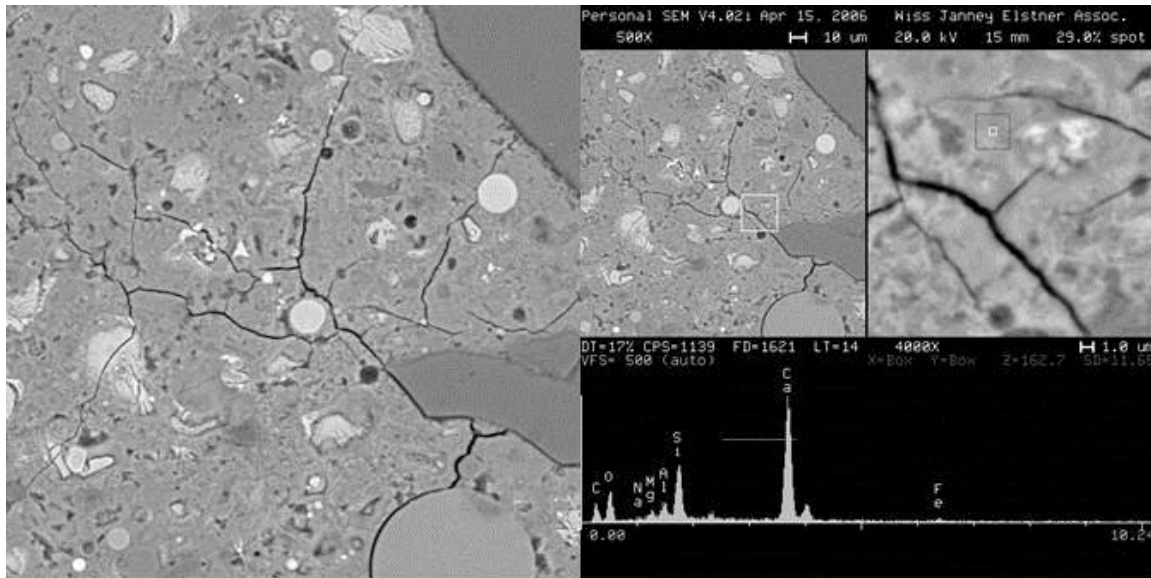
Figure 5.6. Left: BSE image of the CS-I-7% sample (500x magnification). Microcracks pass between aggregate particles and fly ash particles. Microcracks also transect Portland cement grains. Separation microcracks around aggregate particles and fly ash particles are common. Right: BSE images at 500x and 4000x showing narrow microcracks branching from the wider, longer microcracks. The X-ray analysis at the bottom is for a small area between microcracks. The area of the analysis is indicated in the image on the right by the gray box containing the small white square.

5.1.1.4   CS-III-7%

Images of the CS-III-7% sample are shown in Figure 5.7. The concrete monolith hydration characteristics are normal. Partly hydrated cement grains are coated with transparent, colorless hydration rims. The level of fly ash replacement/substitution is moderate to high, based on the relative proportions of unhydrated and partly hydrated cement and residual fly ash. Portlandite (calcium hydroxide) is relatively abundant. The crystals are small and uniformly distributed. The concrete is air entrained with an estimated 5% to 7% small, spherical air voids; clustering of the voids is common. No secondary precipitation was observed. The concrete volume is estimated at 30% to 35%, interpreted water-cementitious materials ratio is 0.47 to 0.52.

The outer concrete surfaces are carbonated (fine-grained, impure calcium carbonate) to an average depth of 2 to 4 mm (right image of Figure 5.7). Small patches of similar carbonated concrete are present throughout the body of the sample. No significant cracks or microcracks are observed.
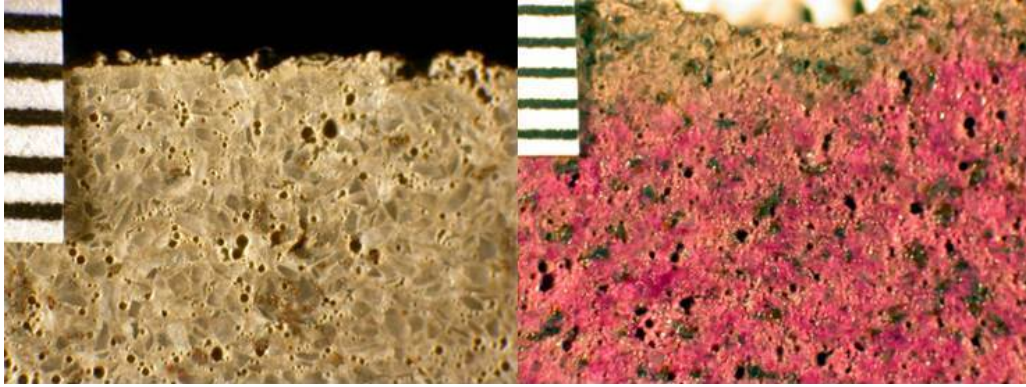
Figure 5.7. Left: Lapped surface of CS-III-7%. The top surface shown is a struck surface. Air voids are non-uniformly distributed. Metallic aggregates are somewhat corroded. Right: Close view of a fracture surface treated with phenolphthalein pH indicator solution. Mottled pink and magenta stain is indicative of patchy carbonation. The top surface of the sample is at the top of the photo. Scale is marked in millimeter increments.

A low magnification view in BSE mode is shown in the left image of Figure 5.8. Narrow microcracks passing between aggregate particles and iron particles are common. Some separation microcracks along the interface between aggregates and concrete are also detected, but these features are not abundant. Higher magnification views are shown in the right image of Figure 5.8. The figures illustrate typical microcracks. The width of the widest microcracks is generally ~1 micrometer. No deposits are detected in the microcracks.
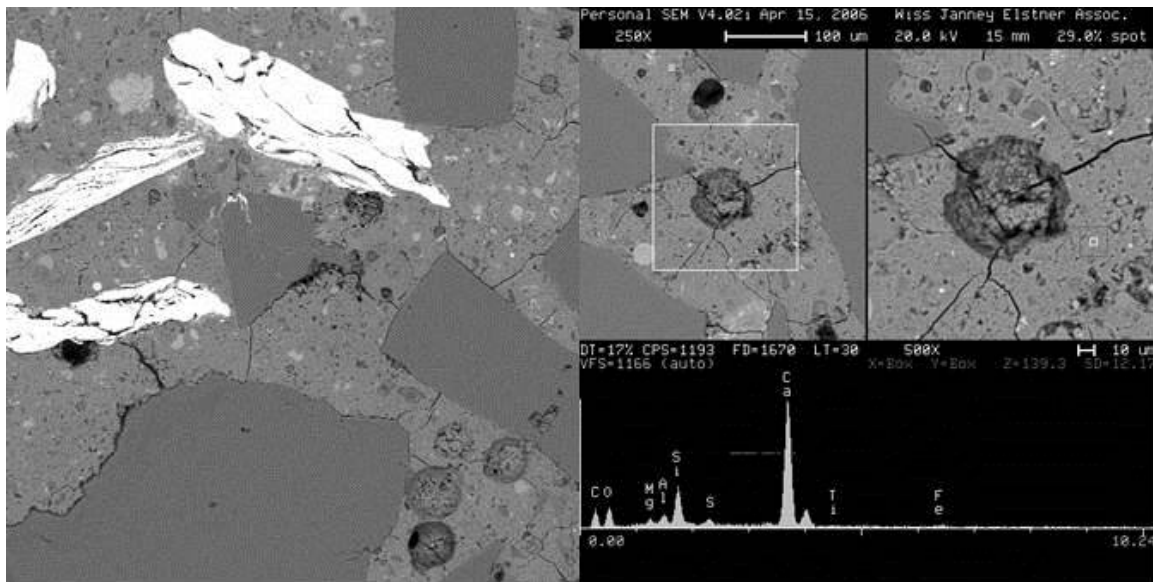
Figure 5.8. Left: BSE image of the CS-III-7% sample (100x magnification). Bright inclusions are iron. Microcracks extended between aggregate particles and iron particles. Some separation microcracks are also visible. Right: BSE images at 250x and 500x showing microcracks intersecting in air voids. The X-ray analysis at the bottom is for a small area near the air void. The area of the analysis is indicated in the image on the right by the gray box containing the small white square.

5.2   Vadose Zone Conditions

Nine concrete monoliths were encased in HFS with moisture contents of 4%, 7%, and 15% by mass and from 6 months to 2 years (Table 2.3). At the end of each set aging period, three monoliths, one representing each respective moisture content, were removed and subjected to petrographic analyses to determine the depth of carbonation under simulated vadose zone conditions.

5.2.1   Petrographic Analysis

5.2.1.1   4% Moisture Content – 6-Month Sample

Images of the 4% moisture content sample at 6-month aging are shown in Figure 5.9. The concrete monolith contains frequent cement lumps (typically 0.3 to 1.2 mm diameter). Small amounts of unhydrated Portland cement clinker particles, abundant partly hydrated Portland cement grains, and fairly abundant residual fly ash particles are observed. The cement hydration characteristics appear normal. The level of fly ash replacement/substitution is moderate, based on the relative proportions of unhydrated and partly hydrated cement and residual fly ash. Portlandite (calcium hydroxide) is relatively abundant. The crystals are small to moderate in size and are uniformly distributed. No secondary precipitates are observed. The concrete is air entrained with an estimated 5% to 7% non-uniformly distributed, small, spherical and oval air voids; clustering of the voids is common. Concrete volume is estimated at 30% to 35%; interpreted water-cementitious materials ratio is 0.50 to 0.55.

The monolith is carbonated to an average depth of 0.3 mm from the cast surfaces and has a fine-grained texture and consists of impure calcium carbonate. No significant cracks or microcracks are observed.

A low magnification view in BSE mode is shown in left image of Figure 5.10. This sample contains relatively few long microcracks that pass between the aggregate particles. Separation microcracks along the paste-aggregate contacts are also rare. A higher magnification view illustrating the microcracks is shown in the right image of Figure 5.10. The width of the widest microcracks is ~1 to 2 micrometers. The longer microcracks are often discontinuous. Short microcracks sometimes branch from the longer microcracks. No deposits are detected in the microcracks.
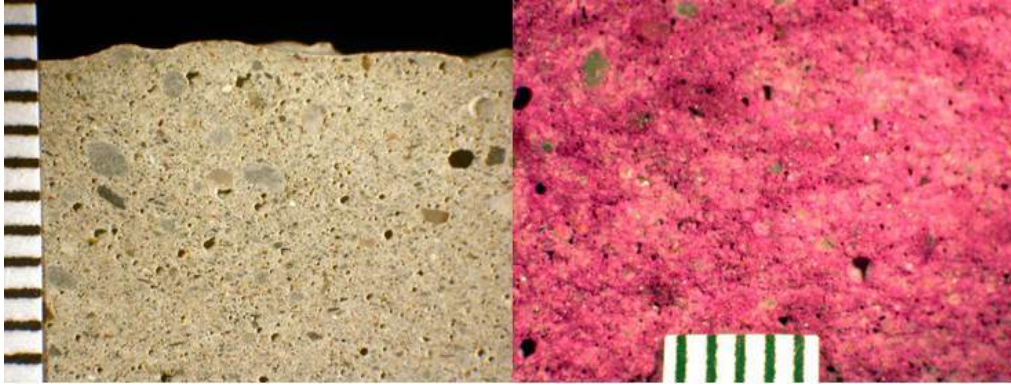
Figure 5.9. Left: Lapped surface of 4% moisture content, 6-month sample. The top surface of the cast specimen is at the top of the photo. Right: Fracture surface of the interior portion of sample after treatment with phenolphthalein pH indicator solution. The mottled coloration is attributed to non-uniform distribution of the cement. Scale is marked in millimeter increments.
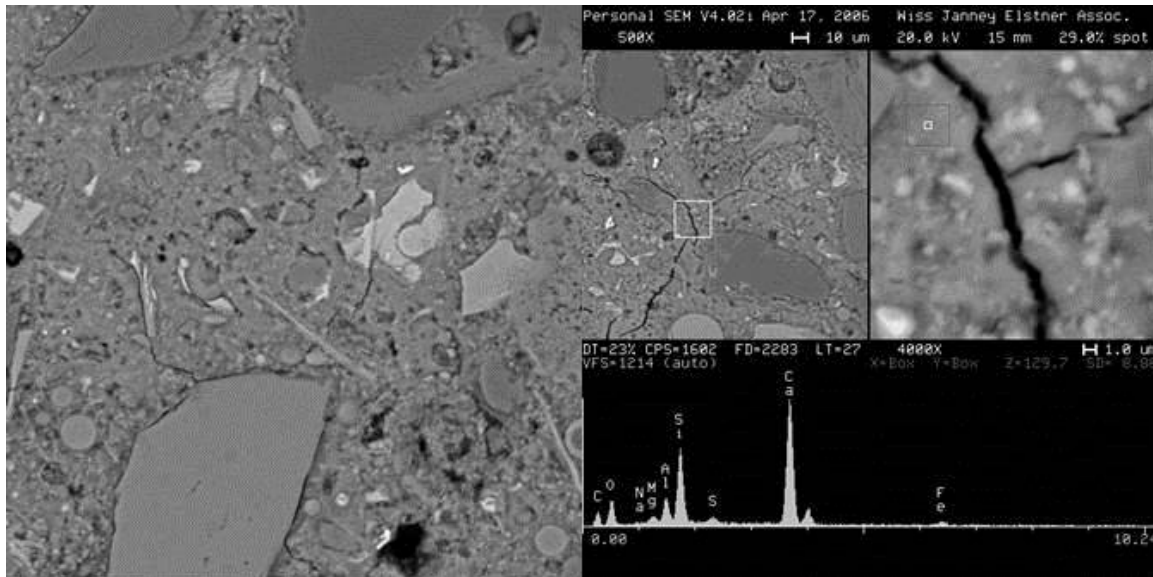
Figure 5.10. Left: BSE image of the 4% moisture content, 6-month sample (500x magnification). Microcracks are rare and are mostly short. Separation microcracks around aggregate particles are also uncommon. Right: BSE images at 500x and 4000x showing the rare, longer and wider microcracks that pass between aggregate particles. The area enclosed by the white box in the image on the left is enlarged in the image on the right. The scale bars are above and below the left and right images, respectively. The X-ray analysis at the bottom is for a small area of concrete near the microcrack. The location of the analysis is indicated by the gray box containing the small white square.

5.2.1.2   4% Moisture Content – 2-Year Sample

Images of the 4% moisture content sample aged 2 years are shown in Figure 5.11. The monolith contains abundant cement balls, mostly less than 1 mm in diameter. The extent of the cement hydration is advanced and substantial hydration rims were observed around most of the cement grains. Portlandite (calcium hydroxide) crystals are small to moderate in size and are not uniformly distributed. Fly ash

spheres are abundant. No secondary precipitates are observed. The concrete was air entrained with an estimated 5% to 7%. Carbonation was observed only at the surface of the monolith.

A low magnification view in BSE mode is shown in the bottom left image of Figure 5.11. This sample contains abundant microcracks and adhesion cracks. A higher magnification view illustrating the microcracks is shown in the bottom right image of Figure 5.11.
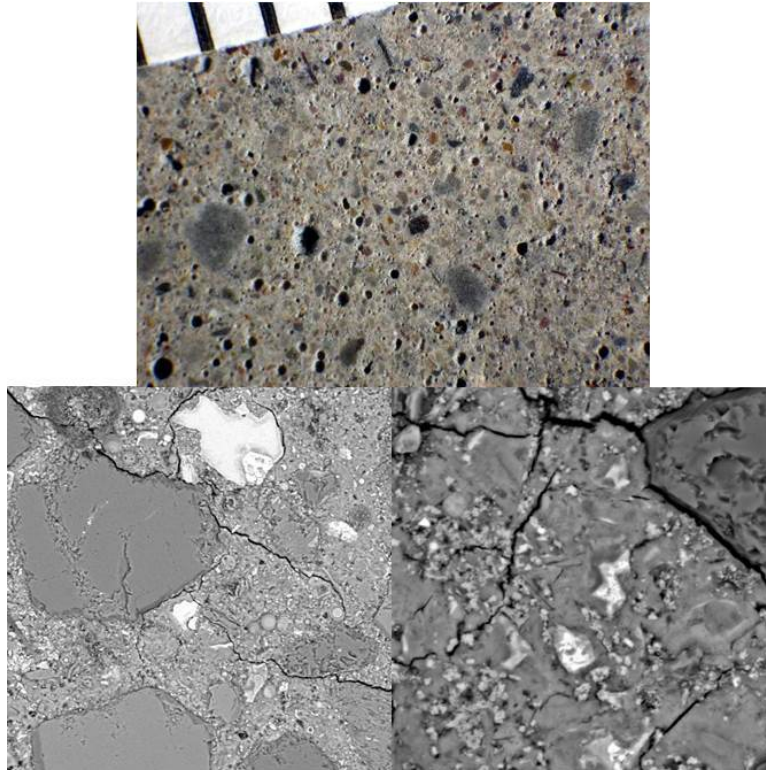
Figure 5.11. Top: Representative view of the lapped surface of the 4% moisture content, 2-year sample (millimeter scale). Bottom left: BSE image of microcracks and adhesion cracks in the sample (250x magnification). Bottom right: BSE image of microcracks and adhesion cracks in the sample (1000x magnification).

5.2.1.3   7% Moisture Content – 6-Month Sample

Images of the 7% moisture content sample aged 6 months are shown in Figure 5.12. The monolith contains frequent cement lumps gray, rounded lumps mostly less than 1 mm in diameter. Small amounts of unhydrated Portland cement clinker particles, abundant partly hydrated Portland cement grains, and fairly abundant residual fly ash particles are observed. The cement hydration characteristics appear normal. The level of fly ash replacement/substitution is moderate, based on the relative proportions of unhydrated and partly hydrated cement and residual fly ash. Portlandite (calcium hydroxide) is relatively abundant. The crystals are small to moderate in size and are uniformly distributed. The concrete is air entrained with an estimated 6% to 8% uniformly distributed, small, spherical air voids. Air voids lined with ettringite deposits are observed in the bottom 3 to 5 mm of the sample. Concrete volume is estimated at 30% to 35%, interpreted water-cementitious materials ratio is 0.50 to 0.55.

The concrete is carbonated to an average depth of 0.3 mm from the cast surfaces. The carbonated concrete has a fine-grained texture and consists of impure calcium carbonate. No significant cracks or microcracks are observed.
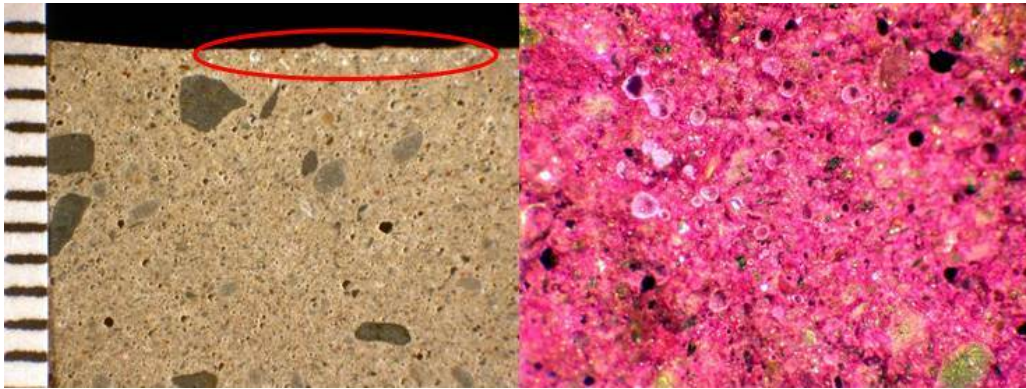
Figure 5.12. Left: Lapped surface of 7% moisture content, 6-month sample (millimeter scale). The top surface of the cast specimen is at the top of the photo. Air voids near top (circled area) are lined with ettringite deposits. Right: Fracture surface of the interior portion of 7% moisture content, 6-month sample after treatment with phenolphthalein pH indicator solution. Air-voids are lined with ettringite deposits.

A low magnification view in BSE mode is shown in the left image of Figure 5.13. This sample contains a few long microcracks that pass between the aggregate particles or between aggregate particles and air voids. Separation microcracks along the paste-aggregate contacts are also rare. A higher magnification view illustrating a typical long, branching microcrack is shown in the right image of Figure 5.13. The width of the widest microcracks is ~1 to 2 micrometers. The longer microcracks are often discontinuous. Short microcracks sometimes branch from the longer microcracks. No deposits are detected in the microcracks.
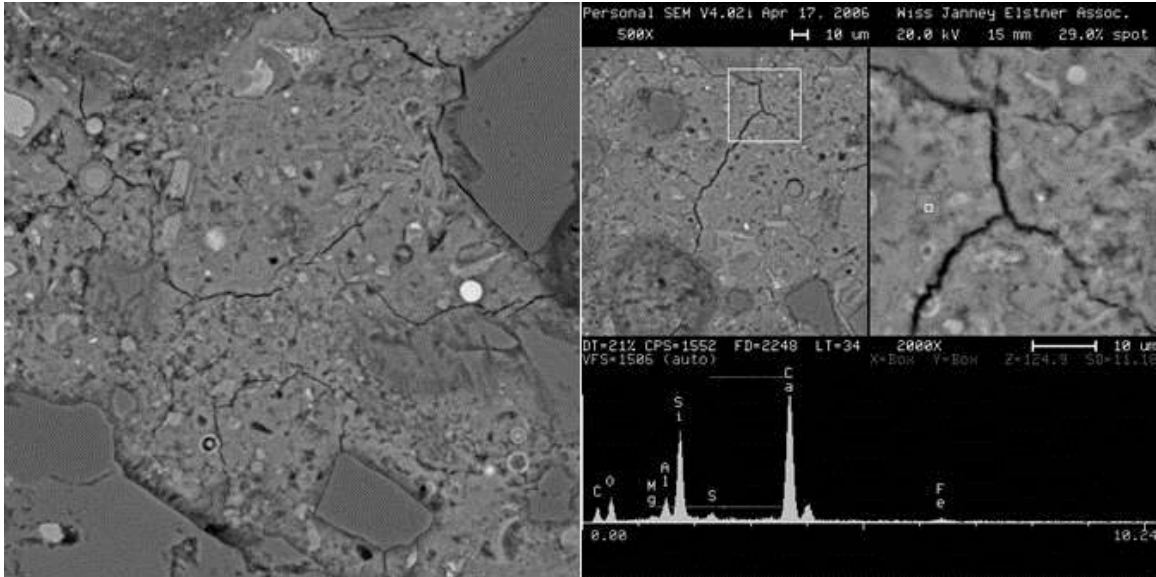
Figure 5.13. Left: BSE image of the 7% moisture content, 6-month sample (500x magnification). Microcracks are fairly rare, narrow, and are discontinuous. Separation microcracks around aggregate particles are also uncommon. Right: BSE images at 500x and 2000x showing a branching microcrack between an air void and an aggregate particle. The white box in the image on the left is enlarged in the image on the right. Scale bars are above and below the left and right images, respectively. The X-ray analysis at the bottom is for a small area of concrete near the wider microcrack. The location of the analysis is indicated by the gray box containing the small white square.

5.2.1.4   7% Moisture Content – 2-Year Sample

Images of the 7% moisture content sample aged 2 years are shown in Figure 5.14. This sample resembled the 4% moisture content sample. The monolith contains abundant cement balls, mostly less than 1 mm in diameter. The extent of the cement hydration is advanced and substantial hydration rims are observed around most of the cement grains. Portlandite (calcium hydroxide) crystals are small to moderate in size and are not uniformly distributed. Fly ash spheres are abundant. The concrete is air entrained with an estimated 5% to 7%. Ettringite is observed in a few of the air voids. Carbonation is observed only at the surface of the monolith.

A low magnification view in BSE mode is shown in the bottom left image of Figure 5.14. This sample contains abundant microcracks and adhesion cracks. Some of the cracks transect aggregate particles. A higher magnification view illustrating the microcracks is shown in the bottom right image of Figure 5.14.
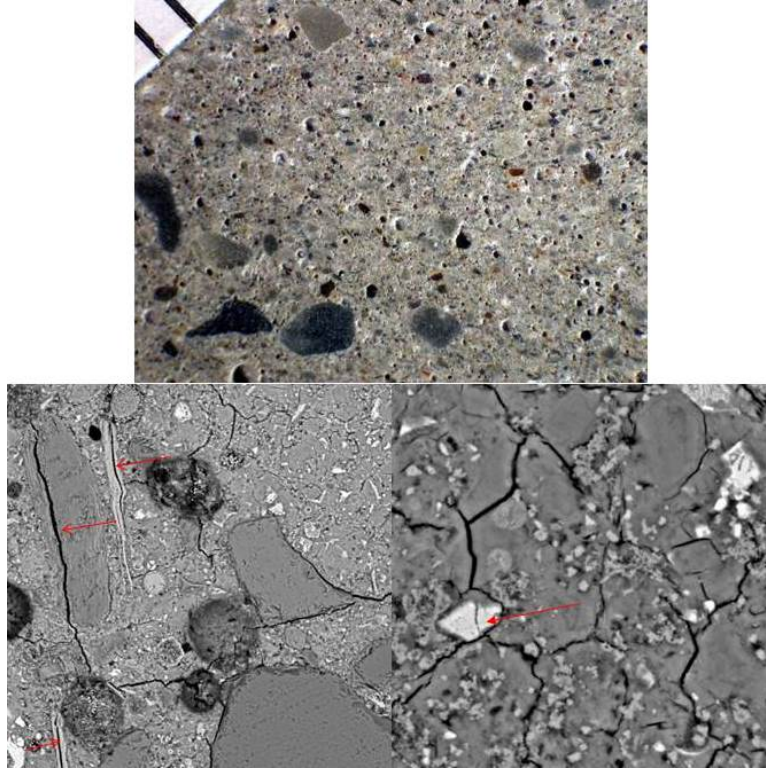
Figure 5.14. Top: Representative view of the lapped surface of the 7% moisture content, 2-year sample (millimeter scale). Bottom left: BSE image of concrete microcracks and adhesion cracks along aggregate particles in the sample. Cracks (red arrows) transect micaceous aggregate particles along cleavage planes (250x magnification). Bottom right: BSE image of concrete microcracks in the sample. The calcite cleavage fragment shown by the red arrow was derived from the aggregate and is not a product of concrete carbonation (1000x magnification).

5.2.1.5   15% Moisture Content – 6-Month Sample

Images of the 15% moisture content sample aged 6 months are shown in Figure 5.15. The concrete contains few of the cement lumps observed in the 4% and 7% 6-month samples. Amounts of unhydrated Portland cement clinker particles, abundant partly hydrated Portland cement grains, and fairly abundant residual fly ash particles are observed. The cement hydration characteristics appear normal. The level of fly ash replacement/substitution is moderate, based on the relative proportions of unhydrated and partly hydrated cement and residual fly ash. Portlandite (calcium hydroxide) is relatively abundant. The crystals are small and are uniformly distributed. The concrete is air entrained with an estimated 6% to 8% small, spherical air voids, some clustering of the voids is observed. Air voids lined with ettringite deposits are observed in the outer 1 to 2 mm of the sample. Concrete volume is estimated at 30% to 35%, interpreted water-cementitious materials ratio is 0.50 to 0.55.

The concrete is carbonated to an average depth of 0.3 mm from the cast surfaces and has a fine-grained texture and consists of impure calcium carbonate. No significant cracks or microcracks are observed.

A low magnification view in BSE mode is shown in Figure 5.16. Random discontinuous microcracks are observed and branching of the microcracks is common. The width of the widest microcracks is approximately 1 to 2 micrometers. No deposits are detected in the microcracks.
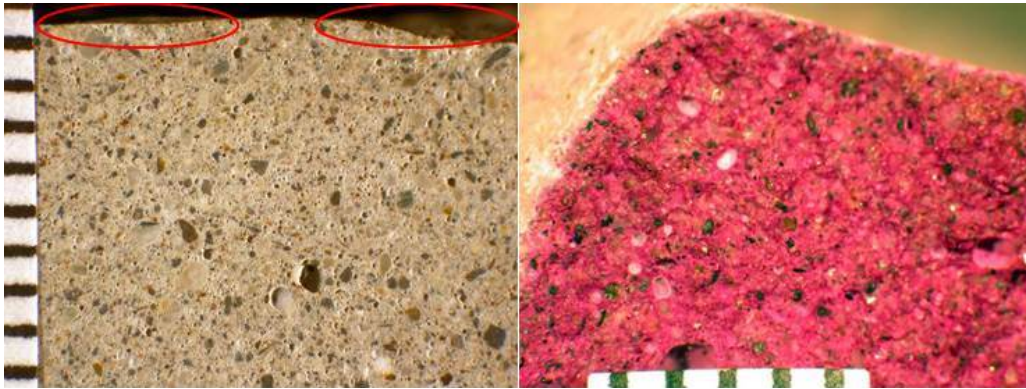
Figure 5.15. Left: Lapped surface of 15% moisture content, 6-month sample. The top surface of the cast specimen is at the top of the photo. Air voids near top (circled areas) are lined with ettringite deposits. Right: Fracture surface of the bottom portion of Sample 7 after treatment with phenolphthalein pH indicator solution. Air voids are lined with ettringite deposits. Scale is marked in millimeter increments.
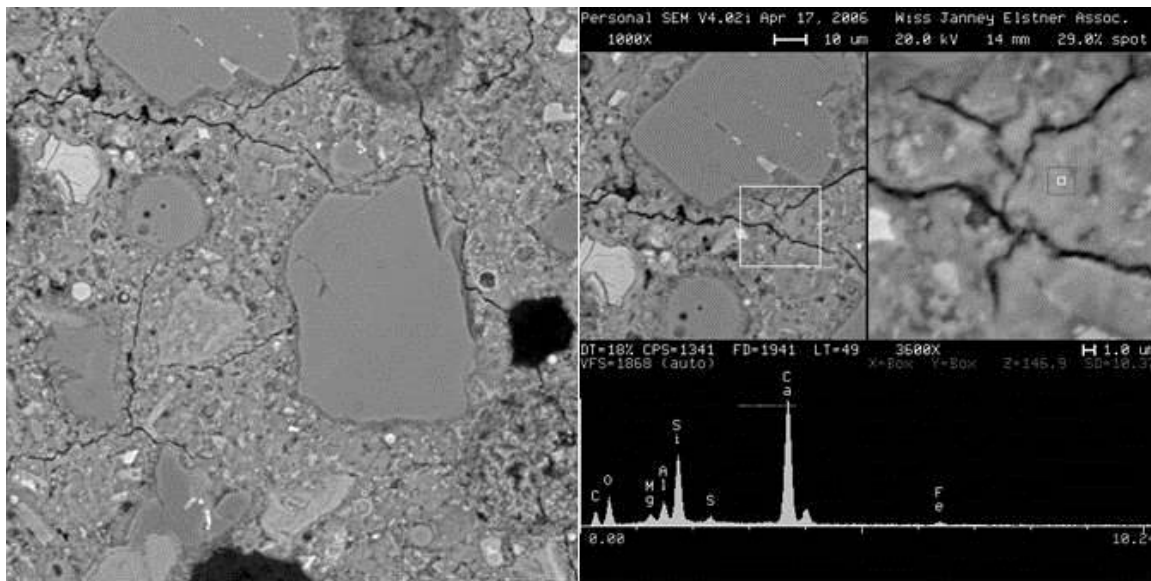
Figure 5.16. Left: BSE image of the 15% moisture content, 6-month sample (500x magnification). Random microcracks are narrow and discontinuous. Right: BSE images at 1000x and 3600x showing short microcracks branching from longer microcracks. The white box in the image on the left is enlarged in the image on the right. Scale bars are above and below the left and right images, respectively. The X-ray analysis at the bottom is for a small area of concrete near the microcracks (gray box containing the small white square).

5.2.1.6   15% Moisture Content – 2-Year Sample

Images of the 15% moisture content sample aged 2 years are shown in Figure 5.17. This sample does not contain cement balls like the 4% and 7% samples. The extent of the cement hydration is advanced and substantial hydration rims are observed around most of the cement grains. Portlandite (calcium hydroxide) crystals are small to moderate in size with non-uniform distribution, with the least abundance in this sample. Fly ash spheres are abundant. The concrete is air entrained with an estimated 6% to 8%. Ettringite is observed in most of the air voids. Carbonation is observed only at the surface of the monolith to a maximum depth of 1.5 mm. Several microcracks 4 to 8 μm wide are observed and narrower (2 μm) microcracks are common.

A low magnification view in BSE mode is shown in the bottom left image of Figure 5.17. This sample contains abundant microcracks and adhesion cracks. Some of the cracks transect aggregate particles. A higher magnification view illustrating the microcracks is shown in the bottom right image of Figure 5.17.
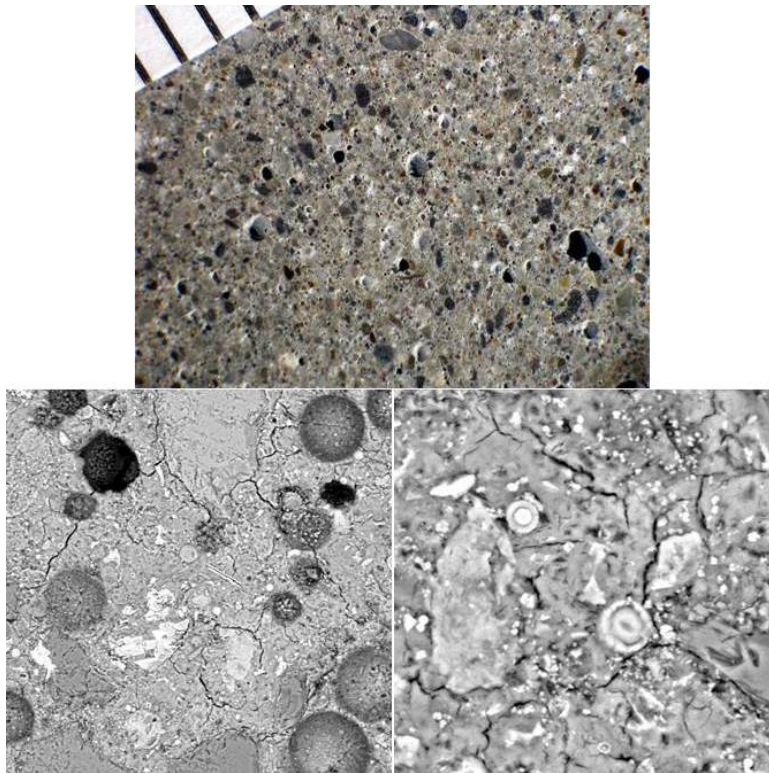
Figure 5.17. Top: Representative view of the lapped surface of the 15% moisture content, 2-year sample (millimeter scale). Middle: BSE image of concrete microcracks and adhesion cracks along aggregate particles in the sample. The large gray spherical objects are air voids (250x magnification). Right: BSE image of concrete microcracks and adhesion cracks along aggregate particles in the sample. Concentrically zoned spherical particles are reacted fly ash spheres (1000x magnification).

5.3   Carbonation of Hanford Site Structures

Core samples were obtained from above-ground, concrete structures on the Hanford Site that had been weather for approximately 14, 28, and 57 years (see Table 5.2; Mattigod et al. 2011). Transverse slices and thin sections from these concrete cores were characterized by petrographic analysis.

The data showed that the depth of carbonation increased with the increasing age of the concrete. In the oldest specimen (213J), the carbonation had extended to about 50 mm into the concrete wall. Given the limited data, the rate of carbonation of concrete at the Hanford site can be estimated at approximately 0.3 to 0.9 mm per year. The rate of carbonation would be affected by several factors such as, concrete composition, porosity, and the degree of exposure to weathering. Additionally, the observations indicated that as the concrete ages and carbonation extends to greater depths, increasing degree of microcracking may occur.

Table 5.2. Characteristics of concrete cores from Hanford Site

Characteristic	FLTF	622C	213J
Age	14	28	57
Carbonation Depth (mm)	1 – 10	2 – 8	48 – 53
Air Content (%)	4 – 5	2 – 4	1 – 2
Water/Cement Ratio	0.50 – 0.55	0.50 – 0.55	0.52 – 0.57
Secondary Deposits	Abundant ettringite lining voids	Ettringite lining voids	None in outer 50 mm – minor ettringite lining voids
Microcracks	Minor	Minor	Common in outer 50 mm
Unit Weight (pcf)	153	152	148
Steel	#4 ~103 mm cover	None	#4 ~80 mm cover
Aggregates	Well-graded siliceous gravel, 19 mm top size	Well-graded siliceous gravel, 23 mm top size	Well-graded siliceous gravel, 21 mm top size
Paste-Aggregate Bond	Moderately tight	Moderately tight	Moderately tight to moderately weak

5.4   Summary of Carbonation Observations

The studies presented here began to look at the physical and chemical effects of carbonation through investigations of two sets of lab-prepared concrete monoliths and a set of Hanford Site. The first set of monoliths was part of a half-cell diffusion study to discern correlations between carbonation and the diffusion of contaminants. Half of the monoliths were carbonated via supercritical CO_2 treatment. The remaining monoliths were left as-is, without carbonation. Table 5.3 summarizes the petrographic observations from the concrete half-cell samples. The second set of monoliths was used to determine the extent of carbonation under simulated vadose zone conditions. A summary of the petrographic observations from the concrete monoliths encased in HFS under simulated vadose zone conditions is listed in Table 5.4.

Carbonation depth was more significant (up to 8 mm depth) in the concrete half-cell samples that had been carbonated by supercritical CO_2 treatment (Table 5.3). Carbonation was only observed on the surface (<2 mm depth) for the samples that did not have the supercritical CO_2 treatment in both sets of

experiments. The largest depth of carbonation observed in the simulated vadose zone conditions was from the sample that had been kept in the 15% moisture content sediment for two years. This result indicates that carbonation under simulated vadose zone conditions is a much slower process than the supercritical CO_2 carbonation process. This is also confirmed by the observed carbonation depth of the Hanford Site concrete cores (Table 5.2) that indicate carbonation rates ranging from 0.3 to 0.9 mm per year.

Ettringite, a secondary deposit that forms as a result of hydration of Portland cement, was observed in the voids of some of the concrete monoliths and all of the Hanford Site cores. In the presence of CO_2, ettringite decomposes to other minerals including gypsum, calcium carbonate and an alumina gel. The oldest Hanford Site core (213J) confirms this effect, as no ettringite was observed within the outer 50 mm portion of the carbonation depth. Formation of ettringite and the decomposition products can expand the volume of the concrete and can cause the formation of microcracks within the concrete structure (Campbell et al. 1991). Microcracking due to CO_2 exposure can increase the depth of carbonation. Preferential pathways for contaminant mobility can also be created by microcracks within the concrete.

In this body of work, concrete samples that had been carbonated via supercritical CO_2 treatment resulted in larger diffusivity values compared to the non-carbonated samples. This observed increase in diffusivity has been attributed to the creation of preferential flow paths through the formation of microcracks caused by the carbonation process. Petrographic analysis of the two concrete monoliths carbonated by supercritical CO_2 treatment indicated at higher magnification microcracks (1 – 2 mm widths) were observed. Though, microcracks were also observed in the non-carbonated monoliths at the same magnification and there was no indication within the analysis reports whether the carbonated monoliths had more significant microcracking.

There were no petrographic analyses of monoliths carbonated by the alternate method of soaking monoliths in a super saturated carbonate prior to use in the half-cell diffusion experiments, so a comparison of carbonation depth, ettringite formation or observed microcracking cannot be completed at this time.

A better understanding of how carbonation effects can limit or enhance the rate of release of contaminants from concrete in Hanford environmental condition is still needed. Depending on the method of carbonation utilized for the half-cell diffusion experiments, an opposite effect was observed. Carbonation by supercritical CO_2 treatment resulted in an increase in diffusivity of both Tc-99 and I that has been attributed to the creation of microcracks and preferential pathways. When the super-saturated carbonate solution method was used to carbonate, a decrease in diffusivity was observed. It is unclear at this time, if the decrease is a carbonation effect or possibly the result of contaminant leaching via carbonate solution. Analysis of the carbonate solution for Tc-99 or I concentrations is needed to determine contaminant leaching. Petrographic analysis of the monoliths carbonated by super-saturated solution would be necessary to examine the effects of this method of carbonation on the monoliths.

As observed in the concrete cores obtained from the Hanford Site, the depth of carbonation increases over time. Investigations on the effect carbonation depth has on contaminant mobility are still needed to understand the effect of carbonation over time. Another avenue of research includes discerning any impact from the formation of ettringite and the decomposition products and the potential to retain contaminants within the concrete.

Table 5.3. Summary of petrographic observations for concrete half-cells

Sample	Fe	Carbonation	Carbonation	Aggregates	Monolith	Secondary Deposits	Estimated Air Content
CS-II-4%	No	No	2 mm at top of sample; incipient on remaining cast surfaces	Manufactured sand	Light beige gray. Moderately hard. Portland cement and fly ash	Ettringite in voids in outer 1 mm	6% to 8% small spherical, clustered voids
CS-IV-4%	Yes	No	1 to 2 mm on top surface; incipient on remaining cast surfaces	Manufactured sand and 25% to 35% metallic fragments	Medium beige gray. Moderately hard. Portland cement and fly ash	None observed	5% to 7% small spherical, clustered voids
CS-I-7%	No	Yes	Uneven, 5 to 8 mm from outside surfaces	Manufactured sand	Medium beige gray. Moderately hard. Portland cement and fly ash	Abundant deposits of ettringite in voids in interior portion of sample	7% to 9% small spherical, clustered and coalesced air voids
CS-III-7%	Yes	Yes	Uneven, 2 to 4 mm from outer surfaces. Patchy in body	Manufactured sand and 30% to 40% metallic fragments	Mottled medium and dark beige gray. Moderately hard. Portland cement and fly ash	None observed	6% to 8% small spherical

Table 5.4. Summary of petrographic observations from concrete monoliths encased under simulated vadose zone conditions

Sample	Carbonation	Aggregates	Monolith	Secondary Deposits	Estimated Air Content
4% moisture content - 6 month	Incipient on cast surfaces only	Natural siliceous sand	Medium beige gray. Moderately hard. Portland cement (lumps) and fly ash	None observed	5% to 7% small spherical to oval, non-uniformly distributed voids. Frequent clusters
4% moisture content - 2 year	On cast surfaces only	Natural siliceous sand	Medium beige gray. Portland cement (lumps) and fly ash	None observed	5% to 7% small, spherical air voids with diameters of less than 1 mm
7% moisture content - 6 month	Incipient on cast surfaces only	Natural siliceous sand	Medium beige gray. Moderately hard. Portland cement (lumps) and fly ash	Ettringite in voids in bottom 3 to 5 mm	6% to 8% small spherical, generally uniformly distributed voids
7% moisture content - 2 year	On cast surfaces only	Natural siliceous sand, one larger (7 mm diameter) observed	Medium beige gray. Portland cement (lumps) and fly ash	Ettringite in voids	5% to 7% small, spherical air voids with diameters of less than 1 mm
15% moisture content - 6 month	Incipient on cast surfaces only	Natural siliceous sand	Medium beige gray. Moderately hard. Portland cement and fly ash	Ettringite in voids in bottom 1 to 2 mm	6% to 8% small spherical, clustered voids.
15% moisture content - 2 year	On cast surfaces only, to a maximum depth of 1.5 mm	Natural siliceous sand	Medium beige gray. Portland cement and fly ash	Ettringite in voids	6% to 8% small, spherical air voids with diameters of less than 1 mm

6.0   Predicting Contaminant Diffusion

To model the diffusion of I and Tc-99 from a reservoir through a concrete enclosure (6 inches thick) into the surrounding sediment, pairs of high- and low-diffusivity values were selected and are listed in Table 6.1.

Table 6.1. Diffusivity values for concrete and sediment used in the simulations

Diffusing Component	Material	Low Diffusivity, cm^2/s	High Diffusivity, cm^2/s
I	Concrete	1.30×10^{-10}	2.30×10^{-9}
	Sediment	1.70×10^{-9}	2.50×10^{-8}
Tc	Concrete	3.10×10^{-11}	3.60×10^{-10}
	Sediment	1.30×10^{-8}	5.80×10^{-8}

6.1   Modeling Approach

The computational fluid dynamics (CFD) code STAR-CD[1] was used for the calculations. STAR-CD is a commercial CFD code that solves the finite volume formulations for conservation of mass, momentum, and energy for general-purpose thermal-fluids simulations. STAR-CD was used to simulate the I and Tc-99 species diffusion through the concrete encasement box and into the sediment using the analogy of thermal conduction,

$$\frac{dT}{dt} = \frac{k}{\rho C_p}\frac{d^2T}{dx^2}$$

(6.1)

and mass diffusion:

$$\frac{dC}{dt} = D\frac{d^2C}{dx^2}$$

(6.2)

In the heat conduction equation (6.1), T is the absolute temperature in kelvin, ρ is the density, and C_p is the specific heat of the material. In the mass diffusion equation (6.2), C is the specie concentration and D is the specie diffusivity. In STAR-CD, specie diffusion through the porous concrete and sediment can be simulated by setting the coefficients of (6.1) and (6.2) as equal and solving the thermal conduction problem through the two materials.

The following assumptions were made for performing the simulations:

- Constant specie concentration reservoir exists adjacent to inside wall of concrete encasement box.

- One-dimensional (1-D) diffusion through encasement box wall and into the surrounding sediment.

- No additional resistance between concrete and sediment to decrease the specie diffusion.

---

[1] STAR-CD, *Version 4.14 Methodology* 2010: Computational Dynamics Ltd.

A 1-D finite volume model was constructed to represent the species transport through the concrete encasement wall and into the sediment. A 1-D rectangular mesh was used for transport through the encasement wall. As the species exit the concrete and enter the surrounding sediment, the environment is more cylindrical in nature as the species are free to diffuse radially into the sediment. Thus, the mesh for the concrete wall was mated to a cylindrical mesh extending out into the surrounding sediment as shown schematically in Figure 6.1. The model domain is shown outlined with a dashed line in the figure. In the model, the concrete wall is assumed to be in contact with a constant specie reservoir (at location 1 in the figure). The contact between concrete and sediment (at location 2 in the figure) is assumed to be perfect with no additional resistance there for specie diffusion. The outer radius of the model was established far away from the reservoir such that specie concentration remained zero for the times examined (1000, 3000, 10,000, and 30,000 years). Simulations were performed for diffusion of I and Tc-99 under low-diffusivity and high-diffusivity conditions (Table 6.1).
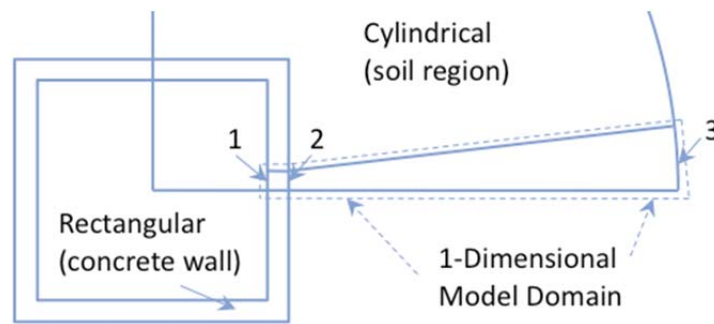
Figure 6.1. Plan-view schematic of the model domain (dashed outline) where the rectangular concrete encasement wall is in contact with the surrounding sediment region into which the species diffuse radially. (1) Concrete wall in contact with specie reservoir. (2) Concrete in contact with sediment. (3) Outer radius is established far enough away from the reservoir that species concentration is zero at long times (i.e., 3×10^4 years).

6.2 Results

The results of the simulations are provided in Table 6.2 and Table 6.3 and the diffusion profiles are shown in Figure 6.2 through Figure 6.5.

The normalized concentrations (C/C_0) at the concrete (6 inches thick) sediment interface as a function of time are listed in Table 6.2. The data indicate that under low-diffusivity conditions, the C/C_0 for both I and Tc-99 at all simulated times are very low (0 to 0.07). Under high-diffusivity conditions, the C/C_0 values for Tc-99 ranged from 0 to 0.03, whereas, I had C/C_0 values ranging from 0.05 to 0.22, indicating deeper penetration into concrete.

Table 6.2. Normalized concentration values for I and Tc-99 at the concrete-sediment interface

	Time (Y)			
	1000	3000	10,000	30,000
Diffusivity	C/C_0			
I Low	0.00	0.00	0.02	0.07
I High	0.05	0.10	0.17	0.22
Tc-99 Low	0.00	0.00	0.00	0.00
Tc-99 High	0.00	0.01	0.02	0.03

The depths of penetration, defined as C/C_0 of ~0.005 for various simulated time periods, are listed in Table 6.3. Under low diffusivity conditions, I at the end of 30,000 years is predicted to penetrate about 27 inches into sediment (Table 6.3 and Figure 6.2), whereas Tc-99 appears to be confined within the encasing of 6-inch-thick concrete (Table 6.3 and Figure 6.4). Under higher diffusivity conditions, the simulations indicated higher depths of penetration of I and Tc-99 into sediment. For instance, I is predicted to penetrate from ~ 15 to 160 inches into the sediment for the time period ranging from 1 to 30,000 years (Table 6.3 and Figure 6.3). Tc-99 under high diffusivity conditions is predicted to penetrate ~44 to 113 inches into the sediment at the end of 10,000 and 30,000 years, respectively (Table 6.3 and Figure 6.5).

Table 6.3. Depth of penetration I and Tc-99 into sediment as a function of time

	Time (yr)			
	1000	3000	10,000	30,000
	Depth of Sediment Penetration (inches) at $C/C_0 =$ ~0.005			
Diffusivity				
I Low	0	0	7	27
I High	15	39	85	157
Tc-99 Low	0	0	0	0
Tc-99 High	0	0	44	113
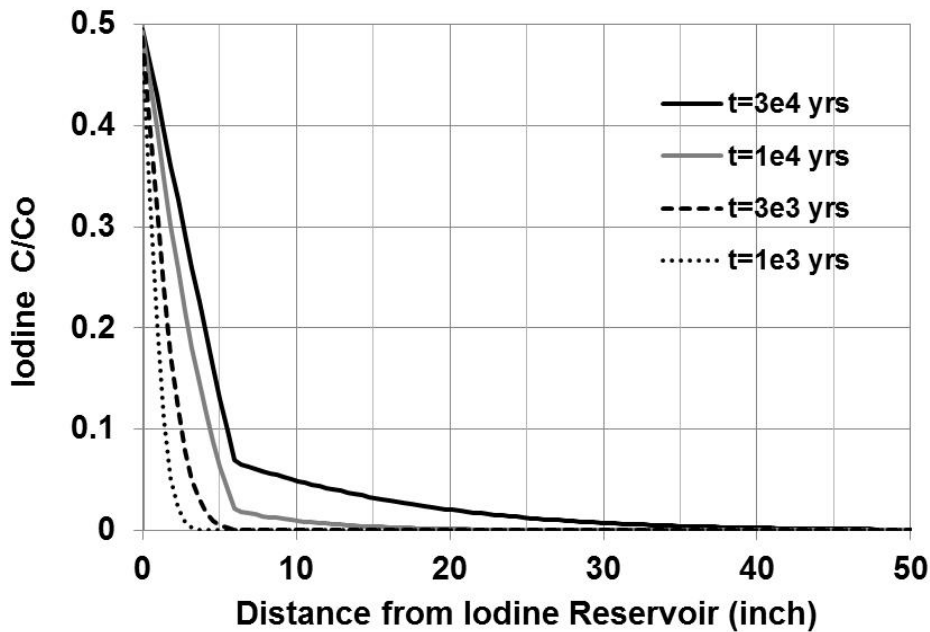
Figure 6.2. Iodine concentration profiles for the low diffusivity case. Zero to six inches represents concentrations within the concrete encasement wall. Six inches and beyond are concentrations in the surrounding sediment. $C/C_0 = 0.005$ was about 27 inches into the sediment at $t = 3 \times 10^4$ years.
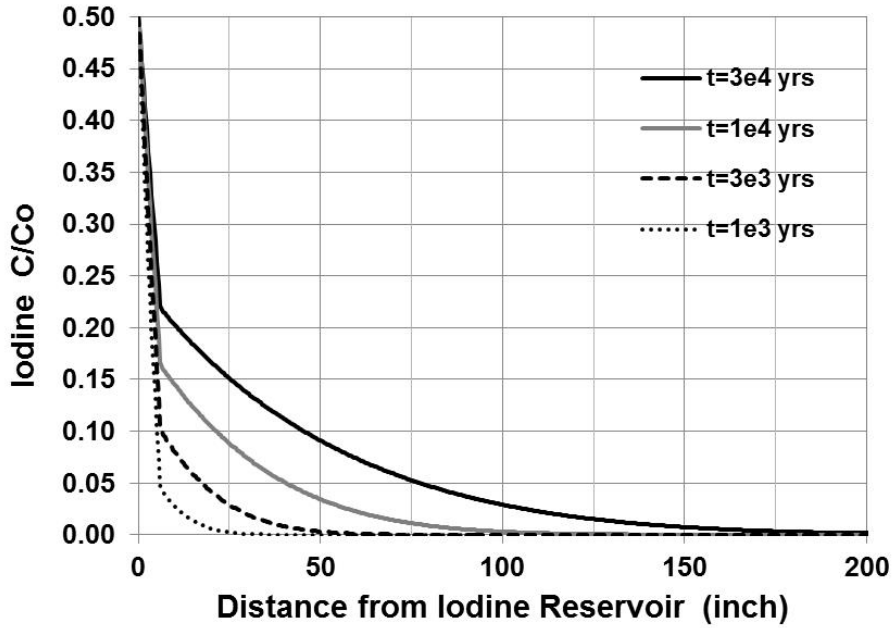
Figure 6.3. Iodine concentration profiles for the high diffusivity case. Zero to six inches represents concentrations within the concrete encasement wall. Six inches and beyond are concentrations in the surrounding sediment. $C/C_0 = 0.005$ was about 157 inches into the sediment depth at $t = 3 \times 10^4$ years.
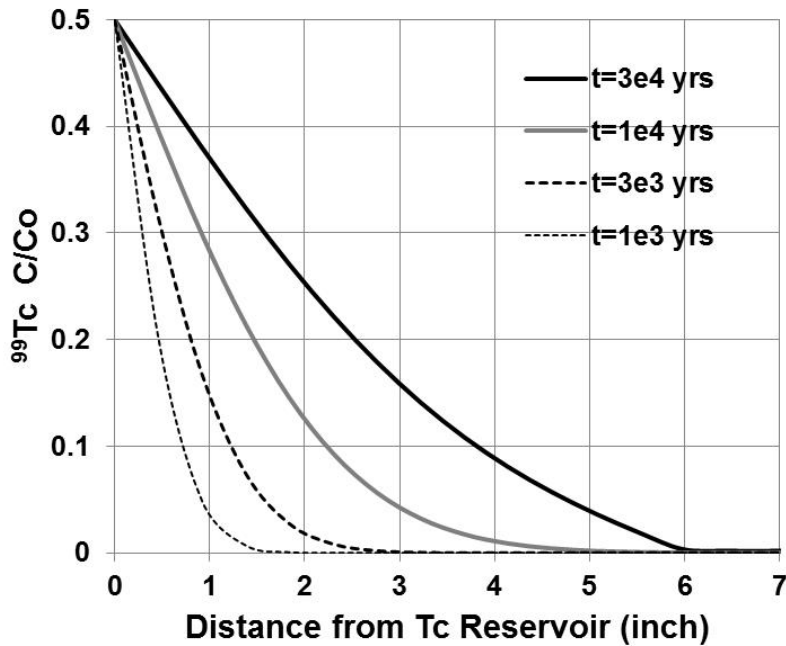
Figure 6.4. Technetium concentration profiles for the low diffusivity case. Zero to six inches represents concentrations within the concrete encasement wall. Six inches and beyond are concentrations in the surrounding sediment. $C/C_0 = 0.005$ was about to the outer edge of the concrete encasement (6 inches total penetration depth) at $t = 3 \times 10^4$ years.

6.4
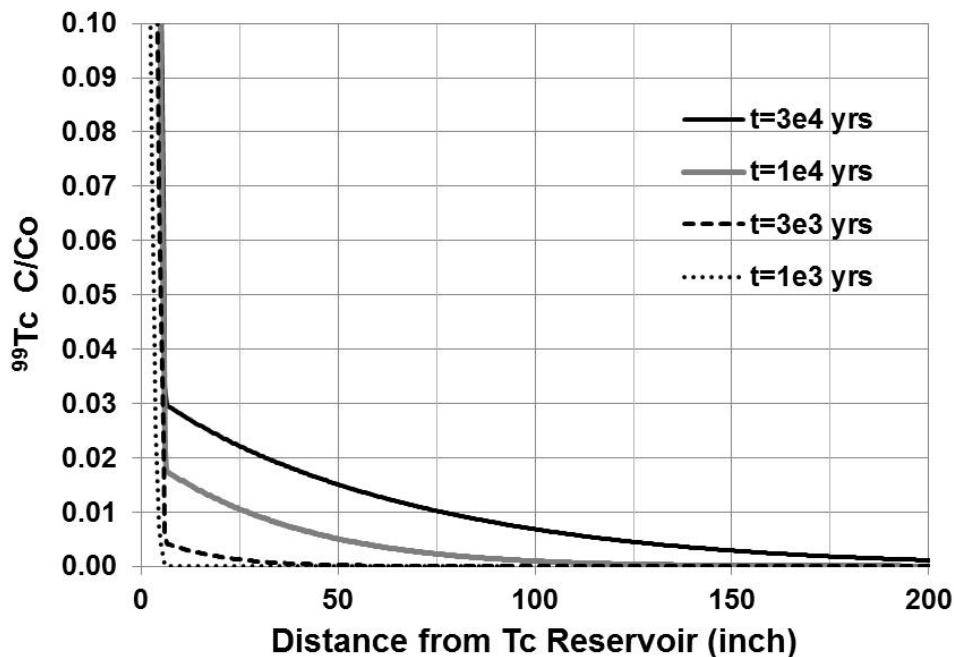
Figure 6.5. Technetium concentration profiles for the high diffusivity case. Zero to six inches represents concentrations within the concrete encasement wall. Six inches and beyond are concentrations in the surrounding sediment. $C/C_0 = 0.005$ was about 113 inches into the sediment at $t = 3 \times 10^4$ years.

The experimental data presented in section 4.0 indicate that low diffusivity for I and Tc-99 is engendered when encasing concrete is surrounded by sediment with very low moisture contents. Comparatively, higher diffusivities of I and Tc-99 are typically observed when higher moisture content sediment is in contact with encasing concrete. Based on these results, it is anticipated that the diffusion of Tc-99 and I bearing waste forms disposed at Hanford under planned unsaturated and atmospheric (carbonated) conditions will provide a significant delay in radionuclide release into the subsurface.

7.0   Uranium Experiments

Unlike the diffusion trends observed for I and Tc, U exhibited no measurable rate of diffusion. As such, the results of U leaching and diffusion are presented in the following section with results of additional investigations conducted to understand the potential mechanisms resulting in the observed differences.

7.1   Diffusion and Leaching

Uranium diffusion was investigated as part of the sediment-sediment half-cell experiments initiated in 1999. Half-cell diffusion experiments are described in section 2.4. Characteristics of the sediment-sediment half-cells are described in Table 4.1. Trench 8 sediment was spiked with U (5.6×10^{-7} mg/g sediment) and tests were run for 64 and 170 days. As shown in Figure 7.1, measureable concentration gradient profiles were not obtained from the sediment-sediment half-cell experiment for either the 4% or 7% moisture content under either test duration (64 or 170 days).
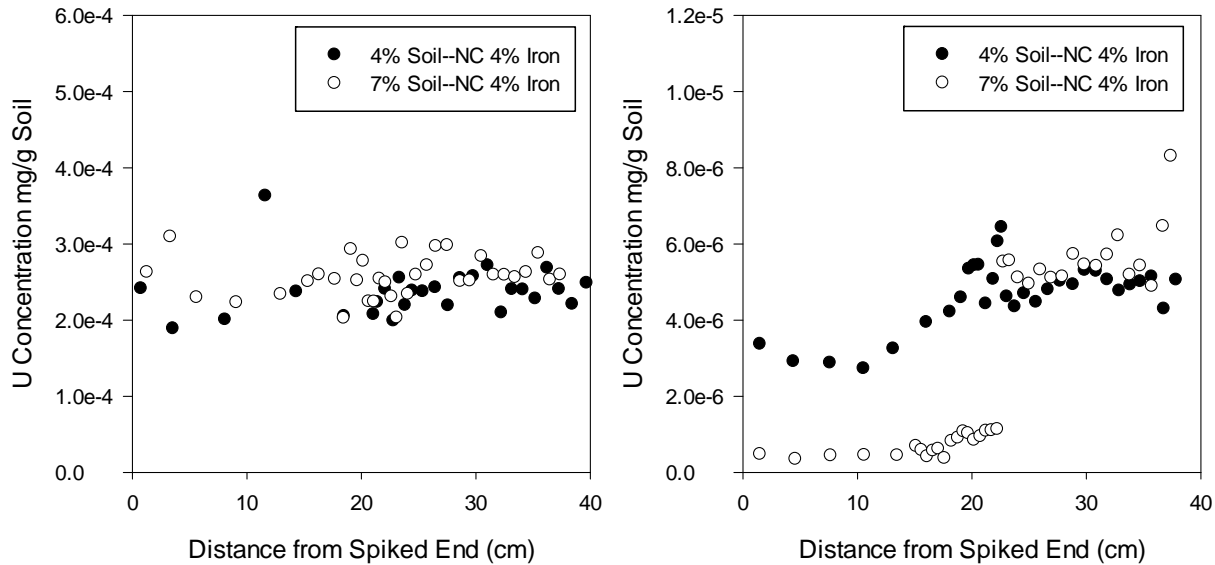
Figure 7.1. Uranium concentration profiles for 64-day (left) and 170-day (right) sediment-sediment half-cell experiments

Dynamic and static leach tests, described in section 2.5, also investigated leaching of U from the concrete specimens. Results obtained from both the static and the dynamic leach tests demonstrated that negligible U leached from the concrete monoliths (Figure 7.2). In fact, the concrete specimens retained U from the Hanford Site groundwater used in these experiments. Even though the total mass of U in each specimen exceeded the mass of U in contacting groundwater by more than two orders of magnitude, no U leaching was observed from any of the specimens. These data indicated that the spiked U in the specimens was in a nonleachable, recalcitrant solid form, and that the cement matrix had a strong affinity to immobilize additional U from solution. Such U retention from groundwater by cement specimens has been observed previously by Serne et al. (1989). Overall, the cement specimens in the static tests on average retained 50% more U than specimens in the dynamic tests. The higher immobilization observed in the static tests can be explained on the basis of continual long contact of leach solutions (with fractional

solution exchange) with the specimens. Comparatively, in the dynamic leach tests, the leach solutions are renewed frequently; therefore, the specimens are in contact with leach solution for shorter periods. The leach test pH also would likely affect the amount of U retained. Uranium immobilization increases with pH and in static leach tests, the pH conditions are higher than in dynamic tests.
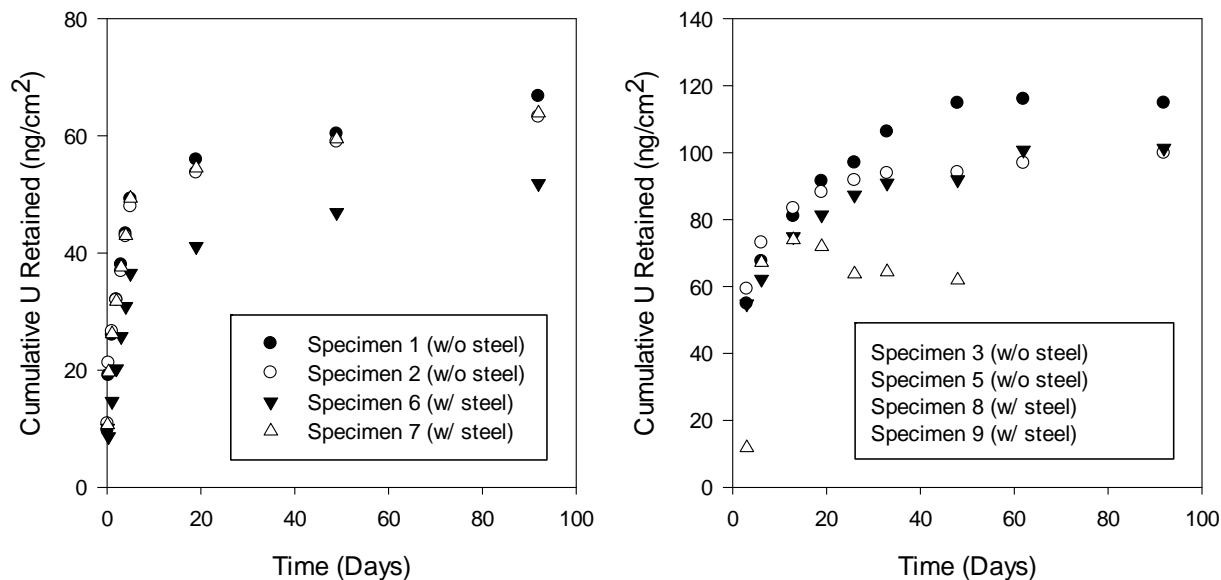
Figure 7.2. Cumulative U retained as a function of time. Left: dynamic leach test. Right: static leach test.

7.2   Materials and Methods for Uranium Phases and Solubility

In an effort to explain the results obtained from the diffusion and leach tests and quantify the long-term stability of U in concrete waste forms, solubility studies were conducted on select U mineral phases.

7.2.1   Uranium-Spiked Portland Concrete

A series of 200 mL batches were prepared of the nominal laboratory-scale composition (Table 2.2), with varying steel and aqueous U compositions (Table 7.1). Uranium-spiked samples were prepared by dissolving the U within the water fraction of the concrete composition to promote homogeneous distribution of U within the concrete waste package. The U concentrations were chosen such that the 10^{-3} M uranium-spike yielded an overall concentration of 30 ppm, which is under-saturated with respect to U and within the concentration range in which sorption is believe to be the controlling mechanism for U retention. The 0.1 M uranium-spike gives an overall concentration over-saturated with respect to U solid phases of 3000 ppm. The concrete was hand mixed in a stainless steel bowl with a stainless steel whisk for approximately 10 minutes, divided into three equal sub-samples, loaded into zip-lock bags, pressed into flat sheets, and sealed. The samples were allowed to set for predetermined time intervals of 2 weeks to 3 months prior to analysis.

Table 7.1. Concrete compositions for U mineral phases

Normalized Laboratory Design	Comp. #1	Comp. #2	Comp. #3	Comp. #4	Comp. #5	Comp. #6	Comp. #7
0.27	Cement	Cement	Cement	Cement	Cement	Cement	Cement
0.04	Fly Ash	Fly Ash	Fly Ash	Fly Ash	Fly Ash	Fly Ash	Fly Ash
0.04	Coarse Aggregate	Coarse Aggregate	Coarse Aggregate	Coarse Aggregate	Coarse Aggregate	Coarse Aggregate	Coarse Aggregate
0.51	Fine Aggregate	Fine Aggregate	Fine Aggregate	Fine Aggregate	Fine Aggregate	Fine Aggregate	Fine Aggregate
0.10	Water	10^{-3} M^a U (aq)	10^{-3} M^a U (aq)	10^{-3} M^a U (aq)	0.1 M^b U (aq)	0.1 M^b U (aq)	0.1 M^b U (aq)
0.04	Steel Fiber	--	Steel Fiber	Iron Filings	--	Steel Fiber	Iron Filings

(a) 10^{-3} M spike = 30 ppm final concentration
(b) 0.1 M spike = 3000 ppm final concentration

7.2.2   Synthesis of U(VI) Phases

All solutions were prepared with reagent-grade chemicals and 18 MΩ deionized water.

7.2.2.1   Becquerelite Precipitation

Direct precipitation of becquerelite was accomplished using the methods of Burns et al. (personal communication with Peter Burns at the University of Notre Dame). Uranyl acetate (0.313 g) [$UO_2(CH_3COO)_2 \cdot 2H_2O$] was combined with 0.05 g calcium carbonate ($CaCO_3$) in 4 mL of deionized water. The solution was placed in a Parr bomb and heated at 160°C for 50 hours. The light-mustard-colored precipitate was recovered from solution through centrifugation. The crystals were washed with four aliquots of boiling deionized water. The crystals were dried at room temperature until a constant weight was achieved.

7.2.2.2   Soddyite Precipitation

Direct precipitation of soddyite was conducted based on modified procedures presented by Casas et al. (1997) and Nguyen et al. (1992). Deionized water (50 mL) was boiled for 30 minutes while sparging with nitrogen to remove all CO_2. A 0.15-M uranyl nitrate, $UO_2(NO_3)_2 \cdot 6H_2O$ (Alfa Aesar) solution was prepared by adding 3.138 g uranyl nitrate to 40 mL of de-air water, which was boiled and sparged with nitrogen. Sodium metasilicate (1.77 g), $NaSiO_3 \cdot 9H_2O$ (Alfa Aesar), was added to 10 mL of de-aired water, which was boiled and sparged with nitrogen, to prepare a 0.30 M solution. The sodium metasilicate solution was added drop-wise, with stirring, to the 0.15 M uranyl nitrate solution under anaerobic conditions. Concentrated ammonium hydroxide solution was added drop-wise stirring until the pH was within a range of 4.5 to 5.0. The solution was allowed to stir under anaerobic conditions for 100 hours. The crystals were washed with boiling deionized water. The solid phase was placed into a Parr reactor with 75 mL of boiling deionized water. The reactor was sealed and heated for 14 days at

130°C. The resulting crystals were washed with boiling deionized water, recovered from solution through centrifugation, and dried at room temperature until a constant weight was achieved.

7.2.2.3   Uranophane Precipitation

Direct precipitation of uranophane was accomplished using the methods of Burns et al. (personal communication with Peter Burns at the University of Notre Dame). Uranyl acetate (0.42 g) [$UO_2(CH_3COO)_2 \bullet 2H_2O$] was combined with 0.23 g of sodium metasilicate [$NaSiO_3 \bullet 9H_2O$] and 0.28 g of calcium acetate [$Ca(CH_2OOH)_2 \bullet H_2O$] in 5 mL of deionized water. The pH of the solution was adjusted to 5.5 using glacial acetic acid [CH_3COOH]. The solution was placed in a Parr bomb and heated at 100°C for 24 hours. The pale yellow precipitate was recovered from solution through centrifugation. The crystals were washed with four aliquots of boiling deionized water. The crystals were dried at room temperature until a constant weight was achieved.

7.2.2.4   Acquisition of Natural Autunite

Natural calcium meta-autunite I, $Ca[(UO_2)(PO_4)]_2 \cdot 3H_2O$, was obtained from northeastern Washington State. The material was previously characterized using ICP-OES and ICP-MS analyses, XRD, and SEM to confirm the composition, structure, and morphology of the autunite minerals as 98% to 99% pure autunite with calculated anhydrous structural formula consistent with Ca-autunite: $Ca[(UO_2)(PO_4)]_2$. Electron microprobe analyses further indicated that the autunite mineral contains ~3 waters of hydration per formula unit (p.f.u.) (Wellman et al. 2007a, 2006a).

7.2.3   Characterization of U(VI) Phases

7.2.3.1   XRD of U(VI) Phases

X-ray diffraction is a commonly used technique for identifying crystalline minerals that are ≥ 5% (by weight) of the bulk composition. Before mounting the samples, a representative sample of the bulk material was ground using an agate mortar and pestle to improve the diffraction patterns. X-ray diffraction data were obtained at 45 kV and 40 mA, using a Scintag® automated powder diffractometer (Model 3520). Tungsten-filtered copper radiation, CuK_α = 1.54 Å, was used to obtain diffraction patterns. The samples were analyzed over the 2-theta (2θ) range from 2° to 45°, using a step size of 0.04°, and a 2-second count time at each step.

7.2.3.2   SEM-EDS of U(VI) Phases

Photomicrographs of pristine and post-reaction solid phases were obtained by means of a JEOL 840 scanning electron microscope equipped with a Robinson 6.0 backscatter detector. The beam conditions were 20 KeV acceleration and a 1 nA beam current. The samples were mounted on an aluminum plate using double-sided tape and carbon-coated under a vacuum. The carbon coat provides a conductive path for the electrons and helps secure the particles. Images were acquired using GATAN DM software version 3.2, 1996.

An Oxford ISIS 300 series energy dispersive spectrometer was used to determine chemical composition. EDS spectra were stored electronically using Oxford ISIS 300 version 3.2 software. An

EDS spectrum represents the chemical composition of a particle found within a sample; while not all particles are counted for the same live/dead time period, a typical EDS spectrum is counted for 100 s with a 30% dead time.

7.2.4   Solubility Testing of U(VI) Minerals

Uranium will readily react with CO_2 to form stable uranyl-carbonate complexes. However, to quantify the solubility of U minerals under environmentally relevant conditions, and those representative of long-term storage conditions, all solubility experiments were done under ambient conditions. The solubility of soddyite, becquerelite, and uranophane was measured in simulated concrete porewater. Ewart et al. (1992) measured the elemental compositions of porewaters equilibrated with a series of Portland cement compositions: sulfate-resistant Portland cement (SRPC)/limestone (L), ordinary Portland cement (OPC)/blast furnace slag (BFS)/L, BFS/OPC, OPC/L, and Harwell. Based on these data, a series of synthetic cement leachates were prepared with 18 MΩ deionized water and reagent-grade chemicals from Aldrich Chemicals, namely calcium chloride [$CaCl_2 \cdot 2H_2O$], magnesium chloride [$MgCl_2 \cdot 6H_2O$], calcium sulfate [$CaSO_4$], sodium hydroxide [NaOH], calcium carbonate [$CaCO_3$], calcium hydroxide [$Ca(OH)_2$], silicic acid [$SiO_2 \bullet 2H_2O$], and aluminum nitrate [$Al(NO_3)_3 \cdot 9H_2O$] (Table 7.2).

Table 7.2. Chemical composition of Portland cement-equilibrated waters (from Ewart et al. 1992)

| Cement | Concentration, M | | | | | | | | |
	Ca	Na	Mg	Cl	SO_4^{2-}	CO_3^{2-}	Al	Si	pH
SRPC/L	6.7×10^{-3}	2.0×10^{-4}	$<8.0 \times 10^{-8}$	4.0×10^{-5}	4.0×10^{-5}	8.5×10^{-5}	7.4×10^{-4}	5.3×10^{-6}	12.5
9:1 BFS/OPC	6.8×10^{-3}	3.4×10^{-3}	4.7×10^{-7}	6.2×10^{-5}			1.0×10^{-4}	8.0×10^{-5}	2.3×10^{-5}	12.2
OPC/BFS/L	6.7×10^{-3}	5.0×10^{-3}	$<8.0 \times 10^{-7}$	2.4×10^{-3}	6.0×10^{-3}	2.8×10^{-4}	9.5×10^{-5}	7.0×10^{-4}	12.1
OPC/L	2.0×10^{-2}	8.3×10^{-4}	$<4.0 \times 10^{-8}$	9.0×10^{-5}	1.0×10^{-5}	2.0×10^{-5}	1.0×10^{-5}	-	12.0
HARWELL	1.0×10^{-2}	5.0×10^{-5}	5.0×10^{-6}	2.0×10^{-3}	3.0×10^{-3}	3.0×10^{-5}	-	-	12.0

The solubility of becquerelite, soddyite, uranophane, and autunite in the synthetic porewater solutions was measured over a period of 4 months. Approximately 0.25 g of the respective U phase was added to polypropylene tubes containing 20 mL of the respective porewater solution. The tubes were sealed and shaken for predetermined sample intervals of 1, 7, 14, 21, 28, 42, 56, 70, 84, 98, and 112 days. A set of duplicate tubes were started for each sampling interval to prevent volume changes that could affect saturation indices over the duration of the experiment. The suspensions were centrifuged and the supernatant was filtered through 0.45 µm filters. The filtrate was analyzed for silicon and calcium using ICP-OES and for U using ICP-MS. Selected samples of equilibrated solids were taken for XRD and SEM to compare the structures of the materials during reaction and identify the formation of secondary phases.

7.2.5   Extended X-Ray Absorption Fine Structure (EXAFS) Analysis of Uranium Phases

EXAFS analysis was conducted on pristine U phases, and the U phases reacted with simulated concrete porefluids. Uranium L_{III}- EXAFS measurements of the samples were taken at room temperature on the Molecular Environmental Sciences Beamline 11-2 (Bargar et al. 2002) at the Stanford Synchrotron Radiation Laboratory (SSRL) using a cryogenically cooled Si (220), $\phi = 0°$, double-crystal

monochromator. Fluorescence-yield data were collected using an argon-filled Stern-Heald-type detector (Lytle et al. 1984). A collimating mirror before the monochromator was used for harmonic rejection, with a cutoff of 19.6 keV. Yttrium metal foil was mounted between two ionization chambers downstream of the sample for energy calibration; the first inflection point in the yttrium K-edge was set to 17,038 eV. Background-subtracted k^3-weighted EXAFS data were analyzed using the SixPACK (Webb 2004) interface to IFEFFIT (Newville 2001).

7.3 Uranium Mineral Phases

In effort to explain the results obtained from the diffusion and leach tests and quantify the long-term stability of U in concrete waste forms, solubility studies have been conducted on proposed U mineral phases that have been predicted via geochemical modeling to be the dominant controls on U (Atkins et al. 1988; Brownsword et al. 1990; Glasser 2001; Glasser et al. 1985; Sutton 1999; Sutton et al. 1999; Zhao et al. 1999). However, limited experimental conditions (Brownsword et al. 1990) and the presence of multiple U phases have complicated experimental solubility results (Brownsword et al. 1990; Glasser et al. 1985; Zhao et al. 1999). It is important to note that because of the complex chemistry of U, there is significant debate within the literature regarding the stoichiometry and the thermodynamic values assigned to aqueous U species and secondary mineral phases. As such, the solubility calculations are based on current knowledge, but may have significant uncertainty associated with them. Determination of U phases only by prediction, rather than experimentation, hinders the accuracy of predicting the long-term fate of U in concrete waste forms (Cooper and Hodgkinson 1987). Although previous studies provide necessary information regarding the reactions of U with various cementitious materials, concrete is a continuously reacting solid whose component phases continue to change over hundreds of years, albeit very slowly (Bogue 1955; Taylor 1990). Therefore, to accurately assess the performance of concrete for radionuclide encasement, it is necessary to understand the interactions between radionuclides and the concrete matrix to identify in situ the formation of U phases.

7.3.1   Precipitates from Uranium-Spiked Porewaters

Figure 7.3 displays XRD patterns obtained from solids precipitated under ambient conditions in the uranium-spiked porewater after a 2-hour reaction period. XRD patterns display few reflections, indicating the phases were predominantly amorphous in nature, yet a number of significant features are present within the XRD patterns. All of the patterns, with the exception of BFS/OPC, display a small peak at 5.58 $^{o}2\theta$ which is a characteristic low angle peak of ettringite, $Ca_6Al_2(SO_4)_3(OH)_{12} . 26H_2O$, a calcium-aluminum-sulfate compound, commonly found in concrete. BFS/OPC lacks sulfate as a compositional element; therefore, ettringite was not suggested as a precipitated phase. Additionally, comparison of the intensity of this reflection can be directly correlated to the sulfate concentration present within the composition and decreases accordingly.
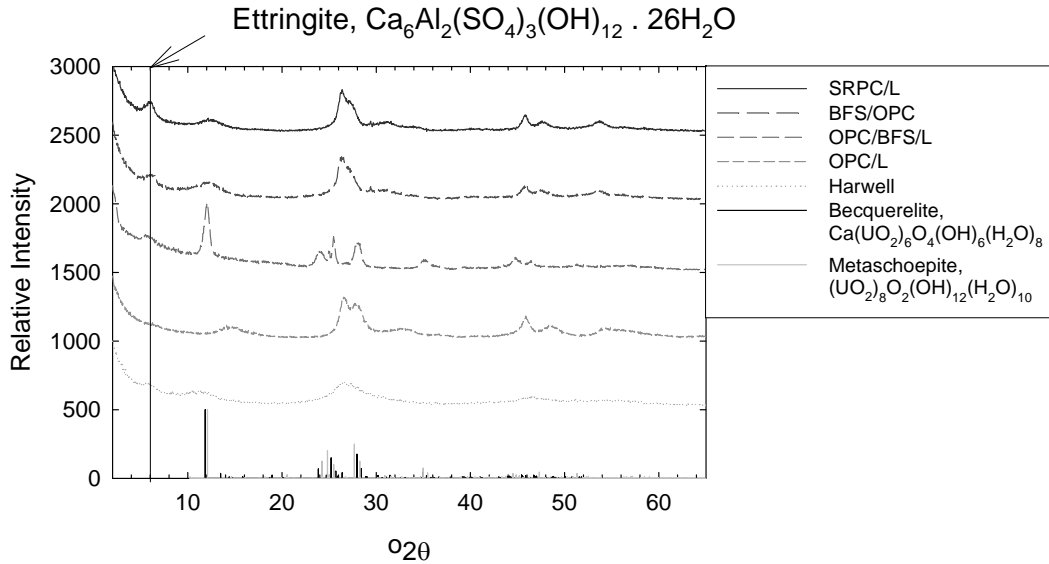
Figure 7.3. X-ray diffraction patterns from Portland Cement Leachate-U(VI) precipitates at room temperature

Uranium precipitates from all compositions, except OPC/BFS/L, display a small, amorphous, low-angle peak within the region of 11.8 to 12.1 °2θ (Figure 7.3), which is a major reflection for both becquerelite and meta-schoepite. The precipitate from OPC/BFS/L displays a sharp peak within this region. However, the lack of additional reflections, characteristic of either becquerelite or meta-schoepite, precludes a clear distinction from being made regarding the dominant phase controlling the solubility of U based solely on diffraction patterns. Additionally, all precipitates display a broad peak within the region of approximately 25 to 29 °2θ. Both becquerelite and meta-schoepite display a series of minor reflections within this regions; however, calcium and sodium diuranate dihydrate also have major reflections within this region. The significance of becquerelite and schoepite phases in concrete waste forms has been noted (Atkins et al. 1988; Glasser 2001; Glasser et al. 1985; Moroni and Glasser 1995; Sutton et al. 1999). Uranophane has been identified as a dominant U phase in corroded cement, but other possible phases were not identified even with the use of multiple techniques (Kienzler et al. 2010). Likewise, a number of investigations have previously suggested diuranate dihydrate salts as predominant phases for controlling the solubility of U under conditions relevant to concrete porewaters (Atkins et al. 1988; Moroni and Glasser 1995; Yamamura et al. 1998). Without defined reflections of the solid phase, the dominant control on the solubility of U cannot be conclusively identified through XRD alone.

After 1 year, all compositions, with the exception of BFS/OPC, exhibited a characteristic low angle reflection, 5.58 °2θ, of ettringite, $Ca_6Al_2(SO_4)_3(OH)_{12} \cdot 26H_2O$ (Figure 7.4), the intensity of which had not changed given the prolonged reaction period. All precipitates display a broad peak within the region of 11.8 to 12.1 °2θ. Both becquerelite and meta-schoepite display reflections in this region and no clear distinction between the two solid phases was possible (Figure 7.4). XRD patterns for all solids also display a large amorphous hump centered at approximately 20 °2θ, suggestive of SiO_2 (am). Also prominent in all patterns, except SRPC/L, is a sharp reflection at 29°2θ due to the presence of calcite.
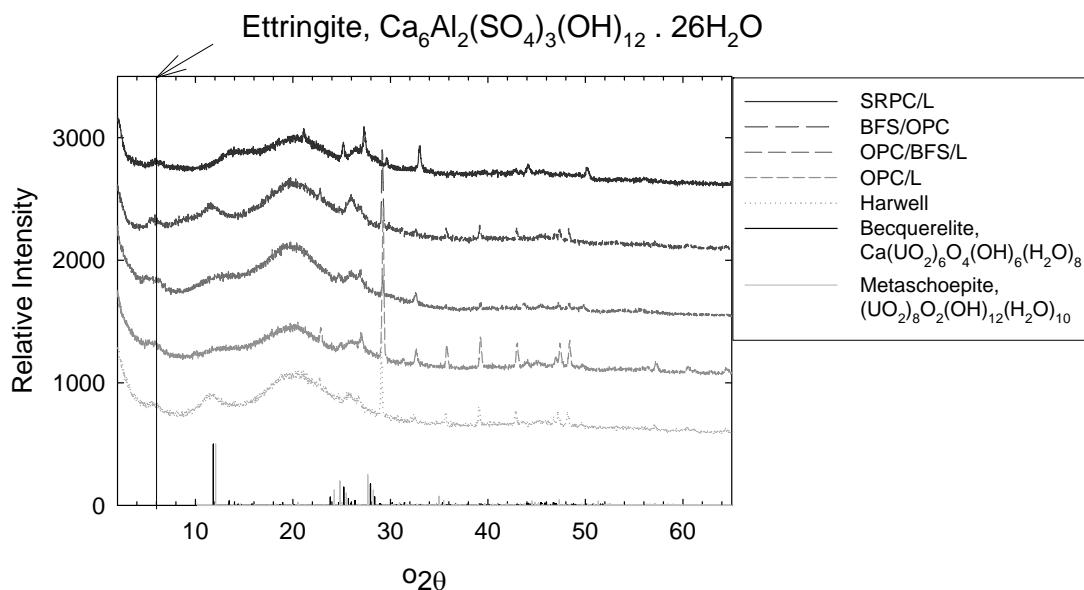
Figure 7.4. X-ray diffraction patterns from Portland Cement Leachate-U(VI) precipitates at room temperature after 1 year

XRD results presented here illustrate the significant challenges of discerning U solid phase(s) in complex matrices. The structural similarity of U solid phases, and formation of additional phases such as calcium phases typically present in concrete, complicate interpretation of powder diffraction data. This precludes conclusive identification of solid phases precipitated from concrete porewaters based solely on XRD analyses. Short-term batch tests, commonly used to elucidate the solid phases controlling the long-term retention of U within concrete, oversimplify the complexities of U chemistry, especially when coupled with constantly changing conditions of concrete porewaters. XRD results from batch tests conducted under ambient conditions for a period of 2 hours versus 1 year suggest changes in the chemical composition of the precipitate, but little change in the crystallinity of the precipitate. Although the composition of concrete is dominated by calcium hydroxide and silicate hydrates (Bogue 1955), as the concrete ages into a more complicated polymeric framework, contaminants such as U may diffuse and react, significantly altering the presumed retention mechanism based on the results from short-term investigations (Spalding 2000).

Precipitates from uranium-laden porewaters that formed at 90°C yield XRD patterns that indicate a significant increase in crystallinity and exhibit the formation of phases that did not form under ambient conditions (Table 7.3, Figure 7.5). Notably absent from the XRD patterns are the major peaks for becquerelite and/or meta-schoepite within the region of 11.8 to 12.1 °2θ, which were evident in precipitates formed under ambient conditions. Yet, a broad peak, indicative of the amorphous nature of the material, remains evident in all patterns from 25° to 30°2θ, which is within the region where multiple reflections are displayed for schoepite, becquerelite, and calcium uranium oxides. However, no clear distinction between the solid phases can be inferred based solely on XRD data. Moreover, because the concentration of U is limited, relative to the major elemental components of the concrete matrix, it is plausible that the increased precipitation of calcium phases (Table 7.3), typically present in concrete, is masking reflections from the minor inclusions of uranyl-phases. Comparison of the results presented here for short-term batch tests conducted under ambient conditions versus those conducted at 90°C illustrate that an increase in temperature increases the crystallinity of the precipitate, but may also afford changes in

the chemical composition of the precipitated phase(s). Additionally, the behavior of radionuclides such as U may be significantly different in thermally treated concrete waste forms.

Table 7.3. Mineralogical composition of 90°C precipitates determined by XRD peaking-fitting

	OPC	Harwell	BFS/OPC	SRPC	OPC/BFS
Portlandite, Ca(OH)$_2$	X	X	X		Trace
Thermonatrite, Na$_2$CO$_3$•H$_2$O	X			X	Trace
Halite, NaCl		X			
Aragonite, CaCO$_3$		X	X		Trace
Phlogotite, KMg$_3$(AlSi$_3$O$_{10}$)(OH)$_2$		X			
Calcite, CaCO$_3$			X	X	X
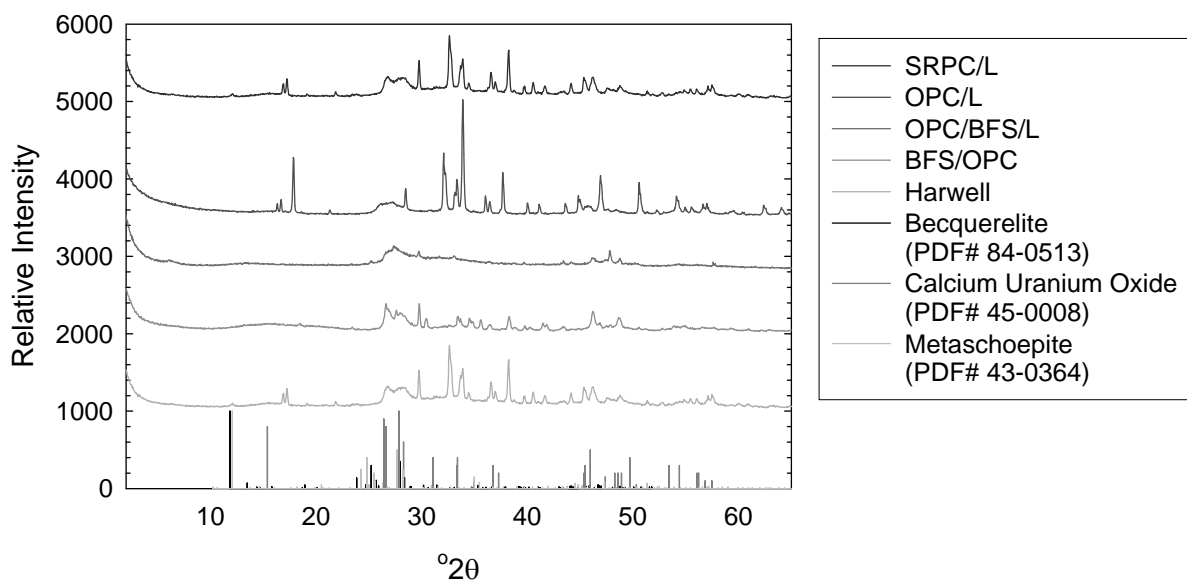
Figure 7.5. X-ray diffraction patterns from Portland Cement Leachate-U(VI) precipitates at 90°C after 2 hours

7.3.2   In Situ Characterization of Uranium Precipitates in Concrete

7.3.2.1   10^{-3} M Uranium-Spikes Concrete Samples

The left-hand image in Figure 7.6 displays SEM-EDS analyses of concrete samples containing 30 ppm U after a 2-week reaction period. The SEM image reveals a small area of concentrated U. The occurrence of these regions was minimal and the majority of the U appeared to have been equally distributed throughout the concrete matrix. EDS analysis of the concentrated regions indicated the major components to be U and oxygen (right-hand image in Figure 7.6). Sutton et al. (2003) previously noted that even under high pH conditions present in grout, where both the surface sites and uranyl hydroxide ion are anionic, sorption is observed via an inner sphere complexation between by the hydroxide bridging between the uranyl hydroxide ions and the hydroxylated grout surfaces. Additional EXAFS/XANES studies have supported the observed formation of inner sphere bidentate bound U ion to silicate surfaces

(Hudson et al. 1999; Reich et al. 1996; Sylwester et al. 2000). This is significant for two reasons: (1) inner-sphere sorption complexes, relative to other mechanisms of sorption, are the most stable sorptive complexes and least susceptible to desorption (Sposito 1989); and (2) sorption occurring via inner-sphere complexes is believed to be an important precursor step in surface precipitation of uranyl minerals (Sutton et al. 2003).
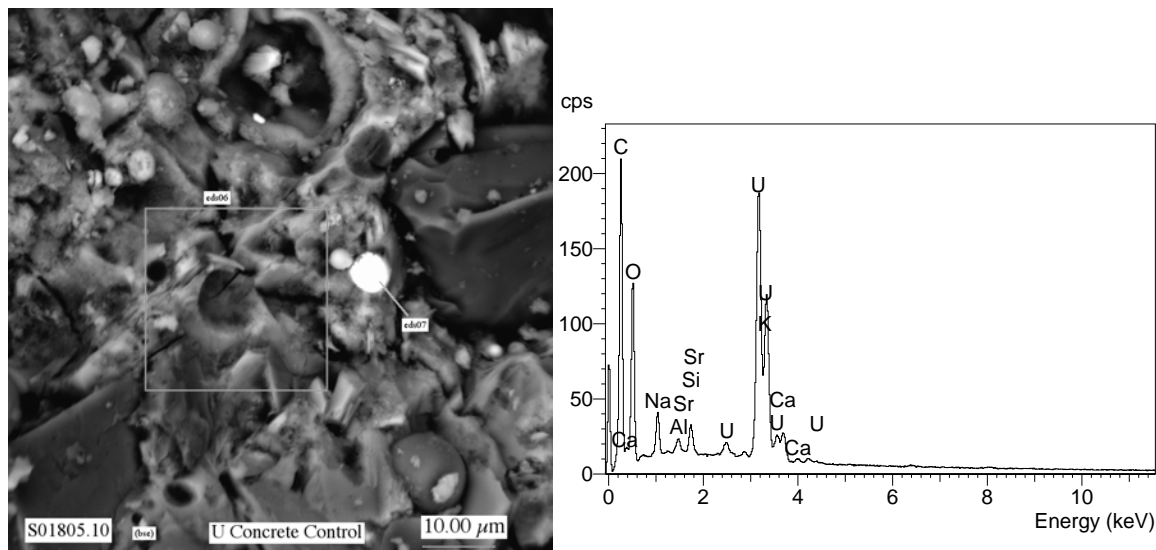
Figure 7.6. Left: SEM photomicrograph of U phase formed within OPC spiked with 10^{-3} M uranium after 2 weeks. Right: Energy dispersive spectroscopic pattern indicates the phase is a uranyl-oxyhydroxide.

Although U was initially observed to be evenly distributed throughout the concrete matrix on a microscopic scale, after a period of 1 month, SEM analyses display a cluster of uranyl phases (similar observations were previously noted by Maroni and Glasser (1995) (Figure 7.7). EDS analyses indicate a significant oxygen content and a minor silicon concentration. Based on the silica-oxygen-uranium ratio, identifying the uranyl phase solely as a uranyl-silicate phase results in an excess of U and oxygen. This indicates the phase is a mixed uranyl-oxyhydroxide-silicate phase, possibly uranophane mixed with becquerelite and/or schoepite, as suggested by XRD results of uranium-porewater precipitates. This suggests advanced uranyl mineral phases may act as a long-term control of U even at very low U concentrations. This accords with previous suggestions that the solubility of U is not primarily a function of U loading; rather, the solubility is controlled by the nature of the U precipitates (Moroni and Glasser 1995). The apparent formation of uranyl-oxyhydroxide/silicate phases after 1 month supports the hypothesis that sorption through inner-sphere mechanisms is a precursor for precipitation of U mineral phases (Sutton et al. 2003; Sylwester et al. 1999).
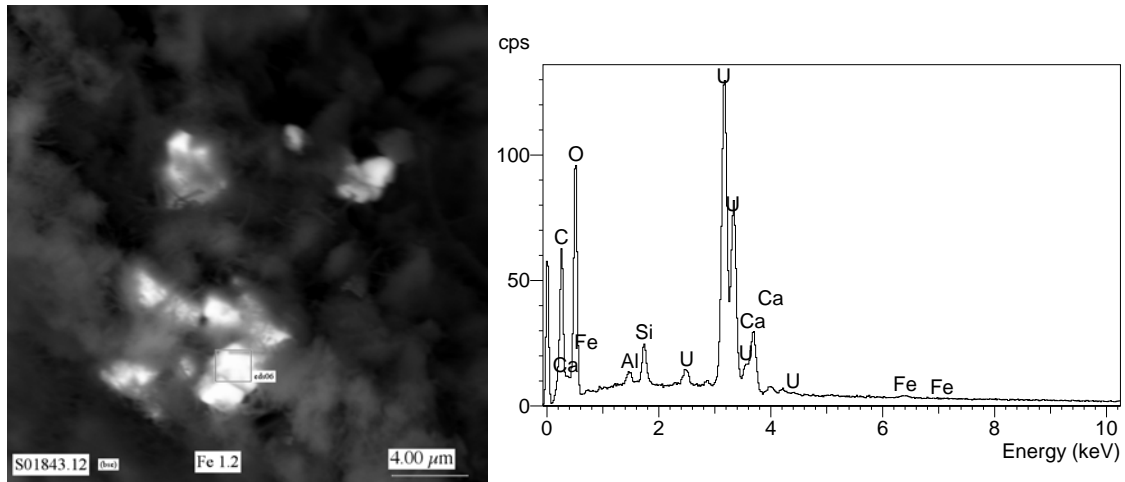
Figure 7.7. Left: Scanning-electron photomicrograph of U phase formed within OPC spiked with 10^{-3} M uranium after 1 month. Right: Energy dispersive spectroscopic pattern indicates the phase is a mixed uranyl-oxide/silicate phase.

7.3.2.2   0.1 M Uranium-Spikes Concrete Samples

SEM images of concrete samples containing 3000 ppm U revealed extensive formation of uranium-bearing precipitates after only 2 weeks. Figure 7.8a and b demonstrate the formation of tabular-shaped uranium-bearing precipitates embedded within the concrete matrix; additionally, cubic-shaped crystals are also clearly identifiable in Figure 7.8b. EDS analyses of the tabular-shaped precipitates provide a stoichiometric uranium-silica ratio of 2:1. The acicular morphology and stoichiometry of this phase are consistent with soddyite, $(UO_2)_2SiO_4(H_2O)_2$ (Figure 7.8c). The cubic-shaped crystals contain Ca in addition to U, O, and Si (Figure 7.8d). The stoichiometry, in conjunction with morphological considerations, is suggestive of uranophane, $Ca(UO_2)_2(SiO_3OH)_2(H_2O)_5$ (Figure 7.8d). Subsequent SEM-EDS analyses of concrete samples were conducted on monthly intervals. The occurrence of uranyl-oxyhydroxides decreased while the presence of uranyl-silicates increased after a period of 1 month. Stoichiometrically, uranyl-silicate compositions identified by EDS analyses remained suggestive of uranophane and soddyite phases and was corroborated by morphological observations from SEM analyses.
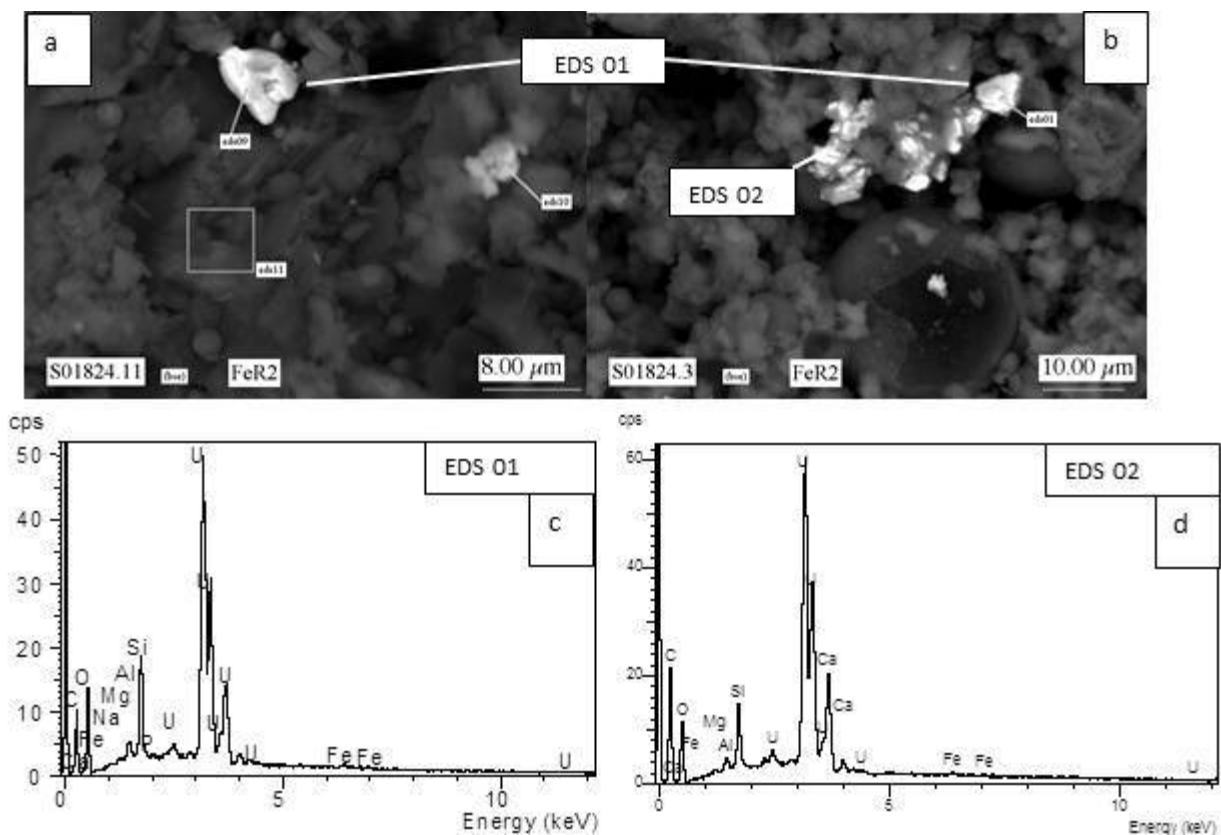
Figure 7.8. (a) and (b) Scanning-electron photomicrographs of tabular U mineral precipitated in situ from 0.1 M uranium nitrate spiked concrete after 2 weeks. (c) and (d) EDS analyses of tabular U precipitates; results indicate the stoichiometry of the precipitates is consistent with uranium-silicates: (c) EDS 01 is suggestive of soddyite, $(UO_2)_2SiO_4(H_2O)_2$ and (d) EDS 02 is suggestive of uranophane, $Ca(UO_2)_2(SiO_3OH)_2(H_2O)_5$

Analyses after 2 and 3 months demonstrated an increase in the formation of mixed uranyl-silicate/phosphate and uranyl-phosphate minerals. Figure 7.9a and b show regions of high U concentrations; EDS analyses of these regions indicate the co-existence of mixed uranium-silicate/phosphate phases (Figure 7.9c) and uranium-phosphate phases (Figure 7.9d). Morphologically, the mixed uranium-silicate/phosphate and uranium-phosphate regions appeared visually amorphous in SEM images (Figure 7.9a and b). This is consistent with the fact there are no known, naturally occurring, mixed uranyl-silicate/phosphate crystalline phases. However, more detailed analyses may reveal structure on a nanoscopic scale wherein uranium-silicate and/or uranium-phosphate phases may be evident.
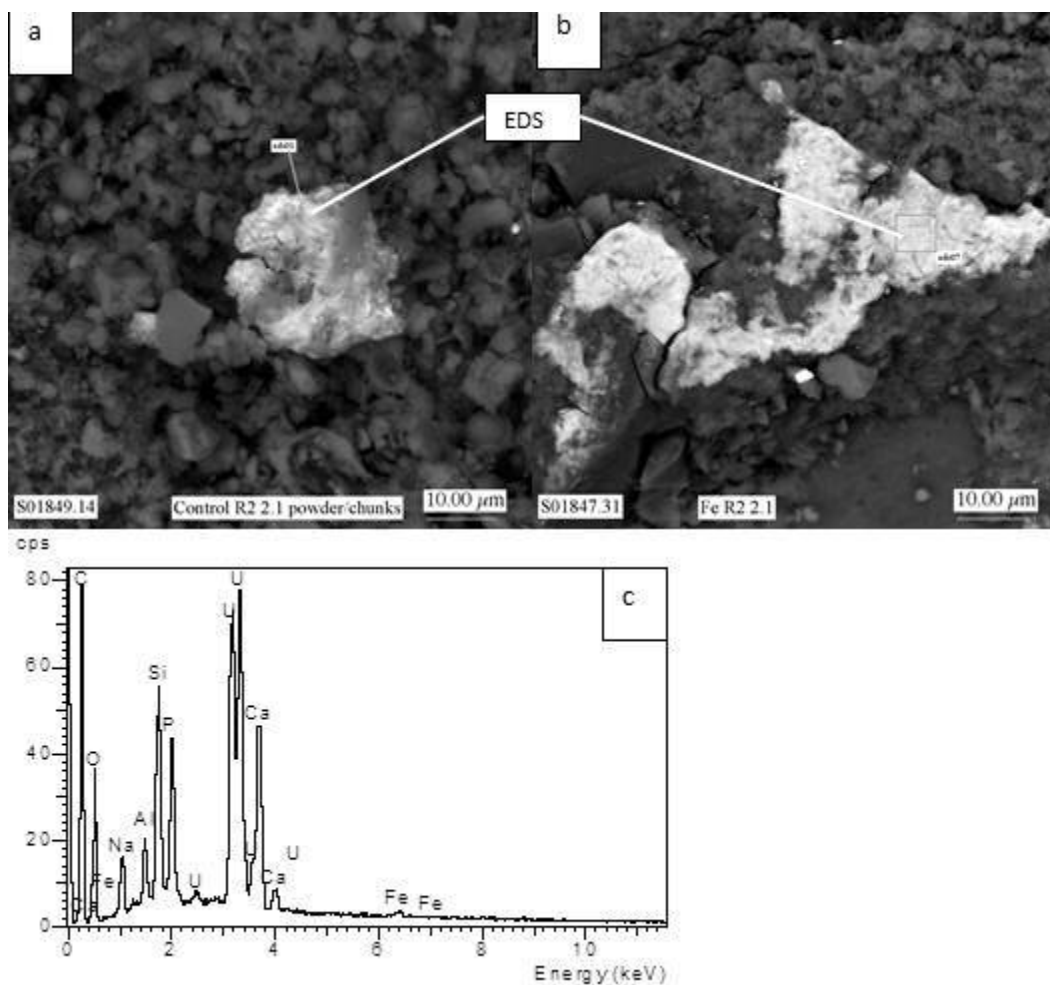
Figure 7.9. (a) and (b) Scanning-electron photomicrographs of tabular U mineral precipitated in situ from 0.1 M uranium nitrate spiked concrete within concrete sample composition five after 2 months. (c) EDS corresponds to a mixed calcium-uranium-silicate/phosphate phase.

Figure 7.10 illustrates regions of concentrated calcium-uranium-phosphate after 2 months. In contrast to the mixed uranyl-silicate/phosphate phases, some structural definition of tabular-shaped morphology was evident in the uranyl-phosphate minerals. EDS analyses demonstrate an increase in oxygen concentration with an increasing phosphorus concentration and concurrent decrease in silicon concentration; the overall stoichiometry approaching that consistent with autunite phases, $Ca_2[(UO_2)_2(PO_4)_2] \cdot xH_2O$ (Figure 7.10).
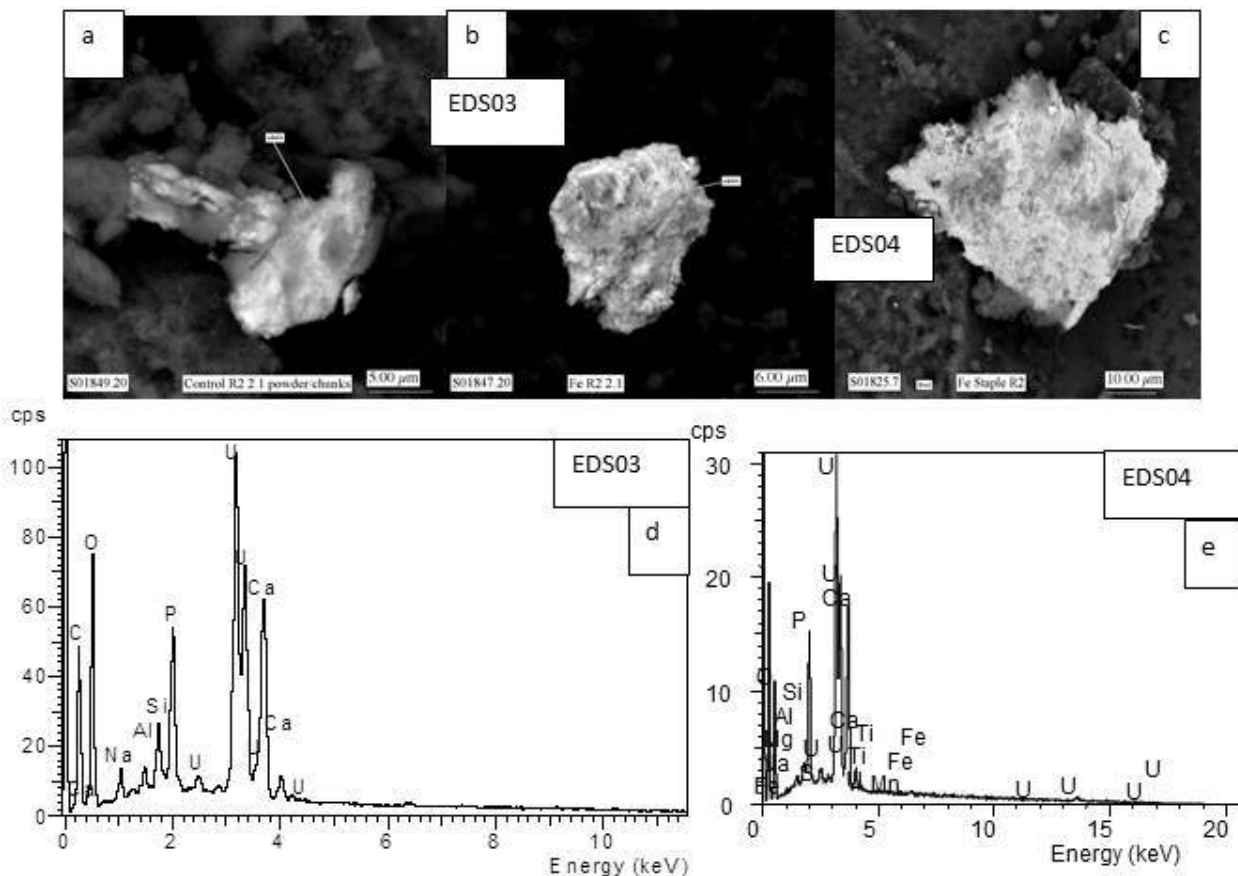
Figure 7.10. (a)-(c) Scanning-electron photomicrograph of tabular U phase formed within OPC spiked with 0.1 M uranium after two months. Photomicrographs of uranium-phosphate phases exhibiting tabular morphology characteristic of autunite mineral; precipitates were identified in OPC spiked with 0.1 M uranium after 2 months. Energy dispersive spectroscopic pattern indicates the stoichiometry is consistent with autunite, $Ca_2[(UO_2)_2(PO_4)_2] \cdot xH_2O$.

The paragenesis of more soluble uranyl-oxyhydroxides to the more stable uranyl-silicate and -phosphate minerals is commonly observed in natural ore bodies (Finch and Ewing 1992; Murakami et al. 1997) and areas with residual contamination from past nuclear activities undergoing natural attenuation (Buck et al. 1996; Elless and Lee 1994, 1998; Lee and Marsh 1992; Tidwell et al. 1996). However, this transformation has not been observed nor has the potential occurrence been considered in the context of radioactive waste management. Compositionally, the concentration of phosphorus within the starting materials is approximately 10 ppm, whereas the concentration of silica is nearly 200 ppm. However, as previously noted by Bogue (1955) and Taylor (1990), concrete is a continuously reacting solid whose component phases continue to change over hundreds of years, albeit very slowly. This may allow diffusion and reaction of contaminants, such as U, within the matrix and eventually result in limited formation of more thermodynamically stable phases exhibiting long-term stabilization of U. Results presented here provide evidence, after 1 to 3 months, for all major divisions of the U paragenetic sequence (i.e., uranyl-oxyhydroxides, -silicates, and -phosphates). While, uranyl-silicate phases are the dominant uranyl minerals present within concrete matrices after 1 month, dependent on the composition of the concrete waste form, the presence of phosphorus may have significant implications for the long-term retention of U within the waste form.

7.14

7.3.3   Mineral Phase Conclusions

Under ambient conditions, XRD data suggest diuranate salts and uranium-oxyhydroxides and -silicates are important in determining the solubility of U within concrete porewaters. However, uranium-oxyhydroxides and -silicates are dominant U solid phases present in thermally cured porewaters with increased crystallinity. These results support previous investigations suggesting the importance of uranium-oxyhydroxides, and, to a limited degree, -silicate minerals, on the retention of U within cementitious matrices. Kienzler et al. (2010) found uranophane to be a major U phase in cement specimens that had been leached in salt brines for 17 years through XRD.

However, results of in situ characterization of U phases in concrete waste forms illustrate the interaction between components within the concrete matrix and U affording significant control on the long-term solubility. Under both undersaturated and oversaturated conditions with respect to U solid phases, U solid phases were prevalent throughout concrete waste forms after 2 weeks. The significance of the U paragenetic sequence is evident during the subsequent 2 months. Uranyl-oxyhydroxide phases were followed by the formation of mixed uranyl-oxyhydroxide/silicates, leading to the formation of uranyl-silicates, then mixed uranyl-silicate/phosphate and uranyl-phosphate phases. The importance of uranyl-phosphate minerals in concrete waste forms has, to date, been neglected due to the minimal amount of phosphorus present in most concrete compositions. However, because concrete is a continuously reacting solid, the thermodynamic stability of advanced uranyl minerals may substantially influence the long-term fate of U.

Short-term batch tests conducted with cement-equilibrated porewaters have frequently been used to identify the solubility-limiting phases controlling the long-term fate of contaminants immobilized in concrete waste forms. Results presented here illustrate that the assumptions within this line of investigation may oversimplify the complexities of U chemistry, especially when coupled with constantly changing conditions of concrete porewaters. Moreover, because co-existing solids of the concrete matrix are absent from the system, the systems generally lacks buffering capacity and the influence of heterogeneous surfaces to promote nucleation of significant phases. Additionally, XRD results presented here for the identification of U phases precipitated from simulated concrete porewaters illustrate the significant challenges of discerning the solid phase(s) controlling the long-term solubility of U in complex matrices. The structural similarity of U solid phases and formation of additional phases such as Ca phases typically present in concrete, complicate interpretation of powder diffraction data. This precludes conclusive identification of solid phases precipitated from concrete porewaters based solely on XRD analyses and demonstrates the necessity to conduct multi-faceted spectroscopic investigations to unambiguously identify solubility-limiting U phases. Future investigations should consider the potential benefit of including phosphorus in concrete waste forms and quantify the solubility of well-characterized U solid phases under conditions relevant to concrete matrices.

7.4   Solubility Testing of U(VI) Minerals

7.4.1   Becquerelite, $Ca(UO_2)_6O_4(OH_6)(H_2O)_8$

The aqueous concentration of U obtained for becquerelite in the simulated Portland cement-equilibrated porewaters are represented in Figure 7.11 in the form of $log10$ [U(VI)]aq (molality) versus time. The aqueous concentrations of U reached steady-state within 100 days in all simulated porewaters,

except 9:1 BFS/OPC. The aqueous concentration of U in the 9:1 BFS/OPC porewater deviated widely throughout the testing. Test periods longer than those presented here are necessary to reach steady-state for becquerelite in 9:1 BFS/OPC porewaters. The aqueous, equilibrium U concentration increases in the respective porewaters in the following order: OPC/L < Harwell ≈ SRPC/L< OPC/BFS/L. The increase in aqueous U concentrations is correlated with decreasing concentration of Ca in the simulated porewater. Additionally, porewater 9:1 BFS/OPC contains the highest concentration of carbonate.

The SEM analyses do not suggest the formation of secondary phases in 9:1 BFS/OPC, OPC/L, OPC/BFS/L, or SRPC/L porewaters. In the Harwell porewater, however, the formation of a secondary precipitate, which did not possess a well-defined morphology, was observed on the surface of some becquerelite crystals (Figure 7.12). The EDS analyses indicated this was a mixed calcium-sodium-uranium phase that was composed of 1.45 wt% Na, 2.66 wt% Ca, and 54.99 to 92.36 wt% U. This phase is poorly crystalline mixed sodium- and calcium-oxyhydroxide. EXAFS analysis and geochemical modeling of aqueous solutions have been used to elucidate the formation and identity of secondary U phases in Harwell porewater and are described in sections 7.5 and 7.6.
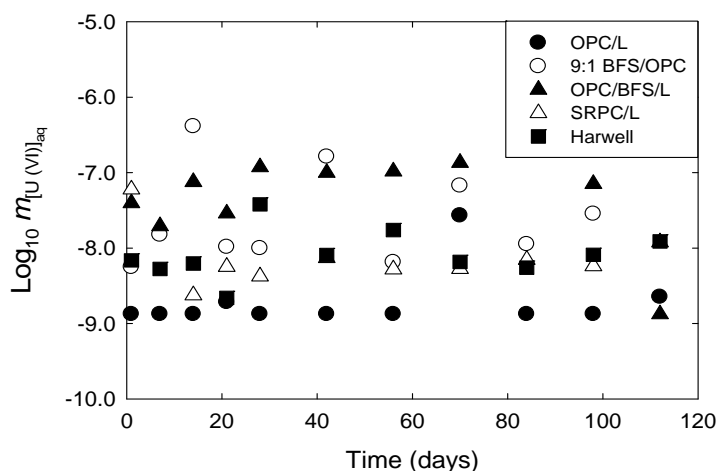
Figure 7.11. Solubility of becquerelite in simulated Portland cement-equilibrated waters
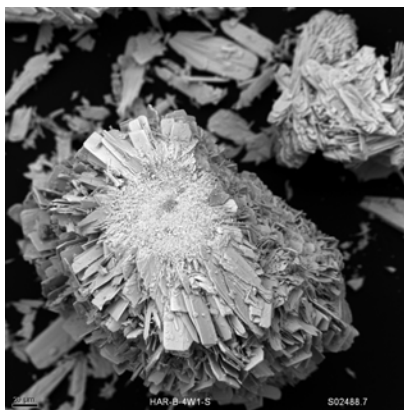
Figure 7.12. Scanning-electron photomicrographs of solids material from the reaction of becquerelite in Harwell porewater displaying the formation of poorly crystalline, mixed sodium- and calcium-oxyhydroxide phase on the surface of becquerelite crystals

Results presented here suggest that becquerelite attains equilibrium conditions rapidly within concrete porewaters. There was no observed effect of carbonate or sulfate within the porewaters on the stability of becquerelite, or the formation of secondary phases. The becquerelite will persist within concrete waste forms as a long-term control on U.

7.4.2   Soddyite, $(UO_2)_2SiO_4(H_2O)_2$

The aqueous concentrations of U obtained for soddyite in the simulated Portland cement-equilibrated porewaters are represented in Figure 7.13 in the form or $\log_{10}$ [U(VI)]$_{aq}$ (molality) versus time. The aqueous concentration of U reached steady-state within 100 days in all simulated porewaters, except Harwell. The aqueous concentration of U in the Harwell solution appeared to reach steady-state at ~10 days. However, at 70 days the aqueous concentration of U began to increase. Test periods longer than those presented here are necessary to reach steady-state for soddyite in Harwell porewaters. Moreover, the rate at which equilibrium is reached in the other porewaters differs depending on the porewater composition. Equilibrium is rapidly attained within ≤ 50 days for soddyite in BFS and 9:1 BFS/OPC. Longer periods, 60 to 100 days, are required to reach equilibrium in SRPC/L and OPC/L porewaters. The aqueous, equilibrium U concentration increases in the respective porewaters in the following order: of Harwell < OPC/L < OPC/BFS/L < 9:1 BFS/OPC = SPRC/L. Comparable to aqueous U concentrations measured from solubility tests conducted with becquerelite, the increase in aqueous U concentrations is correlated with decreasing concentration of Ca in the simulated porewater. Moreover, the increase in aqueous U concentration in OPC/BFS/L, 9:1 BFS/OPC, SPRC/L exhibits a relationship with increasing concentration of aqueous Si.
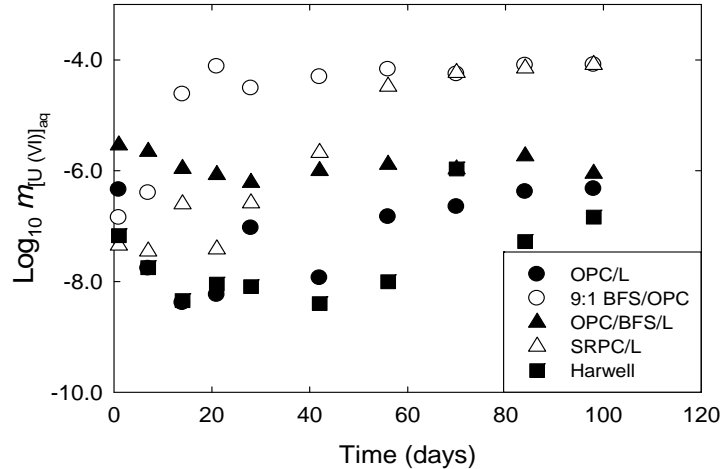
Figure 7.13. Solubility of soddyite in simulated Portland cement-equilibrated waters

The SEM of soddyite in BFS and 9:1 BFS/OPC at 100 days does not reveal the formation of any secondary phases. The SEM analysis of soddyite in Harwell porewaters reveals a morphologically different phase is present as a minor component of the solid phase (Figure 7.14). Analysis using EDS indicates the phase is a calcium-bearing uranium-silicate containing 1.43-2.01 wt% Ca, 4.55 – 5.62 wt% Si, 47.83 to 62.99 wt% U, and 29.40 to 44.04 wt% O. The morphology is suggestive of uranophane; however, the chemical composition is not strictly consistent with any one calcium-uranium-silicate phase. Further investigation is necessary to discern the identity of this phase. The formation of a minor inclusion

of acicular, fibrous fine-grained crystal tuffs, comparable to the results in Harwell, was also observed in OPC/BFS/L, 9:1 BFS/OPC, SRPC/L porewaters; no additional secondary phases were observed.
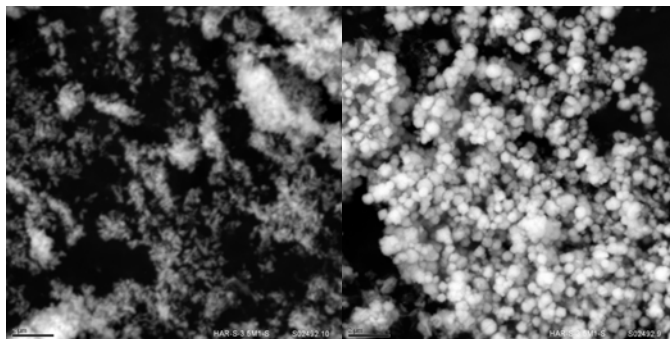
Figure 7.14. Scanning-electron photomicrographs of solids material from the reaction of soddyite in Harwell porewater. The image on the right shows the persistence of soddyite; the image on the left displays the formation of acicular, fibrous fine-grained crystal tuffs.

Similar results were observed from SEM images of reacted solid phases extracted from the reaction of soddyite in OPC/L. However, the higher concentration of Ca present in OPC/L relative to the Harwell solution resulted in substantial formation of calcium-bearing, fibrous fine-grained tuffs; additionally, the formation acicular, fibrous coarse-grained crystal tuffs also was observed (Figure 7.15). Analysis by EDS indicates that the phase is a sodium-bearing uranium-silicate containing 3.27 wt% Na, 6.29 wt% Si, 51.33 wt% U, and 39.11 wt% O. The morphology is consistent with sodium-boltwoodite, a uranophane-group mineral. EXAFS analysis and geochemical modeling of aqueous solutions have been used to elucidate the formation and identity of secondary U phases and are described in sections 7.5 and 7.6.
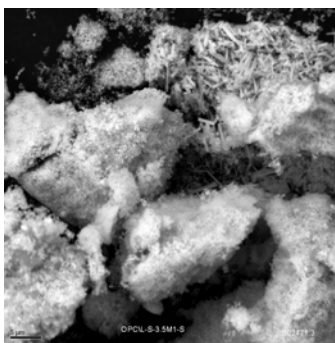
Figure 7.15. Scanning-electron photomicrographs of solids material from the reaction of soddyite in OPC/L porewater displaying the formation of acicular, fibrous coarse-grained tuffs

7.4.3   Uranophane, $Ca(UO_2)_2(SiO_3OH)_2(H_2O)_5$

The aqueous concentrations of U obtained for uranophane in the simulated Portland cement-equilibrated porewaters are represented in Figure 7.16 in the form of $\log_{10}$ $[U(VI)]_{aq}$ (molality) versus time. The aqueous concentration of U reached steady-state within 100 days in all simulated porewaters. Additionally, the rate at which equilibrium was reached is relatively consistent and does not depend on the porewater composition. Equilibrium is rapidly attained within ≤ 30 days. The aqueous, equilibrium U concentration increases in the respective porewaters in the following order: Harwell $\approx$ OPC/L < 9:1 BFS/OPC < SRPC/L < OPC/BFS/L. As observed with becquerelite and soddyite, the increase in aqueous

U concentrations is correlated with decreasing concentration of Ca in the simulated porewater. There was no clear correlation with any other aqueous ligands.
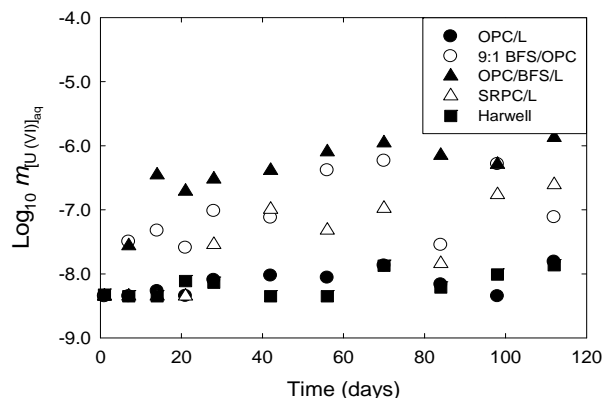
Figure 7.16. Solubility of uranophane in simulated Portland cement-equilibrated waters
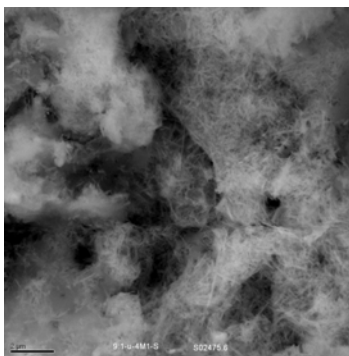
Figure 7.17. Scanning-electron photomicrographs of solids material from the reaction of uranophane in 9:1 BFS/OPC porewater displaying the formation of acicular, fibrous fine-grained crystal tuffs

No secondary phases were identified in any of the other porewaters. The morphology of all reacted solid phases was the acicular, fibrous fine-grained tuffs consistent with the unreacted uranophane (Figure 7.17). Further, the lack of secondary phases supports the possibility that the acicular, fibrous fine-grained tuff phase present in the soddyite post-reaction solids (discussed above) is an uranophane group phase.

7.4.4 Autunite, $Ca(UO_2)_2(PO_4)_2(H_2O)_{12}$

The aqueous concentrations of U obtained for autunite in the simulated Portland cement-equilibrated porewaters are represented in Figure 7.18 in the form of $\log_{10}[U(VI)]_{aq}$ (molality) versus time. The aqueous concentration of U reached steady-state within 100 days in all simulated porewaters, except OPC/L and SRPC/L. The aqueous concentration of U in the OPC/L and SRPC/L porewaters deviated widely throughout the testing. Test periods longer than those presented here are necessary to reach steady-state for autunite in OPC/L and SRPC/L porewaters. The aqueous, equilibrium U concentration increases in the respective porewaters in the following order: Harwell < OPC/BFS/L < 9:1 BFS/OPC. As observed with other U (VI) minerals, the increase in aqueous U concentrations is correlated with the

decrease in the concentration of Ca in the simulated porewater. There was no clear correlation with any other aqueous ligands.
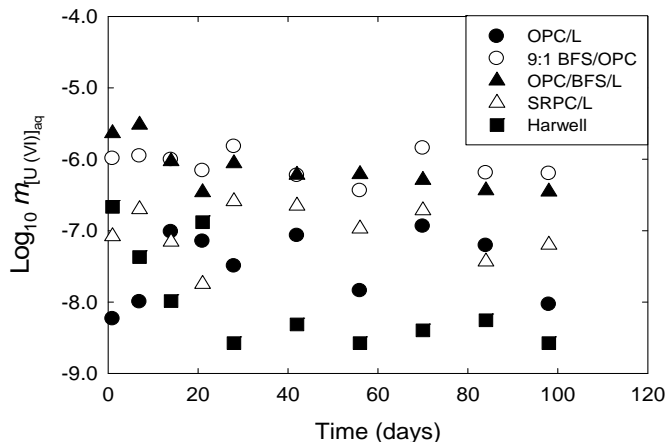
Figure 7.18. Solubility of autunite in simulated Portland cement-equilibrated waters

The SEM analyses do not suggest the formation of secondary phases in 9:1 BFS/OPC, OPC/L, Harwell, or SRPC/L porewaters. The formation of secondary phases was observed in the OPC/BFS/L porewater (Figure 7.19). Analysis using EDS indicates the spherical phase is a mixed sodium-calcium-bearing uranium-phosphate containing 1.22 wt% Na, 16.57 wt% Ca, 10.10 wt% P, 16.15 wt% U, and 55.97 wt% O. The rod-like phase is a mixed sodium-calcium-bearing uranium-phosphate containing 1.31 wt% Na, 14.34 wt% Ca, 8.30 wt% P, 28.02 wt% U, and 46.26 wt% O. EXAFS analysis and geochemical modeling of aqueous solutions have been used to elucidate the formation and identity of secondary U phases in Harwell porewater and are described in sections 7.5 and 7.6.
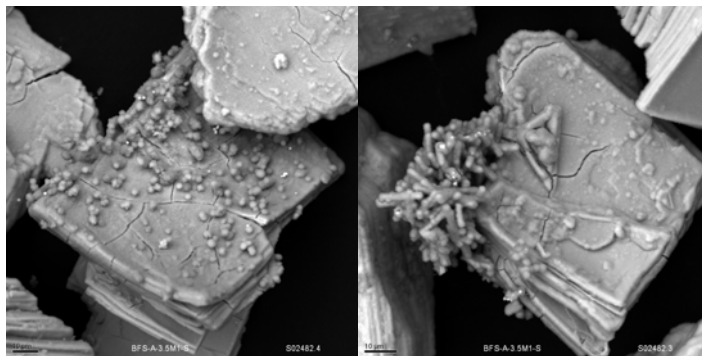
Figure 7.19. Scanning-electron photomicrographs of solids material from the reaction of autunite in OPC/BFS/L porewater. Photo on the left displays the formation of spherical secondary precipitates; photo on the right indicates the formation of a rod-like secondary phase.

7.5   EXAFS Analysis of Uranium Phases

Although SEM-EDS and XRD provide preliminary information regarding the possible secondary phases that form and may control U mobility in concrete porefluids, they provide limited structural and speciation information on phases present at <5 wt%. Therefore, to precisely understand the mechanisms of transformation and identity of U phases controlling the long-term mobility of U in concrete waste

forms, EXAFS analysis was conducted on pristine U phases, and the U phases reacted with simulated concrete porefluids.

Data were fit as linear combinations of the χ data from k = 3-12, k^3 weighted for the original U mineral and potential secondary phase minerals. A suite of model compound combinations was run to determine the best possible fit of the spectra. Combinations of autunite, schoepite, boltwoodite, uranium-rich calcite, soddyite, and uranophane were run based on starting mineral, porewater chemistry, and secondary phases suggested from SEM-EDS analysis and geochemical modeling. Samples were down selected for EXAFS analysis due to the limited availability of analysis time at SSRL. Samples were selected based on results from SEM-EDS and geochemical modeling, which indicated the formation of secondary phases.

Figure 7.20 shows EXAFS analysis of autunite minerals in Harwell and OPC/BFS/L porewaters for 3.5 months and 1 year. The spectra indicate the retention of uranium phosphate minerals over the course of 3.5 months and 1 year for both the Harwell and OPC/BFS/L porewaters. The results of linear combination fits for Figure 7.20 are presented in Table 7.4. When fitting EXAFS spectra, a linear combination equaling 100% is rare. As with all modeling and spectroscopic fitting, there is a degree of uncertainty that results in a less than 100% fit. The spectra were well fit using solely autunite. Harwell autunite reacted for 3.5 months is well fit as a 95% linear combination fit for autunite. Harwell autunite reacted for 1 year is well fit with an 89% linear combination. This indicates the material is predominately autunite; the exact composition did not fit the model compounds. It is possible that the low percentage of the fit is due to a change in cation (from Ca to Na or Mg). The OPC/BFS/L reacted autunite was 84% autunite after 3.5 months and 85% autunite after 1 year. As above, the best fit spectra consisted of solely autunite.
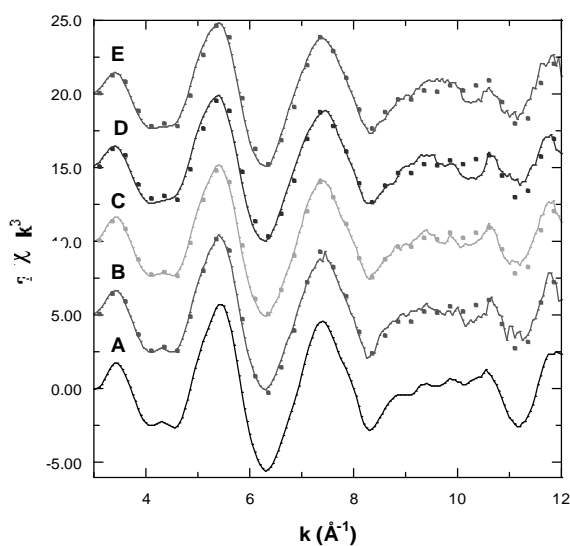
Figure 7.20. EXAFS of 3.5 and 1 year autunite solubility tests (a) autunite mineral, (b) Harwell reacted autunite after 3.5 months (HAR_A_3.5M), (c) Harwell reacted autunite after 1 year (HAR_A_1YR), (d) BFS reacted autunite after 3.5 months (BFS_A_3.5M), and (e) BFS reacted autunite after 1 year. The dots are the best fit to the EXAFS spectra using linear combination of autunite and uranophane mineral.

Table 7.4. Results of linear combination fit of autunite solubility tests

	Autunite
HAR_A_3.5M	0.95
HAR_A_1YR	0.89
BFS_A_3.5M	0.84
BFS_A_1YR	0.85
SRPC_A_3.5M	0.93

Figure 7.21 shows the EXAFS spectra for autunite reacted for 3.5 months in Harwell, OPC/BFS/L, and SRPC porewaters. As in Figure 7.20, the EXAFS spectra indicate that after 3.5 months in the different concrete porewaters, the autunite was either unreactive or transformed to another uranium phosphate phase. Table 7.4 gives the results of linear combination fits from the 3.5 month reacted autunite solubility experiments. The autunite reacted in SRPC porewater for 3.5 months was best fit as 93% autunite.

Uranium phosphate minerals are structurally very similar, which affords spectroscopic analyses that are relatively indistinguishable from one another (Catalano and Brown Jr. 2004). Because autunite was the known starting phase within these experiments, the reacted minerals were fit using autunite as a model mineral for comparison. However, it cannot be ascertained from EXAFS data alone whether the autunite solubility tests were stable over the duration of the test or if secondary uranium-phosphate phases were also formed. SEM-EDS analysis supported the formation of secondary phase(s) on the autunite reacted samples, with mixed sodium-calcium uranium phosphates tentatively identified through EDS analysis. Geochemical modeling using element concentrations indicated a mixed sodium-calcium uranium phosphate secondary phase in Portland cement porewater. The combination of SEM imaging, which showed secondary phase formation; EDS analysis and geochemical modeling, which predicted the formation of uranium phosphate secondary phases; and EXAFS linear combination fits, which indicated the reacted autunite sample contained only uranium phosphates, support the hypothesis that in contact with Portland cement porewaters, autunite undergoes a dissolution-precipitation reaction which results in the formation of uranium phosphate species. From these results, the ability of concrete waste forms to retain U is high, due to the re-precipitation of high stability phosphate phases. Among the paragenetic sequence of U, phosphate species are among the most stable.
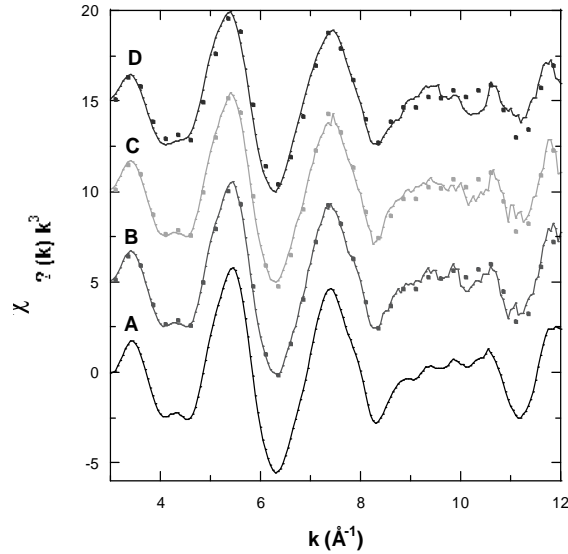
Figure 7.21. EXAFS of 3.5 month reacted autunite solubility tests (a) autunite mineral, (b) SRPC reacted autunite after 3.5 months, (c) Harwell reacted autunite after 3.5 months, and (d) BFS reacted autunite after 3.5 months. The dots are the best fit to the EXAFS spectra using linear combination of autunite.

Figure 7.22 and Table 7.5 show the results from EXAFS analysis of soddyite mineral solubility tests. Provided in Figure 7.22 are the EXAFS spectra of soddyite and uranophane model compounds, Harwell reacted soddyite after 3.5 months, OPC/L reacted soddyite after 3.5 months, and OPC/BFS/L reacted soddyite after 3.5 months. Based on the sharpening of the peak between k 7 and 8, the introduction of the uranophane hump around k 9.2, and the minimization of the soddyite peak at k 10, the EXAFS spectra suggest that soddyite changes to a mixture of soddyite uranophane across the three different porewaters (Harwell, OPC/L, and OPC/BFS/L). Table 7.5 lists the results from the linear combination fits. The spectra were well fit using a mixture of soddyite and uranophane. For the Harwell reacted soddyite, the best fit was 59% soddyite and 33% uranophane; for OPC/L it was 55% soddyite and 33% uranophane and for OPC/BFS/L it was 19% soddyite and 72% uranophane. These results indicate that irrespective of porewater silicate concentration, soddyite minerals transform into a more stable uranophane group mineral, which will further control the stability of these minerals within concrete porewaters. These results correspond to geochemical modeling and SEM-EDS data reports that suggested the formation of uranophane/becquerelite group mineral phases for the soddyite solubility tests.
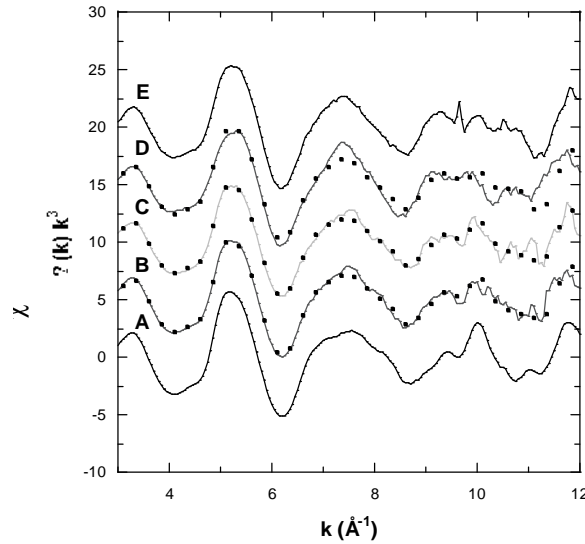
Figure 7.22. EXAFS of 3.5 month reacted soddyite solubility tests (a) soddyite mineral, (b) Harwell reacted soddyite after 3.5 months, (c) OPC/L reacted soddyite after 3.5 months, (d) BFS reacted soddyite after 3.5 months, and (e) uranophane mineral. The dots are the best fit to the EXAFS spectra using linear combination of soddyite and uranophane.

Table 7.5. Results of linear combination fit of soddyite solubility tests

	Soddyite	Uranophane
HAR_S_3.5M	0.59	0.33
OPC_S_3.5M	0.55	0.33
BFS_S_3.5M	0.19	0.72

EXAFS analysis of becquerelite concrete solubility tests was performed. However, a suitable model compound for becquerelite was not available and linear combination fits could not be performed. Additionally, EXAFS analysis of uranophane concrete solubility tests was not performed due to the evaluation of the uranophane tests with SEM-EDS and geochemical modeling, which did not suggest the formation of secondary phases.

7.6 Modeling Uranium Phases

Geochemical models MINTEQA2 (Allison et al. 1991) and EQ3NR (Wolery 1992) were applied to element concentrations under steady-state conditions to evaluate the aqueous speciation and saturation state of the effluent solutions with respect to key minerals, solids, and aqueous phases. Thermodynamic databases from numerous literature sources were used to update the computer codes (Alwan and Williams 1980; Chen et al. 1999; Finch 1997; Grenthe et al. 1992; Kalmykov and Choppin 2000; Langmuir 1978; Nguyen et al. 1992; O'Hare et al. 1976; Sergeyeva et al. 1972; Vochten and Haverbeke 1990). It is important to note that because of the complex chemistry of U, there is significant debate within the literature regarding the stoichiometry and the thermodynamic values assigned to aqueous U species and secondary mineral phases. As such, the solubility calculations are based on current knowledge, but may have significant uncertainty associated with them. Modeling results identifying U phases in simulated concrete porefluids are listed in Table 7.6.

Table 7.6. Thermodynamic geochemical modeling results for simulated concrete porefluids in equilibrium with U phases identified as primary controls on U mobility in concrete waste forms

Autunite			
Phase/End-member	Log moles	Aqueous Species	% Total
9:1 BFS/OPC			
Autunite-Ca: $Ca(UO_2)_2(PO4)_2 \cdot 10\text{-}12(H_2O)$	-1.95	$UO_2(HPO_4)_2^{2-}$	99.40
Autunite-Na: $Na_2(UO_2)_2(PO4)_2 \cdot 8(H_2O)$	-2.80		
Schoepite-JZ: $(UO_2)_8O_2(OH)_{12} \cdot 12(H_2O)$	-3.04		
Soddyite: $(UO_2)_2(SiO_4) \cdot 2(H_2O)$	-4.64		
OPC/BFS/L			
Autunite-Ca: $Ca(UO_2)_2(PO4)_2 \cdot 10\text{-}12(H_2O)$	-1.85	$UO_2(HPO_4)_2^{2-}$	76.01
Autunite-Na: $Na_2(UO_2)_2(PO4)_2 \cdot 8(H_2O)$	-2.80	$UO_2(OH)_2(aq)$	10.82
Schoepite-JZ: $(UO_2)_8O_2(OH)_{12} \cdot 12(H_2O)$	-4.55	$Ca_2UO_2(CO_3)_3(aq)$	4.28
Soddyite: $(UO_2)_2(SiO_4) \cdot 2(H_2O)$	-3.15	$UO_2(CO_3)_2^{2-}$	2.24
		$(UO_2)_2CO_3(OH)_3^-$	4.06
		$UO_2CO_3(aq)$	1.49
		$UO_2PO_4^-$	0.29
Harwell			
Autunite-Ca: $Ca(UO_2)_2(PO4)_2 \cdot 10\text{-}12(H_2O)$	-1.87	$UO_2(HPO_4)_2^{2-}$	87.98
Schoepite-JZ: $(UO_2)_8O_2(OH)_{12} \cdot 12(H_2O)$	-3.19	$UO_2(OH)_2(aq)$	10.43
Soddyite : $(UO_2)_2(SiO_4) \cdot 2(H_2O)$	-7.25	$UO_2PO_4^-$	0.31
		$UO_2(OH)+$	0.23
		UO_2OH^+	0.23
OPC/L			
Autunite-Ca: $Ca(UO_2)_2(PO4)_2 \cdot 10\text{-}12(H_2O)$	-2.16	$UO_2(HPO_4)_2^{2-}$	99.50
Autunite-Na: $Na_2(UO_2)_2(PO4)_2 \cdot 8(H_2O)$	-3.51		
Schoepite-JZ: $(UO_2)_8O_2(OH)_{12} \cdot 12(H_2O)$	-2.66		
Soddyite: $(UO_2)_2(SiO_4) \cdot 2(H_2O)$	-6.02		
SRPC/L			
Autunite-Ca: $Ca(UO_2)_2(PO4)_2 \cdot 10\text{-}12(H_2O)$	-1.86	$UO_2(HPO_4)^{2-}$	99.29
Schoepite-JZ: $(UO_2)_8O_2(OH)_{12} \cdot 12(H_2O)$	-3.14		
Soddyite: $(UO_2)_2(SiO_4) \cdot 2(H_2O)$	-5.28		
Soddyite			
Phase/End-member	Log moles	Aqueous Species	% Total
9:1 BFS/OPC			
Boltwoodite-Na $(H_3O)(Na,K)(UO_2)SiO_4 \cdot (H_2O)$	-2.65	$UO_2(OH)_3^-$	99.00
$CaUO_4$	-2.19	$UO_2(OH)_2(aq)$	0.83
Haiweeite: $Ca[(UO_2)_2Si_5O_{12}(OH)_2] \cdot 3(H_2O)$	-3.50		
Autunite			
Phase/End-member	Log moles	Aqueous Species	% Total
Soddyite: $(UO_2)_2(SiO_4) \cdot 2(H_2O)$	-1.93		
OPC/BFS/L			
$CaUO_4$	-2.81	$UO_2(OH)_3^-$	94.14
Haiweeite: $Ca[(UO_2)_2Si_5O_{12}(OH)_2] \cdot 3(H_2O)$	-3.60	$UO_2(OH)_2(aq)$	5.81
Soddyite: $(UO_2)_2(SiO_4) \cdot 2(H_2O)$	-1.82		

	Harwell		
$CaUO_4$	-2.26	$UO_2(OH)_3^-$	94.00
Haiweeite: $Ca[(UO_2)_2Si_5O_{12}(OH)_2] \cdot 3(H_2O)$	-3.27	$UO_2(OH)_2(aq)$	5.96
Soddyite: $(UO_2)_2(SiO_4) \cdot 2(H_2O)$	-1.89		
	OPC/L		
$CaUO_4$	-1.74	$UO_2(OH)_3^-$	98.29
Haiweeite: $Ca[(UO_2)_2Si_5O_{12}(OH)_2] \cdot 3(H_2O)$	-2.76	$UO_2(OH)_4^{2-}$	1.62
Soddyite $(UO_2)_2(SiO_4) \cdot 2(H_2O)$	-2.28		
	SRPC/L		
$CaUO_4$	-2.22	$UO_2(OH)_3^-$	98.03
Haiweeite $Ca[(UO_2)_2Si_5O_{12}(OH)_2] \cdot 3(H_2O)$	-3.34	$UO_2(OH)_2(aq)$	1.89
Soddyite $(UO_2)_2(SiO_4) \cdot 2(H_2O)$	-1.88		
	Becquerelite		
Phase/End-member	**Log moles**	**Aqueous Species**	**% Total**
	9:1 BFS/OPC		
$CaUO_4$	-2.06	$UO_2(OH)_3^-$	97.17
Clarkeite-JZ: $(Na,Ca,Pb)(UO_2)O(OH) \cdot 0-1(H_2O)$	-2.87	$UO_2(OH)_4^{2-}$	2.77
Becquerelite-JZ: $Ca(UO_2)_6O_4(OH)_6 \cdot 8(H_2O)$	-1.83		
Soddyite: $(UO_2)_2(SiO_4) \cdot 2(H_2O)$	-4.64		
	OPC/BFS/L		
$CaUO_4$	-2.61	$UO_2(OH)_3^-$	99.07
Becquerelite-JZ: $Ca(UO_2)_6O_4(OH)_6 \cdot 8(H_2O)$	-1.80		
Soddyite: $(UO_2)_2(SiO_4) \cdot 2(H_2O)$	-3.15		
	Harwell		
$CaUO_4$	-2.14	$UO_2(OH)_3^-$	97.59
Becquerelite-JZ: $Ca(UO_2)_6O_4(OH)_6 \cdot 8(H_2O)$	-1.83	$UO_2(OH)_4^{2-}$	2.34
Soddyite: $(UO_2)_2(SiO_4) \cdot 2(H_2O)$	-7.33		
	OPC/L		
$CaUO_4$	-1.62	$UO_2(OH)_3^-$	93.91
Clarkeite-JZ: $(Na,Ca,Pb)(UO_2)O(OH) \cdot 0-1(H_2O)$	-4.04		
Becquerelite-JZ: $Ca(UO_2)_6O_4(OH)_6 \cdot 8(H_2O)$	-1.92		
Soddyite $(UO_2)_2(SiO_4) \cdot 2(H_2O)$	-6.18		
	SRPC/L		
$CaUO_4$	-2.10	$UO_2(OH)_3^-$	97.65
Becquerelite-JZ: $Ca(UO_2)_6O_4(OH)_6 \cdot 8(H_2O)$	-1.81	$UO_2(OH)_4^{2-}$	2.28
Soddyite: $(UO_2)_2(SiO_4) \cdot 2(H_2O)$	-5.28		
	Uranophane		
Phase/End-member	**Log moles**	**Aqueous Species**	**% Total**
	9:1 BFS/OPC		
Boltwoodite-Na-JZ: $(H_3O)(Na,K)(UO_2)SiO_4 \cdot (H_2O)$	-2.65	$UO_2(OH)_3^-$	98.28
$CaUO_4$	-1.73	$UO_2(OH)_4^{2-}$	1.62
Haiweeite: $Ca[(UO_2)_2Si_5O_{12}(OH)_2] \cdot 3(H_2O)$	-2.31		
Soddyite: $(UO_2)_2(SiO_4) \cdot 2(H_2O)$	-2.86		
	OPC/BFS/L		
$CaUO_4$	-1.87	$UO_2(OH)_3^-$	99.18
Haiweeite: $Ca[(UO_2)_2Si_5O_{12}(OH)_2] \cdot 3(H_2O)$	-2.32		
Soddyite: $(UO_2)_2(SiO_4) \cdot 2(H_2O)$	-2.30		

		Harwell		
CaUO$_4$		-1.76	UO$_2$(OH)$_3^-$	98.44
Haiweeite: Ca[(UO$_2$)$_2$Si$_5$O$_{12}$(OH)$_2$]•3(H$_2$O)		-2.31	UO$_2$(OH)$_4^{2-}$	1.44
Soddyite: (UO$_2$)$_2$(SiO$_4$)•2(H$_2$O)		-2.59		
		OPC/L		
CaUO$_4$		-1.49	UO$_2$(OH)$_3^-$	98.29
			UO$_2$(OH)$_4^{2-}$	1.62
		SRPC/L		
CaUO$_4$		-1.74	UO$_2$(OH)$_3^-$	98.31
Haiweeite: Ca[(UO$_2$)$_2$Si$_5$O$_{12}$(OH)$_2$]•3(H$_2$O)		-2.30	UO$_2$(OH)$_4^{2-}$	1.59
Soddyite: (UO$_2$)$_2$(SiO$_4$)•2(H$_2$O)		-2.58		

7.6.1   Uranium Modeling Discussion

Precipitation of uranyl minerals follows the thermodynamic progression of precipitating those which have the lowest solubilities, for which precipitation kinetics do not present significant barriers to nucleation, followed by precipitation of the advanced U minerals that occurs over a considerable time frame (Finch et al. 1999; Smith 1984). The general sequence begins with the uranyl-hydroxides, followed by the -carbonate, -silicates, and finally the highly stable uranyl-phosphates. Therefore, it was hypothesized that the measured solubility of the uranyl-oxyhydroxide (becquerelite), uranyl-silicates (soddyite and uranophane), and uranyl-phosphate (autunite) tested here would decrease accordingly. However, the aqueous concentration of U released from all uranyl phases in the simulated Portland cement-equilibrate porewaters ranged from $\log_{10}$ [U(VI)]$_{aq}$ = -5 to -9, suggesting that porewater cations and anions may be influencing the solubility of U through complexation. The significance of porewater cation and anions on the U mineral solubility is also suggested by the formation of secondary phases.

Complexation of aqueous U can increase the solubility of U minerals (Langmuir 1997a, b). Two mechanisms may contribute to the increase in aqueous U: 1) a chelating effect, whereby oxygen-containing ligands (i.e., carbonate, phosphate, and hydroxide) bind to U in the mineral structure and subsequently release U complexes into solution, or 2) release of U from the mineral structure is followed by complexation by aqueous ligand. The latter would, thereby, reduce the activity of U in solution, allowing further release of U from the mineral structure. The composition of the porewaters contains numerous ligands that form stable complexes with uranyl in solution and can significantly increase the aqueous concentration of U. Uranyl cations will form strong complexes with hydroxide (Cordfunke 1964, 1969; Grenthe et al. 1992; Langmuir 1978, 1997a; Mattigod et al. 2012b), carbonate (Clark et al. 1995; Langmuir 1978), sulfate (Langmuir 1978, 1997a), silicate (Cordfunke 1964, 1969; Grenthe et al. 1992; Langmuir 1978, 1997a), and phosphate (Grenthe et al. 1992; Langmuir 1978, 1997a; Sandino and Bruno 1992).

System pH can strongly influence the solubility, hydrolysis, sorption, complexation, and colloid formation of U. Hydrolysis reactions are highly sensitive to the activity and concentration of hydrogen ions in solution (Baes Jr. and Schreyer 1953; Cordfunke 1969; Langmuir 1978; Sylva and Davidson 1979). For example, Figure 7.23 is a chart, generated using MINTEQA2, displaying U speciation at 25°C in the absence of all ligands except hydroxide. The plot shows that stepwise monomeric species dominate the distribution of U across the pH range.
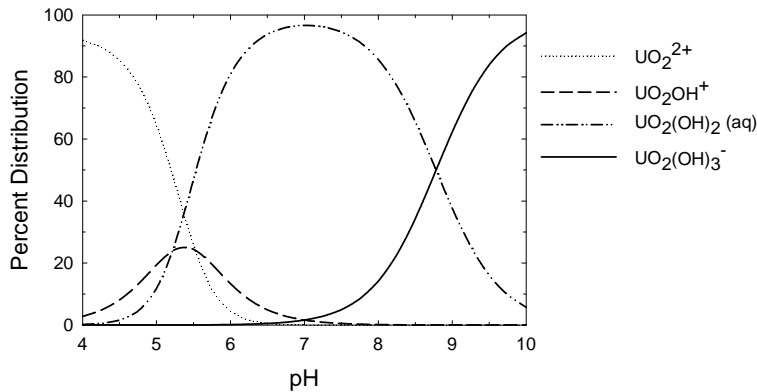
Figure 7.23. Percent distribution of U^{6+}-H_2O system at 25°C, I = 0.1 M, P_{CO2} = 0 bar and $\Sigma U^{6+} = 10^{-6}$ M in the absence of complexing ligands other than hydroxide

Figure 7.24 demonstrates the significance of pH and ligand identity on the speciation of U. The extent to which carbonate competes for U over hydroxyl complexes, especially above pH 6, is evident. Uranyl-carbonate species are very significant in the U geochemical cycle. They increase the solubility of U minerals, facilitate U(IV) oxidation, and because these species are anionic in nature, they limit the extent of sorption in oxidized waters, thereby increasing the mobility of U (Langmuir 1997a, b).
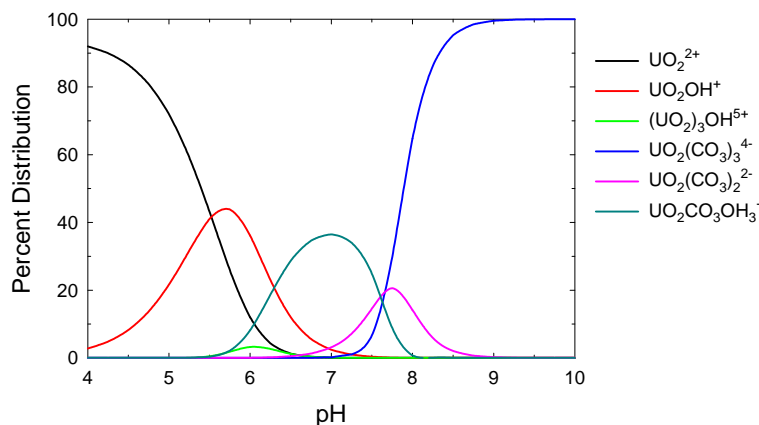
Figure 7.24. Percent distribution of U^{6+} species calculated using MINTEQA2 at 25°C, I = 0.1 M, and $pCO_2 = 10^{-3.5}$ bar for $\Sigma U^{6+} = 10^{-6}$ M

Uranyl-sulfate complexes are important in aqueous environments where pH < 6, the evaporation rate is high, sulfides are being oxidized, and carbonate is absent (Garrels and Christ 1965; Ondrus et al. 2003). There are few aqueous uranyl-silicate complexes that are moderately insoluble and readily precipitate to form uranyl-silicate minerals. As such, uranyl-silicate minerals are of relatively low solubility and do not rapidly dissolve on exposure to fresh water. In the pH range of 6 to 9, phosphate complexes dominate the system when $[PO_4]/[CO_3] > 0.1$. Uranyl forms more stable complexes with phosphate than with any other ligand (Langmuir 1978). Figure 7.25 illustrates the significance of the ligand species and concentration in determining the dominant U species at a given pH value.
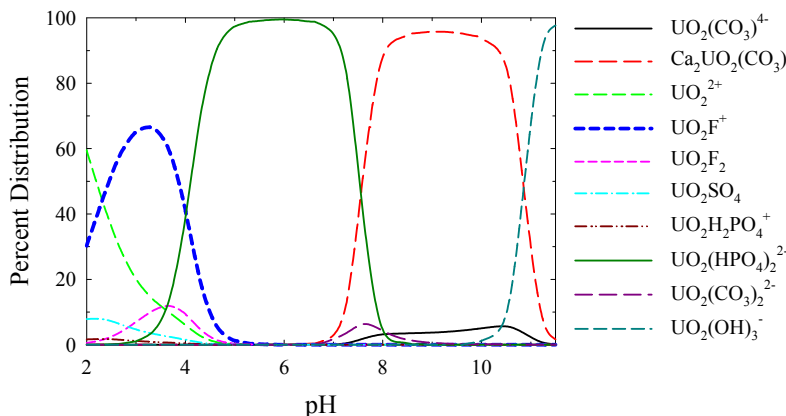
Figure 7.25. Percent distribution of U^{6+} aqueous species calculated using MINTEQA2 in Hanford groundwater Well-699-S3-25

There was no observed effect of carbonate or sulfate within the porewaters on the stability of the uranyl minerals, or on the formation of secondary phases. However, Ca and Si in the porewaters had a clear effect on the stability of all U minerals, as well as on the formation of secondary phases. Although confirmation of secondary phases is still necessary, preliminary results suggest the formation of (1) a calcium-uranium oxide from the reaction of becquerelite, (2) uranophane group minerals from the reaction of soddyite, and (3) mixed sodium-calcium uranium phosphate secondary phases from the reaction of autunite in simulated Portland cement-equilibrated porewater. Completion of analytical analyses to quantify aqueous cations and anions, coupled with geochemical thermodynamic modeling, will aid in further understanding the stability and long-term control of U provided by concrete waste forms. However, it is suggested here that (1) the release of U from the degradation of uranium oxyhydroxides will be controlled by the formation of secondary uranium oxides; 2) regardless of the replacement of soddyite by uranophane, uranyl-silicate phases will persist within concrete waste forms; and 3) the release of U from the degradation of uranium-phosphate phases will be controlled by the formation of secondary uranyl-phosphate phases.

7.7   Conclusions and Future Direction

These investigations provided in situ identification of U-bearing minerals formed within concrete and demonstrated the importance of U mineralization as a mechanism of retention within concrete waste forms. Results demonstrated the formation of U minerals, after only 2 weeks, within concrete waste forms that were under-saturated with respect to U solid phases and where sorption has been believed to be the mechanism of retention. Concrete matrices over-saturated with respect to U mineral phases exhibited extensive formation of uranium oxyhydroxide phases during the initial 2-week period. The significance of the U paragenetic sequence was clearly demonstrated during the subsequent 2-month time frame. Uranyl-oxyhydroxide phases were followed by the formation of mixed uranyl-oxyhydroxide/silicates, leading to the formation of uranyl-silicates, then mixed uranyl-silicate/phosphate phases and finally uranyl-phosphate phases.

Future investigations should consider the potential benefit of including phosphorus in concrete waste forms and quantification of the solubility of well-characterized U solid phases under conditions relevant to concrete matrices. In addition, solubility of U minerals should be examined with longer test periods

than those presented here. Becquerelite did not reach steady-state in 9:1 BFS/OPC porewaters during the 100 day experiment. Soddyite needed more than 100 days to reach steady-state in Harwell porewaters.

8.0 Summary

Cement-based solidification and stabilization is considered for hazardous waste disposal because it is easily done and cost-efficient. Concrete encasement would contain and isolate waste packages from the hydrologic environment and act as an intrusion barrier to control and minimize the release of radionuclide constituents in waste into the surrounding environment. Therefore, it is necessary to assess the performance of the concrete encasement structure and the ability of the surrounding soil to retard radionuclide migration.

Each of the test methods performed has focused on different aspects of the concrete waste form weathering process. Diffusion of different analytes has been quantified from experiments under both saturated and unsaturated conditions. The water-saturated conditions provide a conservative estimate of the concrete's performance in situ, and the unsaturated conditions provide a more accurate estimate of the diffusion of contaminants from the concrete.

Dynamic and static leach tests (section 3.0) have been conducted to determine the effect of iron particle incorporation on the leaching of contaminants in concrete specimens. Contaminants in these experiments include Tc-99, I-125, U, and Re. Iron sources contained within the concrete specimens for the two sets of experiments included steel fibers, metallic iron (-40 to +60 mesh), or reactive nanoscale zero valent iron particles (RNIP).

- I-125 in the concrete formulations used in these studies was about two orders of magnitude less leachable than Tc-99.

- Inclusion of RNIP relative to metallic iron particles significantly increases the leachability of Re and I from waste form specimens.

- The leaching indices indicate that in the presence of 4% and 8% RNIP, Tc-99 had higher leachability than Re. Given these test results, Re is not a suitable surrogate for Tc-99.

A series of half-cell diffusion experiments (section 4.0) were completed to investigate the effects of test duration, sediment moisture content, concrete carbonation, concrete fractures, and concrete iron content on diffusivity of I and Tc-99 from sediment and from concrete.

- Half-cell diffusion experiments with unsaturated Hanford sediment showed that diffusion coefficients varied over a range of 3 orders of magnitude with Tc-99 being slightly more retarded than I. Diffusion coefficients for I ranged from 3.63×10^{-9} to 5.99×10^{-6} cm^2/s and Tc-99 diffusion coefficients ranged from 1.96×10^{-9} to 3.07×10^{-6} cm^2/s throughout all the half-cell diffusion experiments.

- Increasing the sediment moisture content from 4% to 7% or 15% within the half-cell leads to an increase in both I and Tc-99 diffusion rates.

- Carbonation by supercritical CO_2 treatment increased diffusivity of I and Tc-99 through preferential pathways in the microcracks that were created.

- Using a super-saturated carbonate solution to carbonate concrete resulted in a decrease in diffusivity coefficients through a chemical or physical change within the concrete or due to a reduction in available nuclide through leaching during the carbonation process.

- The addition of iron resulted in a decrease in diffusivity in comparison to half-cells that did not contain iron, though increasing the amount of iron added did not consistently enhance the reduction of diffusivity values.

- Lengthening the test duration results in a decrease in measured diffusion coefficients.

Petrographic studies (section 5.0) began to investigate the physical and chemical effects of carbonation through observations of two sets of lab-prepared concrete monoliths and a set of Hanford Site. One set of monoliths was part of a half-cell diffusion study to discern correlations between carbonation and the diffusion of contaminants. Half of the monoliths were carbonated via supercritical CO_2 treatment. The remaining monoliths were left as-is, without carbonation. Another set of monoliths was encased in HFS under simulated vadose zone conditions for up to 2 years.

- Carbonation depth was more significant (up to 8 mm depth) in the concrete half-cell samples that had been carbonated by supercritical CO_2 treatment.

- Surface carbonation (<2 mm depth) was observed for the monoliths that did not have the supercritical CO_2 treatment.

- Carbonation under simulated vadose zone conditions is a much slower process than the supercritical CO_2 carbonation process.

- Carbonation of concrete using supercritical CO_2 increased the rate of the natural carbonation process and, in turn, resulted in increased diffusivity of I and Tc-99.

- The depth of carbonation increases over time, as observed in the concrete cores obtained from the Hanford Site with carbonation rates ranging from 0.3 to 0.9 mm per year.

- Petrographic analysis of the concrete monoliths carbonated by supercritical CO_2 treatment indicated at higher magnification microcracks (1 – 2 mm widths) were observed. Microcracks were also observed in the non-carbonated monoliths at the same magnification and there was no indication within the analysis reports whether the carbonated monoliths had more significant microcracking.

- Ettringite, a secondary deposit that forms as a result of hydration of Portland cement, was observed in the voids of some of the concrete monoliths and all of the Hanford Site cores. Formation of ettringite and the decomposition products can cause the formation of microcracks within the concrete structure through concrete volume expansion (Campbell et al. 1991).

Unlike the diffusion trends observed for I and Tc-99, U exhibited no measurable rate of diffusion. As such, additional investigations were conducted to understand the potential mechanisms resulting in the observed differences (section 7.0).

- Under ambient conditions, XRD data suggest diuranate salts and uranium-oxyhydroxides and silicates are important in determining the solubility of U within concrete porewaters.

- Uranium-oxyhydroxides and -silicates are dominant U solid phases present in thermally cured porewaters with increased crystallinity.

- Under both undersaturated and oversaturated conditions with respect to U solid phases, U solid phases were prevalent throughout concrete waste forms after 2 weeks. The significance of the U paragenetic sequence was clearly demonstrated during the subsequent 2-month time frame.

- Uranyl-oxyhydroxide phases were followed by the formation of mixed uranyl-oxyhydroxide/silicates, leading to the formation of uranyl-silicates, then mixed uranyl-silicate/phosphate and uranyl-phosphate phases.

As demonstrated through the saturated leaching tests presented in section 3.0 and comparing these results to those measured from the unsaturated diffusion tests in section 4.0, concrete encasement of waste disposed at Hanford under planned unsaturated and atmospheric (carbonated) conditions will provide a significant delay in radionuclide release into the subsurface.

9.0   Future Direction

The diffusion coefficients presented in this report are specific to the material composition tested, as described in section 2.0. Previous studies have shown that leaching of Tc-99 varies as a function of waste type, waste loading (mix ratio), grout fluid density, and amount of blast furnace slag in the blend (Serne et al. 1993a, b; 1992). A focused set of half-cell diffusion experiments using Hanford Site sediments is needed to investigate the diffusion coefficients for current and future compositions considered for waste encasement.

Carbonation can affect the structure of cement-based waste forms as well as the release rates of heavy metals. Therefore, it is important to understand the impact carbonation has on potential waste forms. As discussed in the introduction, the extent of carbonation is dependent on cement composition, water-to-cement ratios, curing times, level of hydration prior to carbonation, compaction pressure, relative humidity, and others. Bertos et al. (2004) found that water:cement ratios affect the penetration and diffusion of CO_2 into the waste forms and ultimately waste form strength. The compaction pressure of the granular material before it is subjected to carbonation also influences the CO_2 diffusivity. The porosity and permeability are decreased when the compaction pressure increases, which results in a stronger waste form. Future lines of investigation that should be considered include varying the water:cement ratio to evaluate the effect of waste form strength on contaminant mobility.

Precipitate products form as a result of reactions of the structure of the waste form with the leachate and carbonate, including calcite in the pores, a calcium silica gel, formation of ettringite and subsequent formation of gypsum from decomposition of the ettringite. The formation of these precipitates in the pore spaces of the waste form leads to the formation of microcracks where the carbonation reaction occurs. Microcracks can play a significant role in the depth of carbonation and it has been proposed that microcracks create preferential pathways for diffusion of contaminants. A more detailed investigation is needed into the degree of carbonation (time and depth) and the development of microcracks as carbonation of waste form increases. Additional examination of the precipitation products formed as a function of carbonation and effect of product formation on radionuclide retention or release.

The potential benefit of including phosphorus in concrete waste forms should be considered, as well as the quantification of the solubility of well-characterized U solid phases under conditions relevant to current concrete matrices. In addition, solubility of U minerals should be examined with longer test periods than those presented here, as some of the becquerelite and soddyite experiments did not reach steady state within the 100-day time period.

10.0 References

Al-Khayat, H, MN Haque, and NI Fattuhi. 2002. "Concrete Carbonation in Arid Climate." *Materials and Structures* 35:421-26.

Allison, JD, DS Brown, and KJ Novo-Gradac. 1991. *MINTEQA2/PRODEFA2, a Geochemical Assessment Model for Environmental Systems: Version 3 User's Manual*. Report, Environmental Research Laboratory, Office of Research and Development, U.S. Environmental Protection Agency, Athens, Georgia.

Alwan, AK and PA Williams. 1980. "The Aqueous Chemistry of Uranium Minerals. Part 2. Minerals of the Liebigite Group." *Mineralogical Magazine* 43:665-67.

ANSI. 1986. *Measurement of the Leachability of Solidified Low-Level Radioactive Wastes Short-Term Test Procedure*. Chicago, American Nuclear Society.

ASTM C1308-08. 2008. *Standard Test Method for Accelerated Leach Test for Diffusive Releases from Solidified Waste and a Computer Program to Model Diffusive, Fractional Leaching from Cylindrical Waste Forms*, ASTM International, West Conshohocken, PA.

Atkins, M, AN Beckley, and FP Glasser. 1988. "Influence of Cement on the Near Field Environment and Its Specific Interactions with Uranium and Iodine." *Radiochimica Acta* 44/45:255-61.

Atkinson, A and AK Nickerson. 1988. "Diffusion and Sorption of Cesium, Strontium, and Iodine in Water-Saturated Cement." *Nuclear Technology* 81:100-13.

Baes Jr., CF and JM Schreyer. 1953. *The Chemistry of Uranium (VI) Orthophosphate Solutions: Part III, the Solubility Behavior of $UO_2HPO_4*4H_2O$ in Perchloric Acid Solutions*. Report, Oak Ridge National Laboratory, Oak Ridge, TN.

Bargar, JR, GEB Jr., I Evans, T Rabedeau, M Rowen, and J Rogers. 2002. "A New Hard X-Ray XAFS Spectroscopy Facility for Environmental Samples, Including Actinides, at the Stanford Synchrotron Radiation Laboratory. Proceedings of the Euroconference and NEA Workshop on Speciation, Techniques and Facilities for Radioactive Materials at Synchrotron Light Sources." *NEA/OECD Paris*:57-68.

Bertos, MF, SJR Simons, CD Hills, and PJ Carey. 2004. "A Review of Accelerated Carbonation Technology in the Treatment of Cement-Based Materials and Sequestration of CO_2." *Journal of Hazardous Materials* (B112):193-205.

Bhunia, P, A Pal, and M Bandyopadhyay. 2007. "Assessing Arsenic Leachability from Pulverized Cement Concrete Produced from Arsenic-Laden Solid Calsico-Sludge." *Journal of Hazardous Materials* 141:826-33.

Bobirica, C, L Bobirica, R Stanescu, and I Constantinescu. 2010. "Leaching Behavior of Cement-Based Solidified Wastes Containing Hexavalent Chromium." UPB Scientific Bulletin, Series B: *Chemistry and Materials Science* 72(1):121-28.

Bogue, RH. 1955. *Chemistry of Portland Cement*. Reinhold Publishing Corporation, New York.

Bovaird, CC, DP Jansik, DM Wellman, and MI Wood. 2011. *Radionuclide Retention in Concrete Wasteforms*. Report No. PNNL-20760, Pacific Northwest National Laboratory, Richland, WA.

Brodda, BG. 1988. "Leachability of Technetium from Concrete." *The Science of the Total Environment* 69:319-45.

Brown, DA, BE Fulton, and RE Phillips. 1964. "Ion diffusion: I. A quick-freeze method for the measurement of ion diffusion in soil and clay systems." *Soil Science Society of America Journal* 28: 628-632.

Brownsword, M, AB Buchan, FT Ewart, R McCrohon, GJ Ormerod, JL Smith-Briggs, and HP Thomason. 1990. "The Solubility and Sorption of Uranium (VI) in a Cementitious Repository." In *Proceedings of Materials Research Society Symposium*, 577-82 pp.

Buck, EC, NR Brown, and NL Dietz. 1996. "Contaminant Uranium Phases and Leaching at the Fernald Site in Ohio." *Environmental Science and Technology* 30:81-88.

Campbell, DH, RD Sturm, and SH Kosmatka. 1991. "Detecting Carbonation." *Concrete Technology Today* 12(1):1-5.

Casas, I, I Perez, E Torrero, J Bruno, E Cera, and L Duro. 1997. *Dissolution Studies of Synthetic Soddyite and Uranophane*. Report, Swedish Nuclear Fuel and Waste Management Co., Stockholm, Sweden.

Castel, A, R Francois, and G Arliguie. 1999. "Effect of Loading on Carbonation Penetration in Reinforced Concrete Elements." *Cement and Concrete Research* 29:561-65.

Catalano, JG and GE Brown Jr. 2004. "Analysis of Uranyl-Bearing Phases by EXAFS Spectroscopy: Interferences, Multiple Scattering, Accuracy of Structural Parameters, and Spectral Differences." *American Mineralogist* 89:1004-21.

Chang, C-F and J-W Chen. 2006. "The Experimental Investigation of Concrete Carbonation Depth." *Cement and Concrete Research* 36:1760-67.

Chen, F, RC Ewing, and SB Clark. 1999. "The Gibbs Free Energies and Enthalpies of Formation of U6+ Phases: An Empirical Method of Prediction." *American Mineralogist* 84:650-64.

Chen, Q, Y Ke, L Zhang, M Tyrer, CD Hills, and G Xue. 2009. "Application of Accelerated Carbonation with a Combination of Na_2CO_3 and CO_2 in Cement-Based Solidification/Stabilization of Heavy Metal-Bearing Sediment." *Journal of Hazardous Materials* 166:421-27.

Clark, DL, DE Hobart, and MP Neu. 1995. "Actinide Carbonate Complexes and Their Importance in Actinide Environmental Chemistry." *Chemical Reviews* 95:25 - 48.

Cooper, MJ and DP Hodgkinson. 1987. *The Nirex Safety Assessment Research Programme: Annual Report for 1986/87.* Report No. NSS/R101, Nuclear Decommissioning Authority.

Cordfunke, EHP. 1969. *The Chemistry of Uranium*. Elsevier Publishing Company, Amsterdam, The Netherlands.

Cordfunke, EHP. 1964. "Heats of Formation of Some Hexavalent Uranium Compounds." *Journal of Physical Chemistry* 68(11):3353-56.

Crane, PJ, HL Benny, and MI Wood. 1992. *Physical Modeling of Contaminant Diffusion from a Cementitious Waste Form*. Report, Westinghouse Hanford Company, Richland, WA.

Crank, J. 1975. *The Mathematics of Diffusion*. 2nd ed., Clarendon Press, Oxford.

Dewaele, PJ, EJ Reardon, and R Dayal. 1991. "Permeability and Porosity Changes Associated with Cement Grout Carbonation." *Cement and Concrete Research* 21:441-54.

Elless, MP and SY Lee. 1994. *Physicochemical and Mineralogical Characterization of Transuranic Contaminated Soils for Uranium Soil Integrated Demonstration*. Report, Oak Ridge National Laboratory, Oak Ridge, TN.

Elless, MP and SY Lee. 1998. "Uranium Solubility of Carbonate-Rich Uranium-Contaminated Soils." *Water, Air, and Soil Pollution* 107:147-62.

Ewart, FT, JL Smith-Briggs, HP Thompson, SJ Williams. 1992. "The Solubility of Actinides in a Cementitious Near-Field Environment." *Waste Management* 12: 241-252.

Finch, RJ. 1997. "Thermodynamic Stabilities of U(Vi) Minerals: Estimated and Observed Relationships." *Material Research Society Symposium Proceedings* 465:1185-92.

Finch, RJ, EC Buck, PA Finn, and JK Bates. 1999. "Oxidative Corrosion of Spent UO_2 Fuel in Vapor and Dripping Groundwater at 90°C." In *Proceedings of 1998 Material Research Society Fall Meeting*.

Finch, RJ and RC Ewing. 1992. "The Corrosion of Uraninite under Oxidizing Conditions." *Journal of Nuclear Materials* 190:133-56.

Finney, DJ. 1971. *Probit Analysis*. 3rd ed., Cambridge University Press, Cambridge.

Garrabrants, AC, DS Kosson, R DeLapp, and HAvd Sloot. 2014. "Effect of Coal Combustion Fly Ash Use in Concrete on the Mass Transport Release of Constituents of Potential Concern." *Chemosphere* 103:131-39.

Garrabrants, AC, F Sanchez, C Gervais, P Moszkowicz, and DS Kosson. 2002. "The Effect of Storage in an Inert Atmosphere on the Release of Inorganic Constituents During Intermittent Wetting of a Cement-Based Material." *Journal of Hazardous Materials* B91:159-85.

Garrabrants, AC, F Sanchez, and DS Kosson. 2004. "Changes in Constituent Equilibrium Leaching and Pore Water Characteristics of a Portland Cement Mortar as a Result of Carbonation." *Waste Management* 24:19-36.

Garrels, RM and CL Christ. 1965. *Solutions, Minerals and Equilibria*. Harper and Row Publishing Co., New York, NY.

Gervais, C, AC Garrabrants, F Sanchez, R Barna, P Maszkowicz, and DS Kosson. 2004. "The Effects of Carbonation and Drying During Intermittent Leaching on the Release of Inorganic Constituents from a Cement-Based Matrix." *Cement and Concrete Research* 34:119-31.

Giergiczny, Z and A Krol. 2008. "Immobilization of Heavy Metals (Pb, Cu, Cr, Zn, Cd, Mn) in the Mineral Additions Containing Concrete Composites." *Journal of Hazardous Materials* 160:247-55.

Glasser, FP. 1997. "Fundamental Aspects of Cement Solidification and Stabilisation." *Journal of Hazardous Materials* 52:151-70.

Glasser, FP. 2001. "Mineralogical Aspects of Cement in Radioactive Waste Disposal." *Mineralogical Magazine* 65(5):621-33.

Glasser, FP, AA Rahman, D Macphee, MJ Angus, and M Atkins. 1985. *Immobilization of Radioactive Waste in Cement-Based Matrices*. Report, University of Aberdeen, Old Aberdeen.

Greenfield, BF, DJ Ilett, M Ito, R McCrohon, TG Heath, and CJ Tweed. 1998. "The Effect of Cement Additives on Radionuclide Solubilities." *Radiochimica Acta* 82:27-32.

Grenthe, I, J Fuger, RJM Konings, RJ Lemire, AB Muller, C Nguyen-Trung, and H Wanner. 1992. "Chemical Thermodynamics of Uranium." *Chemical Thermodynamics 1*, OECD Nuclear Energy Agency, Amsterdam.

Haque, MN and H Al-Khaiat. 1997. "Carbonation of Concrete Structures in Hot Dry Coastal Regions." *Cement and Concrete Composites* 19:123-29.

Harfouche, M, E Wieland, R Dahn, T Fujita, J Tits, D Kunz, and M Tsukamoto. 2006. "EXAFS Study of U(VI) Uptake by Calcium Silicate Hydrates." *Journal of Colloid and Interface Science* 303:195-204.

Hartmann, T, P Paviet-Hartmann, JB Rubin, MR Fitzsimmons, and KE Sickafus. 1999. "The Effect of Supercritical Carbon Dioxide Treatment on the Leachability and Structure of Cemented Radioactive Waste-Forms." *Waste Management* 19:355-61.

Hills, CD, REH Sweeney, and NR Buenfeld. 1999. "Microstructural Study of Carbonated Cement-Solidified Synthetic Heavy Metal Waste." *Waste Management* 19:325-31.

HNF-1981. 1998. *Specification for Concrete Encasement for Contact-Handled Category 3 Waste*, Rev. 0, Waste Management Federal Services of Hanford, Inc., Richland, Washington.

Hudson, EA, LJ Terminello, BE Viani, MA Denecke, T Reich, PG Allen, JJ Bucher, DK Shuh, and NM Edelstein. 1999. "The Structure of U (Super 6+) Sorption Complexes on Vermiculite and Hydrobiotite." *Clay and Clay Minerals* 47:439-57.

Kalmykov, SN and GR Choppin. 2000. "Mixed $Ca_2+/UO_22+/CO_32-$ Complex Formation at Different Ionic Strengths." *Radiochimica Acta* 88:603-06.

Khan, MI and CJ Lynsdale. 2002. "Strength, Permeability, and Carbonation of High-Performance Concrete." *Cement and Concrete Research* 32:123-31.

Kienzler, B, V Metz, B Brendebach, N Finck, M Plaschke, T Rabung, J Rothe, and D Schild. 2010. "Chemical Status of U(VI) in Cemented Waste Forms under Saline Conditions." *Radiochimica Acta* 98:675-84.

Kienzler, B, P Vejmelka, H-J Herbert, H Meyer, and C Altenhein-Haese. 2000. "Long-Term Leaching Experiments of Full-Scale Cemented Waste Forms: Experiments and Modeling." *Nuclear Technology* 129:101-18.

Kosson, DS, AC Garrabrants, R DeLapp, and HAvd Sloot. 2014. "Ph-Dependent Leaching of Constituents of Potential Concern from Concrete Materials Containing Coal Combustion Fly Ash." *Chemosphere* 103:140-47.

Kosson, DS, HAvd Sloot, F Sanchez, and AC Garrabrants. 2002. "An Integrated Framework for Evaluating Leaching in Waste Management and Utilization of Secondary Materials." *Environmental Engineering Science* 19(3):159-204.

Lamar, DW. (1989). *Measurement of Nitrate Diffusivity in Hanford Sediments via the Half-Cell Method.* Report, Pacific Northwest National Laboratory, Richland, WA.

Lange, LC, CD Hills, and AB Poole. 1996a. "The Effect of Accelerated Carbonation on the Properties of Cement-Solidified Waste Forms." *Waste Management* 16(8):757-63.

Lange, LC, CD Hills, and AB Poole. 1996b. "The Influence of Mix Parameters and Binder Choice on the Carbonation of Cement Solidified Wastes." *Waste Management* 16(8):749-56.

Lange, LC, CD Hills, and AB Poole. 1996c. "Preliminary Investigation into the Effects of Carbonation on Cement-Solidified Hazardous Wastes." *Environmental Science and Technology* 30(1):25-30.

Langmuir, D. 1997a. *Aqueous Environmental Chemistry*. Prentice-Hall, Upper Saddle River, NJ.

Langmuir, D. 1997b. "Aqueous Geochemistry of Uranium." In *Aqueous Environmental Chemistry*, ed. R McConnin, pp. 494 - 512. Prentice-Hall, Upper Saddle River.

Langmuir, D. 1978. "Uranium Solution-Mineral Equilbria at Low Temperatures with Applications to Sedimentary Ore Deposits." *Geochimica et Cosmochimica Acta* 42:547-69.

Lee, SY and JD Marsh. 1992. *Characterization of Uranium-Contaminated Soils from DOE Fernald Environmental Management Project Site: Results of Phase I Characterization.* Report, Oak Ridge National Laboratory, Oak Ridge, TN.

Lytle, FW, RB Greegor, DR Sandstrom, EC Marques, J Wong, CL Spiro, GP Huffman, and FE Huggins. 1984. "Measurement of Soft X-Ray Absorption Spectra with a Fluorescent Ion Chamber Detector." *Nuclear Instruments & Methods in Physics Research, Section A: Accelerators, Spectrometers, Detectors, and Associated Equipment* 226:542-48.

Macias, A, A Kindness, and FP Glasser. 1997. "Impact of Carbon Dioxide on the Immobilization Potential of Cemented Wastes: Chromium." *Cement and Concrete Research* 27(2):215-25.

Malviya, R and R Chaudhary. 2006. "Factors Affecting Hazardous Waste Solidification/Stabilization: A Review." *Journal of Hazardous Materials* B137:267-76.

Mann, FM, RJ Puigh II, SH Finfrock, J Freeman, E.J., R Khaleel, DH Bacon, MP Bergeron, PB McGrail, and SK Wurstner. 2001. *Hanford Immobilized Low-Activity Waste Performance Assessment: 2001 Version*. Report, Pacific Northwest National Laboratory, Richland, WA.

Martin, PF, RJ Serne, VL Legore, and CW Lindenmeier. 1994. *Status Report on Ionic Diffusion through Asphalt*. Report, Pacific Northwest National Laboratory, Richland, WA.

Maset, ER, SH Sidhu, A Fisher, A Heydon, PJ Worsfold, AJ Cartwright, and MJ Keith-Roach. 2006. "Effect of Organic Co-Contaminants on Technetium and Rhenium Speciation and Solubility under Reducing Conditions." *Environmental Science and Technology* 40(17):5472-77.

Mattigod, SV, GA Whyatt, KE Schwab, PF Martin, and RJ Serne. 1999. *Diffusion of Selected Radionuclides (^{129}I and ^{99}TC) through Degraded Concrete and Vault Fill Material: Progress Report for FY 99*. Report, Pacific Northwest National Laboratory, Richland, WA.

Mattigod, SV, GA Whyatt, RJ Serne, PF Martin, KE Schwab, and MI Wood. 2001. *Diffusion and Leaching of Selected Radionuclides (Iodine-129, Technetium-99, and Uranium) through Category 3 Waste Encasement Concrete and Soil Fill Material*. Report No. PNNL-13639, Pacific Northwest National Laboratory, Richland, WA.

Mattigod, SV, GA Whyatt, RJ Serne, and MI Wood. 2004. "Diffusion of Iodine and Technetium-99 through Waste Encasement Concrete and Unsaturated Soil Fill Material." Presented at *Material Research Society Symposium*, 391-98 pp.

Mattigod, SV, DM Wellman, EA Cordova, CC Bovaird, DJ Skinner, and MI Wood. 2009. *Effect of Concrete Waste Form Properties on Radionuclide Migration*. Report No. PNNL-18745, Pacific Northwest National Laboratory, Richland, WA.

Mattigod, SV, CC Bovaird, DM Wellman, and MI Wood. 2010. *Radionuclide Retention in Concrete Waste Forms*. Report No. PNNL-19823, Pacific Northwest National Laboratory, Richland, WA.

Mattigod, SV, CC Bovaird, DM Wellman, KE Parker, and MI Wood. 2012a. "An Experimental Study of Diffusivity of Technetium-99 in Hanford Vadose Zone Sediments." *Vadose Zone Journal* 11(4).

Mattigod, SV, DM Wellman, CC Bovaird, KE Parker, LN Clayton, L Powers, KP Recknagle, and MI Wood. 2011b. *Diffusion and Leaching Behavior of Radionuclides in Category 3 Waste Encasement Concrete and Soil Fill Material - Summary Report*. Report No. PNNL-20683, Pacific Northwest National Laboratory, Richland, WA.

Mattigod, SV, DM Wellman, CC Bovaird, KE Parker, KP Recknagle, L Clayton, and MI Wood. 2012b. "Diffusion of Radionuclides in Concrete and Soil." In *Radioactive Waste*, ed.. RA Rahman, pp. 331-50. InTech.

Matzen, SL, JM Beiriger, PC Torretto, P Zhao, and BE Viani. 2000. "Uranium(VI) and Neptunium(V) Transport through Fractured, Hydrothermally Altered Concrete." *Radiochimica Acta* 88:657-64.

McGlinn, PJ, DRM Brew, LP Aldridge, TE Payne, KP Olufson, KE Prince, and IJ Kelly. 2008. "Durability of a Cementitious Wasteform for Intermediate Level Waste." Presented at *Materials Research Society Symposium*, Materials Research Society.

Moroni, LP and FP Glasser. 1995. "Reactions between Cement Components and U(VI) Oxide." *Waste Management* 15:243-54.

Murakami, T, T Ohnuki, H Isobe, and T Sato. 1997. "Mobility of Uranium During Weathering." *American Mineralogist* 82:888-99.

Newville, M. 2001. "IFEFFIT: Interactive XAFS Anaylsis and FEFF Fitting." *Journal of Synchrotron Radiation* 8:322-24.

Nguyen, SN, RJ Silva, HC Weed, and J Andrews, John E. 1992. "Standard Gibbs Free Energies of Formation at the Temperature 303.15k of Four Uranyl Silicates: Soddyite, Uranophane, Sodium Boltwoodite, and Sodium Weeksite." *Journal of Chemical Thermodynamics* 25:359-76.

O'Hare, PAG, HR Hoekstra, and DR Frederickson. 1976. "Thermochemistry of Uranium Compounds: VII. Solution Calorimetry of Alpha and Beta-Na_2UO_4, Standard Enthalpy of Formation of Beta-Na2uo4 and the Enthalpy of the Alpha to Beta Transition at 298.15 K." *Journal of Chemical Thermodynamics* 8:255-58.

Ondrus, P, R Skala, F Veselovsky, J Sejkora, and C Vitti. 2003. "Cejkaite, the Triclinic Polymorph of $Na_4(UO_2)(CO_3)_3$ - a New Mineral from Jachymov, Czech Republic." *American Mineralogist* 88:686-93.

Papadakis, VG, CG Vayenas, and MN Fardis. 1989. "A Reaction Engineering Approach to the Problem of Concrete Carbonation." *American Institute of Chemical Engineers* 35(10):1639-50.

Pourbaix, M. 1966. *Atlas of Electrochemical Equilibria in Aqueous Solutions*. 2nd ed., Pergamon Press, Houston, TX.

Reich, T, H Moll, MA Denecke, G Geipel, G Bernhard, H Nitsche, PG Allen, JJ Bucher, N Kaltsoyannis, NM Edelstein, and DK Shuh. 1996. "Characterization of Hydrous Uranyl Silicate by EXAFS." *Radiochimica Acta* 74:219-24.

Sanchez, F, AC Garrabrants, and DS Kosson. 2003. "Effects of Intermittent Wetting on Concentration Profiles and Release from a Cement-Based Waste Matrix." *Environmental Engineering Science* 20(2):135-53.

Sanchez, F, C Gervais, AC Garrabrants, R Barna, and DS Kosson. 2002. "Leaching of Inorganic Contaminants from Cement-Based Waste Materials as a Result of Carbonation During Intermittent Wetting." *Waste Management* (22):249-60.

Sandino, A and J Bruno. 1992. "The Solubility of $(UO_2)_3(PO_4)_2 \cdot 4H_2O(S)$ and the Formation of U(VI) Phosphate Complexes: Their Influence Speciation in Natural Waters." *Geochimica et Cosmochimica Acta* 56:4135-45.

Sergeyeva, EI, AA Nikitin, IL Khodakovkiy, and GB Naumov. 1972. "Experimental Investigation of Equilibria in the System $UO_3\text{-}CO_2H_2O$ in 25 - 200°C Temperature Interval." *Geochemistry International* 9:900-10.

Serne, RJ, JL Conca, VL LeGore, KJ Cantrell, CW Lindenmeier, JA Campbell, JE Amonette, MI Wood. 1993a. *Solid-Waste Leach Characterization and Contaminant-Sediment Interactions*. Report, Pacific Northwest Laboratory, Richland, WA.

Serne, RJ, LL Ames, PFC Martin, VL LeGore, CW Lindenmeier, and SJ Phillips. 1993b. *Leach Testing of in Situ Stabilization Grouts Containing Additives to Sequester Contaminants*. Report, Pacific Northwest Laboratory, Richland, WA.

Serne, RJ, RO Lokken, and LJ Criscenti. 1992. "Characterization of Grouted LLW to Support Performance Assessment." *Waste Management* 12:271-87.

Serne, RJ, WJ Martin, and VL LeGore. 1995. *Leach Test of Cladding Removal Waste Grout Using Hanford Groundwater*. Report, Pacific Northwest Laboratory, Richland, WA.

Serne, RJ, WJ Martin, VL LeGore, CW Lindenmeier, SB McLaurine, PFC Martin, and RO Lokken. 1989. *Leach Tests on Grouts Made with Actual and Trace Metal-Spiked Synthetic Phosphate/Sulfate Waste*. Report, Pacific Northwest Laboratory, Richland, WA.

Sims, I. 1994. "The Assessment of Concrete for Carbonation." *Concrete* 28(6):33-38.

Smith, J, D. K. 1984. *Uranium Geochemistry, Mineralogy, Geology, Exploration, and Resources*. Institute of Mining and Metallurgy, London.

Snyder, MMV, EC Golovich, DM Wellman, JV Crum, R Lapierre, D Dage, KE Parker, and E Cordova. 2013. *Radionuclide Retention in Concrete Wasteforms-FY13*. Report No. PNNL-22880, Pacific Northwest National Laboratory, Richland, WA.

Spalding, BP. 2000. "Volatility and Extractability of Strontium-85, Cesium-134, Cobalt-57, and Uranium after Heating Hardened Portland Cement Paste." *Environmental Science and Technology* 34:5051-58.

Sposito, G. 1989. *The Chemistry of Soils*. Oxford University Press, New York, NY.

Sutton, M. 1999. *Uranium Solubility, Speciation and Complexation at High PH*. Loughborough University, PhD Doctoral.

Sutton, M, P Warwick, and A Hall. 2003. "Uranium (VI) Interactions with OPC/PFA Grout." *Journal of Environmental Monitoring* 5:922-28.

Sutton, M, P Warwick, A Hall, and C Jones. 1999. "Carbonate Induced Dissolution of Uranium Containing Precipitates under Cement Leachate Conditions." *Journal of Environmental Monitoring* 1:177.

Sylva, RN and MR Davidson. 1979. "The Hydrolysis of Metal Ions. Part 2. Dioxouranium (VI)." *Dalton Transactions* 8:465-71.

Sylwester, ER, PG Allen, P Zhao, and BE Viani. 1999. "Interactions of Uranium and Neptunium with Cementitious Materials Studied by XAFS." Presented at Materials Research Society.

Sylwester, ER, EA Hudson, and PG Allen. 2000. "The Structure of Uranium (VI) Sorption Complexes on Silica, Alumina, and Montmorillonite." *Geochimica et Cosmochimica Acta* 64(14):2431-38.

Szanto, Z, E Svingor, M Molnar, L Palcsu, I Futo, and Z Szucs. 2002. "Diffusion of ^{3}H, ^{99}TC, ^{125}I, ^{36}Cl and ^{85}Sr in Granite, Concrete and Bentonite." *Journal of Radioanalytical and Nuclear Chemistry* 252(1):133-38.

Taylor, HFW. 1990. *Cement Chemistry*. Academic Press, New York, NY.

Tidwell, VC, DE Morris, JC Cunnane, and SY Lee. 1996. "Characterizing Soils Contaminated with Heavy Metals: A Uranium Contamination Case Study." *Remediation Journal*:81-96.

U.S. Environmental Protection Agency (EPA). 2009. *Mass Transfer Rates of Constituents in Monolith or Compacted Granular Materials Using a Semi-Dynamic Tank Leaching Test*. Draft Method 1315.

van der Sloot, HA, Av Zomeren, JCL Meeussen, P Seignette, and R Bleijerveld. 2007. "Test Method Selection, Validation against Field Data, and Predictive Modelling for Impact Evaluation of Stabilised Waste Disposal." *Journal of Hazardous Materials* (141):354-69.

Venhuis, MA and EJ Reardon. 2001. "Vacuum Method for Carbonation of Cementitious Wasteforms." *Environmental Science and Technology* 35:4120-25.

Vochten, R and LV Haverbeke. 1990. "Transformation of Schoepite into the Uranyl Oxide Hydrates: Becquerelite, Billietite, and Wolsendorfite." *Contributions to Mineralogy and Petrology* 43:65-72.

Webb, SM. 2005. "SixPACK: A Graphical User Interface for XAS Anaylsis Using IFEFFIT." *Physica Scripta* T115:1011-1014.

Wellman, DM, JP Icenhower, AP Gamerdinger, and SW Forrester. 2006a. "Effects of pH, Temperature, and Aqueous Organic Material on the Dissolution Kinetics of Meta-Autunite Minerals, (Na, Ca)$_{2-1}$[(UO$_2$)(PO$_4$)]$_2$ 3H$_2$O." *American Mineralogist* 91:143-58.

Wellman, DM, SV Mattigod, GA Whyatt, L Powers, KE Parker, LN Clayton, and MI Wood. 2006b. *Diffusion of Iodine and Rhenium in Category 3 Waste Encasement Concrete and Soil Fill Material*. Report No. PNNL-16268, Pacific Northwest National Laboratory, Richland, WA.

Wellman, DM, KM Gunderson, JI Icenhower, and SW Forrester. 2007a. "Dissolution Kinetics of Synthetic and Natural Meta-Autunite Minerals, X_3-N^{n+}[(UO$_2$)(PO$_4$)]$_2$ xH$_2$O, under Acidic Conditions." *Geochemistry Geophysics Geosystems* 8(Q11001):1-16. DOI 10.1029/2007GC001695.

Wellman, DM, SV Mattigod, BW Arey, MI Wood, and SW Forrester. 2007b. "Experimental Limitations Regarding the Formation and Characterization of Uranium-Mineral Phases in Concrete Waste Forms." *Cement and Concrete Research* 37:151-60.

Wellman, DM, SV Mattigod, L Powers, KE Parker, LN Clayton, and MI Wood. 2007c. *Concrete Property and Radionuclide Migration Tests*. Report No. PNNL-17676, Pacific Northwest National Laboratory, Richland, WA.

Wellman, DM, CC Bovaird, SV Mattigod, KE Parker, RM Ermi, and MI Wood. 2008a. *Effect of Concrete Waste Form Properties on Radionuclide Migration*. Report No. PNNL-17808, Pacific Northwest National Laboratory, Richland, WA.

Wellman, DM, KE Parker, L Powers, GA Whyatt, LN Clayton, SV Mattigod, and MI Wood. 2008b. "Effect of Iron and Carbonation on the Diffusion of Iodine and Rhenium in Waste Encasement Concrete and Soil Fill Material under Hydraulically Unsaturated Conditions." *Applied Geochemistry* 23:2256-71.

Wellman, DM, DP Jansik, EC Golovich, and EA Cordova. 2012. *Radionuclide Retention in Concrete Wasteforms*. Report No. PNNL-21794, Pacific Northwest National Laboratory, Richland, WA.

Wolery, TJ. 1992. *EQ3NR, a Computer Program for Geochemical Aqueous Speciation-Solubility Calculations: Theoretical Manual, User's Guide, and Related Documentation (Version 7.0)*. Report, Lawrence Livermore National Laboratory, Livermore, CA.

Wood, MI, R Khaleel, PD Rittman, AH Lu, S Finfrock, RJ Serne, and KJ Cantrell. 1995. *Performance Assessment for the Disposal of Low-Level Waste in the 218-W-5 Burial Ground*. Report, Westinghouse Hanford Company, Richland, WA.

Yamamura, T, A Kitamura, A Fukui, S Nishikawa, T Yamamoto, and H Moriyama. 1998. "Solubility of U(Vi) in Highly Basic Solutions." *Radiochimica Acta* 83(3):139-46.

Zhao, P, PG Allen, ER Sylwester, and BE Viani. 1999. *The Partitioning of Uranium and Neptunium onto Hydrothermally Altered Concrete*. Report, Lawrence Livermore National Laboratory, Livermore, CA.

Appendix A

Leaching and Adsorption Tables

Appendix A

Leaching and Adsorption Tables

This appendix contains the incremental and cumulative leach fractions of iodine-125 (I-125) and technetium-99 (Tc-99) as well as the cumulative adsorbed uranium (U) from the American National Standards Institute (ANSI)-16.1 tests discussed in section 3.1. These data are also shown in Figure 3.1 and Figure 3.3.

Table A.1. ANSI leach test: I-125 leaching data for specimen 1 (without steel fibers)

Interval	Incremental Time (day)	Cumulative Time (day)	Incremental Leach Fraction	Cumulative Leach Fraction	D_{ei} (cm^2/s)	D_{ci} (cm^2/s)
1	0.09	0.09	5.91×10^{-3}	5.91×10^{-3}	6.55×10^{-10}	6.55×10^{-10}
2	0.21	0.29	1.91×10^{-3}	7.81×10^{-3}	9.48×10^{-11}	3.36×10^{-10}
3	0.77	1.06	9.48×10^{-4}	8.76×10^{-3}	5.96×10^{-12}	1.16×10^{-10}
4	0.94	2.00	3.61×10^{-4}	9.12×10^{-3}	1.43×10^{-12}	6.67×10^{-11}
5	1.00	3.00	5.40×10^{-4}	9.66×10^{-3}	4.63×10^{-12}	4.99×10^{-11}
6	1.00	4.00	5.16×10^{-4}	1.02×10^{-2}	5.95×10^{-12}	4.15×10^{-11}
7	1.00	5.00	4.13×10^{-4}	1.06×10^{-2}	4.91×10^{-12}	3.60×10^{-11}
8	13.99	18.99	7.54×10^{-4}	1.13×10^{-2}	2.03×10^{-13}	1.09×10^{-11}
9	29.94	48.93	6.73×10^{-4}	1.20×10^{-2}	1.04×10^{-13}	4.73×10^{-12}
10	42.99	91.92	4.18×10^{-3}	1.62×10^{-2}	4.17×10^{-12}	4.58×10^{-12}

Table A.2. ANSI leach test: Tc-99 leaching data (LCS data) for specimen 1 (without steel fibers)

Interval	Incremental Time (day)	Cumulative Time (day)	Incremental Leach Fraction	Cumulative Leach Fraction	D_{ei} (cm^2/s)	D_{ci} (cm^2/s)
1	0.09	0.09	4.25×10^{-2}	4.98×10^{-1}	3.39×10^{-8}	3.39×10^{-8}
2	0.21	0.29	9.54×10^{-3}	4.62×10^{-2}	2.38×10^{-9}	1.49×10^{-8}
3	0.77	1.06	3.28×10^{-3}	4.24×10^{-3}	7.13×10^{-11}	4.61×10^{-9}
4	0.94	2.00	2.19×10^{-3}	2.34×10^{-3}	5.24×10^{-11}	2.65×10^{-9}
5	1.00	3.00	2.64×10^{-3}	2.64×10^{-3}	1.11×10^{-10}	1.94×10^{-9}
6	1.00	4.00	2.77×10^{-3}	2.77×10^{-3}	1.71×10^{-10}	1.59×10^{-9}
7	1.00	5.00	2.55×10^{-3}	2.55×10^{-3}	1.86×10^{-10}	1.38×10^{-9}
8	13.99	18.99	2.15×10^{-3}	1.54×10^{-4}	1.65×10^{-12}	3.86×10^{-10}
9	29.94	48.93	1.13×10^{-3}	3.78×10^{-5}	2.95×10^{-13}	1.55×10^{-10}
10	42.99	91.92	1.22×10^{-3}	2.85×10^{-5}	3.58×10^{-13}	8.55×10^{-11}

Table A.3. ANSI leach test: Tc-99 leaching data (ICP-MS data) for specimen 1 (without steel fibers)

Interval	Incremental Time (day)	Cumulative Time (day)	Incremental Leach Fraction	Cumulative Leach Fraction	D_{ei} (cm^2/s)	D_{ci} (cm^2/s)
1	0.09	0.09	4.28×10^{-2}	5.02×10^{-1}	3.45×10^{-8}	3.45×10^{-8}
2	0.21	0.29	6.96×10^{-3}	3.37×10^{-2}	1.26×10^{-9}	1.36×10^{-8}
3	0.77	1.06	3.05×10^{-3}	3.95×10^{-3}	6.18×10^{-11}	4.21×10^{-9}
4	0.94	2.00	1.56×10^{-3}	1.67×10^{-3}	2.66×10^{-11}	2.37×10^{-9}
5	1.00	3.00	9.25×10^{-4}	9.25×10^{-4}	1.36×10^{-11}	1.64×10^{-9}
6	1.00	4.00	5.48×10^{-4}	5.48×10^{-4}	6.70×10^{-12}	1.25×10^{-9}
8	13.99	18.99	9.89×10^{-4}	7.07×10^{-5}	3.48×10^{-13}	1.00×10^{-9}
9	29.94	48.93	6.40×10^{-5}	2.14×10^{-6}	9.45×10^{-16}	2.73×10^{-10}
10	42.99	91.92	4.27×10^{-5}	9.93×10^{-7}	4.34×10^{-16}	1.06×10^{-10}

Table A.4. ANSI leach test: U adsorption data (ICP-MS data) for specimen 1 (without steel fibers)

Interval	Incremental Time (day)	Cumulative Time (day)	Incremental Adsorbed (ng)	Cumulative Adsorbed (ng)
1	0.09	0.09	338.1	338.1
2	0.21	0.29	323.5	662
3	0.77	1.06	239.8	901
4	0.94	2.00	208.6	1110
5	1.00	3.00	205.6	1316
6	1.00	4.00	185.3	1501
7	1.00	5.00	204.5	1705
8	13.99	18.99	231.9	1937
9	29.94	48.93	153.7	2091
10	42.99	91.92	221.4	2312

Table A.5. ANSI leach test: I-125 leaching data for specimen 2 (without steel fibers)

Interval	Incremental Time (day)	Cumulative Time (day)	Incremental Leach Fraction	Cumulative Leach Fraction	D_{ei} (cm^2/s)	D_{ci} (cm^2/s)
1	0.09	0.09	3.90×10^{-3}	4.56×10^{-2}	2.8×10^{-10}	2.8×10^{-10}
2	0.21	0.29	1.57×10^{-3}	7.61×10^{-3}	6.4×10^{-11}	1.6×10^{-10}
3	0.77	1.06	3.56×10^{-4}	4.61×10^{-4}	8.3×10^{-13}	5.1×10^{-11}
4	0.94	2.00	4.75×10^{-4}	5.07×10^{-4}	2.4×10^{-12}	3.1×10^{-11}
5	1.00	3.00	2.43×10^{-4}	2.43×10^{-4}	9.3×10^{-13}	2.3×10^{-11}
6	1.00	4.00	3.13×10^{-4}	3.13×10^{-4}	2.2×10^{-12}	1.9×10^{-11}
7	1.00	5.00	1.83×10^{-4}	1.83×10^{-4}	9.5×10^{-13}	1.6×10^{-11}
8	13.99	18.99	6.53×10^{-4}	4.67×10^{-5}	1.5×10^{-13}	4.9×10^{-12}
9	29.94	48.93	3.28×10^{-4}	1.10×10^{-5}	2.5×10^{-14}	2.1×10^{-12}
10	42.99	91.92	4.90×10^{-3}	1.14×10^{-4}	5.7×10^{-12}	2.9×10^{-12}

Table A.6. ANSI leach test: Tc-99 leaching data (LCS data) for specimen 2 (without steel fibers)

Interval	Incremental Time (day)	Cumulative Time (day)	Incremental Leach Fraction	Cumulative Leach Fraction	D_{ei} (cm^2/s)	D_{ci} (cm^2/s)
1	0.09	0.09	2.76×10^{-2}	3.23×10^{-1}	1.41×10^{-8}	1.41×10^{-8}
2	0.21	0.29	7.93×10^{-3}	3.85×10^{-2}	1.63×10^{-9}	6.87×10^{-9}
3	0.77	1.06	2.76×10^{-3}	3.58×10^{-3}	5.02×10^{-11}	2.19×10^{-9}
4	0.94	2.00	2.57×10^{-3}	2.75×10^{-3}	7.19×10^{-11}	1.32×10^{-9}
5	1.00	3.00	2.01×10^{-3}	2.01×10^{-3}	6.37×10^{-11}	9.72×10^{-10}
6	1.00	4.00	1.64×10^{-3}	1.64×10^{-3}	5.98×10^{-11}	7.86×10^{-10}
7	1.00	5.00	1.53×10^{-3}	1.53×10^{-3}	6.65×10^{-11}	6.73×10^{-10}
8	13.99	18.99	2.07×10^{-3}	1.48×10^{-4}	1.51×10^{-12}	1.94×10^{-10}
9	29.94	48.93	1.97×10^{-3}	6.59×10^{-5}	8.88×10^{-13}	8.14×10^{-11}
10	42.99	91.92	1.28×10^{-3}	2.97×10^{-5}	3.86×10^{-13}	4.56×10^{-11}

Table A.7. ANSI leach test: U adsorption data (ICP-MS data) for specimen 2 (without steel fibers)

Interval	Incremental Time (day)	Cumulative Time (day)	Incremental Adsorbed (ng)	Cumulative Adsorbed (ng)
1	0.09	0.09	370.1	370
2	0.21	0.29	351.8	722
3	0.77	1.06	182.1	904
4	0.94	2.00	181.5	1085
5	1.00	3.00	166.9	1252
6	1.00	4.00	204.6	1457
7	1.00	5.00	171.9	1629
8	13.99	18.99	195.8	1825
9	29.94	48.93	180.1	2005
10	42.99	91.92	143.7	2149

Table A.8. ANSI leach test: I-125 leaching data for specimen 6 (with steel fibers)

Interval	Incremental Time (day)	Cumulative Time (day)	Incremental Leach Fraction	Cumulative Leach Fraction	D_{ei} (cm^2/s)	D_{ci} (cm^2/s)
1	0.09	0.09	4.92×10^{-3}	5.71×10^{-2}	4.63×10^{-10}	4.63×10^{-10}
2	0.21	0.29	4.89×10^{-4}	2.37×10^{-3}	6.43×10^{-12}	1.65×10^{-10}
3	0.77	1.07	7.48×10^{-4}	9.67×10^{-4}	3.81×10^{-12}	5.85×10^{-11}
4	0.94	2.00	4.75×10^{-4}	5.07×10^{-4}	2.54×10^{-12}	3.62×10^{-11}
5	1.00	3.00	5.39×10^{-4}	5.39×10^{-4}	4.74×10^{-12}	2.82×10^{-11}
6	1.00	4.00	4.38×10^{-4}	4.38×10^{-4}	4.40×10^{-12}	2.38×10^{-11}
7	1.00	5.00	4.38×10^{-4}	4.38×10^{-4}	5.68×10^{-12}	2.13×10^{-11}
8	13.99	18.99	7.48×10^{-4}	5.35×10^{-5}	2.05×10^{-13}	6.71×10^{-12}
9	29.94	48.93	5.83×10^{-4}	1.95×10^{-5}	8.04×10^{-14}	2.96×10^{-12}
10	42.99	91.92	3.87×10^{-3}	9.01×10^{-5}	3.68×10^{-12}	3.14×10^{-12}

Table A.9. ANSI leach test: Tc-99 leaching data (LCS data) for specimen 6 (with steel fibers)

Interval	Incremental Time (day)	Cumulative Time (day)	Incremental Leach Fraction	Cumulative Leach Fraction	D_{ei} (cm²/s)	D_{ci} (cm²/s)
1	0.09	0.09	3.56×10^{-2}	4.13×10^{-1}	2.42×10^{-8}	2.42×10^{-8}
2	0.21	0.29	4.77×10^{-3}	2.31×10^{-2}	6.13×10^{-10}	9.17×10^{-9}
3	0.77	1.07	3.46×10^{-3}	4.48×10^{-3}	8.18×10^{-11}	2.97×10^{-9}
4	0.94	2.00	2.39×10^{-3}	2.56×10^{-3}	6.46×10^{-11}	1.76×10^{-9}
5	1.00	3.00	1.09×10^{-3}	1.09×10^{-3}	1.93×10^{-11}	1.23×10^{-9}
6	1.00	4.00	1.64×10^{-3}	1.64×10^{-3}	6.17×10^{-11}	9.86×10^{-10}
7	1.00	5.00	1.99×10^{-3}	1.99×10^{-3}	1.17×10^{-10}	8.54×10^{-10}
8	13.99	18.99	1.77×10^{-3}	1.26×10^{-4}	1.14×10^{-12}	2.41×10^{-10}
9	29.94	48.93	1.99×10^{-3}	6.64×10^{-5}	9.37×10^{-13}	1.01×10^{-10}
10	42.99	91.92	1.30×10^{-3}	3.03×10^{-5}	4.16×10^{-13}	5.61×10^{-11}

Table A.10. ANSI leach test: U adsorption data (ICP-MS data) for specimen 6 (with steel fibers)

Interval	Incremental Time (day)	Cumulative Time (day)	Incremental Adsorbed (ng)	Cumulative Adsorbed (ng)
1	0.09	0.09	417.8	370
2	0.21	0.29	-52.8	317
3	0.77	1.07	220.4	538
4	0.94	2.00	202.8	741
5	1.00	3.00	201.9	942
6	1.00	4.00	188.6	1131
7	1.00	5.00	206.6	1338
8	13.99	18.99	168.8	1506
9	29.94	48.93	213.1	1719
10	42.99	91.92	180.6	1900

Table A.11. ANSI leach test: I-125 leaching data for specimen 7 (with steel fibers)

Interval	Incremental Time (day)	Cumulative Time (day)	Incremental Leach Fraction	Cumulative Leach Fraction	D_{ei} (cm²/s)	D_{ci} (cm²/s)
1	0.09	0.09	4.86×10^{-3}	5.64×10^{-2}	4.40×10^{-10}	4.40×10^{-10}
2	0.21	0.29	1.64×10^{-3}	7.94×10^{-3}	7.03×10^{-11}	2.31×10^{-10}
3	0.77	1.07	7.25×10^{-4}	9.38×10^{-4}	3.49×10^{-12}	7.85×10^{-11}
4	0.94	2.00	6.80×10^{-4}	7.27×10^{-4}	5.07×10^{-12}	5.00×10^{-11}
5	1.00	3.00	5.39×10^{-4}	5.39×10^{-4}	4.61×10^{-12}	3.81×10^{-11}
6	1.00	4.00	6.93×10^{-4}	6.93×10^{-4}	1.07×10^{-11}	3.34×10^{-11}
7	1.00	5.00	4.77×10^{-4}	4.77×10^{-4}	6.54×10^{-12}	2.96×10^{-11}
8	13.99	18.99	5.57×10^{-4}	3.98×10^{-5}	1.10×10^{-13}	8.73×10^{-12}
9	29.94	48.93	5.92×10^{-4}	1.98×10^{-5}	8.07×10^{-14}	3.79×10^{-12}
10	42.99	91.92	3.87×10^{-3}	9.00×10^{-5}	3.57×10^{-12}	3.73×10^{-12}

Table A.12. ANSI leach test: Tc-99 leaching data (LCS data) for specimen 7 (with steel fibers)

Interval	Incremental Time (day)	Cumulative Time (day)	Incremental Leach Fraction	Cumulative Leach Fraction	D_{ei} (cm^2/s)	D_{ci} (cm^2/s)
1	0.09	0.09	3.52×10^{-2}	4.09×10^{-1}	2.31×10^{-8}	2.31×10^{-8}
2	0.21	0.29	5.11×10^{-3}	2.48×10^{-2}	6.86×10^{-10}	8.93×10^{-9}
3	0.77	1.07	3.70×10^{-3}	4.79×10^{-3}	9.09×10^{-11}	2.92×10^{-9}
4	0.94	2.00	2.86×10^{-3}	3.06×10^{-3}	8.99×10^{-11}	1.76×10^{-9}
5	1.00	3.00	1.42×10^{-3}	1.42×10^{-3}	3.18×10^{-11}	1.25×10^{-9}
6	1.00	4.00	2.45×10^{-3}	2.45×10^{-3}	1.35×10^{-10}	1.03×10^{-9}
7	1.00	5.00	1.49×10^{-3}	1.49×10^{-3}	6.37×10^{-11}	8.77×10^{-10}
8	13.99	18.99	2.61×10^{-3}	1.87×10^{-4}	2.43×10^{-12}	2.54×10^{-10}
9	29.94	48.93	1.28×10^{-3}	4.28×10^{-5}	3.79×10^{-13}	1.03×10^{-10}
10	42.99	91.92	1.55×10^{-3}	3.61×10^{-5}	5.76×10^{-13}	5.81×10^{-11}

Table A.13. ANSI leach test: U adsorption data (ICP-MS data) for specimen 7 (with steel fibers)

Interval	Incremental Time (day)	Cumulative Time (day)	Incremental Adsorbed (ng)	Cumulative Adsorbed (ng)
1	0.09	0.09	398.4	370.1
2	0.21	0.29	310.9	681.0
3	0.77	1.07	225.9	906.9
4	0.94	2.00	192.2	1099.1
5	1.00	3.00	201.7	1300.8
6	1.00	4.00	187.8	1488.6
7	1.00	5.00	220.1	1708.8
8	13.99	18.99	178.5	1887.3
9	29.94	48.93	171.7	2059.0
10	42.99	91.92	154.1	2213.1

Appendix B

Half-Cell Diffusion Concentration Tables

Appendix B

Half-Cell Diffusion Concentration Tables

This appendix contains the concentration profiles for the half-cell diffusion tests described in section 4.0. These tables are organized by contaminant, then by type of diffusion test.

B.1 Iodine Concentrations

B.1.1   Sediment to Sediment

Table B.1. Concentrations of I in sediment from sediment-sediment half-cell experiments

4% Moisture Content		7% Moisture Content	
Distance from Spiked End (cm)	Stable I (mg/g sediment)	Distance from Spiked End (cm)	Stable I (mg/g sediment)
1.50	7.43×10^{-1}	1.50	6.56×10^{-1}
4.42	6.83×10^{-1}	4.59	6.09×10^{-1}
7.60	6.60×10^{-1}	7.67	5.78×10^{-1}
10.54	5.84×10^{-1}	10.61	4.61×10^{-1}
13.14	4.68×10^{-1}	13.48	3.70×10^{-1}
16.03	2.34×10^{-1}	15.13	3.10×10^{-1}
17.50	2.22×10^{-1}	15.61	2.89×10^{-1}
18.08	2.25×10^{-1}	16.10	2.66×10^{-1}
19.06	1.78×10^{-1}	16.60	2.33×10^{-1}
19.76	2.25×10^{-1}	17.08	2.41×10^{-1}
20.21	1.83×10^{-1}	17.61	2.32×10^{-1}
20.60	1.96×10^{-1}	18.24	2.15×10^{-1}
21.22	1.61×10^{-1}	18.80	1.91×10^{-1}
21.87	1.32×10^{-1}	19.26	1.84×10^{-1}
22.28	1.27×10^{-1}	19.67	1.72×10^{-1}
22.60	1.17×10^{-1}	20.19	1.61×10^{-1}
23.06	1.02×10^{-1}	20.75	1.50×10^{-1}
23.75	6.68×10^{-2}	21.24	1.35×10^{-1}
24.57	6.32×10^{-2}	21.73	1.27×10^{-1}
25.61	4.41×10^{-2}	22.24	1.18×10^{-1}
26.66	3.04×10^{-2}	22.76	1.09×10^{-1}
27.72	1.91×10^{-2}	23.29	9.41×10^{-2}
28.84	1.30×10^{-2}	24.02	7.37×10^{-2}
29.86	8.25×10^{-3}	25.00	6.06×10^{-2}
30.86	7.74×10^{-3}	25.98	4.81×10^{-2}
31.84	2.67×10^{-4}	26.94	4.43×10^{-2}
32.87	1.51×10^{-3}	27.92	2.96×10^{-2}
33.84	8.87×10^{-4}	28.87	2.83×10^{-2}
34.72	5.77×10^{-4}	29.83	1.66×10^{-2}
35.71	3.93×10^{-4}	30.89	1.53×10^{-2}
36.78	2.83×10^{-4}	31.83	1.03×10^{-2}
37.85	2.55×10^{-4}	32.79	7.83×10^{-3}
-	-	33.79	4.90×10^{-3}
-	-	34.72	4.16×10^{-3}
-	-	35.74	2.11×10^{-3}
-	-	36.70	2.70×10^{-3}
-	-	37.40	1.30×10^{-3}

B.1.2 Sediment to Concrete

Table B.2. Concentrations of I in sediment from FY 2006 sediment-concrete half-cell experiments

Distance from Core (cm)	I (mg/g sediment)	Distance from Core (cm)	I (mg/g sediment)	Distance from Core (cm)	I (mg/g sediment)	Distance From Core (cm)	I (mg/g sediment)
4% Sediment Moisture, Non-Carbonated 0% Iron		4% Sediment Moisture, Non-Carbonated 4% Iron		4% Sediment Moisture, Carbonated 0% Iron		4% Sediment Moisture, Carbonated 4% Iron	
Interface	8.1	Interface	10.3	Interface	9.8	Interface	8.8
0.3	9.6	0.3	10.8	0.3	10.3	0.3	9.3
0.8	9.6	0.8	7.0	0.8	9.5	0.8	8.6
1.5	9.5	1.5	10.7	1.5	10.1	1.5	9.0
2.5	10.5	2.5	10.8	2.5	10.7	2.5	9.1
3.5	10.4	3.5	11.7	3.5	11.0	3.5	9.3
4.5	10.1	4.5	10.8	4.5	11.4	4.5	9.7
5.5	10.6	5.5	11.3	5.5	13.0	5.5	9.7
7.0	10.0	7.0	11.4	7.0	9.8	7.0	10.0
9.0	10.5	9.0	12.2	9.0	10.4	9.0	9.9
7% Sediment Moisture, Non-Carbonated 0% Iron		7% Sediment Moisture, Non-Carbonated 4% Iron		7% Sediment Moisture, Carbonated 0% Iron		7% Sediment Moisture, Carbonated 4% Iron	
Interface	8.5	Interface	9.1	Interface	8.2	Interface	8.3
0.3	10.0	0.3	9.9	0.3	9.1	0.3	8.8
0.8	10.0	0.8	10.0	0.8	8.5	0.8	8.9
1.5	10.2	1.5	10.3	1.5	8.5	1.5	8.4
2.5	10.4	2.5	10.0	2.5	8.7	2.5	8.5
3.5	10.3	3.5	10.2	3.5	8.7	3.5	8.5
4.5	10.0	4.5	10.3	4.5	8.6	4.5	8.8
5.5	11.0	5.5	10.3	5.5	8.4	5.5	8.6
7.0	9.8	7.0	10.3	7.0	9.3	7.0	9.2
9.0	9.5	9.0	10.8	9.0	9.1	9.0	8.7
15% Sediment Moisture, Non-Carbonated 0% Iron		15% Sediment Moisture, Non-Carbonated 4% Iron		15% Sediment Moisture, Carbonated 0% Iron		15% Sediment Moisture, Carbonated 4% Iron	
Interface	10.3	Interface	9.1	Interface	10.3	Interface	8.1
0.3	10.3	0.3	10.1	0.3	10.0	0.3	11.4
0.8	11.5	0.8	9.9	0.8	10.1	0.8	9.9
1.5	12.0	1.5	10.1	1.5	10.3	1.5	10.3
2.5	12.6	2.5	11.1	2.5	9.9	2.5	10.1
3.5	10.7	3.5	10.4	3.5	10.1	3.5	9.8
4.5	11.4	4.5	10.3	4.5	10.2	4.5	10.4
5.5	10.5	5.5	10.0	5.5	10.1	5.5	10.4
7.0	10.7	7.0	10.0	7.0	8.0	7.0	9.1
9.0	9.8	9.0	8.7	9.0	9.0	9.0	8.4

Table B.3. Concentrations of I in concrete from FY 2006 sediment-concrete half-cell experiments

Distance from Face (mm)	I (mg/g concrete)	Distance from Face (mm)	I (mg/g concrete)	Distance from Face (mm)	I (mg/g concrete)	Distance from Face (mm)	I (mg/g concrete)
4% Sediment Moisture, Non-Carbonated 0% Iron		4% Sediment Moisture, Non-Carbonated 4% Iron		4% Sediment Moisture, Carbonated 0% Iron		4% Sediment Moisture, Carbonated 4% Iron	
1.80	43.20	1.50	56.79	1.20	21.28	1.30	33.93
4.41	35.78	3.21	14.07	2.51	33.53	2.90	55.87
7.52	19.06	6.12	3.32	6.32	14.73	6.10	27.11
11.63	7.36	10.53	2.01	13.73	4.08	9.20	8.01
14.44	4.46	13.74	1.59	23.14	1.20	13.80	5.34
20.85	3.59	19.75	0.89	29.65	0.82	18.50	5.39
29.26	1.87	28.06	0.80	38.56	1.65	27.10	4.66
33.47	1.45	36.27	0.56	41.47	1.76	35.20	1.93
7% Sediment Moisture, Non-Carbonated 0% Iron		7% Sediment Moisture, Non-Carbonated 4% Iron		7% Sediment Moisture, Carbonated 0% Iron		7% Sediment Moisture, Carbonated 4% Iron	
1.30	14.89	1.40	18.21	1.54	10.89	2.90	17.65
6.99	14.69	4.11	12.27	4.74	14.89	5.71	19.66
9.46	8.76	7.12	7.36	7.24	15.34	8.52	16.94
12.30	7.67	9.43	4.56	10.29	12.74	12.33	12.04
16.96	3.37	13.54	2.44	13.15	2.50	17.14	9.30
20.41	1.07	17.55	1.17	22.17	7.13	20.55	5.62
28.40	1.12	20.16	0.80	27.33	3.92	29.16	2.05
34.20	1.46	29.27	0.58	31.22	2.87	38.37	1.81
15% Sediment Moisture, Non-Carbonated 0% Iron		15% Sediment Moisture, Non-Carbonated 4% Iron		15% Sediment Moisture, Carbonated 0% Iron		15% Sediment Moisture, Carbonated 4% Iron	
1.69	12.91	1.49	18.95	1.40	7.25	1.97	8.41
3.58	10.90	3.87	19.08	4.11	12.28	4.14	13.35
5.88	7.54	5.95	17.18	7.12	13.60	7.96	12.42
7.87	6.16	7.91	17.13	9.43	10.73	10.69	10.23
10.44	4.07	9.78	16.54	13.54	11.57	13.85	9.32
12.67	3.09	11.77	13.99	17.55	10.62	18.14	6.35
15.23	2.55	14.57	8.51	20.16	8.39	22.68	3.38
17.54	1.84	16.56	4.22	29.27	6.33	-	-

Table B.4. Concentrations of I in sediment from FY 2008 sediment-concrete half-cell experiments

Distance from Core (cm)	I (mg/g sediment)	Distance from Core (cm)	I (mg/g sediment)	Distance from Core (cm)	I (mg/g sediment)	Distance From Core (cm)	I (mg/g sediment)
4% Sediment Moisture, Carbonated 0% Iron		4% Sediment Moisture, Carbonated 4% Iron		4% Sediment Moisture, Carbonated 8% Iron		4% Sediment Moisture, Carbonated 12% Iron	
0.25	4.47	0.25	3.40	0.25	2.93	0.25	3.49
0.75	4.87	0.75	4.08	0.75	3.38	0.75	3.54
1.25	5.11	1.25	4.11	1.25	3.65	1.25	3.34
2.00	4.76	2.00	4.16	2.00	3.70	2.00	4.01
3.00	4.83	3.00	4.29	3.00	3.87	3.00	4.15
4.00	4.72	4.00	4.56	4.00	4.53	4.00	4.17
5.00	4.86	5.00	4.26	5.00	4.39	5.00	4.20
6.00	5.17	6.00	4.39	6.00	4.32	6.00	4.41
7.50	4.98	7.50	4.95	7.50	4.37	7.50	4.48
9.50	5.05	9.50	4.38	9.50	4.43	9.50	4.54
4% Sediment Moisture, Non-Carbonated 0% Iron		4% Sediment Moisture, Non-Carbonated 4% Iron		4% Sediment Moisture, Non-Carbonated 8% Iron		4% Sediment Moisture, Non-Carbonated 12% Iron	
0.25	4.05	0.25	2.16	0.25	3.33	0.25	2.74
0.75	4.26	0.75	1.96	0.75	3.85	0.75	2.99
1.25	4.05	1.25	2.19	1.25	3.99	1.25	3.30
2.00	4.17	2.00	2.79	2.00	4.05	2.00	3.25
3.00	4.40	3.00	2.90	3.00	4.30	3.00	3.53
4.00	4.16	4.00	3.07	4.00	4.24	4.00	3.79
5.00	4.22	5.00	3.35	5.00	4.17	5.00	3.71
6.00	4.24	6.00	3.29	6.00	4.34	6.00	4.04
7.50	4.37	7.50	4.04	7.50	4.36	7.50	4.24
9.50	4.65	9.50	3.85	9.50	4.44	9.50	4.20
7% Sediment Moisture, Carbonated 0% Iron		7% Sediment Moisture, Carbonated 4% Iron		7% Sediment Moisture, Carbonated 8% Iron		7% Sediment Moisture, Carbonated 12% Iron	
0.25	3.99	0.25	6.05	0.25	3.85	0.25	6.48
0.75	6.24	0.75	6.15	0.75	4.53	0.75	4.79
1.25	5.56	1.25	6.26	1.25	4.19	1.25	4.59
2.00	4.93	2.00	6.15	2.00	4.25	2.00	4.84
3.00	5.14	3.00	5.94	3.00	3.07	3.00	4.77
4.00	5.26	4.00	6.13	4.00	4.28	4.00	4.88
5.00	5.17	5.00	5.87	5.00	4.54	5.00	4.60
6.00	5.51	6.00	6.18	6.00	4.42	6.00	4.96
7.50	5.38	7.50	5.95	7.50	4.47	7.50	4.64
9.50	5.28	9.50	6.66	9.50	4.61	9.50	5.13
7% Sediment Moisture, Non-Carbonated 0% Iron		7% Sediment Moisture, Non-Carbonated 4% Iron		7% Sediment Moisture, Non-Carbonated 8% Iron		7% Sediment Moisture, Non-Carbonated 12% Iron	
0.25	5.39	0.25	1.84	0.25	4.39	0.25	4.42
0.75	4.74	0.75	1.78	0.75	4.56	0.75	5.02
1.25	4.92	1.25	1.85	1.25	3.47	1.25	4.74
2.00	4.91	2.00	2.72	2.00	4.52	2.00	4.55
3.00	4.59	3.00	2.42	3.00	4.69	3.00	4.93
4.00	4.80	4.00	2.53	4.00	4.94	4.00	4.59
5.00	5.13	5.00	2.90	5.00	4.65	5.00	4.50
6.00	5.63	6.00	3.41	6.00	4.94	6.00	4.77
7.50	5.13	7.50	3.62	7.50	4.86	7.50	4.75
9.50	5.16	9.50	4.08	9.50	4.93	9.50	4.84

Distance from Core (cm)	I (mg/g sediment)	Distance from Core (cm)	I (mg/g sediment)	Distance from Core (cm)	I (mg/g sediment)	Distance From Core (cm)	I (mg/g sediment)
15% Sediment Moisture, Carbonated 0% Iron		15% Sediment Moisture, Carbonated 4% Iron		15% Sediment Moisture, Carbonated 8% Iron		15% Sediment Moisture, Carbonated 12% Iron	
0.25	5.63	0.25	6.28	0.25	4.09	0.25	3.79
0.75	4.92	0.75	5.92	0.75	4.31	0.75	3.74
1.25	4.98	1.25	5.84	1.25	4.01	1.25	3.52
2.00	4.83	2.00	6.29	2.00	3.82	2.00	3.62
3.00	5.17	3.00	6.25	3.00	3.71	3.00	3.29
4.00	4.76	4.00	6.10	4.00	3.93	4.00	3.53
5.00	5.25	5.00	6.46	5.00	4.11	5.00	3.48
6.00	4.72	6.00	6.71	6.00	4.12	6.00	3.29
7.50	5.11	7.50	6.25	7.50	3.88	7.50	3.84
9.50	4.71	9.50	6.21	9.50	3.97	9.50	7.57
15% Sediment Moisture, Non-Carbonated 0% Iron		15% Sediment Moisture, Non-Carbonated 4% Iron		15% Sediment Moisture, Non-Carbonated 8% Iron		15% Sediment Moisture, Non-Carbonated 12% Iron	
0.25	9.79	0.25	4.42	0.25	3.19	0.25	3.78
0.75	9.32	0.75	5.18	0.75	3.97	0.75	5.55
1.25	7.20	1.25	4.80	1.25	4.01	1.25	5.59
2.00	6.86	2.00	5.50	2.00	3.48	2.00	5.41
3.00	6.64	3.00	5.76	3.00	3.57	3.00	5.47
4.00	6.59	4.00	4.77	4.00	3.38	4.00	5.31
5.00	6.48	5.00	5.48	5.00	3.46	5.00	4.99
6.00	6.92	6.00	4.74	6.00	3.77	6.00	5.15
7.50	5.70	7.50	4.76	7.50	3.60	7.50	5.31
9.50	5.61	9.50	4.38	9.50	3.55	9.50	4.92

Table B.5. Concentrations of I in concrete from FY 2008 sediment-concrete half-cell experiments

Distance from Face (mm)	I (mg/g concrete)	Distance from Face (mm)	I (mg/g concrete)	Distance from Face (mm)	I (mg/g concrete)	Distance from Face (mm)	I (mg/g concrete)
4% Sediment Moisture, Carbonated 0% Iron		4% Sediment Moisture, Carbonated 4% Iron		4% Sediment Moisture, Carbonated 8% Iron		4% Sediment Moisture, Carbonated 12% Iron	
2.91	11.58	1.48	21.20	2.44	14.18	2.03	13.41
9.49	5.76	5.18	11.38	6.77	8.58	5.55	10.85
15.14	2.38	9.83	8.15	11.1	4.25	10.19	7.07
19.91	1.90	14.59	4.21	15.89	2.31	15.59	4.21
24.08	1.51	18.58	2.96	19.96	1.72	19.06	3.89
27.35	1.85	22.23	2.19	23.52	1.28	22.43	2.79
30.92	1.52	25.61	1.53	27.13	1.01	26.42	2.04
35.13	1.71	28.94	1.01	30.97	0.84	29.78	1.49
40.62	1.33	32.49	0.73	35.60	0.65	32.57	0.91
-	-	36.55	0.56	41.47	0.46	36.48	0.65
4% Sediment Moisture, Non-Carbonated 0% Iron		4% Sediment Moisture, Non-Carbonated 4% Iron		4% Sediment Moisture, Non-Carbonated 8% Iron		4% Sediment Moisture, Non-Carbonated 12% Iron	
1.61	19.08	2.02	17.07	1.70	16.17	1.77	20.94
5.53	11.76	5.81	10.43	6.13	8.94	5.23	13.41
10.63	8.37	10.05	6.56	11.32	4.72	9.82	8.09
15.55	4.26	14.22	3.79	16.43	3.17	15.23	3.92
19.70	2.80	17.56	2.72	20.48	2.46	19.95	2.95
23.97	2.22	20.96	2.43	23.77	2.81	23.94	2.91
28.07	1.42	24.41	1.93	27.21	2.72	27.63	2.28

Distance from Face (mm)	I (mg/g concrete)	Distance from Face (mm)	I (mg/g concrete)	Distance from Face (mm)	I (mg/g concrete)	Distance from Face (mm)	I (mg/g concrete)
32.22	1.30	27.69	1.47	30.57	2.75	31.43	1.58
38.20	0.88	31.00	1.38	34.64	2.39	35.40	1.72
-	-	35.51	1.07	39.70	1.62	39.80	1.25
7% Sediment Moisture, Carbonated 0% Iron		7% Sediment Moisture, Carbonated 4% Iron		7% Sediment Moisture, Carbonated 8% Iron		7% Sediment Moisture, Carbonated 12% Iron	
1.56	17.31	1.46	8.44	1.71	14.49	1.70	15.08
5.31	12.51	4.76	4.63	5.54	8.14	5.78	8.25
10.54	6.86	9.67	2.55	10.14	4.93	10.18	5.20
15.86	2.46	14.99	1.47	14.71	2.12	14.43	1.77
19.85	1.19	18.79	1.36	18.66	1.96	18.46	1.06
23.55	0.85	22.21	1.26	22.53	1.68	21.95	0.76
27.28	0.72	25.46	1.01	26.38	2.36	25.47	0.89
31.46	0.66	28.68	0.92	30.23	1.68	29.38	0.81
35.43	0.78	31.68	0.86	34.68	1.33	33.17	0.72
40.15	0.48	35.5	0.76	39.8	1.03	37.93	0.64
7% Sediment Moisture, Non-Carbonated 0% Iron		7% Sediment Moisture, Non-Carbonated 4% Iron		7% Sediment Moisture, Non-Carbonated 8% Iron		7% Sediment Moisture, Non-Carbonated 12% Iron	
3.15	12.45	2.3	17.60	1.70	16.71	1.84	15.33
9.25	6.50	7.22	12.08	6.57	9.49	5.59	10.17
14.72	1.82	11.47	9.47	12.04	7.05	10.41	6.32
18.86	1.16	15.68	6.36	16.51	3.02	15.58	2.47
21.88	1.01	19.82	5.33	20.06	1.90	19.91	2.09
25.24	0.98	23.24	4.12	23.16	1.59	23.84	2.08
28.77	0.66	26.75	3.45	26.31	1.38	27.22	2.15
32.72	0.56	30.36	2.94	29.71	1.31	30.78	1.64
37.31	0.36	34.14	2.68	33.05	1.26	34.64	1.32
42.77	0.38	38.77	2.06	37.45	0.91	39.88	1.12
15% Sediment Moisture, Carbonated 0% Iron		15% Sediment Moisture, Carbonated 4% Iron		15% Sediment Moisture, Carbonated 8% Iron		15% Sediment Moisture, Carbonated 12% Iron	
1.99	15.8	1.23	9.16	1.15	17.13	1.97	18.02
6.26	14.04	4.27	5.96	4.52	12.48	6.29	10.58
10.75	9.13	7.65	4.27	9.10	9.44	10.95	7.64
15.08	4.76	11.66	2.51	14.1	3.83	15.50	2.97
19.02	2.23	16.00	0.81	18.22	1.29	19.28	1.01
22.79	1.43	19.97	0.59	21.83	0.41	22.77	0.30
26.33	1.23	23.77	0.32	25.52	0.27	25.95	0.21
30.01	1.14	27.60	0.14	29.22	0.23	28.79	0.31
34.07	1.17	31.36	0.09	33.67	0.19	32.12	0.13
38.89	1.26	36.22	0.11	38.97	0.16	36.26	0.26
15% Sediment Moisture, Non-Carbonated 0% Iron		15% Sediment Moisture, Non-Carbonated 4% Iron		15% Sediment Moisture, Non-Carbonated 8% Iron		15% Sediment Moisture, Non-Carbonated 12% Iron	
2.05	19.23	2.39	18.79	1.50	19.81	1.51	10.19
6.12	14.28	7.97	10.96	5.17	10.86	5.00	5.42
11.59	11.79	13.59	5.72	9.90	6.85	9.41	3.38
16.91	7.66	17.70	3.25	14.44	2.76	13.79	1.71
20.35	5.31	20.94	1.88	18.21	1.25	17.33	0.98
23.84	3.09	24.70	0.86	21.87	0.66	21.22	0.65
27.26	1.99	28.35	0.54	25.25	0.45	25.45	0.43
30.72	1.27	31.98	0.44	28.66	0.33	30.16	0.36
35.02	0.73	37.05	0.40	32.27	0.27	34.37	0.28
40.69	1.18			36.84	0.22	39.50	0.22

B.1.3 Concrete to Sediment

Table B.6. Concentrations of I in sediment from FY 1999 concrete-sediment half-cell experiments

4% Moisture Content Sediment		7% Moisture Content Sediment	
Distance from Face (cm)	I (mg/g sediment)	Distance from Face (cm)	I (mg/g sediment)
0.65	1.23×10^{-4}	0.52	1.87×10^{-3}
1.71	6.14×10^{-5}	1.27	3.01×10^{-4}
2.55	4.56×10^{-5}	1.77	2.95×10^{-4}
3.31	5.29×10^{-5}	2.24	2.79×10^{-4}
3.82	3.06×10^{-5}	2.75	3.05×10^{-4}
4.49	1.65×10^{-5}	3.29	2.81×10^{-4}
5.47	6.80×10^{-6}	3.77	2.72×10^{-4}
		4.24	2.73×10^{-4}
		4.74	3.18×10^{-4}
		5.23	2.90×10^{-4}
		5.65	2.27×10^{-4}
		6.34	2.17×10^{-4}
		7.29	1.49×10^{-4}
		8.29	1.40×10^{-4}
		9.24	1.11×10^{-4}
		10.24	6.71×10^{-5}
		11.22	1.21×10^{-5}
		12.07	1.46×10^{-5}
		12.94	4.08×10^{-5}

Table B.7. Concentrations of I in sediment from FY 2002 and FY 2004 concrete-sediment half-cell experiments

Distance from Core (mm)	I (mg/g sediment)	Distance from Core (cm)	I (mg/g sediment)	Distance from Core (cm)	I (mg/g sediment)	Distance from Core (cm)	I (mg/g sediment)
4% Sediment Moisture, Non-Carbonated 0% Iron		4% Sediment Moisture, Non-Carbonated 4% Iron		4% Sediment Moisture, Carbonated 0% Iron		4% Sediment Moisture, Carbonated 4% Iron	
0.00	7.73×10^{-3}	0.00	4.73×10^{-3}	0.00	6.59×10^{-2}	0.00	5.14×10^{-2}
0.75	3.13×10^{-3}	1.00	6.94×10^{-4}	1.25	1.91×10^{-2}	0.75	3.28×10^{-2}
2.25	1.12×10^{-3}	3.00	1.65×10^{-4}	2.25	1.10×10^{-2}	2.25	1.58×10^{-2}
3.50	3.57×10^{-4}	4.50	6.36×10^{-5}	3.50	4.14×10^{-3}	3.50	5.35×10^{-3}
5.00	1.00×10^{-4}	6.00	2.22×10^{-5}	5.00	1.68×10^{-3}	5.00	1.71×10^{-3}
7.00	4.33×10^{-5}	8.00	2.09×10^{-5}	7.00	3.14×10^{-4}	7.00	4.08×10^{-4}
9.00	2.29×10^{-5}	10.00	1.78×10^{-5}	9.00	1.45×10^{-4}	9.00	1.43×10^{-4}
11.00	1.70×10^{-5}	12.00	1.69×10^{-5}	11.00	3.82×10^{-5}	11.00	5.05×10^{-5}
13.00	1.64×10^{-5}	14.00	1.69×10^{-5}	13.00	2.98×10^{-5}	13.00	4.18×10^{-5}
14.75	1.68×10^{-5}	15.75	1.70×10^{-5}	14.75	2.58×10^{-5}	14.75	3.01×10^{-5}
16.25	1.55×10^{-5}	17.25	1.54×10^{-5}	16.25	2.87×10^{-5}	16.25	2.88×10^{-5}
17.75	1.59×10^{-5}	18.75	1.27×10^{-5}	17.75	6.94×10^{-6}	17.75	2.74×10^{-5}
19.25	1.76×10^{-5}	20.25	1.34×10^{-5}	19.25	7.35×10^{-6}	19.25	1.90×10^{-5}
20.75	1.62×10^{-5}	21.75	1.20×10^{-5}	20.75	7.52×10^{-6}	20.75	2.93×10^{-5}
22.25	1.83×10^{-5}	23.25	1.14×10^{-5}	22.25	9.31×10^{-6}	22.25	2.68×10^{-5}
24.00	2.14×10^{-5}	25.00	1.22×10^{-5}	24.00	8.07×10^{-6}	24.00	2.40×10^{-5}
26.00	2.72×10^{-5}	27.00	1.35×10^{-5}	26.00	1.11×10^{-6}	26.00	2.16×10^{-5}
28.00	1.99×10^{-5}	29.00	1.62×10^{-5}	28.00	1.21×10^{-6}	28.00	2.83×10^{-5}
30.00	2.51×10^{-5}	31.00	1.06×10^{-5}	30.00	6.24×10^{-6}	30.00	2.59×10^{-5}
32.00	2.48×10^{-5}	33.00	1.56×10^{-5}	32.00	9.05×10^{-6}	32.00	2.15×10^{-5}

Distance from Core (mm)	I (mg/g sediment)	Distance from Core (cm)	I (mg/g sediment)	Distance from Core (cm)	I (mg/g sediment)	Distance from Core (cm)	I (mg/g sediment)
7% Sediment Moisture, Non-Carbonated 0% Iron		7% Sediment Moisture, Non-Carbonated 4% Iron		7% Sediment Moisture, Carbonated 0% Iron		7% Sediment Moisture, Carbonated 4% Iron	
0.25	3.37×10^{-3}	0.25	3.00×10^{-4}	0.00	1.91×10^{-2}	0.25	3.86×10^{-2}
0.75	3.26×10^{-3}	0.75	2.70×10^{-4}	0.75	1.54×10^{-2}	0.75	3.96×10^{-2}
1.25	2.18×10^{-3}	1.25	2.50×10^{-4}	2.25	1.19×10^{-2}	1.25	3.57×10^{-2}
2.50	1.99×10^{-3}	2.50	1.81×10^{-4}	3.50	1.02×10^{-2}	2.50	2.52×10^{-2}
4.50	1.35×10^{-3}	4.50	1.31×10^{-4}	5.00	8.03×10^{-3}	4.50	1.96×10^{-2}
6.50	1.16×10^{-3}	6.50	1.01×10^{-4}	7.00	5.26×10^{-3}	6.50	1.53×10^{-2}
8.50	7.22×10^{-4}	8.50	6.01×10^{-5}	9.00	3.80×10^{-3}	8.50	9.83×10^{-3}
10.50	4.05×10^{-4}	10.50	5.01×10^{-5}	11.00	3.02×10^{-3}	10.50	6.06×10^{-3}
12.50	2.14×10^{-4}	12.50	4.07×10^{-5}	13.00	2.03×10^{-3}	12.50	3.82×10^{-3}
14.50	1.13×10^{-4}	14.50	2.01×10^{-5}	14.75	1.41×10^{-3}	14.50	2.38×10^{-3}
16.50	6.74×10^{-5}	16.50	1.00×10^{-5}	16.25	1.07×10^{-3}	16.50	1.25×10^{-3}
18.50	3.42×10^{-5}	18.50	1.01×10^{-5}	17.75	9.72×10^{-4}	18.50	7.69×10^{-4}
20.50	1.57×10^{-5}	20.50	1.01×10^{-5}	19.25	5.45×10^{-4}	20.50	4.88×10^{-4}
22.50	7.00×10^{-6}	22.50	1.00×10^{-5}	20.75	4.77×10^{-4}	22.50	2.24×10^{-4}
24.50	4.05×10^{-6}	24.50	1.00×10^{-5}	22.25	1.92×10^{-4}	24.50	1.17×10^{-4}
26.50	2.40×10^{-6}	26.50	1.00×10^{-5}	24.00	2.31×10^{-4}	26.50	6.16×10^{-5}
28.50	2.55×10^{-6}	28.50	1.00×10^{-5}	26.00	1.21×10^{-4}	28.50	2.90×10^{-5}
30.50	5.23×10^{-6}	30.50	1.00×10^{-5}	28.00	6.01×10^{-5}	30.50	1.22×10^{-5}
-	-	-	-	30.00	3.01×10^{-5}	-	-
-	-	-	-	32.00	3.00×10^{-5}	-	-

B.1.4 Fractured Concrete to Sediment

Table B.8. Concentrations of I in concrete from fractured concrete-sediment half-cell experiments

Distance from Face (mm)	I (mg/g concrete)	Distance from Face (mm)	I (mg/g concrete)	Distance from Face (mm)	I (mg/g concrete)	Distance from Face (mm)	I (mg/g concrete)
4% Sediment Moisture, Non-Carbonated 0% Iron		4% Sediment Moisture, Non-Carbonated 4% Iron		4% Sediment Moisture, Carbonated 0% Iron		4% Sediment Moisture, Carbonated 4% Iron	
2.37	15.96	2.05	17.80	1.85	14.46	2.19	5.32
8.03	15.90	6.09	18.68	6.06	15.07	6.54	4.81
13.32	18.15	9.37	16.92	10.77	15.03	12.56	5.41
17.83	17.56	13.08	17.18	15.30	16.57	18.50	5.81
21.68	18.81	17.42	18.12	19.43	17.62	22.37	5.94
24.70	19.20	21.52	16.99	23.91	16.08	26.67	5.39
28.55	18.30	25.57	16.10	28.61	16.13	31.01	5.81
32.84	16.50	30.26	15.73	33.07	13.96	35.08	4.45
36.95	14.84	35.62	12.60	39.51	12.59	38.94	10.23
4% Sediment Moisture, Non-Carbonated 8% Iron		4% Sediment Moisture, Non-Carbonated 12% Iron		4% Sediment Moisture, Carbonated 8% Iron		4% Sediment Moisture, Carbonated 12% Iron	
1.92	16.53	1.99	19.69	1.98	12.16	2.38	14.76
6.61	15.30	6.54	16.57	6.60	12.33	7.33	14.85
11.58	15.52	11.50	17.85	11.18	12.58	12.19	15.05
16.07	16.82	16.00	17.95	15.77	13.42	16.99	16.50
20.95	19.15	20.12	18.18	20.49	13.55	21.43	15.91
25.66	15.62	24.81	17.45	25.11	13.10	25.69	16.41
30.15	17.39	29.85	17.73	30.02	13.69	30.38	15.46
34.68	15.36	34.47	15.97	34.60	12.47	34.59	14.08
39.46	12.56	38.67	12.90	39.05	10.82	38.54	10.62

Distance from Face (mm)	I (mg/g concrete)	Distance from Face (mm)	I (mg/g concrete)	Distance from Face (mm)	I (mg/g concrete)	Distance from Face (mm)	I (mg/g concrete)
7% Sediment Moisture, Non-Carbonated 0% Iron		7 Sediment Moisture, Non-Carbonated 4% Iron		7% Sediment Moisture, Carbonated 0% Iron		7% Sediment Moisture, Carbonated 4% Iron	
2.05	13.38	2.04	12.14	2.44	10.81	1.49	15.10
6.42	12.62	6.39	13.43	7.45	12.44	5.78	11.31
11.11	14.57	10.25	14.58	11.75	13.27	10.77	12.04
15.90	16.54	14.36	15.90	15.74	14.76	15.53	9.99
20.15	16.49	18.84	15.13	20.37	14.82	20.72	13.61
24.39	16.84	23.35	16.72	24.64	15.05	26.10	12.04
28.85	15.71	27.41	17.04	29.06	14.35	31.02	11.51
33.13	14.00	30.48	15.79	34.10	12.08	35.20	11.08
37.30	10.58	33.82	14.39	38.72	7.98	39.18	7.03
-	-	38.35	10.72	-	-	-	-
7% Sediment Moisture, Non-Carbonated 8% Iron		7% Sediment Moisture, Non-Carbonated 12% Iron		7% Sediment Moisture, Carbonated 8% Iron		7% Sediment Moisture, Carbonated 12% Iron	
2.79	11.65	2.56	12.40	1.67	11.24	2.38	11.63
9.43	13.24	7.40	12.11	5.70	10.89	7.71	12.59
16.17	15.08	11.43	13.06	9.80	10.63	13.15	13.74
22.30	15.18	15.45	14.58	14.28	12.23	18.24	14.44
28.81	14.64	19.81	15.15	19.07	11.49	22.44	14.64
34.59	13.46	24.52	14.49	23.95	11.85	26.86	14.45
39.19	9.39	29.06	13.61	29.14	11.81	31.52	14.49
-	-	33.01	12.67	33.78	9.62	35.72	12.63
-	-	37.44	9.58	37.92	7.69	40.41	9.91
15% Sediment Moisture, Non-Carbonated 0% Iron		15% Sediment Moisture, Non-Carbonated 4% Iron		15% Sediment Moisture, Carbonated 0% Iron		15% Sediment Moisture, Carbonated 4% Iron	
1.74	9.87	1.46	9.73	1.55	12.74	2.20	9.68
6.52	11.89	5.56	8.74	5.18	10.55	6.86	6.74
11.84	13.23	10.53	9.96	9.62	11.37	11.83	8.91
16.79	14.16	15.77	11.11	14.58	11.75	16.43	8.73
21.35	13.58	20.75	10.72	19.05	11.36	20.77	9.41
25.83	14.71	25.19	10.37	23.52	11.61	25.14	8.48
30.23	12.52	29.02	11.30	27.95	11.51	29.24	8.47
34.57	12.60	32.68	8.70	31.63	11.09	33.23	6.86
39.48	8.20	-	-	34.96	10.25	37.18	3.88
-	-	-	-	39.31	6.34	-	-
15% Sediment Moisture, Non-Carbonated 8% Iron		15% Sediment Moisture, Non-Carbonated 12% Iron		15% Sediment Moisture, Carbonated 8% Iron		15% Sediment Moisture, Carbonated 12% Iron	
2.63	11.70	2.56	11.44	2.34	10.10	1.99	10.42
7.98	12.02	7.40	12.88	6.55	11.14	6.83	12.03
13.41	12.44	12.02	13.00	10.23	11.33	11.65	12.99
18.46	12.41	16.87	14.10	14.67	11.86	15.69	13.33
22.49	11.87	20.85	13.52	19.62	12.65	19.59	13.28
26.66	12.11	24.35	13.03	23.91	12.06	23.82	13.45
31.01	11.67	28.18	12.30	27.65	12.23	28.33	13.06
34.85	10.23	31.85	10.24	32.52	10.48	32.59	10.62
38.74	7.94	35.70	7.91	37.66	7.55	36.53	7.73

Table B.9. Concentrations of I in sediment from fractured concrete-sediment half-cell experiments

Distance from Core (cm)	I (mg/g sediment)	Distance from Core (cm)	I (mg/g sediment)	Distance from Core (cm)	I (mg/g sediment)	Distance from Core (cm)	I (mg/g sediment)
4% Sediment Moisture, Non-Carbonated 0% Iron		4% Sediment Moisture, Non-Carbonated 4% Iron		4% Sediment Moisture, Carbonated 0% Iron		4% Sediment Moisture, Carbonated 4% Iron	
0.25	1.16	0.25	2.05	0.25	0.68	0.25	0.26
0.75	1.09	0.75	0.98	0.75	0.54	0.75	0.74
1.25	1.05	1.25	0.97	1.25	0.53	1.25	0.82
2.00	0.87	2.00	0.85	2.00	0.47	2.00	0.69
3.00	0.72	3.00	0.76	3.00	0.34	3.00	0.55
4.00	0.53	4.00	0.58	4.00	0.14	4.00	0.41
6.00	0.18	5.00	0.43	5.00	0.06	5.00	0.24
7.50	0.07	6.00	0.25	6.00	0.02	6.00	0.12
9.50	0.00	7.50	0.10	7.50	ND	7.50	0.03
-	-	9.50	0.02	9.50	ND	9.50	ND
4% Sediment Moisture, Non-Carbonated 8% Iron		4% Sediment Moisture, Non-Carbonated 12% Iron		4% Sediment Moisture, Carbonated 8% Iron		4% Sediment Moisture, Carbonated 12% Iron	
0.25	2.19	1.25	1.37	0.25	1.73	0.25	1.09
0.75	1.28	0.75	1.03	0.75	1.13	0.75	0.77
1.25	1.43	1.50	0.86	1.25	1.10	1.50	0.62
2.00	1.36	2.50	0.80	2.00	1.05	2.50	0.42
3.00	1.09	3.50	0.66	3.00	0.88	3.50	0.28
4.00	0.87	4.50	0.37	4.00	0.68	4.50	0.14
5.00	0.67	5.50	0.18	5.00	0.50	5.50	0.05
6.00	0.46	7.00	0.03	6.00	0.33	7.00	0.01
7.50	0.17	9.00	ND	7.50	0.11	9.00	ND
9.50	0.03	-	-	9.50	0.01	-	-
7% Sediment Moisture, Non-Carbonated 0% Iron		7% Sediment Moisture, Non-Carbonated 4% Iron		7% Sediment Moisture, Carbonated 0% Iron		7% Sediment Moisture, Carbonated 4% Iron	
0.25	1.82	0.25	1.80	0.25	2.09	0.25	2.09
0.75	1.93	0.75	1.68	1.00	1.83	0.75	2.06
1.25	1.57	1.50	1.81	2.00	2.16	1.50	1.89
2.00	1.51	2.50	1.63	3.00	1.61	2.50	1.66
3.00	1.66	3.50	1.65	4.00	0.34	3.50	1.56
4.00	1.38	4.50	1.77	5.00	1.54	4.50	1.58
5.00	1.49	5.50	1.56	6.50	1.41	5.50	1.50
6.00	1.45	7.00	1.61	8.50	1.42	7.00	1.47
7.50	1.38	9.00	1.57	-	-	9.00	1.41
9.18	1.31	-	-	-	-	-	-
7% Sediment Moisture, Non-Carbonated 8% Iron		7% Sediment Moisture, Non-Carbonated 12% Iron		7% Sediment Moisture, Carbonated 8% Iron		7% Sediment Moisture, Carbonated 12% Iron	
0.25	1.80	0.25	1.93	0.25	1.57	0.25	1.86
0.75	1.93	0.75	2.07	1.00	1.62	1.00	1.77
1.50	1.90	1.50	1.94	2.00	1.61	2.00	1.57
2.50	1.81	2.50	1.87	3.00	1.49	3.00	1.54
3.50	1.88	3.50	1.99	4.00	1.56	4.00	1.28
4.50	1.77	4.50	1.97	5.00	1.42	5.00	1.32
5.50	1.71	5.50	1.87	6.50	1.33	6.50	1.23
7.00	1.77	7.00	1.96	8.50	1.33	8.50	1.24
9.00	2.10	9.00	1.93	-	-	-	-

Distance from Core (cm)	I (mg/g sediment)	Distance from Core (cm)	I (mg/g sediment)	Distance from Core (cm)	I (mg/g sediment)	Distance from Core (cm)	I (mg/g sediment)
15% Sediment Moisture, Non-Carbonated 0% Iron		15% Sediment Moisture, Non-Carbonated 4% Iron		15% Sediment Moisture, Carbonated 0% Iron		15% Sediment Moisture, Carbonated 4% Iron	
0.25	2.50	0.25	2.74	0.25	2.52	0.25	1.86
0.75	2.65	0.75	2.82	0.75	3.40	0.75	1.67
1.50	2.45	1.25	2.83	1.50	2.27	1.50	1.67
2.50	2.55	2.00	2.82	2.50	1.95	2.50	1.69
3.50	2.44	3.00	2.73	3.50	1.95	3.50	2.26
4.50	2.33	4.00	2.48	4.50	2.06	4.50	1.91
5.50	2.57	5.00	2.65	5.50	2.05	5.50	1.82
7.00	1.91	6.00	2.56	7.00	1.87	7.00	1.75
9.00	2.40	7.50	2.83	9.00	1.82	9.00	1.64
-	-	9.50	2.62	-	-	-	-
15% Sediment Moisture, Non-Carbonated 8% Iron		15% Sediment Moisture, Non-Carbonated 12% Iron		15% Sediment Moisture, Carbonated 8% Iron		15% Sediment Moisture, Carbonated 12% Iron	
0.25	2.27	0.25	1.65	0.25	3.01	0.25	2.20
0.75	2.53	0.75	2.90	0.75	2.08	0.75	1.94
1.25	2.50	1.50	2.80	1.50	2.36	1.25	1.90
2.00	2.37	2.50	2.77	2.50	2.23	2.00	1.99
3.00	2.51	3.50	2.74	3.50	1.97	3.00	1.96
4.00	2.53	4.50	2.62	4.50	1.90	4.00	1.80
5.00	2.24	5.50	2.59	5.50	1.83	5.00	1.87
6.00	1.79	7.00	2.57	7.00	2.58	6.00	1.85
7.50	1.93	9.00	2.62	9.00	1.89	7.50	1.84
9.50	1.87	-	-	-	-	9.50	1.86

B.1.5 Sediment to Fractured Concrete

Table B.10. Concentrations of I in sediment from sediment-fractured concrete half-cell experiments

Distance from Core (cm)	I (mg/g sediment)	Distance from Core (cm)	I (mg/g sediment)	Distance from Core (cm)	I (mg/g sediment)	Distance From Core (cm)	I (mg/g sediment)
4% Sediment Moisture, Non-Carbonated 0% Iron		4% Sediment Moisture, Non-Carbonated 4% Iron		4% Sediment Moisture, Carbonated 0% Iron		4% Sediment Moisture, Carbonated 4% Iron	
0.25	4.4	0.13	4.1	0.13	3.7	0.25	3.9
0.75	4.1	0.50	4.3	0.50	3.7	1.00	3.9
1.25	4.0	1.25	3.8	1.00	4.3	2.00	3.8
1.75	3.8	2.25	4.1	1.50	3.9	3.00	3.9
2.25	3.8	3.25	3.8	2.25	4.2	4.00	4.2
3.00	4.1	4.25	4.2	3.25	3.9	5.00	3.9
4.00	3.8	5.25	3.9	4.25	4.4	6.50	3.9
5.00	3.7	6.75	4.4	5.25	3.8	8.50	4.0
6.00	3.9	8.75	4.2	6.25	4.2	-	-
7.00	4.0	-	-	7.75	3.9	-	-
8.50	3.9	-	-	9.75	4.3	-	-
10.50	4.0	-	-	-	-	-	-
7% Sediment Moisture, Non-Carbonated 0% Iron		7% Sediment Moisture, Non-Carbonated 4% Iron		7% Sediment Moisture, Carbonated 0% Iron		7% Sediment Moisture, Carbonated 4% Iron	
0.13	4.2	0.25	3.5	0.13	3.4	0.25	3.1
0.50	4.6	0.75	3.3	0.50	3.7	0.75	4.0
1.00	4.5	1.50	3.2	1.00	3.5	1.25	3.9
1.75	4.1	2.50	3.4	1.50	3.2	2.00	4.2

Distance from Core (cm)	I (mg/g sediment)	Distance from Core (cm)	I (mg/g sediment)	Distance from Core (cm)	I (mg/g sediment)	Distance From Core (cm)	I (mg/g sediment)
2.75	4.2	3.50	3.5	2.00	3.4	3.00	4.3
3.75	4.6	4.50	3.7	2.75	3.4	4.00	4.5
4.75	4.1	5.50	3.4	3.75	3.8	5.00	3.9
5.75	4.0	7.00	3.7	4.75	3.6	6.00	4.0
7.25	4.4	9.00	3.5	5.75	2.9	7.50	4.0
9.25	4.2	-	-	6.75	3.5	9.50	4.2
-	-	-	-	8.25	3.6	-	-
-	-	-	-	10.25	3.5	-	-
15% Sediment Moisture, Non-Carbonated 0% Iron		15% Sediment Moisture, Non-Carbonated 4% Iron		15% Sediment Moisture, Carbonated 0% Iron		15% Sediment Moisture, Carbonated 4% Iron	
0.25	2.7	0.75	2.5	0.13	4.9	0.50	2.8
0.75	2.8	1.25	2.5	0.50	4.9	1.00	2.7
1.50	2.6	2.00	2.5	1.25	4.0	1.75	2.6
2.50	2.4	3.00	2.6	2.25	3.6	2.75	2.6
3.50	2.8	4.00	2.7	3.25	3.3	3.75	2.7
4.50	2.5	5.00	2.8	4.25	3.4	4.75	2.9
5.50	2.8	6.00	2.7	5.25	3.4	5.75	2.9
7.00	2.6	7.50	2.5	6.75	3.1	7.25	2.8
9.00	2.6	9.50	2.5	8.75	3.2	9.25	2.7

Table B.11. Concentrations of I in concrete from sediment-fractured concrete half-cell experiments

Distance From Face (mm)	I (mg/g concrete)	Distance From Face (mm)	I (mg/g concrete)	Distance From Face mm	I (mg/g concrete)	Distance From Face (mm)	I (mg/g concrete)
4% Sediment Moisture, Non-Carbonated 0% Iron		4% Sediment Moisture, Non-Carbonated 4% Iron		4% Sediment Moisture, Carbonated 0% Iron		4% Sediment Moisture, Carbonated 4% Iron	
0.9	20.11	1.5	14.76	1.2	8.55	0.9	11.81
2.8	13.17	4.7	10.26	3.5	8.74	3.5	9.10
5.1	9.95	7.3	8.58	6.0	6.88	5.8	7.93
7.7	6.90	10.1	5.69	8.9	6.32	8.0	6.19
10.3	5.35	13.2	3.70	11.4	6.03	10.4	5.32
12.7	3.74	16.7	1.57	14.0	5.10	13.1	3.90
15.1	2.12	22.4	0.12	16.9	3.94	15.8	3.19
17.8	0.80			19.6	3.03	18.4	2.28
7% Sediment Moisture, Non-Carbonated 0% Iron		7% Sediment Moisture, Non-Carbonated 4% Iron		7% Sediment Moisture, Carbonated 0% Iron		7% Sediment Moisture, Carbonated 4% Iron	
1.1	7.04	1.3	10.66	1.5	9.08	1.0	7.15
3.6	5.92	4.1	8.77	4.0	9.65	3.7	4.64
6.1	3.54	6.8	6.24	6.1	8.73	6.5	4.03
8.7	2.90	9.2	5.20	8.2	7.45	9.0	2.91
11.3	1.30	11.8	3.24	10.4	7.28	11.5	2.24
13.8	0.50	14.7	2.21	13.0	6.06	13.9	1.64
16.4	0.07	17.1	0.66	15.6	5.08	16.2	1.04
19.2	0.00	20.2	0.28	18.1	4.54	18.7	0.62
15% Sediment Moisture, Non-Carbonated 0% Iron		15% Sediment Moisture, Non-Carbonated 4% Iron		15% Sediment Moisture, Carbonated 0% Iron		15% Sediment Moisture, Carbonated 4% Iron	
1.0	11.65	1.2	10.12	1.4	9.42	1.2	9.26
3.6	8.09	3.9	7.45	4.0	9.71	3.7	8.09
6.4	7.69	6.5	6.96	6.4	8.47	6.2	8.26
9.0	8.55	9.4	6.75	8.7	8.34	8.6	7.49

Distance From Face (mm)	I (mg/g concrete)	Distance From Face (mm)	I (mg/g concrete)	Distance From Face mm	I (mg/g concrete)	Distance From Face (mm)	I (mg/g concrete)
11.2	7.62	12.4	6.75	11.0	8.10	11.2	6.63
13.5	7.05	15.2	5.78	13.3	7.29	13.8	6.01
16.0	5.62	18.2	5.50	15.6	6.84	16.5	4.98
18.4	5.62	20.9	5.18	18.2	5.85	19.0	4.74

Table B.12. Concentrations of I in concrete from sediment-fractured concrete half-cell experiments sectioned perpendicular to the concrete-sediment interface (parallel to the concrete fracture)

Distance from Face (mm)	I (mg/g concrete)	Distance from Face (mm)	I (mg/g concrete)	Distance from Face (mm)	I (mg/g concrete)	Distance from Face (mm)	I (mg/g concrete)
4% Sediment Moisture, Non-Carbonated 0% Iron		4% Sediment Moisture, Non-Carbonated 4% Iron		4% Sediment Moisture, Carbonated 0% Iron		4% Sediment Moisture, Carbonated 4% Iron	
1.9	2.11	1.4	9.00	2.2	1.91	1.2	4.57
5.2	3.15	4.3	3.28	5.9	2.84	3.8	5.34
7.9	2.79	7.6	2.26	9.1	2.30	6.5	1.89
10.4	1.16	11.0	2.82	12.3	2.69	9.5	2.88
13.0	3.16	14.0	2.00	15.5	2.17	12.4	2.77
7% Sediment Moisture, Non-Carbonated 0% Iron		7% Sediment Moisture, Non-Carbonated 4% Iron		7% Sediment Moisture, Carbonated 0% Iron		7% Sediment Moisture, Carbonated 4% Iron	
1.9	0.93	1.9	3.02	1.1	5.10	1.8	2.58
5.5	0.20	5.2	5.04	3.7	3.78	5.4	2.06
8.4	1.48	7.6	4.57	6.2	4.26	8.5	2.68
11.0	0.82	10.0	4.23	8.9	4.03	11.5	2.58
13.6	1.23	12.6	5.10	11.7	3.80	14.2	2.21
15% Sediment Moisture, Non-Carbonated 0% Iron		15% Sediment Moisture, Non-Carbonated 4% Iron		15% Sediment Moisture, Carbonated 0% Iron		15% Sediment Moisture, Carbonated 4% Iron	
1.9	5.85	1.9	5.93	1.6	4.10	2.0	4.24
5.2	5.91	5.6	5.62	4.6	5.62	5.4	5.46
7.8	5.48	8.6	4.93	7.3	4.05	8.0	5.89
10.2	5.50	11.5	5.60	10.1	5.03	10.6	4.76
12.7	5.68	14.5	5.36	12.8	5.83	13.1	6.25

B.2 Technetium Concentrations

B.2.1 Sediment to Sediment

Table B.13. Concentrations of Tc-99 in sediment from sediment-sediment half-cell experiments

64 Day Testing				170 Day Testing			
4% Moisture Content Sediment		7% Moisture Content Sediment		4% Moisture Content Sediment		7% Moisture Content Sediment	
Distance from spiked end (cm)	Tc-99 (mg/g sediment)	Distance from spiked end (cm)	Tc-99 (mg/g sediment)	Distance from spiked end (cm)	Tc-99 (mg/g sediment)	Distance from spiked end (cm)	Tc-99 (mg/g sediment)
0.74	6.26×10^{-4}	1.26	8.45×10^{-4}	1.50	7.31×10^{-4}	1.50	9.91×10^{-4}
3.54	5.40×10^{-4}	3.31	9.68×10^{-4}	4.42	6.28×10^{-4}	4.59	8.94×10^{-4}
8.09	5.13×10^{-4}	5.60	8.01×10^{-4}	7.60	6.03×10^{-4}	7.67	8.51×10^{-4}
11.61	5.13×10^{-4}	9.07	7.69×10^{-4}	10.54	5.28×10^{-4}	10.61	7.29×10^{-4}
14.31	3.30×10^{-4}	12.94	7.07×10^{-4}	13.14	4.72×10^{-4}	13.48	5.87×10^{-4}
18.48	4.47×10^{-4}	15.34	6.68×10^{-4}	16.03	3.11×10^{-4}	15.13	4.90×10^{-4}
21.06	3.66×10^{-4}	16.29	5.79×10^{-4}	17.50	2.79×10^{-4}	15.61	4.47×10^{-4}
21.39	2.40×10^{-4}	17.03	5.01×10^{-4}	18.08	2.29×10^{-4}	16.10	4.16×10^{-4}
22.07	1.93×10^{-4}	17.69	4.13×10^{-4}	19.06	2.16×10^{-4}	16.60	3.73×10^{-4}
22.79	1.38×10^{-4}	18.45	1.96×10^{-4}	19.76	1.79×10^{-4}	17.08	3.49×10^{-4}
23.33	1.23×10^{-4}	19.08	3.83×10^{-4}	20.21	1.64×10^{-4}	17.61	3.26×10^{-4}
23.82	1.00×10^{-4}	19.63	1.94×10^{-4}	20.60	1.57×10^{-4}	18.24	2.94×10^{-4}
24.44	7.49×10^{-5}	20.15	2.02×10^{-4}	21.22	1.34×10^{-4}	18.80	2.62×10^{-4}
25.35	4.72×10^{-5}	20.64	1.79×10^{-4}	21.87	1.05×10^{-4}	19.26	2.45×10^{-4}
26.45	2.35×10^{-5}	21.10	1.55×10^{-4}	22.28	9.61×10^{-5}	19.67	2.23×10^{-4}
27.57	1.02×10^{-5}	21.58	1.22×10^{-4}	22.60	8.76×10^{-5}	20.19	2.07×10^{-4}
28.62	4.44×10^{-6}	22.10	1.10×10^{-4}	23.06	7.72×10^{-5}	20.75	1.89×10^{-4}
29.77	2.33×10^{-6}	22.62	8.40×10^{-5}	23.75	5.94×10^{-5}	21.24	1.76×10^{-4}
-	-	23.09	6.79×10^{-5}	24.57	4.00×10^{-5}	21.73	1.56×10^{-4}
-	-	23.57	6.04×10^{-5}	25.61	2.66×10^{-5}	22.24	1.42×10^{-4}
-	-	24.05	4.82×10^{-5}	26.66	1.56×10^{-5}	22.76	1.26×10^{-4}
-	-	24.77	3.56×10^{-5}	27.72	8.81×10^{-6}	23.29	1.10×10^{-4}
-	-	25.72	2.45×10^{-5}	28.84	4.67×10^{-6}	24.02	9.19×10^{-5}
-	-	26.50	1.55×10^{-5}	29.86	2.37×10^{-6}	25.00	7.04×10^{-5}
-	-	27.50	1.16×10^{-5}	30.86	1.14×10^{-6}	25.98	5.21×10^{-5}
-	-	-	-	31.84	5.43×10^{-7}	26.94	3.97×10^{-5}
-	-	-	-	32.87	1.86×10^{-7}	27.92	2.90×10^{-5}
-	-	-	-	33.84	5.91×10^{-8}	28.87	2.08×10^{-5}
-	-	-	-	34.72	2.50×10^{-8}	29.83	1.48×10^{-5}
-	-	-	-	-	-	30.89	9.77×10^{-6}
-	-	-	-	-	-	31.83	6.71×10^{-6}
-	-	-	-	-	-	32.79	4.34×10^{-6}
-	-	-	-	-	-	33.79	2.55×10^{-6}
-	-	-	-	-	-	34.72	1.52×10^{-6}
-	-	-	-	-	-	35.74	9.37×10^{-7}
-	-	-	-	-	-	36.70	6.45×10^{-7}
-	-	-	-	-	-	37.40	7.11×10^{-7}

B.2.2   Sediment to Concrete

Table B.14. Concentrations of Tc-99 in sediment from sediment-concrete half-cell experiments

Distance from Core (cm)	Tc-99 (mg/g sediment)	Distance from Core (cm)	Tc-99 (mg/g sediment)	Distance from Core (cm)	Tc-99 (mg/g sediment)	Distance from Core (cm)	Tc-99 (mg/g sediment)
4% Sediment Moisture, Non-Carbonated 0% Iron		4% Sediment Moisture, Non-Carbonated 4% Iron		4% Sediment Moisture, Carbonated 0% Iron		4% Sediment Moisture, Carbonated 4% Iron	
0.25	2.34×10^{-4}	0.25	1.44×10^{-4}	0.25	3.36×10^{-4}	0.25	2.87×10^{-4}
0.75	2.48×10^{-4}	0.75	1.40×10^{-4}	0.75	3.71×10^{-4}	0.75	3.09×10^{-4}
1.25	2.32×10^{-4}	1.25	1.35×10^{-4}	1.25	3.23×10^{-4}	1.25	3.00×10^{-4}
2.00	2.12×10^{-4}	2.00	1.57×10^{-4}	2.00	2.71×10^{-4}	2.00	2.80×10^{-4}
3.00	2.13×10^{-4}	3.00	1.57×10^{-4}	3.00	2.72×10^{-4}	3.00	2.45×10^{-4}
4.00	2.06×10^{-4}	4.00	1.56×10^{-4}	4.00	2.52×10^{-4}	4.00	2.46×10^{-4}
5.00	2.08×10^{-4}	5.00	1.56×10^{-4}	5.00	2.39×10^{-4}	5.00	2.40×10^{-4}
6.00	2.17×10^{-4}	6.00	1.50×10^{-4}	6.00	2.39×10^{-4}	6.00	2.43×10^{-4}
7.50	2.83×10^{-4}	7.50	1.82×10^{-4}	7.50	2.31×10^{-4}	7.50	2.44×10^{-4}
9.50	2.16×10^{-4}	9.50	1.66×10^{-4}	9.50	2.32×10^{-4}	9.50	2.39×10^{-4}
4% Sediment Moisture, Non-Carbonated 8% Iron		4% Sediment Moisture, Non-Carbonated 12% Iron		4% Sediment Moisture, Carbonated 8% Iron		4% Sediment Moisture, Carbonated 12% Iron	
0.25	2.71×10^{-4}	0.25	1.31×10^{-4}	0.25	2.91×10^{-4}	0.25	2.38×10^{-4}
0.75	2.64×10^{-4}	0.75	1.57×10^{-4}	0.75	2.75×10^{-4}	0.75	2.28×10^{-4}
1.25	2.52×10^{-4}	1.25	1.45×10^{-4}	1.25	2.62×10^{-4}	1.25	2.20×10^{-4}
2.00	2.45×10^{-4}	2.00	1.63×10^{-4}	2.00	2.36×10^{-4}	2.00	2.07×10^{-4}
3.00	2.45×10^{-4}	3.00	1.80×10^{-4}	3.00	2.25×10^{-4}	3.00	2.10×10^{-4}
4.00	2.43×10^{-4}	4.00	1.95×10^{-4}	4.00	2.29×10^{-4}	4.00	2.14×10^{-4}
5.00	2.41×10^{-4}	5.00	1.97×10^{-4}	5.00	2.28×10^{-4}	5.00	2.12×10^{-4}
6.00	2.49×10^{-4}	6.00	2.07×10^{-4}	6.00	2.29×10^{-4}	6.00	2.21×10^{-4}
7.50	2.51×10^{-4}	7.50	2.11×10^{-4}	7.50	2.35×10^{-4}	7.50	2.22×10^{-4}
9.50	2.56×10^{-4}	9.50	2.11×10^{-4}	9.50	2.36×10^{-4}	9.50	2.28×10^{-4}
7% Sediment Moisture, Non-Carbonated 0% Iron		7% Sediment Moisture, Non-Carbonated 4% Iron		7% Sediment Moisture, Carbonated 0% Iron		7% Sediment Moisture, Carbonated 4% Iron	
0.25	2.24×10^{-4}	0.25	9.16×10^{-5}	0.25	2.51×10^{-4}	0.25	3.15×10^{-4}
0.75	1.92×10^{-4}	0.75	8.27×10^{-5}	0.75	2.89×10^{-4}	0.75	3.79×10^{-4}
1.25	1.98×10^{-4}	1.25	8.65×10^{-5}	1.25	2.39×10^{-4}	1.25	3.81×10^{-4}
2.00	2.08×10^{-4}	2.00	1.26×10^{-4}	2.00	2.11×10^{-4}	2.00	3.59×10^{-4}
3.00	1.97×10^{-4}	3.00	1.10×10^{-4}	3.00	2.15×10^{-4}	3.00	3.45×10^{-4}
4.00	2.04×10^{-4}	4.00	1.13×10^{-4}	4.00	2.19×10^{-4}	4.00	2.92×10^{-4}
5.00	2.20×10^{-4}	5.00	1.30×10^{-4}	5.00	2.22×10^{-4}	5.00	2.72×10^{-4}
6.00	2.32×10^{-4}	6.00	1.34×10^{-4}	6.00	2.32×10^{-4}	6.00	3.01×10^{-4}
7.50	2.16×10^{-4}	7.50	1.48×10^{-4}	7.50	2.30×10^{-4}	7.50	2.63×10^{-4}
9.50	2.09×10^{-4}	9.50	1.53×10^{-4}	9.50	2.33×10^{-4}	9.50	3.28×10^{-4}
7% Sediment Moisture, Non-Carbonated 8% Iron		7% Sediment Moisture, Non-Carbonated 12% Iron		7% Sediment Moisture, Carbonated 8% Iron		7% Sediment Moisture, Carbonated 12% Iron	
0.25	2.38×10^{-4}	0.25	2.53×10^{-4}	0.25	2.69×10^{-4}	0.25	2.22×10^{-4}
0.75	2.37×10^{-4}	0.75	2.70×10^{-4}	0.75	2.76×10^{-4}	0.75	2.45×10^{-4}
1.25	2.48×10^{-4}	1.25	2.50×10^{-4}	1.25	2.62×10^{-4}	1.25	2.50×10^{-4}
2.00	2.36×10^{-4}	2.00	2.32×10^{-4}	2.00	2.62×10^{-4}	2.00	2.33×10^{-4}
3.00	2.37×10^{-4}	3.00	2.48×10^{-4}	3.00	1.75×10^{-4}	3.00	2.36×10^{-4}
4.00	2.47×10^{-4}	4.00	2.28×10^{-4}	4.00	2.33×10^{-4}	4.00	2.39×10^{-4}
5.00	2.28×10^{-4}	5.00	2.19×10^{-4}	5.00	2.37×10^{-4}	5.00	2.20×10^{-4}
6.00	2.34×10^{-4}	6.00	2.29×10^{-4}	6.00	2.29×10^{-4}	6.00	2.20×10^{-4}
7.50	2.39×10^{-4}	7.50	2.31×10^{-4}	7.50	2.30×10^{-4}	7.50	2.25×10^{-4}
9.50	2.36×10^{-4}	9.50	2.24×10^{-4}	9.50	2.33×10^{-4}	9.50	2.12×10^{-4}

Distance from Core (cm)	Tc-99 (mg/g sediment)	Distance from Core (cm)	Tc-99 (mg/g sediment)	Distance from Core (cm)	Tc-99 (mg/g sediment)	Distance from Core (cm)	Tc-99 (mg/g sediment)
15% Sediment Moisture, Non-Carbonated 0% Iron		15% Sediment Moisture, Non-Carbonated 4% Iron		15% Sediment Moisture, Carbonated 0% Iron		15% Sediment Moisture, Carbonated 4% Iron	
0.25	3.29×10^{-4}	0.25	1.42×10^{-4}	0.25	2.28×10^{-4}	0.25	3.07×10^{-4}
0.75	3.27×10^{-4}	0.75	2.05×10^{-4}	0.75	1.93×10^{-4}	0.75	3.01×10^{-4}
1.25	2.50×10^{-4}	1.25	1.97×10^{-4}	1.25	1.91×10^{-4}	1.25	2.99×10^{-4}
2.00	2.27×10^{-4}	2.00	2.04×10^{-4}	2.00	1.99×10^{-4}	2.00	2.97×10^{-4}
3.00	2.47×10^{-4}	3.00	2.14×10^{-4}	3.00	1.96×10^{-4}	3.00	2.83×10^{-4}
4.00	1.79×10^{-4}	4.00	1.86×10^{-4}	4.00	1.96×10^{-4}	4.00	2.85×10^{-4}
5.00	2.47×10^{-4}	5.00	1.90×10^{-4}	5.00	2.11×10^{-4}	5.00	3.49×10^{-4}
6.00	2.35×10^{-4}	6.00	1.88×10^{-4}	6.00	2.03×10^{-4}	6.00	2.96×10^{-4}
7.50	2.20×10^{-4}	7.50	1.89×10^{-4}	7.50	1.96×10^{-4}	7.50	2.86×10^{-4}
9.50	2.16×10^{-4}	9.50	1.98×10^{-4}	9.50	1.95×10^{-4}	9.50	3.57×10^{-4}
15% Sediment Moisture, Non-Carbonated 8% Iron		15% Sediment Moisture, Non-Carbonated 12% Iron		15% Sediment Moisture, Carbonated 8% Iron		15% Sediment Moisture, Carbonated 12% Iron	
0.25	1.11×10^{-4}	0.25	1.96×10^{-4}	0.25	2.22×10^{-4}	0.25	1.75×10^{-4}
0.75	1.78×10^{-4}	0.75	2.53×10^{-4}	0.75	1.94×10^{-4}	0.75	1.56×10^{-4}
1.25	1.55×10^{-4}	1.25	2.60×10^{-4}	1.25	1.79×10^{-4}	1.25	1.50×10^{-4}
2.00	1.45×10^{-4}	2.00	2.46×10^{-4}	2.00	1.85×10^{-4}	2.00	1.55×10^{-4}
3.00	1.51×10^{-4}	3.00	2.50×10^{-4}	3.00	1.79×10^{-4}	3.00	1.51×10^{-4}
4.00	1.44×10^{-4}	4.00	2.45×10^{-4}	4.00	1.89×10^{-4}	4.00	1.57×10^{-4}
5.00	1.49×10^{-4}	5.00	2.31×10^{-4}	5.00	2.02×10^{-4}	5.00	1.54×10^{-4}
6.00	1.60×10^{-4}	6.00	2.38×10^{-4}	6.00	2.02×10^{-4}	6.00	1.62×10^{-4}
7.50	1.60×10^{-4}	7.50	2.44×10^{-4}	7.50	2.00×10^{-4}	7.50	1.67×10^{-4}
9.50	1.59×10^{-4}	9.50	2.26×10^{-4}	9.50	1.93×10^{-4}	9.50	1.59×10^{-4}

Table B.15. Concentrations of Tc-99 in concrete from sediment-concrete half-cell experiments

Distance from Face (mm)	Tc-99 (mg/g concrete)	Distance from Face (mm)	Tc-99 (mg/g concrete)	Distance from Face (mm)	Tc-99 (mg/g concrete)	Distance from Face (mm)	Tc-99 (mg/g concrete)
4% Sediment Moisture, Non-Carbonated 0% Iron		4% Sediment Moisture, Non-Carbonated 4% Iron		4% Sediment Moisture, Carbonated 0% Iron		4% Sediment Moisture, Carbonated 4% Iron	
1.61	6.39×10^{-4}	2.02	5.40×10^{-4}	2.91	1.95×10^{-4}	1.48	4.94×10^{-4}
5.53	4.17×10^{-4}	5.81	2.68×10^{-4}	9.49	9.18×10^{-5}	5.18	1.53×10^{-4}
10.63	2.86×10^{-4}	10.05	1.52×10^{-4}	15.14	3.57×10^{-5}	9.83	1.02×10^{-4}
15.55	2.29×10^{-4}	14.22	1.29×10^{-4}	19.91	3.18×10^{-5}	14.59	6.52×10^{-5}
19.70	1.88×10^{-4}	17.56	8.87×10^{-5}	24.08	2.95×10^{-5}	18.58	4.05×10^{-5}
23.97	1.45×10^{-4}	20.96	5.48×10^{-5}	27.35	3.91×10^{-5}	22.23	2.30×10^{-5}
28.07	8.48×10^{-5}	24.41	2.84×10^{-5}	30.92	3.67×10^{-5}	25.61	1.24×10^{-5}
32.22	7.09×10^{-5}	27.69	1.74×10^{-5}	35.13	3.74×10^{-5}	28.94	6.32×10^{-6}
38.20	3.26×10^{-5}	31.00	1.13×10^{-5}	40.62	3.13×10^{-5}	32.49	2.71×10^{-6}
-	-	35.51	4.59×10^{-6}	-	-	36.55	2.16×10^{-6}
4% Sediment Moisture, Non-Carbonated 8% Iron		4% Sediment Moisture, Non-Carbonated 12% Iron		4% Sediment Moisture, Carbonated 8% Iron		4% Sediment Moisture, Carbonated 12% Iron	
1.70	3.58×10^{-4}	1.77	9.15×10^{-4}	2.44	4.38×10^{-4}	2.03	3.73×10^{-4}
6.13	1.54×10^{-4}	5.23	2.04×10^{-4}	6.77	1.48×10^{-4}	5.55	1.30×10^{-4}
11.32	5.68×10^{-5}	9.82	1.20×10^{-4}	11.10	1.02×10^{-4}	10.19	1.37×10^{-4}
16.43	7.00×10^{-5}	15.23	1.02×10^{-4}	15.89	4.42×10^{-5}	15.59	9.48×10^{-5}
20.48	9.91×10^{-5}	19.95	9.70×10^{-5}	19.96	3.63×10^{-5}	19.06	1.09×10^{-4}
23.77	1.06×10^{-4}	23.94	8.22×10^{-5}	23.52	1.74×10^{-5}	22.43	5.60×10^{-5}
27.21	1.07×10^{-4}	27.63	7.73×10^{-5}	27.13	1.38×10^{-5}	26.42	4.12×10^{-5}

Distance from Face (mm)	Tc-99 (mg/g concrete)	Distance from Face (mm)	Tc-99 (mg/g concrete)	Distance from Face (mm)	Tc-99 (mg/g concrete)	Distance from Face (mm)	Tc-99 (mg/g concrete)
30.57	2.17×10^{-4}	31.43	4.08×10^{-5}	30.97	1.22×10^{-5}	29.78	2.81×10^{-5}
34.64	1.91×10^{-4}	35.40	3.98×10^{-5}	35.60	9.04×10^{-6}	32.57	9.99×10^{-6}
39.70	8.94×10^{-5}	39.80	3.16×10^{-5}	41.47	6.49×10^{-6}	36.48	3.56×10^{-6}
7% Sediment Moisture, Non-Carbonated 0% Iron		7% Sediment Moisture, Non-Carbonated 4% Iron		7% Sediment Moisture, Carbonated 0% Iron		7% Sediment Moisture, Carbonated 4% Iron	
3.15	2.43×10^{-4}	2.30	5.90×10^{-4}	1.56	7.01×10^{-4}	1.46	1.97×10^{-4}
9.25	6.50×10^{-5}	7.22	2.60×10^{-4}	5.31	1.75×10^{-4}	4.76	1.05×10^{-4}
14.72	6.41×10^{-5}	11.47	2.19×10^{-4}	10.54	7.98×10^{-5}	9.67	5.08×10^{-5}
18.86	4.48×10^{-5}	15.68	1.70×10^{-4}	15.86	5.45×10^{-5}	14.99	1.63×10^{-5}
21.88	4.09×10^{-5}	19.82	1.60×10^{-4}	19.85	2.76×10^{-5}	18.79	1.71×10^{-5}
25.24	3.75×10^{-5}	23.24	1.26×10^{-4}	23.55	2.21×10^{-5}	22.21	1.60×10^{-5}
28.77	2.22×10^{-5}	26.75	1.05×10^{-4}	27.28	1.98×10^{-5}	25.46	1.45×10^{-5}
32.72	1.72×10^{-5}	30.36	1.11×10^{-4}	31.46	1.70×10^{-5}	28.68	1.28×10^{-5}
37.31	8.37×10^{-6}	34.14	1.02×10^{-4}	35.43	1.74×10^{-5}	31.68	1.05×10^{-5}
42.77	9.87×10^{-6}	38.77	8.16×10^{-5}	40.15	1.09×10^{-5}	35.50	8.69×10^{-6}
7% Sediment Moisture, Non-Carbonated 8% Iron		7% Sediment Moisture, Non-Carbonated 12% Iron		7% Sediment Moisture, Carbonated 8% Iron		7% Sediment Moisture, Carbonated 12% Iron	
1.70	4.88×10^{-4}	1.84	6.62×10^{-4}	1.71	2.03×10^{-4}	1.70	3.68×10^{-4}
6.57	7.55×10^{-5}	5.59	2.56×10^{-5}	5.54	5.91×10^{-5}	5.78	6.13×10^{-5}
12.04	8.65×10^{-5}	10.41	1.44×10^{-4}	10.14	3.12×10^{-5}	10.18	1.36×10^{-5}
16.51	8.46×10^{-5}	15.58	4.99×10^{-5}	14.71	1.33×10^{-5}	14.43	4.25×10^{-6}
20.06	6.01×10^{-5}	19.91	3.25×10^{-5}	18.66	1.89×10^{-5}	18.46	2.75×10^{-6}
23.16	4.69×10^{-5}	23.84	3.85×10^{-5}	22.53	2.22×10^{-5}	21.95	3.07×10^{-6}
26.31	4.55×10^{-5}	27.22	4.92×10^{-5}	26.38	2.19×10^{-5}	25.47	3.31×10^{-6}
29.71	2.92×10^{-5}	30.78	4.80×10^{-5}	30.23	1.96×10^{-5}	29.38	2.63×10^{-6}
33.05	3.75×10^{-5}	34.64	4.13×10^{-5}	34.68	1.35×10^{-5}	33.17	2.22×10^{-6}
37.45	3.02×10^{-5}	39.88	2.75×10^{-5}	39.80	9.38×10^{-6}	37.93	3.59×10^{-6}
15% Sediment Moisture, Non-Carbonated 0% Iron		15% Sediment Moisture, Non-Carbonated 4% Iron		15% Sediment Moisture, Carbonated 0% Iron		15% Sediment Moisture, Carbonated 4% Iron	
2.05	1.02×10^{-3}	2.39	1.11×10^{-3}	1.99	9.59×10^{-4}	1.23	2.56×10^{-4}
6.12	4.65×10^{-4}	7.97	3.03×10^{-4}	6.26	1.68×10^{-4}	4.27	9.19×10^{-5}
11.59	2.48×10^{-4}	13.59	1.31×10^{-4}	10.75	6.41×10^{-5}	7.65	4.87×10^{-5}
16.91	1.29×10^{-4}	17.7	8.15×10^{-5}	15.08	3.64×10^{-5}	11.66	3.20×10^{-5}
20.35	7.70×10^{-5}	20.94	4.64×10^{-5}	19.02	3.25×10^{-5}	16.00	1.81×10^{-5}
23.84	4.39×10^{-5}	24.70	3.15×10^{-5}	22.79	3.52×10^{-5}	19.97	1.64×10^{-5}
27.26	3.04×10^{-5}	28.35	2.55×10^{-5}	26.33	4.21×10^{-5}	23.77	7.65×10^{-6}
30.72	2.92×10^{-5}	31.98	2.13×10^{-5}	30.01	4.00×10^{-5}	27.60	4.00×10^{-6}
35.02	1.62×10^{-5}	37.05	1.62×10^{-5}	34.07	4.32×10^{-5}	31.36	3.06×10^{-6}
40.69	2.55×10^{-5}	-	-	38.89	4.33×10^{-5}	36.22	4.10×10^{-6}
15% Sediment Moisture, Non-Carbonated 8% Iron		15% Sediment Moisture, Non-Carbonated 12% Iron		15% Sediment Moisture, Carbonated 8% Iron		15% Sediment Moisture, Carbonated 12% Iron	
1.50	1.55×10^{-3}	1.51	1.60×10^{-4}	1.15	1.69×10^{-3}	1.97	1.36×10^{-3}
5.17	3.25×10^{-5}	5.00	8.67×10^{-5}	4.52	2.27×10^{-4}	6.29	1.58×10^{-4}
9.90	8.27×10^{-5}	9.41	7.29×10^{-5}	9.10	5.44×10^{-5}	10.95	3.74×10^{-5}
14.44	4.01×10^{-5}	13.79	5.11×10^{-5}	14.10	1.35×10^{-5}	15.50	1.16×10^{-5}
18.21	3.08×10^{-5}	17.33	3.22×10^{-5}	18.22	5.56×10^{-6}	19.28	7.07×10^{-6}
21.87	2.05×10^{-5}	21.22	1.91×10^{-5}	21.83	4.88×10^{-6}	22.77	7.43×10^{-6}
25.25	1.61×10^{-5}	25.45	1.72×10^{-5}	25.52	6.64×10^{-6}	25.95	6.71×10^{-6}
28.66	1.43×10^{-5}	30.16	1.59×10^{-5}	29.22	6.36×10^{-6}	28.79	9.61×10^{-6}
32.27	1.19×10^{-5}	34.37	1.23×10^{-5}	33.67	6.44×10^{-6}	32.12	4.29×10^{-6}
36.84	1.14×10^{-5}	39.50	1.05×10^{-5}	38.97	5.74×10^{-6}	36.26	7.12×10^{-6}

B.2.3 Concrete to Sediment

Table B.16. Concentrations of Tc-99 in sediment from FY 1999 concrete-sediment half-cell experiments

64 Day Testing				169 Day Testing			
4% Moisture Content Sediment		7% Moisture Content Sediment		4% Moisture Content Sediment		7% Moisture Content Sediment	
Distance from Face (cm)	Tc-99 (mg/g sediment)	Distance from Face (cm)	Tc-99 (mg/g sediment)	Distance from Face (cm)	Tc-99 (mg/g sediment)	Distance from Face (cm)	Tc-99 (mg/g sediment)
0.12	5.16×10^{-6}	0.29	9.32×10^{-6}	0.65	1.269×10^{-6}	0.52	4.84×10^{-6}
0.41	3.37×10^{-6}	0.83	1.03×10^{-5}	1.71	1.249×10^{-6}	1.27	5.08×10^{-6}
0.83	3.96×10^{-6}	1.44	9.80×10^{-6}	2.55	1.062×10^{-6}	1.77	4.62×10^{-6}
1.61	4.04×10^{-6}	2.03	7.81×10^{-6}	3.31	1.058×10^{-6}	2.24	4.45×10^{-6}
2.34	2.23×10^{-6}	2.45	7.53×10^{-6}	3.82	8.948×10^{-7}	2.75	4.12×10^{-6}
2.81	1.50×10^{-6}	2.92	5.37×10^{-6}	4.49	7.037×10^{-7}	3.29	3.80×10^{-6}
-	-	3.44	4.69×10^{-6}	5.47	5.744×10^{-7}	3.77	3.58×10^{-6}
-	-	3.93	3.74×10^{-6}	6.38	2.963×10^{-7}	4.24	3.35×10^{-6}
-	-	4.39	2.80×10^{-6}	7.60	1.328×10^{-7}	4.74	3.12×10^{-6}
-	-	4.88	2.53×10^{-6}	8.91	3.782×10^{-8}	5.23	2.86×10^{-6}
-	-	5.39	1.84×10^{-6}	-	-	5.65	2.58×10^{-6}
-	-	6.09	1.34×10^{-6}	-	-	6.34	2.12×10^{-6}
-	-	-	-	-	-	7.29	1.72×10^{-6}
-	-	-	-	-	-	8.29	1.21×10^{-6}
-	-	-	-	-	-	9.24	8.02×10^{-7}
-	-	-	-	-	-	10.24	5.24×10^{-7}
-	-	-	-	-	-	11.22	2.47×10^{-7}
-	-	-	-	-	-	12.07	1.34×10^{-7}
-	-	-	-	-	-	12.94	2.96×10^{-8}

Table B.17. Concentrations of Tc-99 in sediment from FY 2007 concrete-sediment half-cell experiments

Distance from Core (cm)	Tc-99 (mg/g sediment)	Distance from Core (cm)	Tc-99 (mg/g sediment)	Distance from Core (cm)	Tc-99 (mg/g sediment)
4% Sediment Moisture, Non-Carbonated 0% Iron		4% Sediment Moisture, Non-Carbonated 4% Iron		7% Sediment Moisture, Non-Carbonated 0% Iron	
-	-	0.00	6.29×10^{-6}	0.00	1.24×10^{-6}
0.25	7.96×10^{-6}	0.25	3.29×10^{-6}	0.25	1.92×10^{-6}
0.75	8.05×10^{-6}	0.75	3.20×10^{-6}	0.75	2.11×10^{-6}
1.25	7.87×10^{-6}	1.25	3.02×10^{-6}	1.25	2.10×10^{-6}
2.00	7.85×10^{-6}	2.00	2.92×10^{-6}	2.00	2.26×10^{-6}
3.00	7.28×10^{-6}	3.00	2.41×10^{-6}	3.00	2.24×10^{-6}
4.00	6.49×10^{-6}	4.00	2.04×10^{-6}	4.00	2.34×10^{-6}
5.00	5.46×10^{-6}	5.00	1.62×10^{-6}	5.00	2.32×10^{-6}
6.00	4.57×10^{-6}	6.00	1.24×10^{-6}	6.00	2.40×10^{-6}
7.50	3.01×10^{-6}	7.50	7.46×10^{-7}	7.50	2.36×10^{-6}
9.50	1.96×10^{-6}	9.50	5.12×10^{-7}	9.50	2.74×10^{-6}
7% Sediment Moisture, Non-Carbonated 4% Iron		15% Sediment Moisture, Non-Carbonated 0% Iron		15% Sediment Moisture, Non-Carbonated 4% Iron	
0.25	1.29×10^{-6}	0.00	5.17×10^{-6}	0.00	6.95×10^{-6}
0.75	1.32×10^{-6}	0.25	5.23×10^{-6}	0.25	6.13×10^{-6}
1.25	1.30×10^{-6}	0.75	5.38×10^{-6}	1.00	6.48×10^{-6}

Distance from Core (cm)	Tc-99 (mg/g sediment)	Distance from Core (cm)	Tc-99 (mg/g sediment)	Distance from Core (cm)	Tc-99 (mg/g sediment)
2.00	1.53×10^{-6}	1.50	5.18×10^{-6}	2.00	7.02×10^{-6}
3.00	1.42×10^{-6}	2.50	5.38×10^{-6}	3.00	6.61×10^{-6}
4.00	1.56×10^{-6}	3.50	5.45×10^{-6}	4.00	6.50×10^{-6}
5.00	1.67×10^{-6}	4.50	5.26×10^{-6}	5.00	6.31×10^{-6}
6.00	1.66×10^{-6}	5.50	5.30×10^{-6}	6.00	6.47×10^{-6}
7.50	1.84×10^{-6}	7.00	5.02×10^{-6}	7.50	6.02×10^{-6}
9.50	1.89×10^{-6}	9.00	5.19×10^{-6}	9.50	5.95×10^{-6}

B.2.4   Fractured Concrete to Sediment

Table B.18. Concentrations of Tc-99 in concrete from fractured concrete-sediment half-cell experiments

Distance from Face (mm)	Tc-99 (mg/g concrete)	Distance from Face (mm)	Tc-99 (mg/g concrete)	Distance from Face (mm)	Tc-99 (mg/g concrete)	Distance from Face (mm)	Tc-99 (mg/g concrete)
4% Sediment Moisture, Non-Carbonated 0% Iron		4% Sediment Moisture, Non-Carbonated 4% Iron		4% Sediment Moisture, Carbonated 0% Iron		4% Sediment Moisture, Carbonated 4% Iron	
0.55	8.57×10^{-5}	0.5	4.50×10^{-5}	0.63	3.84×10^{-5}	0.75	2.54×10^{-5}
2.34	1.65×10^{-4}	2.16	6.35×10^{-5}	2.34	1.29×10^{-4}	2.46	6.01×10^{-5}
4.40	1.22×10^{-4}	4.17	4.82×10^{-5}	4.22	8.75×10^{-5}	4.27	4.93×10^{-5}
6.26	1.24×10^{-4}	6.06	6.14×10^{-5}	6.06	7.75×10^{-5}	6.21	6.09×10^{-5}
8.07	1.05×10^{-4}	7.97	8.31×10^{-5}	7.79	7.15×10^{-5}	7.92	7.72×10^{-5}
9.78	9.72×10^{-5}	9.88	6.31×10^{-5}	9.55	8.49×10^{-5}	9.75	5.96×10^{-5}
11.64	1.03×10^{-4}	11.81	5.50×10^{-5}	11.26	1.11×10^{-4}	11.71	5.63×10^{-5}
13.62	8.95×10^{-5}	13.9	4.30×10^{-5}	12.97	9.39×10^{-5}	13.67	4.72×10^{-5}
15.91	6.94×10^{-5}	16.08	4.24×10^{-5}	15.43	6.87×10^{-5}	15.53	4.35×10^{-5}
21.69	6.46×10^{-5}	21.72	3.29×10^{-5}	21.52	6.09×10^{-5}	21.44	2.90×10^{-5}
4% Sediment Moisture, Non-Carbonated 8% Iron		4% Sediment Moisture, Non-Carbonated 12% Iron		4% Sediment Moisture, Carbonated 8% Iron		4% Sediment Moisture, Carbonated 12% Iron	
0.9	3.32×10^{-5}	0.65	2.21×10^{-5}	0.9	1.46×10^{-5}	0.85	1.13×10^{-5}
2.96	4.06×10^{-5}	2.74	3.82×10^{-5}	2.84	3.29×10^{-5}	2.79	2.96×10^{-5}
4.87	5.48×10^{-5}	4.95	4.35×10^{-5}	4.87	3.54×10^{-5}	4.62	5.09×10^{-5}
6.71	9.26×10^{-5}	6.78	5.16×10^{-5}	7.01	6.52×10^{-5}	6.46	6.08×10^{-5}
8.64	7.94×10^{-5}	8.54	5.30×10^{-5}	9.04	2.39×10^{-5}	8.47	5.52×10^{-5}
10.83	7.16×10^{-5}	10.63	3.74×10^{-5}	11.2	4.37×10^{-5}	10.68	4.66×10^{-5}
12.74	6.41×10^{-5}	12.99	4.10×10^{-5}	13.14	2.76×10^{-5}	12.86	3.98×10^{-5}
14.7	5.49×10^{-5}	15.57	2.63×10^{-5}	14.87	3.94×10^{-5}	14.92	4.56×10^{-5}
20.71	2.88×10^{-5}	21.83	2.13×10^{-5}	16.76	3.24×10^{-5}	20.78	2.57×10^{-5}
-	-	-	-	22.29	1.82×10^{-5}	-	-

Table B.19. Concentrations of Tc-99 in sediment from fractured concrete-sediment half-cell experiments

Distance from Core (cm)	Tc-99 (mg/g sediment)	Distance from Core (cm)	Tc-99 (mg/g sediment)	Distance from Core (cm)	Tc-99 (mg/g sediment)	Distance from Core (cm)	Tc-99 (mg/g sediment)
4% Sediment Moisture, Non-Carbonated 0% Iron		4% Sediment Moisture, Non-Carbonated 4% Iron		4% Sediment Moisture, Carbonated 0% Iron		4% Sediment Moisture, Carbonated 4% Iron	
0.25	5.55×10^{-7}	0.25	7.69×10^{-7}	0.25	9.11×10^{-7}	0.25	9.72×10^{-7}
0.75	6.11×10^{-7}	0.75	5.47×10^{-7}	0.75	4.12×10^{-7}	0.75	5.51×10^{-7}
1.50	5.92×10^{-7}	1.50	4.00×10^{-7}	1.50	4.06×10^{-7}	1.50	4.15×10^{-7}
2.50	4.25×10^{-7}	2.50	4.08×10^{-7}	2.50	4.14×10^{-7}	2.50	4.04×10^{-7}
3.50	4.07×10^{-7}	3.50	4.07×10^{-7}	3.50	4.02×10^{-7}	3.50	4.07×10^{-7}
4.50	4.05×10^{-7}	4.50	4.09×10^{-7}	4.50	4.10×10^{-7}	4.50	4.09×10^{-7}
5.50	4.15×10^{-7}	5.50	4.06×10^{-7}	5.50	4.09×10^{-7}	5.50	4.06×10^{-7}
7.00	4.08×10^{-7}	7.00	4.08×10^{-7}	7.00	4.08×10^{-7}	7.00	4.11×10^{-7}
9.00	4.09×10^{-7}	9.00	4.25×10^{-7}	9.00	4.09×10^{-7}	9.00	4.15×10^{-7}
4% Sediment Moisture, Non-Carbonated 8% Iron		4% Sediment Moisture, Non-Carbonated 12% Iron		4% Sediment Moisture, Carbonated 8% Iron		4% Sediment Moisture, Carbonated 12% Iron	
0.25	7.31×10^{-7}	0.25	6.09×10^{-7}	0.25	1.19×10^{-6}	0.25	7.39×10^{-7}
0.75	4.61×10^{-7}	0.75	4.60×10^{-7}	0.75	4.84×10^{-7}	0.75	4.92×10^{-7}
1.50	4.08×10^{-7}	1.50	4.08×10^{-7}	1.50	4.07×10^{-7}	1.50	4.02×10^{-7}
2.50	4.14×10^{-7}	2.50	4.20×10^{-7}	2.50	4.10×10^{-7}	2.50	4.12×10^{-7}
3.50	4.12×10^{-7}	3.50	4.10×10^{-7}	3.50	4.02×10^{-7}	3.50	4.05×10^{-7}
4.50	4.08×10^{-7}	4.50	4.24×10^{-7}	4.50	4.15×10^{-7}	4.50	4.19×10^{-7}
5.50	4.07×10^{-7}	5.50	4.08×10^{-7}	5.50	4.04×10^{-7}	5.50	4.10×10^{-7}
7.00	4.11×10^{-7}	7.00	4.12×10^{-7}	7.00	4.13×10^{-7}	7.00	4.11×10^{-7}
9.00	4.12×10^{-7}	9.00	4.15×10^{-7}	9.00	4.12×10^{-7}	9.00	4.16×10^{-7}

B.2.5 Sediment to Fractured Concrete

Table B.20. Concentrations of Tc-99 in sediment from sediment-fractured concrete half-cell experiments

Distance from Core (cm)	Tc-99 (mg/g sediment)	Distance from Core (cm)	Tc-99 (mg/g sediment)	Distance from Core (cm)	Tc-99 (mg/g sediment)	Distance from Core (cm)	Tc-99 (mg/g sediment)
4% Sediment Moisture, Non-Carbonated 0% Iron		4% Sediment Moisture, Non-Carbonated 4% Iron		4% Sediment Moisture, Carbonated 0% Iron		4% Sediment Moisture, Carbonated 4% Iron	
0.25	3.26×10^{-4}	0.25	2.76×10^{-4}	0.25	3.38×10^{-4}	0.25	3.62×10^{-4}
0.75	3.20×10^{-4}	0.75	2.75×10^{-4}	0.75	3.17×10^{-4}	0.75	3.34×10^{-4}
1.50	3.15×10^{-4}	1.50	2.68×10^{-4}	1.50	3.10×10^{-4}	1.50	3.19×10^{-4}
2.50	3.16×10^{-4}	2.50	2.36×10^{-4}	2.50	3.12×10^{-4}	2.50	3.17×10^{-4}
3.50	3.11×10^{-4}	3.50	2.72×10^{-4}	3.50	3.13×10^{-4}	3.50	3.22×10^{-4}
4.50	3.25×10^{-4}	4.50	2.80×10^{-4}	4.50	3.20×10^{-4}	4.50	3.16×10^{-4}
5.50	3.13×10^{-4}	5.50	2.81×10^{-4}	5.50	3.23×10^{-4}	5.50	3.27×10^{-4}
7.00	3.15×10^{-4}	7.00	2.90×10^{-4}	7.00	3.21×10^{-4}	7.00	3.22×10^{-4}
9.00	3.17×10^{-4}	9.00	2.90×10^{-4}	9.00	3.28×10^{-4}	9.00	3.23×10^{-4}
4% Sediment Moisture, Non-Carbonated 8% Iron		4% Sediment Moisture, Non-Carbonated 12% Iron		4% Sediment Moisture, Carbonated 8% Iron		4% Sediment Moisture, Carbonated 12% Iron	
0.25	3.33×10^{-4}	0.25	3.52×10^{-4}	0.25	3.19×10^{-4}	0.25	3.23×10^{-4}
0.75	3.30×10^{-4}	0.75	3.16×10^{-4}	0.75	3.14×10^{-4}	0.75	3.23×10^{-4}
1.25	3.17×10^{-4}	1.50	3.10×10^{-4}	1.25	3.14×10^{-4}	1.50	3.31×10^{-4}
2.00	3.18×10^{-4}	2.50	3.05×10^{-4}	2.00	3.03×10^{-4}	2.50	3.10×10^{-4}
3.00	3.15×10^{-4}	3.50	3.02×10^{-4}	3.00	3.13×10^{-4}	3.50	3.22×10^{-4}
4.00	3.06×10^{-4}	4.50	3.03×10^{-4}	4.00	3.10×10^{-4}	4.50	3.24×10^{-4}
5.00	3.14×10^{-4}	5.50	3.06×10^{-4}	5.00	3.12×10^{-4}	5.50	3.21×10^{-4}

Distance from Core (cm)	Tc-99 (mg/g sediment)	Distance from Core (cm)	Tc-99 (mg/g sediment)	Distance from Core (cm)	Tc-99 (mg/g sediment)	Distance from Core (cm)	Tc-99 (mg/g sediment)
6.00	3.05×10^{-4}	7.00	3.12×10^{-4}	6.00	3.16×10^{-4}	7.00	3.31×10^{-4}
7.50	3.12×10^{-4}	9.00	3.13×10^{-4}	7.50	3.14×10^{-4}	9.00	3.26×10^{-4}
9.50	3.20×10^{-4}	-	-	9.50	3.30×10^{-4}	-	-

Table B.21. Concentrations of Tc-99 in concrete from sediment-fractured concrete half-cell experiments

Distance from Face (mm)	Tc-99 (mg/g concrete)	Distance from Face (mm)	Tc-99 (mg/g concrete)	Distance from Face (mm)	Tc-99 (mg/g concrete)	Distance from Face (mm)	Tc-99 (mg/g concrete)
4% Sediment Moisture, Non-Carbonated 0% Iron		4% Sediment Moisture, Non-Carbonated 4% Iron		4% Sediment Moisture, Carbonated 0% Iron		4% Sediment Moisture, Carbonated 4% Iron	
0.50	5.34×10^{-5}	0.50	3.06×10^{-4}	0.40	7.45×10^{-5}	0.43	1.46×10^{-5}
2.29	1.11×10^{-4}	2.36	4.26×10^{-4}	2.16	4.01×10^{-5}	2.14	1.08×10^{-5}
4.45	5.18×10^{-6}	4.77	3.93×10^{-5}	4.07	2.61×10^{-5}	4.57	5.55×10^{-6}
6.63	4.30×10^{-7}	7.38	1.35×10^{-5}	5.98	8.52×10^{-6}	6.81	1.69×10^{-6}
8.67	8.73×10^{-7}	9.82	7.75×10^{-6}	8.04	4.69×10^{-6}	9.09	1.03×10^{-6}
10.53	2.88×10^{-7}	11.93	1.08×10^{-6}	9.93	2.45×10^{-7}	11.33	1.02×10^{-6}
12.41	1.52×10^{-6}	14.26	9.62×10^{-7}	12.06	2.38×10^{-6}	13.59	2.91×10^{-7}
14.75	2.38×10^{-7}	16.82	1.12×10^{-7}	14.20	1.89×10^{-6}	16.20	1.73×10^{-7}
17.63	9.68×10^{-8}	19.16	3.66×10^{-7}	16.48	1.41×10^{-6}	18.41	3.69×10^{-7}
23.74	9.80×10^{-8}	24.74	2.64×10^{-7}	22.64	5.96×10^{-7}	23.74	2.16×10^{-7}
4% Sediment Moisture, Non-Carbonated 8% Iron		4% Sediment Moisture, Non-Carbonated 12% Iron		4% Sediment Moisture, Carbonated 8% Iron		4% Sediment Moisture, Carbonated 12% Iron	
0.45	8.14×10^{-5}	0.75	1.48×10^{-4}	0.45	5.61×10^{-5}	1.05	1.96×10^{-5}
2.16	1.76×10^{-5}	2.76	3.16×10^{-5}	2.39	7.27×10^{-5}	3.16	1.02×10^{-5}
4.27	6.75×10^{-7}	5.17	2.15×10^{-6}	4.52	1.72×10^{-5}	5.05	4.83×10^{-6}
6.38	2.00×10^{-7}	7.71	7.32×10^{-7}	6.53	8.09×10^{-6}	6.91	2.39×10^{-6}
8.47	1.04×10^{-7}	9.84	4.20×10^{-7}	8.84	2.85×10^{-6}	8.54	1.75×10^{-6}
10.38	1.37×10^{-7}	11.95	2.42×10^{-7}	10.85	2.06×10^{-6}	10.5	6.78×10^{-7}
12.69	8.88×10^{-8}	14.26	7.87×10^{-8}	12.96	1.01×10^{-6}	12.69	4.97×10^{-7}
15.17	1.20×10^{-7}	16.67	7.16×10^{-8}	15.15	1.29×10^{-6}	14.77	5.05×10^{-7}
22.38	5.80×10^{-8}	22.23	4.90×10^{-8}	17.38	1.29×10^{-6}	16.73	4.43×10^{-7}
				23.79	7.03×10^{-7}	21.87	2.23×10^{-7}